Design of Functional Membranes by Anodization of Valve Metals

Inaugural-Dissertation

zur Erlangung des Grades
„Doktor der Naturwissenschaften“
im Promotionsfach Chemie

am Fachbereich Chemie, Pharmazie
und Geowissenschaften der
Johannes Gutenberg-Universität Mainz

vorgelegt von
Hannes Kerschbaumer
geboren in Bielefeld

- 2014 -

Dekan: [redacted]

Erster Gutachter: [redacted]

Zweiter Gutachter: [redacted]

Tag der mündlichen Prüfung: 03.07.2014

Der experimentelle Teil dieser Arbeit wurde in der Zeit vom Juni 2010 bis Januar 2014 am Institut für Anorganische Chemie und Analytische Chemie der Johannes Gutenberg-Universität Mainz im Arbeitskreis von [redacted] angefertigt.

Für meine Familie

Danksagung

[redacted]

[redacted]

[redacted]

[redacted]

Contents

Auszug in deutscher Sprache **1**

Abstract in English **3**

1 Introduction **5**

1.1 Advantages of Nano Structuring 5
1.2 Electrochemistry as Approach for Self-Assembly 6
1.3 Aim of this Project: Filtration and Functional Membranes 8

2 Theory of Electrochemical Anodization **13**

2.1 Types of Electrochemical Oxidation Reaction on Valve Metal Surfaces 14
2.2 The Stages of Pore Formation 15
2.3 Parameters Driving the Pore Structure 16
2.4 Theory Behind the Self-Assembly of Anodic Oxides 17
2.5 Mathematic Models to Describe Pore Formation and Order 18
2.6 Specific Geometries Explained by the Theories 19

3 Anodization of Titanium **21**

3.1 Introduction 21
3.2 Electropolishing and Two-Step Anodization Procedure 21
3.3 Control of Pore Size and Membrane Thickness 26
3.4 ATO Membrane Formation 34
  3.4.1 Membrane Curling 34
  3.4.2 Back Side Pore Opening with HF 35
  3.4.3 Electrochemical Pore Opening 40
3.5 Conclusions and Outlook 42

4 Anodization of Aluminum **45**

4.1 Introduction and Technical Implementation 45
4.2 Electropolishing of Aluminum Foils 47
4.3 First Anodization and Dissolution of the Preliminary Oxide 49
4.4 Second Anodization and Examination of Reaction Parameters 52
  4.4.1 Impact of the Potential on the Pore Size 52
  4.4.2 Factors Influencing the Oxide Layer Thickness 63
  4.4.3 Exact Pore Size Determination: An Excursus 68
4.5 Creation of Self-Supporting Membranes (Pore Opening Procedure) 71

4.5.1 Conventional Wet Chemical Etching Approach 71
4.5.2 Modified Wet Chemical Etching Approach 76
4.5.3 Voltage Pulse Method 81
4.5.4 Pore Widening and Porosity Improvement 88
4.5.5 Impacts on the Channel Shape 93
4.5.6 Improvements toward Pore Shapes of Membranes Produced at Higher Voltage 101
4.6 Variations in Reaction Temperature 104
4.7 Surface Functionalization of AAO 110
4.8 Completed Synthesis of Testing Membranes 114
4.8.1 Screening of Membrane Parameters for the Subsequent Filtration Tests 115
4.8.1.1 Physical Performance Tests 115
4.8.1.2 (Bio-)Chemical Stability Tests 116
4.8.2 Evaluation of Different Filtration Set-Ups 118
4.8.3 Production of Alternative Filter Disc Sizes 121
4.8.4 Filtration of Nanoparticle Dispersions 125
4.8.4.1 Transport Processes through AAO Membranes 125
4.8.4.2 Filtration Tests with As-Prepared AAO Membranes 127
4.8.5 Concepts for an Intrinsic Stabilization of AAO Filtration Membranes 141
4.8.6 Efficiency and Cost Aspects in the Membrane Production Process 147
4.9 Conclusions and Outlook 152

5 Anodization of Vanadium 157

5.1 Introduction 157
5.2 Synthesis of Porous Vanadium Oxide 159
5.2.1 Electropolishing of Vanadium Foils 159
5.2.2 Preliminary Work and Test of Anodization Conditions 162
5.2.3 Identification of the Oxide Layer 167
5.2.4 Variation of the Electrolyte Composition 169
5.2.5 Washing and Drying Procedures to Keep the AVO Layer 171
5.3 Characterization of AVO by XPS Studies 178
5.4 Application of Porous AVO in Catalysis 187
5.5 Conclusions and Outlook 190

6 Experimentals 193

6.1 Starting Materials and Electrochemical Equipment 193
6.1.1 Metal Foils and Chemicals 193

6.1.2 Electrochemical Setups and Equipment ... 194
6.2 Analytical Methods ... 199
6.3 Synthesis of Anodic Titanium Oxide (ATO) ... 203
6.3.1 Electropolishing (E) of Titanium ... 203
6.3.2 Anodization (A1, A2) of Titanium ... 203
6.3.3 Oxide Layer Separation and Wet Chemical Pore Opening Process ... 204
6.3.4 Electrochemical Pore Opening Process and Flattening of the Membranes ... 205
6.4 Synthesis of Anodic Aluminum Oxide (AAO) ... 205
6.4.1 Electropolishing (E) of Aluminum ... 205
6.4.2 Anodization (A1, A2) of Aluminum ... 206
6.4.3 Dissolution of the Preliminary Oxide Layer (DisO) ... 206
6.4.4 Back Side Pore Opening Process (PO) ... 206
6.4.5 Dissolution of Aluminum Base (DisA) and Pore Widening Procedure (PoWi) ... 207
6.4.6 Filtration Experiments with Nanoparticle Dispersions ... 208
6.4.7 Post-Treatments ... 209
6.5 Synthesis of Anodic Vanadium Oxide ... 210
6.5.1 Electropolishing of Vanadium Foils ... 210
6.5.2 Anodization of Vanadium Foils ... 211
6.5.3 Catalytical Activity of the Anodic Oxide ... 212

7 Appendix 215

7.1 Acronyms, Abbreviations ... 215
7.2 List of Figures ... 216
7.3 Aluminum ... 228
7.4 Vanadium ... 231

8 Bibliography 235

Auszug in deutscher Sprache

Thema dieser Forschungsarbeit ist die Herstellung selbst-ordnender, mesoporöser Oxid-Membranen aus den sogenannten Ventil-Metallen Aluminium, Titan und Vanadium durch einen elektrochemischen Oxidationsprozess. Die vielstufigen Synthesewege für die Erzeugung dieser „anodischen Metalloxide“ wurden auf Zuverlässigkeit, Effizienz und Oberflächen-Gleichmäßigkeit hin verbessert, mit dem beabsichtigten technischen Einsatz im Blick: Die anodischen Oxide von Titan (ATO) und Aluminium (AAO) wurden optimiert für den Einsatz in der Filtration, anodisches Vanadiumoxid (AVO) wurde hinsichtlich der Anwendung als katalytische Membran mit großer Oberfläche entwickelt.

Ventil-Metall	Porendurchmesser (Oberfläche) / nm	Membranstärke / µm
Titan	30 – 90	7 – 25
Aluminium	30 – 90	7 – 70
Vanadium	50 – 60	~3

Alle beabsichtigten Filtereigenschaften wurden mit AAO-Membranen erreicht und bis zu einer Fläche von 7 cm² demonstriert: dünn, aber mechanisch stabil und selbsttragend, gleichmäßig über die gesamte Oberfläche und hochporös mit einer engen Porengrößeverteilung. Im Gegensatz zum porösen AAO fehlt ATO lediglich die notwendige mechanische Stabilität aufgrund seines tubularen Aufbaus. Schlüssel zum Erfolg war in beiden Syntheserouten die Wahl des Schritts zum Öffnen der Poren auf der Rückseite der Membran. Elektrochemische Prozeduren erwiesen sich hier den konventionellen nasschemischen Ätzmethoden überlegen. Im Rahmen der Prozessoptimierung bei den AAO-Membranen wurde auch die elektrochemische Apparatur angepasst und eine neuartige, maßgeschneiderte Rotationselektrode eingeführt.

Die Form der Poren in der AAO-Membranen, die von der ideal zylindrischen Geometrie abweicht, wurde als ein Schwerpunkt dieser Arbeit erstmals tiefergehend untersucht. Außerdem wurde die mechanische Stabilität der hergestellten AAO-Membranen bis zu einem Bar Druck und deren Filtrationseigenschaften erfolgreich demonstriert. Mittels der hergestellten Membranen wurden Nanopartikel hinsichtlich ihrer Größe und Oberflächenladung getrennt.

Darüber hinaus beschreibt diese Arbeit die erst zweite bekannte Herstellungsmethode von geordnet porösem AVO, und damit die erste, die ohne HF auskommt. Die katalytische Aktivität des Oxids wurde in einem Peroxidase-Aktivitäts-Test bestätigt. Darüber hinaus wurde die chemische Natur des hergestellten AVO detailliert mittels XPS untersucht und als eine Mischung von hauptsächlich Vanadium(V) und (IV) bestimmt.

Abstract in English

The preparation of self-ordered mesoporous oxide membranes from the valve metals titanium, aluminum, and vanadium by means of an electrochemical oxidation process is the focus of this work. The multi-step synthesis protocols for these so-called anodic metal oxides have been optimized for reliability, efficiency, and surface uniformity with regard to the targeted technical use. Anodic oxides of titanium (ATO) and of aluminum (AAO) have been optimized for filtration applications; the anodic vanadium oxide (AVO) was developed toward a high-surface area catalytic membrane.

Valve metal	Surface pore diameters / nm	Membrane thickness / µm
Titanium	30 – 90	7 – 25
Aluminum	30 – 90	7 – 70
Vanadium	50 – 60	~3

All targeted filter properties – of being thin, but mechanically stable and self-supporting, uniform across a rather large area, and highly porous with a narrow pore size distribution – have been demonstrated with AAO up to an area of 7 cm². ATO lacks only the mechanical stability due to its more tubular meso structure versus AAO, where mechanical stability is conferred by its porous structure. The key to success in the synthesis protocols of both materials was the pore opening step at the back side of the membrane. Methods superior to conventional wet chemical etching approaches were found with different electrochemical pore opening routines. The process optimization of AAO filter membranes led to the re-design of the electrochemical setup by introducing a novel, tailored stirring electrode.

The shape of the pores in AAO membranes, which differ from the ideal cylindrical shape, has been investigated especially for AAO membranes in depth for the first time as a major part of this work. The mechanical stability of AAO membranes up to 1 bar and its filtration properties have been successfully demonstrated. Using AAO membranes, nanoparticles have been separated by their size and surface charge.

Furthermore, this work reports the second known preparation protocol for ordered AVO and is the first to use a HF-free route. Its catalytic activity was verified using a peroxidase activity test. Additionally, the chemical nature of the as-prepared AVO was elucidated in a detailed XPS study to be mainly a mixture of the two oxidation states, vanadium(V) and vanadium(IV).

1 Introduction

1.1 Advantages of Nano Structuring

Diminishing dimensions down to the nanoscale is an imperative consequence of the necessity to achieve smaller and smaller devices that satisfy the requests of the technological evolution (see Figure 1.1). Information storage technologies benefit from improved magnetic and optical properties of nanoparticulated materials. In ceramics made of pressed nanoparticles (NP), higher flexibility can be achieved vs. conventional materials. Moreover, nanoparticles improve the performance of batteries offering high-surface-area electrodes; its addition to polymers might have a reinforcing effect. In chemistry and medical sciences, a maximized specific surface area contributes to drastically accelerated reactions, e.g. in catalysis. In the area of therapeutic drugs, new solid state medicine in nanoparticle form may solve the frequent problem of the low solubility of pharmaceuticals in the bloodstream.[1]

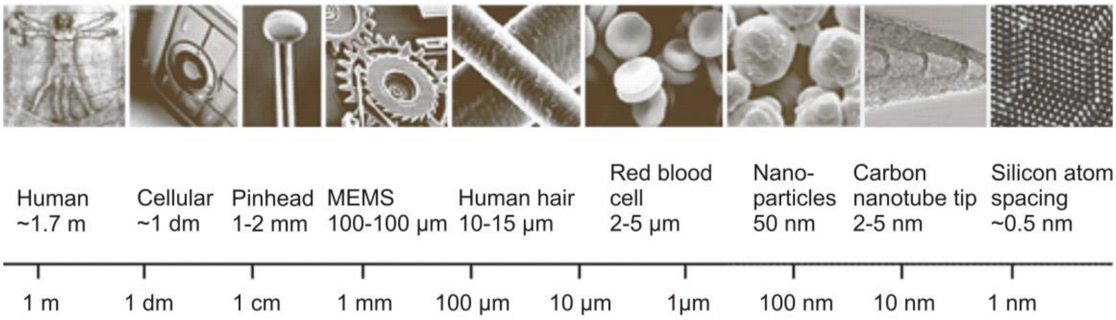

Figure 1.1: Illustration of dimensions down to the nanoscale.[2]

Beyond direct surface effects, nano materials often exhibit considerably altered electronic properties compared to the bulk phase, evoked by quantum size effects or surface curvature.

In particular, micro- or nano-structured transition metal oxides are not only valuable for catalysis and batteries, but also for electrochromic devices, solar cells and sensors where the size-tunable bandgap of semiconductor NPs is advantageous.[1,3]

The classical way to synthesize transition metal oxide nanostructures are sol-gel or hydrothermal approaches,[4] resulting in single particles or loose agglomerates dispersed in a solution. Especially in electrically contacted devices, anisotropic structures as nanorods or nanotubes may allow even higher chemical or physical control, for example offering an electron pathway to an electrode. However, layers formed of randomly oriented rods or tubes cannot take advantage of the anisotropy of the individual particles. Moreover, approaches mimicking biological nanostructures often lack the inherent materials-building properties typical for organisms. These properties are essential if nanostructures shall be organized across large domains and used as functional materials.[5]

Solving the mentioned challenges, self-organization processes represent a parallel method for surface design that does not require an active manipulation on the nano-scale as it is necessary when using slow and tedious sequential writing techniques. Self-organization or self-assembly generally describes the spontaneous organization of small subunits into larger scale ordered structures.[6] Self-Assembly is a process by which disordered parts build an ordered structure through only local interaction.[7] Most famous representatives on the nano scale are self-assembled monolayers (SAMs), monomolecular layers which spontaneously form e.g. when immersing a substrate into a solution containing amphifunctional molecules.[8] SAMs can be characterized as chemisorbed and physisorbed and can be generated also from the vapor phase.[9]

It is obvious that self-organized production processes attract a great scientific and technological interest as they are moreover accepted to be cost-effective.[4]

1.2 Electrochemistry as Approach for Self-Assembly

The electrochemical anodization approach may provide an array of self-organizing, well-defined oxide pores or nanotubes of high aspect ratios, aligned perpendicular to the substrate surface. Metal component parts of almost any shape can be covered with porous oxide, making the method extremely versatile and easy to scale up. The low-cost technique requires only direct-current voltage applied on the anodic substrate immersed in an appropriate electrolyte and has no demand for expensive experimental instrumentation. That is why anodization is for various purposes widely used since decades.

In a conventional way, the technique is used to protect metal from corrosion, to provide a decorative finish, to reduce the friction and prevent abrasion.[10] Already in the 1920s, anodization of aluminum was used on an industrial scale to produce an oxide layer that is thick enough to protect the underlying metal from further oxidation.[11]

Since the 50s, it is scientific knowledge that aluminum can be anodized in acidic electrolytes to form porous structures. Keller *et al.* described its morphology for the first time as an almost hexagonally close-packed structure consisting of a porous and a barrier Al_2O_3 layer.[12]

With technical improvements made in transmission and scanning electron microscopy, O`Sullivan, Thompson, Wood and coworkers developed an understanding of the significant steps in the growth mechanism of anodic aluminum oxide (AAO, see Figure 1.2).[13,14]

The successful use of porous aluminum oxide as a template for the synthesis of functional nanomaterials in the early 90s[15,16] was pushed by the milestone report of Masuda and Fukuda in 1995. Using very well defined anodization conditions and highly pure and pretreated aluminum substrates, a pore growth with a very high degree of self-organization was achieved. Key was a two-step anodization procedure in which the initial porous layer was removed to prepare the fundament for the second anodization.[17]

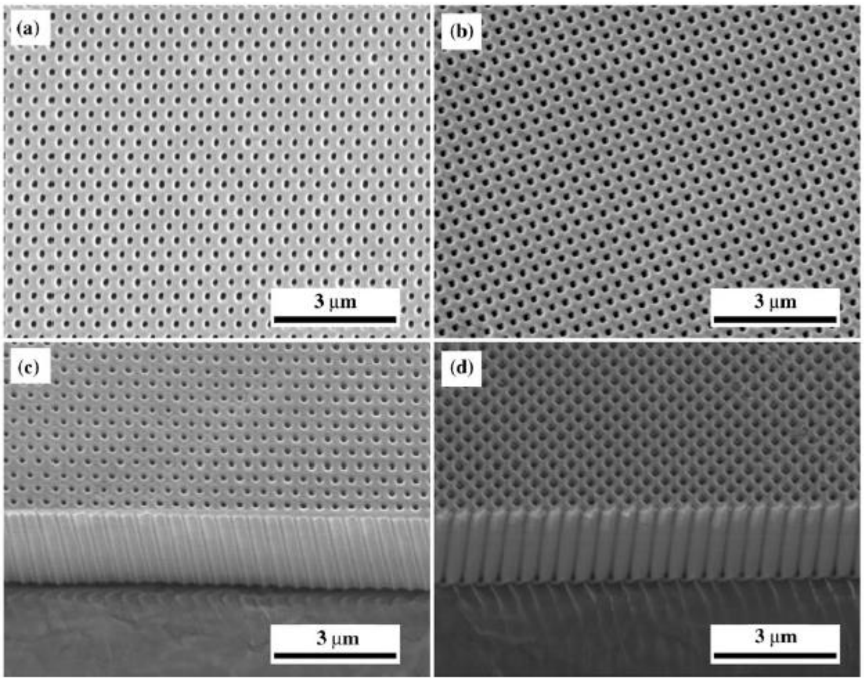

Figure 1.2: SEM images of long-range ordered AAO with (a, c) hexagonal and (b, d) square arrangement of nanopores, generated by imprint stamp pre-structuring.[18]

Since then, especially the “hard anodization method” invented by Gösele and coworkers provided improvements in terms of higher anodization speeds and widened the range of accessible pore parameters.[19,20]

In contrast to AAO, the growth of self-organized porous TiO_2 by electrochemical anodization was difficult to achieve due to its extraordinary chemical stability. Even though probably synthesized but not discovered earlier by Kelly *et al.*,[21] it was not until 1999 that Zwilling *et al.* presented porous anodic titanium oxide (ATO) by anodization in a HF-containing chromic acid electrolyte.[22,23] Key aspect was the discovery that fluoride ions support the formation of self-organized oxide structures.

Nowadays, a wide range of different metals, most often denoted historically as valve metals, was successfully anodized to form porous oxides. However, the definition is vague and it can just be stated that besides Al and Ti also Sn,[24] Nb,[25,26] W,[27,28] Zr,[29] Ta,[30] Fe,[31] Ni,[32] Hf,[33] V,[34] and numerous alloys were found to give promising anodization results.

Nevertheless, AAO and ATO are the most widely used materials for various applications, not only for its instrinsic chemical properties, but also for being able to provide fine-tuned pore diameters from about 10 to several 100 nanometers and oxide layer thicknesses of up to several hundred micrometers.[4,35]

The high self-ordering ability of AAO pores and their easy dissolution in either acids or bases makes AAO a popular template for the preparation of e.g. nanodots,[36] nanowires,[37] metal nanohole arrays,[17] and nanotubes.[38,39]

Metal nanowires produced in AAO templates can be used in lithium ion batteries, solar cells, energy storage and recording media, transistors and switches. Moreover, polymers and carbon nanotubes have been produced.[35]

The applications of ATO focus on the exceptional semiconducting properties of TiO_2, e.g. in dye sensitized solar cells,[40] water splitting,[41] photocatalyic degradation,[42] and sensors,[43] and its high biocompatibility, e.g. in drug delivery[44] and biomedical implants[45].

An additional application, which was not in the main research focus yet, is the use of anodic oxides as membranes and filters. The defined geometry of AAO or ATO can be exploited in case the oxide is separated from the metal substrate followed by opening the pore bottoms.[46] Depending on the specific transition metal oxide and on the potential functionalization with enzymes or synthetic catalysts, membranes can act as catalytic membrane filters with high reaction rates.[35]

1.3 Aim of this Project: Filtration and Functional Membranes

On the nanoscale, membranes and filters can interact in a differentiated manner with molecules depending on their size, shape, and charge. Nano- and mesoporous membranes are therefore promising platforms for fast and efficient separation. The key criteria for selective molecular transport through the filter membrane are high control of pore diameters, narrow size pore distribution, high porosity and tunable surface chemistry, all of which are fulfilled in anodic oxide membranes.

In the context of a joint research project with a commercial partner, Nanoscience for Life GmbH, it was planned to use the benefits of anodic oxide membranes for the nanofluidic separation of fatty acids from aqueous media. The concept of a dialysis technique comprises a continuous cross-flow diafiltration setup with peristaltic pump with the need for a specifically designed separation membrane. Main attributes of the membrane to be developed are pore diameters in the range of ideally 20 – 40 nm of high monodispersity and an overall high porosity. Additionally, the filtration membrane should provide an easy access to further functionalization. Both, small pore size and surface functionalization, accommodate the essential interactions between pore wall and targeted biomolecules to achieve the desired high selectivities.

Most commercially available membranes, e.g. from cellulose acetate, glass fiber, or polytetrafluoroethylene (PTFE), possess a random network of pores with a wide distribution of pore sizes. Moreover, they normally have a tortuous microstructure determined by the production processes.[47] For the above reasons those membranes are not suitable for the described separation purpose. Higher potential can be assigned to polycarbonate track-etched membranes, available with pore diameters from about 10 nm to 10 µm. While the scalability of these membranes is good, applications are in general limited by a low uniformity of pores and a porosity of only 5 – 15 %.[47,48] Another aspect is the low stability of polymeric membranes against heat and certain chemicals, e.g. organic solvents.

The commercial AAO membrane offered under the tradename Whatman® Anopore™ is the only one available in a suitable pore size of 20 nm as indicated by the supplier. However, scanning electron microscopy (SEM) images of such a Whatman® Anopore™ membrane revealed its disadvantages: The membrane consists mainly of a macroporous backbone with pore sizes of about 0.25 – 0.3 µm (see Figure 1.3 (a)) and only a very thin one-sided layer of mesopores (see Figure 1.3 (b, d)). Even though a high porosity is achieved by this geometry, intense interactions between permeate and pore walls are prevented. Aside from unwanted debris covering the membrane surfaces and defects in the mesoporous layer (see Figure 1.3 (c)), another disadvantage is the availability of these commercial membranes in 60 µm thickness only. To achieve high throughputs and reduce permeate loss, membranes should be as thin as possible without losing its mechanical stability.

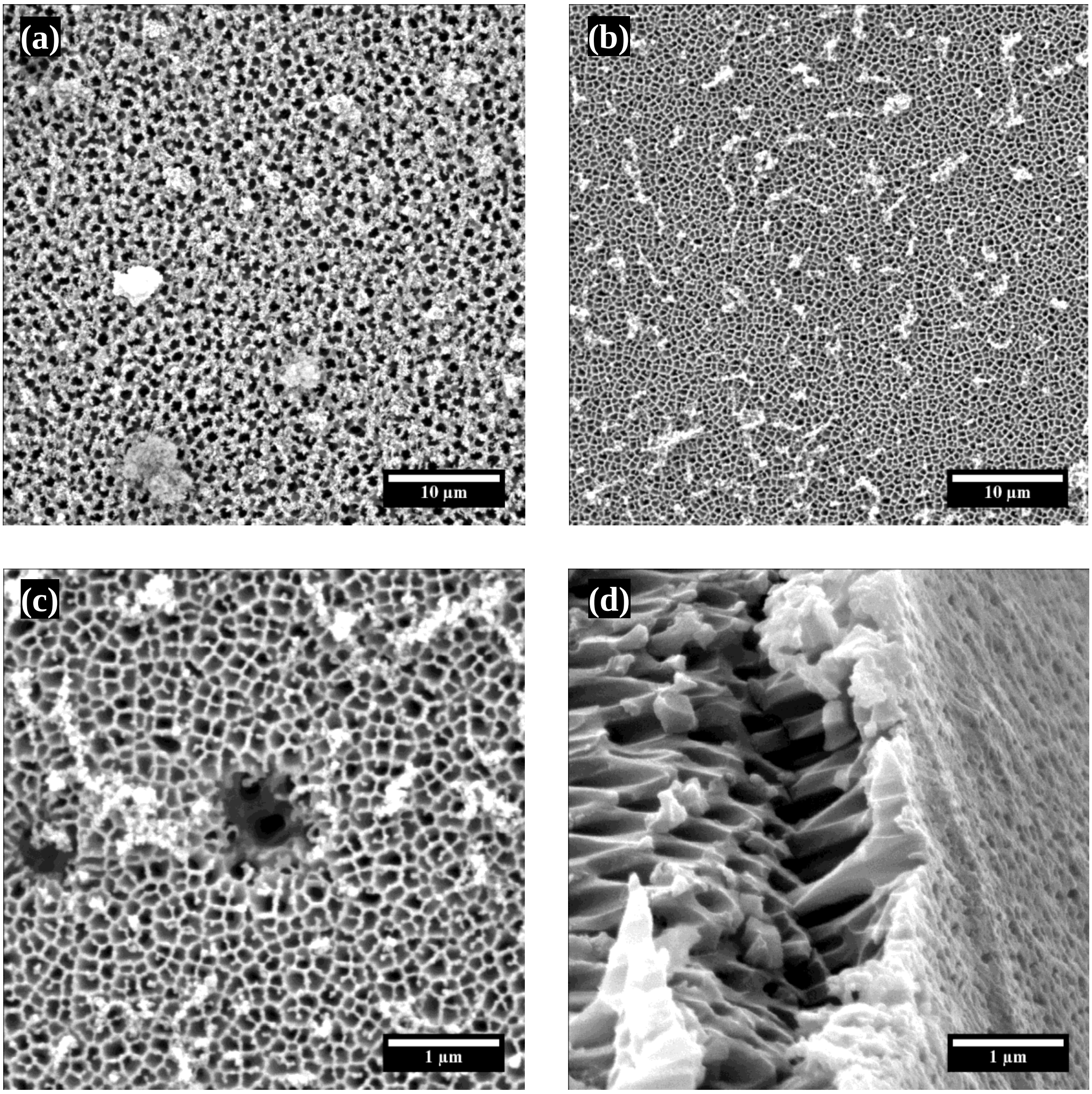

Figure 1.3: SEM images of a Whatman® Anopore^{TM} AAO membrane with pore size of 20 nm (manufacturer specification): (a) Macroporous side as backbone, (b) side with functional layer of mesopores, (c) defects in the functional layer, and (d) cross-sectional view on the thin functional layer.

Thus, the task of the present work was to explore the electrochemical anodization of aluminum, titanium, and vanadium for application as membranes. After an introduction to the theoretic principles of anodization (see Section 2), the work done to produce self-supporting ATO membranes is presented (see Section 3). In Section 4, a complete synthesis route for AAO filtration membranes is developed. The discussion involves approaches for further functionalization, the demonstration of the filter functionality with the separation of nanoparticle (NP) dispersions, as well as several concepts for further improvements. With the aim of extending the applications of anodic oxide membranes, Section 5 provides a new synthesis route for the anodization of vanadium and the use of the generated vanadium oxide in catalysis. The experimental Section 6 meets the need for a detailed description of setups and methods.

2 Theory of Electrochemical Anodization

This chapter gives a review about the basic principles of anodic oxidation of valve metals as well as an insight into the theories currently being discussed concerning the self-ordering effect during pore formation.

Most prominent representatives of oxides produced by anodic oxidation, so-called anodic oxides, are anodic aluminum and titanium oxide (AAO and ATO). Both types are by far the most investigated and research in this field is also a key aspect of the present work. Numerous review articles and reference books deal with the development in this broad discipline. Among more recent articles, the review of Md Jani *et al.*[35] and the contribution of Asoh and Ono[49] to AAO shall be mentioned on the one hand. On the other hand, the review articles by Schmuki and coworkes from 2009[4] and 2011,[46] as well as the very comprehensive book of Grimes and Mor[50] about ATO give a profound insight.

Concerning the principles and mechanisms for self-organization of anodic oxides, the growth of porous Al_2O_3 on aluminum is the best investigated system.

At first sight, the morphologies of AAO and ATO appear considerably different (see Figure 2.1): Porous AAO layers consist of hexagonally arranged pores, separated by solid walls. An ATO film in contrast is built up by a hexagonal array of nanotubes with double-layered wall structure. Only a bottom view on both anodic oxide layers reveals the analogy in structure. It is discussed that the distinct differentiation between the either as porous (AAO) or tubular (ATO) described appearance is not justified.[46]

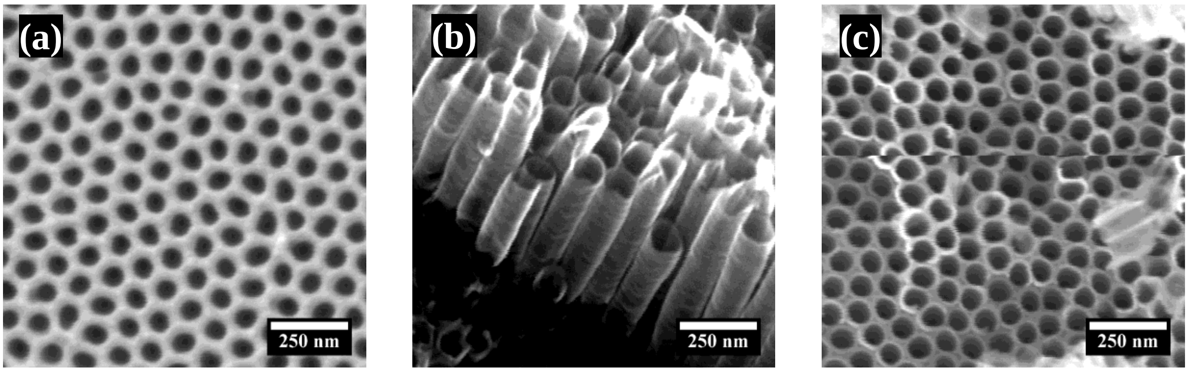

Figure 2.1: SEM images of (a) AAO and (b, c) ATO, showing the differences between both structural types.

Supported is this by a study on e.g. Ti/Al alloys showing that both morphologies can be created depending on the specific electrochemical conditions.[51,52] In consequence, principles and models developed for self-organized porous aluminum oxide can be transferred mostly to other anodic oxides, too.

2.1 Types of Electrochemical Oxidation Reaction on Valve Metal Surfaces

Valve metals applied as anode in an electrochemical reaction allow in general three different types of oxidation reaction, depending mainly on the electrolyte but also other anodization conditions:[46]

(I) If a particularly aggressive electrolyte is used or the formed oxide is soluble to a high degree in the electrolyte, corrosion will occur and the metal will be permanently dissolved. However, applying selected reaction conditions this effect can be used for an electropolishing of metal surfaces.

To enable a perfect self-ordering effect of the oxide pores, the metal foils as starting material have to be smooth and free from disturbing defect structures. Therefore, their surface has typically to be polished before anodization. The electropolishing can selectively remove higher points on the foil providing almost perfect polished metal substrates The reason for this is that the natural oxide layer on the metal is thicker in valleys and thinner on top of small bumps, leading to higher, respectively lower resistance to the electric field. Additionally, during the electropolishing reaction saturation of the surface with dissolved metal is highest over electrical microdepressions.[53]

(II) The process observed in most electrolytes is further passivation by forming a compact metal oxide layer. The metal ions that are anodically formed at the metal/oxide interface react with O^{2-} provided by H_2O in the electrolyte. With growing oxide layer, the electric field becomes weaker and reaches a finite thickness proportional to the applied voltage.[4] This finishing technique is industrially widely used to improve the surface properties of metallic component parts.

(III) Only by choosing the electrochemical conditions accurately, competition between solvatization and oxide formation is established, leading to self-organized pores in the growing anodic oxide. The growth follows a high-field mechanism implying metal and oxide ion migration, M^{z+} and O^{2-}, through the oxide. The migration rate of the ions determines if the growth of the new oxide proceeds at the metal/oxide or the oxide/electrolyte interface. With most experimental conditions the former is achieved.

The general electrochemical process can be represented by a set of chemical reactions, namely the metal ion formation (eq 2.1) and the reaction with O^{2-} by field aided deprotonation of H_2O or OH^- (eq 2.2 and 2.3) at the anode and the counter reaction at the cathode releasing hydrogen (eq 2.4).[46]

Anode:

$$\mathrm{M} \rightarrow \mathrm{M}^{z+} + z\,\mathrm{e}^- \tag{2.1}$$

$$\mathrm{M} + \frac{z}{2}\,\mathrm{H_2O} \rightarrow \mathrm{MO}_{z/2} + z\,\mathrm{H}^+ + z\,\mathrm{e}^- \tag{2.2a}$$

$$\mathrm{M}^{z+} + z\,\mathrm{H_2O} \rightarrow \mathrm{M(OH)}_z + z\,\mathrm{H}^+ \tag{2.2b}$$

$$\mathrm{M(OH)}_z \rightarrow \mathrm{MO}_{z/2} + \frac{z}{2}\,\mathrm{H_2O} \tag{2.3}$$

Cathode:

$$z\,\mathrm{H_2O} + z\,\mathrm{e}^- \rightarrow \frac{z}{2}\,\mathrm{H_2} + z\,\mathrm{OH}^- \tag{2.4}$$

In case of titanium, the presence of fluoride ions is necessary. On the one hand it is needed for the complexation of Ti^{4+} to form water soluble $[TiF_6]^{2-}$ species, and on the other hand to attack the generated TiO_2.[35] For aluminum, already an electrolyte of low pH is sufficient to create porous oxide layers. Besides the widely used oxalic acid, sulfuric, phosphoric, and also chromic acid are common etching agents.[54]

2.2 The Stages of Pore Formation

The stages of pore formation can be typically followed by the current-time curve for an anodization of aluminum or titanium. In general, four stages are differentiated according to Parkhutik and Shershulskii (see Figure 2.2):[55]

Stage I: At the beginning of the electrochemical oxidation, the natural oxide layer present on the metal surface is just increased to form a compact anodic oxide. The thicker film leads to higher electric resistivity and a fast exponential drop of the current density. In this phase, the current-time curve still follows the curve without etching agent in the electrolyte.

Stage II: Inhomogeneities and surface defects affect locally the electric field strength.

Stage III: As a result, localized field-assisted dissolution of the formed oxide occurs and first irregular pores start to form. This breakdown of the oxide layer leads to again increasing current.

Stage IV: The irregular pores serve as sites for further pore growth and under constant voltage conditions. Finally, a steady-state status is reached when pores uniformly cover the surface. Induced by limitations in diffusion due to the growing pore length, the current flow decreases to a greater or lesser extent with time.

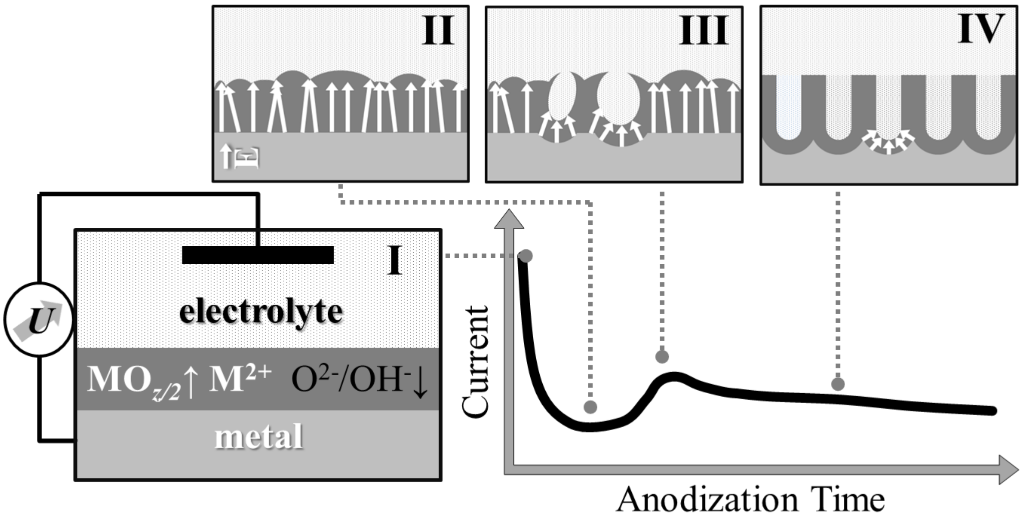

Figure 2.2: Current-time curve and model of the pore formation stages for AAO and ATO, in analogy to literature.[52]

2.3 Parameters Driving the Pore Structure

The regular pore structures can be characterized by parameters such as pore organization (e.g. hexagonal), pore diameter/size d, interpore distance d_I (cell diameter), wall thickness ($d_I - d$), and pore length, respectively oxide layer thickness h (see Figure 2.3).

In crystallographic terms, almost all produced anodic oxides were reported to be of amorphous nature.[56,57]

In general, the applied voltage controls the length scale of self-ordering, more exactly the pore or tube diameter and the interpore distance.[19,58] The anodization time and etching rate define the pore length, respectively the oxide layer thickness. In case of steady-state conditions (stage IV), reaction period and pore length are linearly dependent.

In practice, installations with a beaker as reaction vessel, equipped with two vertical aligned sheet-shaped electrodes and eventually a stir bar, are typical. However, the setup design used for the electrochemical reactions is very crucial to the specific outcome of the performed reactions. Differences in reactor geometry and volume are the main reasons why anodization results in literature are difficult to compare. Because most setups work with a two-electrode array, inter electrode distances and areas have a huge impact on the potential drop. The electrochemical reactions in this work were conducted with two types of setups, introduced here as the so-called “PTFE Setup” and the “Cu-block Setup”, both described in detail in Chapter 6.1.2.

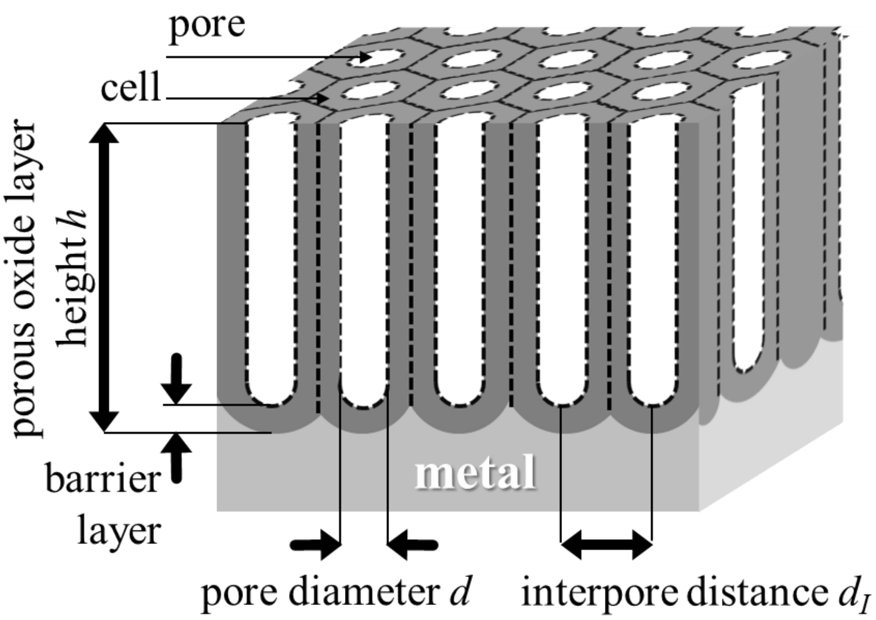

Figure 2.3: Model of porous anodic oxide showing characteristic parameters as pore diameter/size *d*, interpore distance d_I (cell diameter), wall thickness (d_I - d), and pore length, respectively oxide layer thickness *h*, in analogy to literature.[35]

2.4 Theory Behind the Self-Assembly of Anodic Oxides

The reason why pores grow at all and even in a highly self-ordered manner is not fully understood yet, but there are many approaches made in the past to develop theoretical models that lead to quantifiable experimental data.[46] In general, the self-organized arrangement of neighboring pores in hexagonal arrays is most likely attributed to any kind of repulsive interaction between the pores.

For AAO, O’Sullivan and Wood stated already in 1970 that the steady-state barrier-layer thickness (stage IV), cell diameter and pore diameter are all directly proportional to the formation voltage. The pore growth in general was explained by an arising equilibrium between the oxidation of metal by the anions of O^{2-} and OH^- on the one hand and the dissolution of the oxide on the other hand. As long as the oxide is thick, the dissolution reaction dominates due to the weak electric field. A thin oxide layer in turn accelerates the oxidization. This dissolution of the oxide at the pore bases is therefore field-assisted. Stronger, deeper pores grow faster due to the local higher current density there and the steady-state pore order is determined by the equilibrium under the field.[13]

Investigating the growth of ATO, Schmuki and co-workers identified the oxide dissolution to be the dominant factor rather than the electric field aided ion transportation: The order and aspect ratio of oxide tubes was improved using buffered, neutral electrolytes or highly viscous electrolytes suppressing pH bursts at the pore bottom by decreased diffusion.[59,60]

The self-organized structure is explained as a result of an autocatalytic reaction: At the initial growth stage, when pores are not yet ordered and stronger and weaker pores coexist, the pore's inner surface available for further oxidation decides about the growth. In stronger pores with high surface, a larger amount of H^+ is produced according to eq 2.2a and 2.2b leading to further growth. The direction of the growth is affected by the neighboring pores, which likewise consume oxidizable area and prevent that the pores come closer together. The diameter of the nanopores for valve metals as a function of anodization voltage was moreover found to correlate linearly with the anodic growth factor, the oxide thickness that grows at a specific voltage in a valve metal.[61]

Ono *et al.* found, however, the maximum current-flow conditions as being the crucial pore ordering factor in 2004.[62] Su and Zhou argue in a similar way with the local strength of the electrical field in 2008. For both, ATO and AAO, the field strength in the wall or the bottom of an initiated pore is considered to be the same. A sidewards pore growth will then be observed until a high pore density is reached.[63]

Very often material stress is mentioned to be responsible for the self-ordering effect. On the one hand, mechanical stress is induced by the oxide growth: When aluminum or titanium are oxidized to AAO respectively ATO, the insertation of oxygen leads to expansion of the structure, which could be an origin of forces between neighboring pores.[46,64] On the other hand, stress by electrostriction, electrostatic stress induced by the application of an electric field to a dielectric material was calculated to play an important role.[65]

In 2006, a new concept was developed basing on experimental results, challenging the field-assisted dissolution as driving force of pore development for AAO: A tungsten tracer, incorporated into the aluminum metal substrate, showed an unusual distribution in the barrier layer of the AAO. In consequence, it was suggested that the pore formation was mainly due to flow of amorphous aluminum oxide from the barrier layer toward the cell walls, caused by compressive stress from electrostriction or volume expansion.[66,67]

2.5 Mathematic Models to Describe Pore Formation and Order

The concepts introduced so far result in a large part from experimental observations and are supported by mathematic models to describe spontaneous formation of ordered nanoscale porous structures during anodization.

Singh *et al.* proposed in 2006 a model of porous structures in AAO including contributions of elastic stress during oxide growth. A basic element of the theory is the Butler-Volmer relation, which describes the change of an electrochemical current when the electrode potential is changed. The difference between electrode and steady-state potential (stage IV) is the overpotential, exponentially depending on the current. Second basic element of Singh's model is the dependence of the activation energies of the oxide-electrolyte interface reactions on the Laplace pressure representing the surface energy. It was shown that elastic effects in the surface activation energies can result in a short-wave instability which can explain the formation of hexagonally-ordered pores.[68]

Stanton and Golovin, however, included electrostrictive forces instead of mechanical stress into their model. Aside from the Butler-Volmer relations, the Nernst-Planck equation to determine the flux of ions within the oxide was introduced. In doing so, the calculated compressive electrostrictive stresses could be decreased by an increase of the oxide surface area. They also realized a short-wave instability on a scale that matches better with typical self-ordering lengths compared to contributions of purely mechanical effects.[69]

Hebert *et al.* introduced the rather new concept of amorphous aluminum oxide flow into a model in which ion migration was driven by gradients of mechanical stress as well as electrostrictive forces. They suggested that the stress distribution due to the viscoelastic creep of the oxide could assist the pore ordering by regulating the motion of the metal/oxide interface.[70,71]

The huge number of discussed concepts and models, complementary of even opposed, clearly shows that much more research has to be done to understand this complex self-ordered growth of pores in anodic oxides.

2.6 Specific Geometries Explained by the Theories

The presented theories about the self-ordering of anodic oxides into periodic pore structures give furthermore explanations concerning the hemispherical shape of the pore bottoms, by either oxide volume expansion (mechanical stress), electric field line distribution or local acidity at the pore tips.[4] Moreover, the occurance of gaps when tubes are formed instead of pores in the anodic oxides is discussed. Yasuda *et al.* explain the gaps in tubular ATO with compressive and tensile stress. Depending on the high transport number of the cations in relation to the anions, vacancies are produced at the metal/oxide interface leading to free volume in the oxides.[61]

Otherwise, it is common knowledge that the chemistries of the inner and outer part of anodic oxide pores are significantly different, simply because electrolyte anions are incorporated into the inner part. For AAO it was found that only the outer part of the cell walls consists of pure

Al_2O_3. [72] Su *et al.* hold the inhomogeneous chemical composition of pores responsible for the forming of nanotubes. Analysis showed that the outer part of ATO is most likely from titanium oxide hydroxide, which can be further oxidized to dehydrated TiO_2. This dehydration between the walls of the pores forms the gap between the tubes.[63]

Albu *et al.* consider a fluoride rich layer present in the tube walls to be the origin for tube separation as the fluoride at the cell boundaries proliferates the dissolution in this point.[73] Implicating the concept of oxide flow as driving force for pore formation, the accumulation of fluoride at the cell boundaries could even be the result of the fluoride species migrating inwards.[46]

3 Anodization of Titanium

3.1 Introduction

In our workgroup, Dominik Koll started to investigate the formation of ordered nanotube layers of anodized titanium oxide (ATO) with focus on materials for dye sensitized solar cells.[74] He adapted reaction conditions published by Shin *et al.*[75] to homemade electrochemical setups. The “PTFE Setup” and the “Cu-block Setup” (detailed description of the setups is given in Chapter 6.1.2) provide the possibility to electropolish or anodize circular cut metal foils of typically 20 mm diameter in a controlled way from only one side. Inert electrolyte containers from polytetrafluoroethylene (PTFE) allow the use of any electrolyte, the distance between the electrodes can be fixed at different positions, and a reaction temperature control is achieved via internal or external cooling. Combining all advantages, these electrochemical cells outmatch more simple approaches widely used. Generally, descriptions of setups are rarely found in literature, although their designs have a huge impact on the results.

Titanium metal foils were electropolished in order to provide a flat substrate for the subsequent two-step anodization. Reaction parameters, e.g. the concentration of fluoride as the etching agent or the impact of the anodization voltage, were investigated. However, the work of Koll was limited to the examination of very thin ATO layers on top of the anodized Ti metal.[71] Nonsupported oxide or even pervious membranes were not produced yet.

Starting with the experiences from the previous work, it was decided to explore the potential of ATO for the membrane application described in Chapter 1.3. In addition to the mentioned high biocompatibility of anodic titanium oxide, its ability of self-cleaning from contamination upon exposure to ultraviolet (UV) light[76] could help to prevent membrane fouling.

3.2 Electropolishing and Two-Step Anodization Procedure

The as-purchased titanium foils, even though they are of high purity and quality, were rather rough and their surface was uneven, caused by the rolling of the metal (see Figure 3.1 (a, b)). This led to inhomogeneous growth of the titanium oxide films and would prevent the self-ordering effect of pores. In order to provide a smooth surface for the subsequent anodization, polishing of the titanium surface was performed. Electropolishing (E) was carried out using the Cu-block Setup with a titanium sheet cathode. By an alcoholic solution of perchloric acid at 30 V for 15 min, circular 20 mm titanium foils were polished at an active diameter of about 16 mm. At the anodic titanium foil, metal is dissolved and the surface reoxidizes immediately, in a side reaction oxygen is developed. At the cathode, strong hydrogen evolution takes place.[77]

The electrolyte was stored in the freezer to reduce the reaction rate right at the beginning, when the current flow was high. Over the whole reaction period, the temperature of the solution raised from about - 6 °C to almost room temperature (RT).

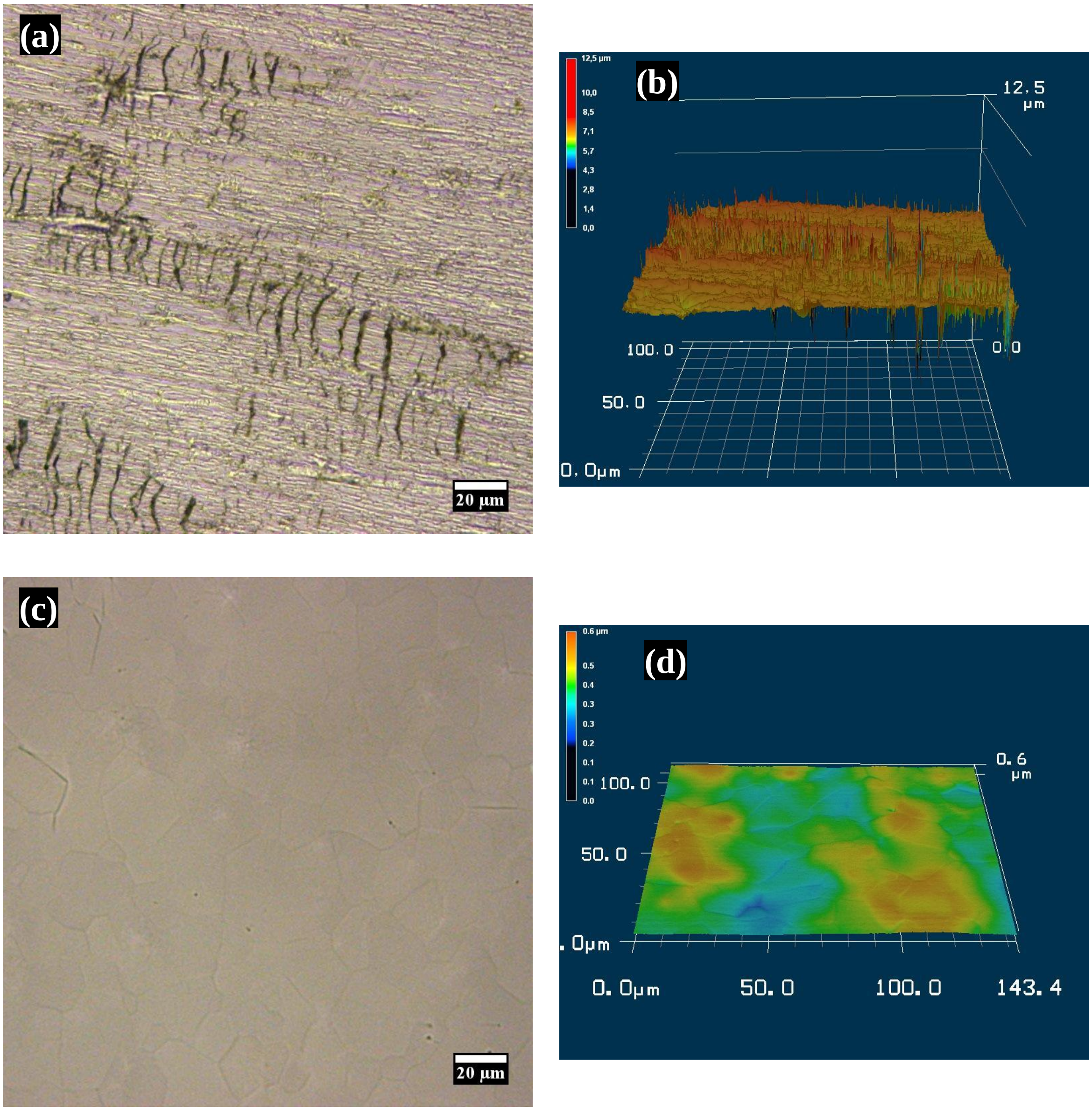

Figure 3.1: Light microscopy (a, c) and 3D topology laser scanning microscopy images (b, d) of a raw (unpolished) standard titanium foil (a, b) and a polished foil (c, d). The 3D images were extended 10-fold in z-axis.

Figure 3.1 (c, d) shows the result of the polishing. Monocrystalline grains of 10 – 20 µm in length became visible. The 3D topological laser microscopy picture pointed out a certain irregularity of the otherwise smooth surface (see also the SEM image in Figure 3.2 (a)).

Obviously, the chemical resistivity of the domains to the etching responds to the crystalline orientation. In particular, at the boundaries often intense etching could be observed. The surface roughness (see Chapter 6.1.2) of the titanium after the polishing was usually in the area of $R_q = 0.06 – 0.09$ µm.

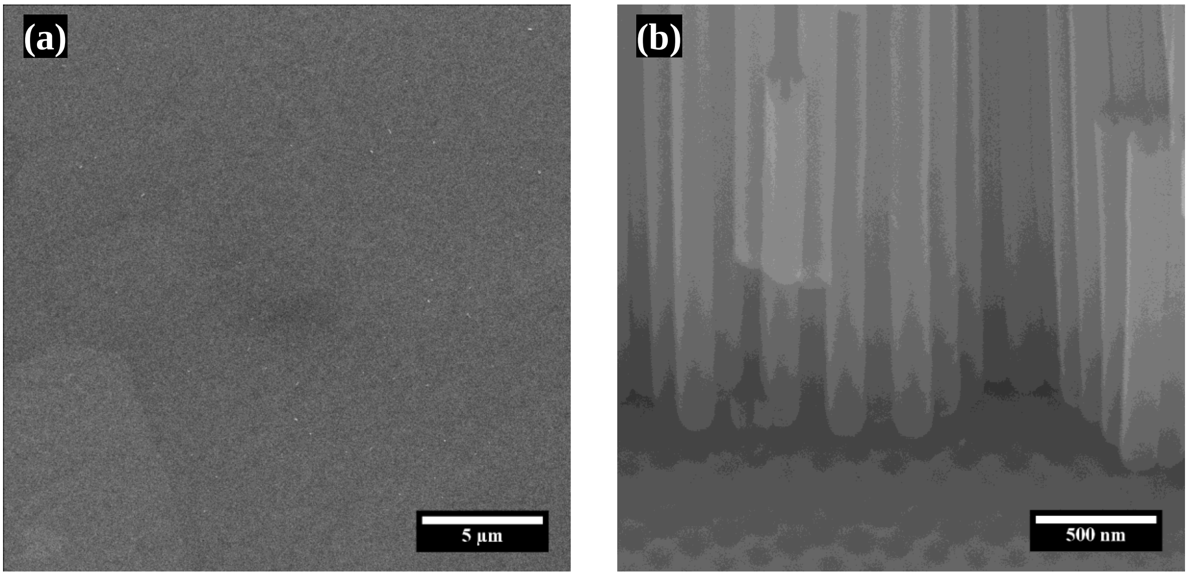

Figure 3.2: SEM images of (a) a polished titanium surface showing grains (different shading) and (b) the imprint pattern with sticking A1 oxide, produced at 50 V (A1).

Even though electrochemical labs provide the necessary equipment for electropolishing, the traditional mechanical finishing techniques are still often used. In the process, impurities on the metals’ surface, such as oil or grease that arise from the processing of the foil, are removed by electropolishing. Moreover, mechanically polished metal surfaces will always exhibit fine scratches caused by the abrading media.

The polishing was followed by the actual anodization. Taking a two-step procedure as a basis (see Section 2), a first anodization (A1) was aimed only at a prestructuring of the titanium foil. Thus, a high order of the pores was achieved directly from the beginning of the second electrochemical oxidation (A2). Because these steps in general were already described by Koll,[74] the discussion does not always go into details.

An electrolyte of ethylene glycol (EG) containing 0.38 % NH_4F and 1.79 % H_2O was employed. Instead of the Cu-block Setup, the PTFE Setup was used in combination with a graphite rod electrode being inert against the fluoride. Typically, the anodizations were performed at a constant temperature between 20 and 25 °C with only small impact of the exact temperature on the results. The reaction was started as soon as the setup, cooled by an external bath, was in a thermal equilibrium. In doing so, it was paid attention to a comparable time span maintained for each reaction.

Koll complied with Shin *et al.*[29] and used a reaction period of 3 h in A1 to create a well-ordered imprint pattern. Figure 3.2 b shows the base of the tubular ATO on top of the indentations in diagonal view. The indentations formed by a two-step process were reported to be about 30 nm in depth measured by atomic force microscopy (AFM).[78]

However, it was discovered that reaction periods of about only 1 h already were sufficient. Further decrease of reaction periods increased the risk that the formed preliminary oxide layer did not separate from the metal. Otherwise, the A1 oxide layer could be easily removed from the metal by attaching scotch tape and peeling off. The lacking adhesion of the two layers is explained with the lattice mismatch of both structures.[26] In some cases, the ATO was sticking in parts on the underlaying metal and the tape removed the oxide only partially leaving oxide tubes behind. Therefore, the adopted procedure was changed. Washing of the oxidized metal with highly volatile acetone and abrupt application of compressed air increased the chance to remove the whole oxide layer.

Following on the A1 anodization, a second (A2) was performed. A well-ordered porous structure was achieved, using the same voltage as before. Figure 3.3 shows the surface of A1 oxide in comparison to an ATO layer on the metal from A2 after only 5 min of reaction.

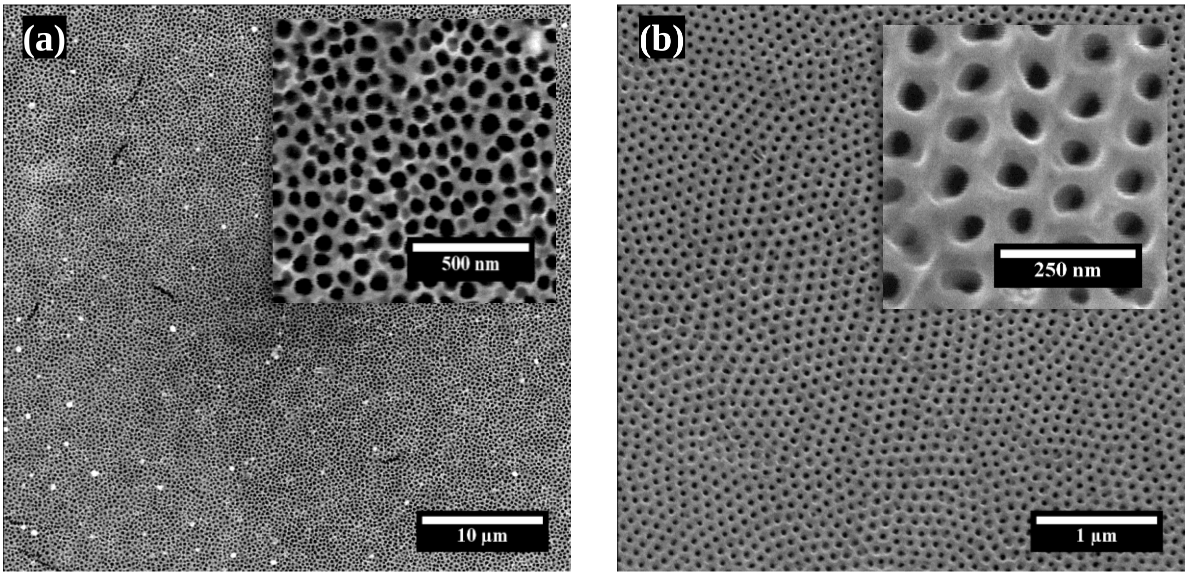

Figure 3.3: SEM images comparing the results of A1 and A2 anodizations at 50 V: (a) A1 oxide for 3 h and (b) A2 for 5 min reaction period. The insets show images with higher magnification.

The preliminary oxide showed no ordering, but a broad pore size distribution. In contrast, the A2 oxide often showed the ideal hexagonal order over large areas. Although ATO, compared to AAO, can be rather described as mesotubular material (see Figure 3.2 (b)), its appearance at the layer's surface is porous. It became obvious in cross-sectional studies that a thin oxide layer was finishing the tubular ATO, which is rarely described in literature. Macák assumed its origin from a stable rutile layer on the bare titanium foil. Long anodization time would dissolve the layer, therefore often not observed any more.[79] This is consistent with reports that electrochemical polishing of titanium led to a thin, perfect rutile layer.[80]

Short A2 anodization period led to adhesion of the formed thin oxide layer, its transparency and structuring resulted in interferencing colors (see Figure 3.4 (a)) as they were analyzed by Gu *et al.*.[81] The porous A2 oxide layers exhibited often superstructures framing the pore openings or even containing more than one pore (see Figure 3.4 (b)). As a secondary effect, the structures seemed to enhance the iridescence of the layer. But much more important, the self-ordering forces of the pores were corrupted.

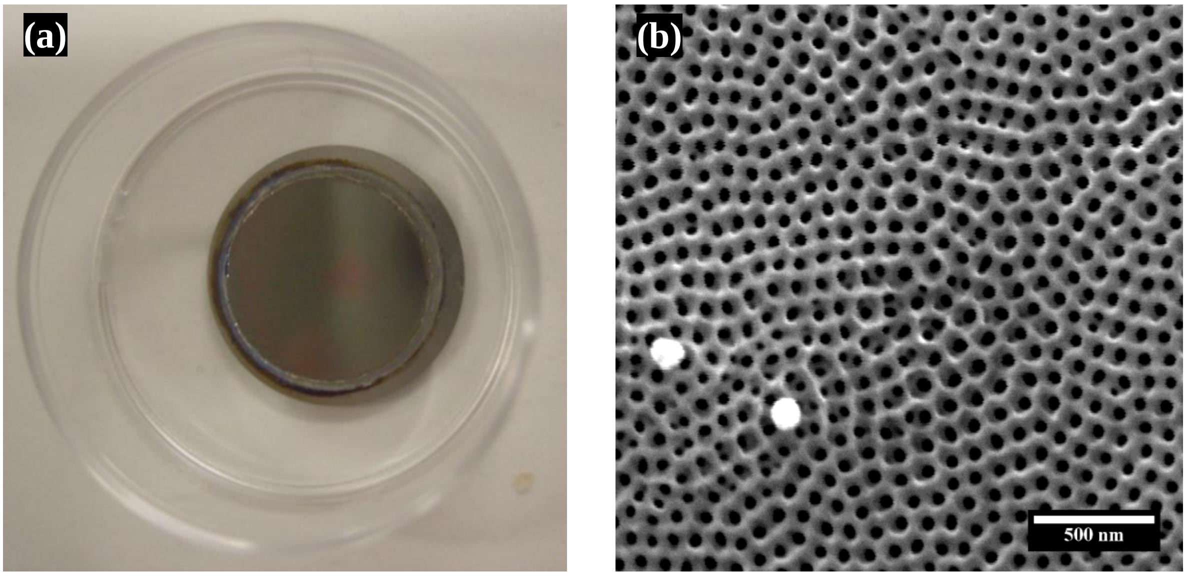

Figure 3.4: (a) Photograph of a thin ATO layer (A2, 50 V, 5 min) and (b) SEM image showing superstructures on its surface.

It is known from literature that for anodic aluminum oxide (AAO) non-parallel adjustment of the electrodes leads to inhomogeneous results by different electric field strength.[82] Therefore, the graphite cathode was mounted on the PTFE vessel of the setup by a newly constructed centering device, also keeping the inter-electrode distance perfectly the same. Concerning the superstructures, however, neither this change had any impact nor the temporary replacement of the electrode material by palladium, regarding results published by Allam *et al.*.[83]

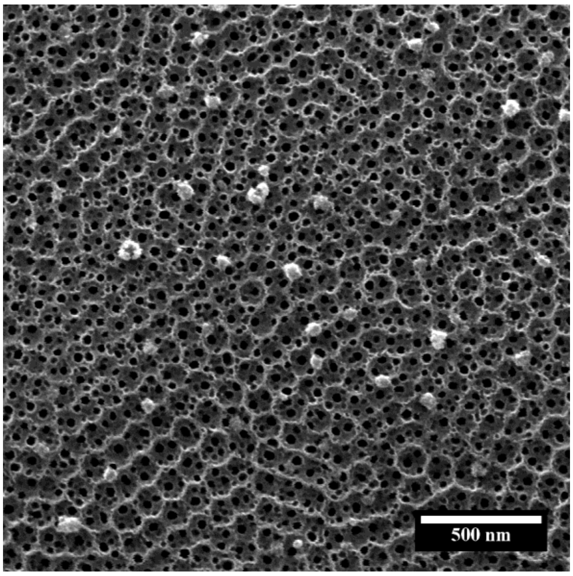

Figure 3.5: SEM image of ATO produced at 50 V for 5 min with initial potential ramp of 1 V/s, resulting in a hexagonal network superstructure.

Gradual increase of the voltage at the beginning of the anodization is often favored in literature to improve the pore order. However, experiments revealed a contrary effect to the superstructures by forming a distinct hexagonal network in the magnitude of about 100 nm on top of disordered pores (see Figure 3.5).

In conclusion, a certain presence of superstructures could not be avoided. It is likely that the polishing was not sufficient to provide a better control of the surface's smoothness. However, superstructures were not observed with the formation of thicker ATO layers being the object of the following chapter. The more intense chemical etching by the longer reaction time obviously dissolved the structures and smoothed the surface.

3.3 Control of Pore Size and Membrane Thickness

Koll described in his thesis the known correlation of pore diameter, in the following often described as pore size, and anodization voltage. The as-prepared ATO showed well-ordered pores in the range between 30 and 50 V, but low voltage of 20 V or high voltage of 80 V led to misorder.[74] In order to obtain oxide layers suitable for filtration applications, the reaction period of only 5 min was increased to result in thicker and more stable oxide layers. Possible combinations of pore sizes, inter-pore distances, and oxide layer thicknesses were recorded in a series of anodization reactions with varying anodization voltages, typically between 30 and 60 V, and different reaction periods. Figure 3.6 displays SEM images and corresponding pore sizes of ATOs produced by a 2 h reaction at different voltages. The pore diameters indicated in the graph represent typical values measured. Several pores with hexagonal surrounding in usually three or more different experiments were analyzed. However, the moderate contrast of SEM images and the slightly irregular shape of the pores prevented the calculation of a reliable pore size distribution. Therefore, no error bar is indicated even though a certain error is associated with the measuring process.

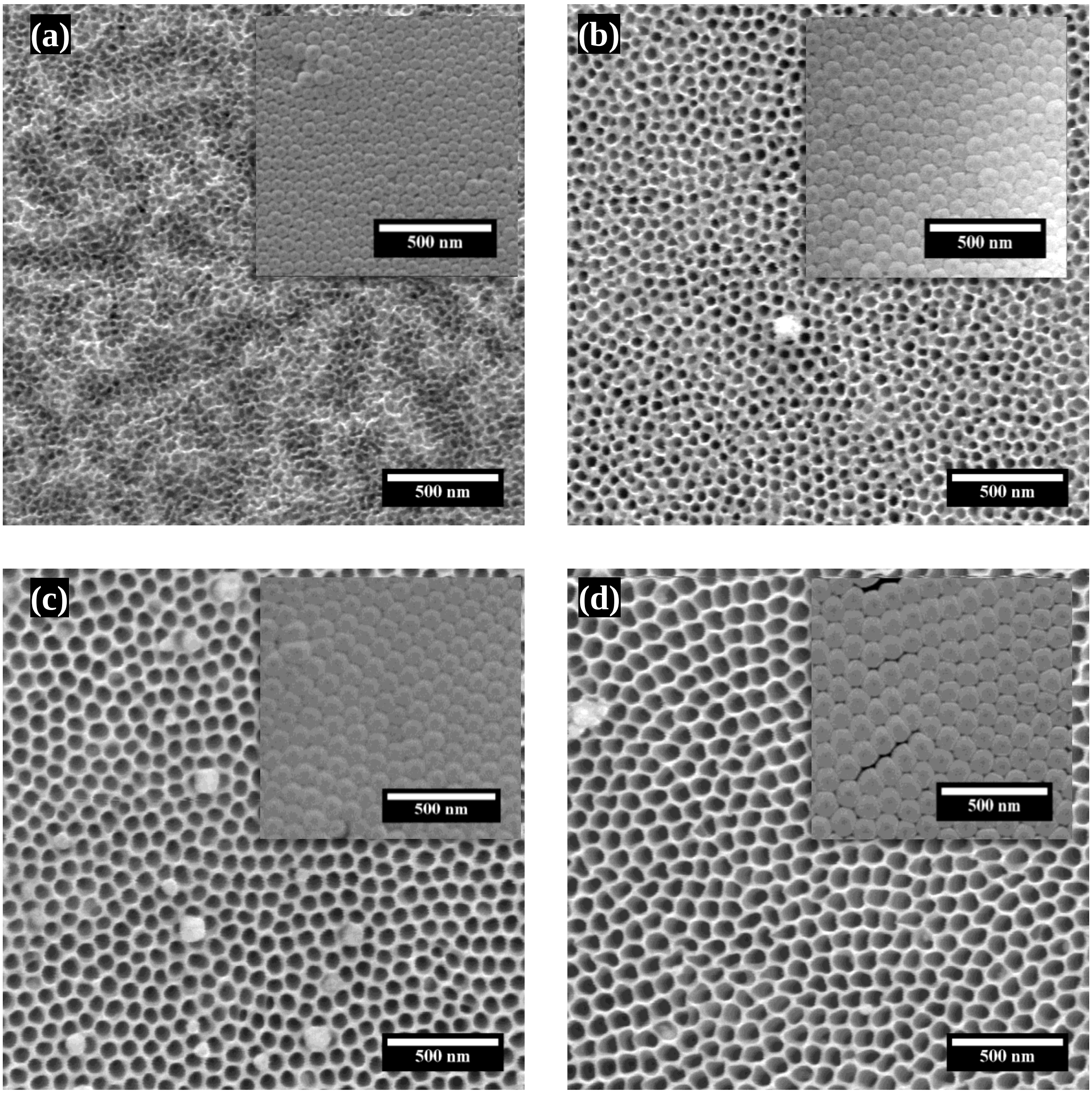

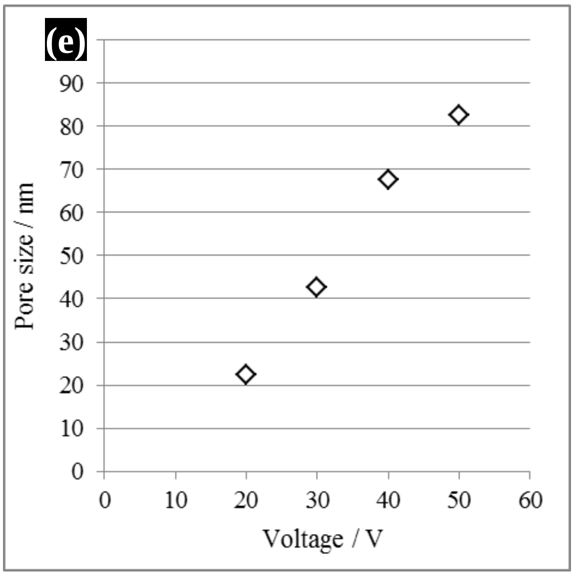

Figure 3.6: SEM images of ATO front side (insets show back side) produced with 2 h reaction period and an anodization voltage of (a) 20 V, (b) 30 V, (c) 40 V, and (d) 50 V; (e) plot of frontal pore diameter against the applied voltage showing a linear trend.

The pore sizes showed the expected linear dependency of the applied voltage (see Section 2). However, anodization with low 20 V gave already very poor results concerning pore shape and distribution. The improved thickness of the ATO layers by the extended reaction period led to self-peeling (see Figure 3.7).

Figure 3.7: Photograph showing the curling of thick ATO layers from the underlying metal.

Upon drying, the oxide layers separated from the metal by curling and showed notably at the front side increased crack formation (detailed discussion in Chapter 3.4.1). The back side was much more homogeneous and showed clearly the tube-like structure. The dark spot visible in the middle of the bottom view SEM images indicated the presence of a hollow space behind the barrier layer (see insets in Figure 3.6 (a – d)).

An increased pore size at the surface was not only observed upon elevated anodization voltage, but also for prolonged reaction periods. Chemical etching dissolved the pore walls gradually. Figure 3.8 gives an overview for the two anodization voltages, that is 40 and 50 V, which yielded the best ordered results. SEM images show the growth of pore diameter as a function of the treatment time. With increasing reaction period, the size of the pores grew until a maximum was reached, shown in Figure 3.8. The maximum pore diameter is dependent on the anodization voltage, which fixes the inter-pore distance. Circular pores visible at short reaction periods became hexagonal in shape with time (see Figure 3.9 (a)). Going beyond this limit, typically via a crimping surface as first indication, the tube walls were thinned out (see Figure 3.9 (b)). Finally, the formation of so-called nano grass was observed (see Figure 3.9 (c)).

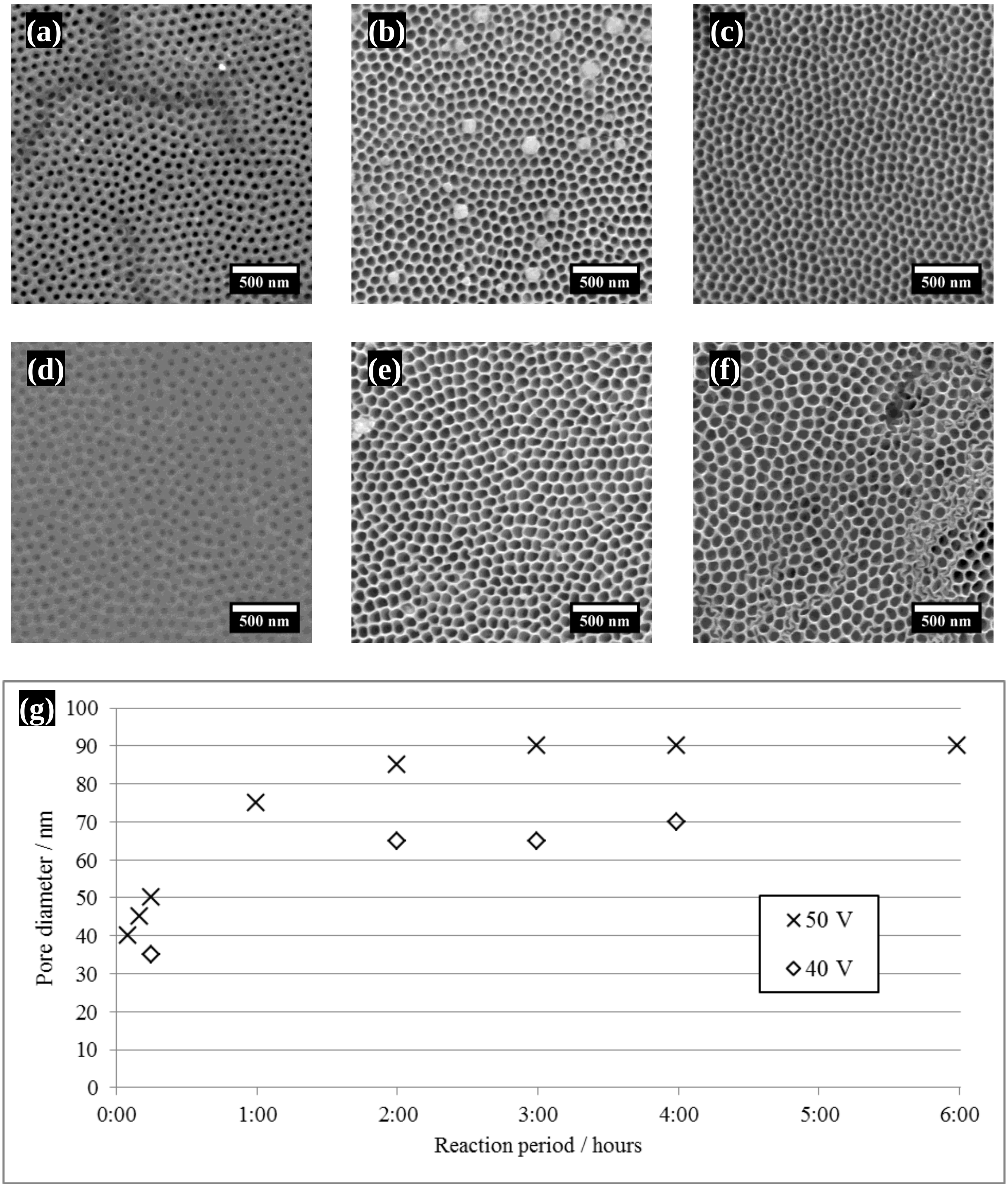

Figure 3.8: SEM images of ATO front side, produced at 40 V (a – c) and 50 V (d – f), the reaction period was 0.25 h for (a, d), 2 h for (b, e), and 4 h for (c, f); (g) plot of diameter against reaction period showing an approximation to a maximum value with time.

The outer tube diameter or cell size, as it was measured easily at the back side of the ATO, remained constant over the reaction period. The anodization at 60 V resulted in outer diameters of about 120 – 140 nm, 50 V in 100 nm, 40 V in 90 nm, and 30 V in 70 nm.

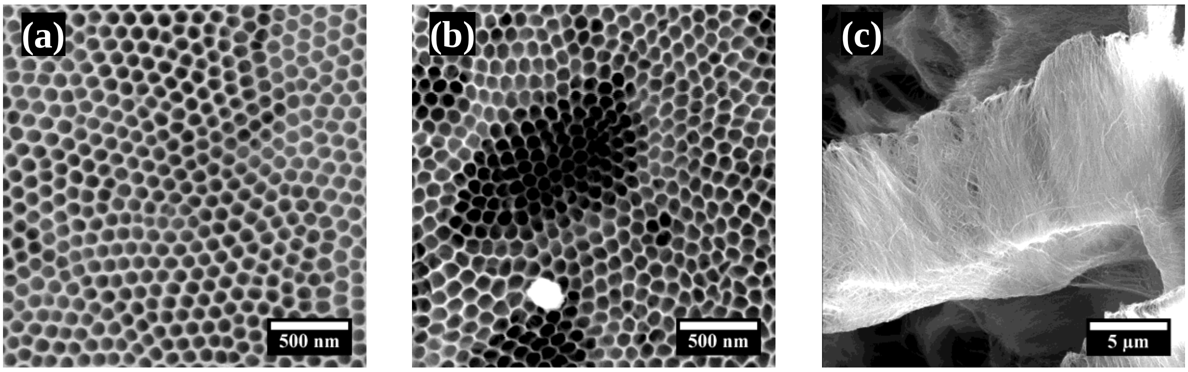

Figure 3.9: SEM images of ATO produced at 50 V in order (a – c) of an increasing reaction period, showing different stages of chemical etching: (a) hexagonal shaped pores, (b) crimping surface with starting degradation, and (c) nano grass forming at the front side as result of intense chemical etching.

However, TiO_2 nanotubes have never been observed instead of pores at the upper surface of the ATO. Figure 3.10 (a) shows the changeover of the tubular structure into the terminal porous layer. Nano grass formation often started underneath the top layer and was observed for longer reaction periods starting at 3 h or more. Therfore, in few cases the layer split off and found elsewhere on the sample surface. In Figure 3.10 (b), a large piece of a hexagonal network is shown which had been moved to the back side of the membrane.

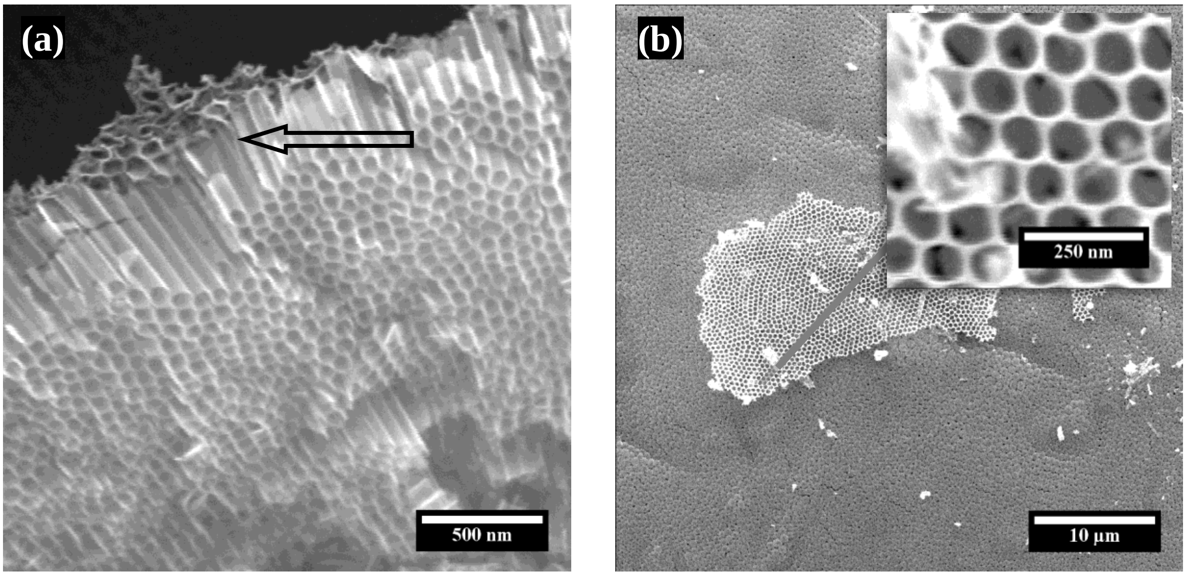

Figure 3.10: SEM images of the chemically robust porous top layer: (a) Layer covering the formed ATO tubes (see arrow) and (b) detached layer, as a result of nano grass formation, found on the ATO back side; the inset shows the network on top of back side tubes.

In order to reduce the chemical etching by lowering the reaction temperature, nano grass formation might be suppressed as well. However, experiments showed that the growth rate of oxide was slowed strongly by the reduced diffusion. As a result, the prolonged reaction period to maintain the thickness of the oxide layer compensated the effect of the reduced chemical etching. In literature, several examples for very thick oxide layers (> 100 µm), produced in dozens of hours, are reported (for further details see Chapter 3.4.3). Typically, the ATO layers were subsequently subjected to ultrasonically cleaning, in abdication of a homogeneous surface after the nano grass removal.[84,85]

Generally, the chemical etching implied a conical shape of the tube channels. The smallest size was observed at the bottom, only depending on the anodization voltage. The diameter widened with increasing oxide layer thickness and tube length. Figure 3.11 shows oxide tubes of a broken ATO layer produced at 45 V for 4.5 h. Close to the bottom, the inner diameter is about 30 nm in diameter, close to the front side it is 40 nm.

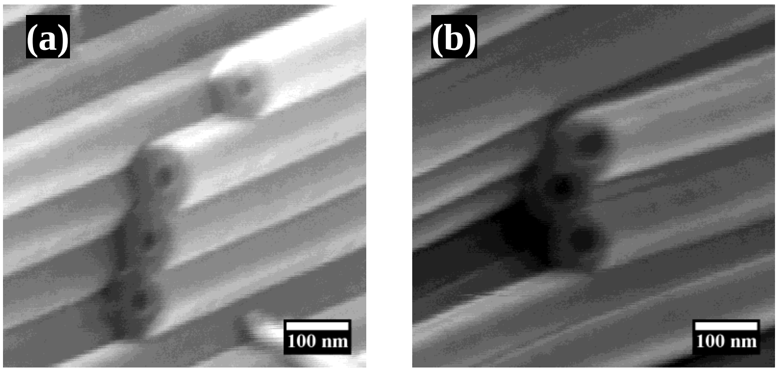

Figure 3.11: SEM images of ATO tubes produced at 45 V for 4.5 h, illustrating the dependency of the inner diameter on the layer thickness: (a) Cross section of tubes close to the back side with diameter of 30 nm and (b) cross section of tubes close to the front side with larger diameter of 40 nm.

The growth rate of the oxide layer slowed down with time (see Figure 3.12) and was found to be equal in A1 and A2 anodizations. This was less caused by the loss of material due to chemical etching, but rather an effect of the decelerated diffusion in the viscous solvent ethylene glycol (EG). All reacting agents had to be transported through the growing channels, limiting the exchange and, therefore, the reaction rate. In addition, the consumption of water as oxygen source as well as the inclusion of the etching agent fluoride into the oxide might have an impact. The SEM cross-sectional images revealed that for various combinations of anodization voltage and reaction period well-defined oxide layers with continuous channels were obtained.

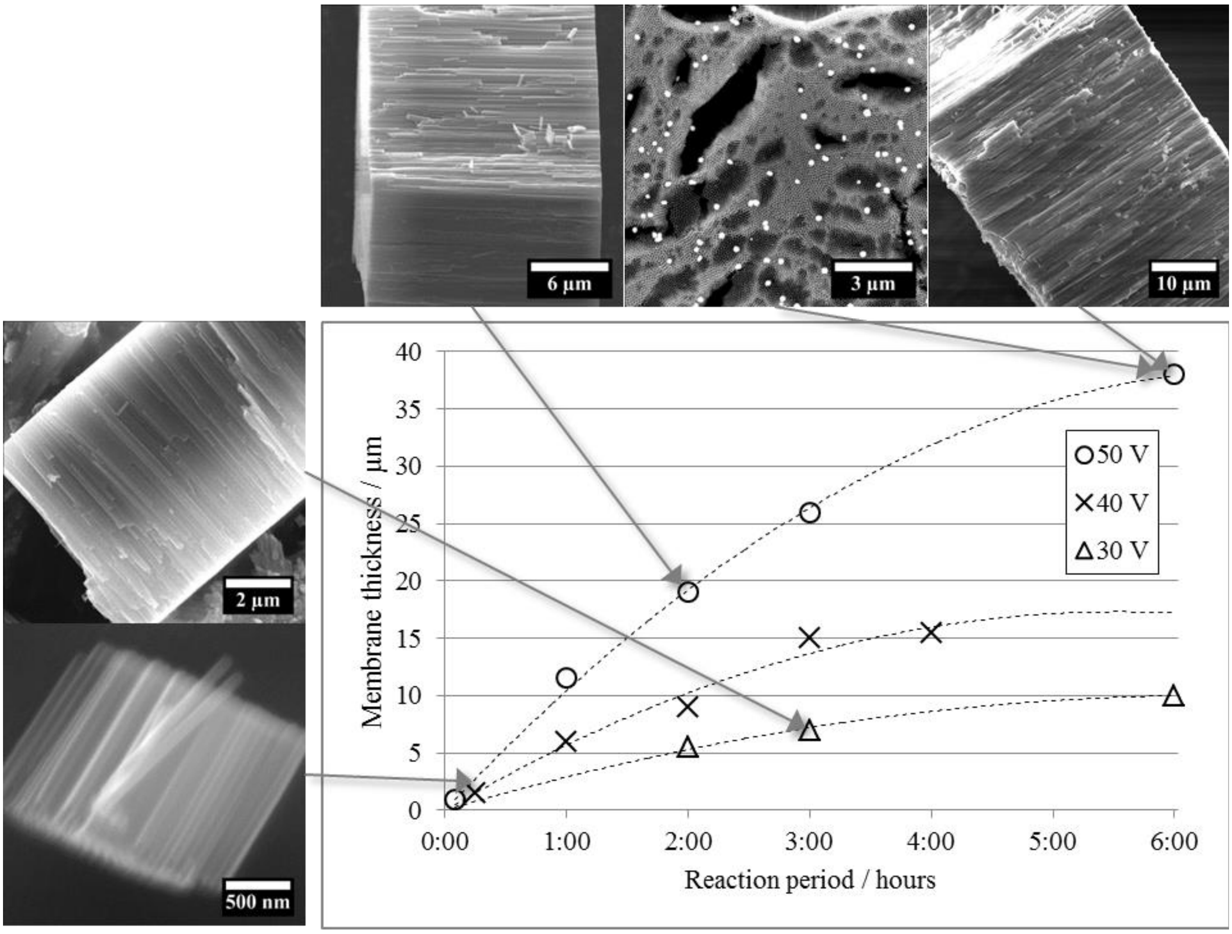

Figure 3.12: Plot of the ATO layer thickness as a function of the reaction period for 30, 40, and 50 V, showing a reduced growth rate with time. The insets show cross-sectional SEM images of variable reaction conditions; for 6 h reaction period, starting attack on the porous front side is shown too.

As a measure for the reaction rate, the current flow decreased with reaction period too. Figure 3.13 shows a current-time curve for an anodiaztion at 45 V that can be interpreted according to Section 2.

Even though identical reaction conditions were compared, the absolute values of the current-time curve varied considerably. Namely, the characteristic extremes, the interjacent interval, as well as the terminal point diversified. Obviously, the overall electric resistivity varied strongly, either by the foils themselves or by setup parameters, e.g. the electrical contacting. However, the actual current flow had no crucial influence on the measured oxide layer thickness thereafter. Thus, it was passed on a detailed analysis of the hight of current flow at different anodization voltages.

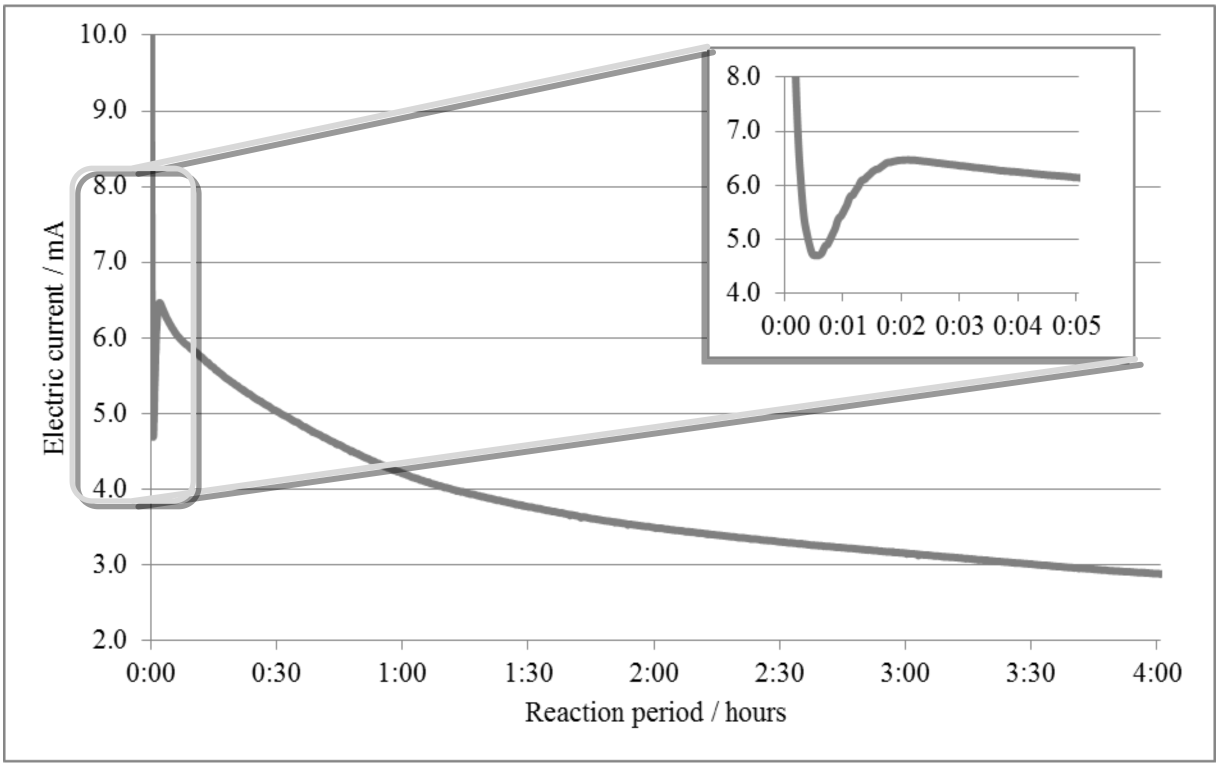

Figure 3.13: Current-time curve for a typical anodization at 45 V, the inset shows the progress of within the first 5 min when the pores start to form.

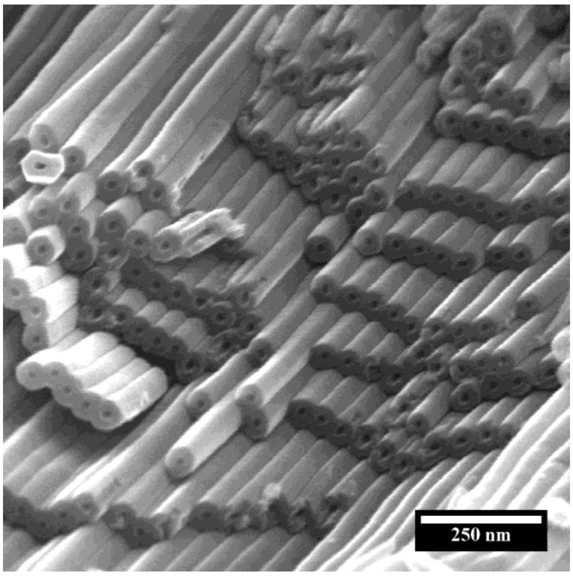

Figure 3.14: SEM image of a diagonal broken ATO layer (50 V, 2 h) showing explicit the tubular structure.

In the SEM cross-sectional image of a broken oxide layer, the splitting between the single tubes becomes obvious (see Figure 3.14). The weak spot is the adhesion of the single tubes at each other, rather than the hollow core of the tubes. That is why hardly fractured tubes were ever observed.

The anodization at 50 V for 2 h or at 30 V for 3 h reflected interesting examples for the planned filtration application with respect to layer thicknesses in the area of about 10 to 20 µm (see Figure 3.12). As mentioned before, the corrosiveness of the fluoride containing electrolyte increased the risk of surface destruction, especially if reaction periods exceeded 3 h. The example of a 6 h-anodization in Figure 3.12 already gave evidence of dissolution at the surface, even though the cross-sectional image showed no abnormalities yet. The oxide layer thickness could not be raised infinitely due to the dissolution as well as the diffusion limitation.

3.4 ATO Membrane Formation

3.4.1 Membrane Curling

As discussed earlier, a strong curling effect caused the detachment of the ATO from the subjacent metal, observed with oxide layer thickness of 2 µm or more (see Figure 3.15 (a)). This problem is often discussed in literature, as demonstrated by the following citation by Paulose *et al.*: “the resulting membrane only remained flat when wet, dramatically cracking, fracturing, and curling into many small pieces upon air drying”.[86] The curling was not only in conflict to a flat membrane suitable as filter, but also came along with unwanted cracks observed at the ATO surface (see Figure 3.15 (b)). Reason for the destructive curling can be found in stresses induced during anodic oxide film formation, in particular by volume expansion of the oxide in comparison to the metal.[87] As long as the electrolyte or other liquids wetted the porous oxide, the flat morphology was maintained.

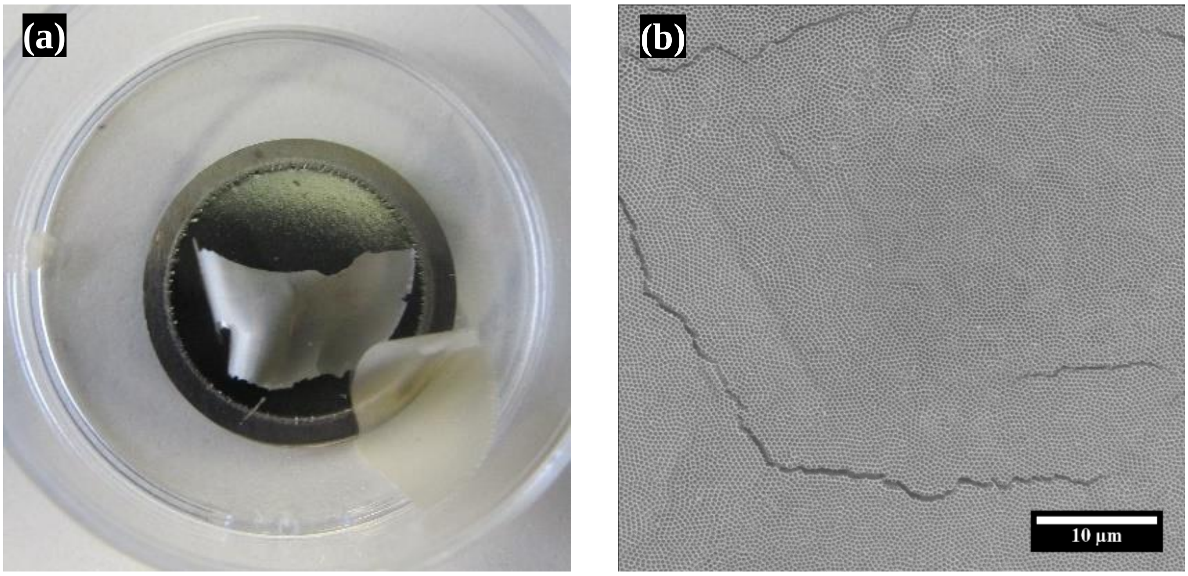

Figure 3.15: (a) Photograph of strongly curling oxide layer when separating from the metal in dry state and (b) SEM image of ATO surface exhibiting stress induced cracks.

In literature, approaches to avoid the curling are proposed. It is reported that wetting the layers after the anodization with low surface tension methanol before drying would prevent the curing.[78,85] The use of methanol instead of acetone for washing the oxidized foils from electrolyte, however, did not bring any difference. Further, the suggestion to use ultrasound for the separation of metal and oxide seems only to work for very thick oxide layers,[86,88] the as-prepared ATO layers were immediately destroyed by the high energy input. Besides the selective dissolution of the metallic substrate by a water-free CH_3OH/Br_2 solution[89] or the application of a CO_2 critical point drying as nonstandard method,[86] ideas concentrated on weakening the oxide-metal interface. Etching with HCl[90] or H_2O_2[91] is suggested, however, the application of an electrochemical method was proved to work with the as-prepared ATO layers. Liao *et al.* used a reverse-bias voltage of -2.25 V for 5 min in diluted H_2SO_4 to separate the oxide from the metal. The success was explained by small amounts of H^+ and F^- still present that would etch the barrier layer and lead to defects. In addition, H_2 gas generated by the process would promote the detachment.[92] The electrochemical approach has the advantage that it can performed subsequently to the anodization, only by exchanging the electrolyte. As a result, the ATO could be separated from the titanium and kept in solution without curling.

3.4.2 Back Side Pore Opening with HF

In order to obtain a filtration membrane, naturally the closed pore bottoms, the so-called barrier layer, had to be opened. Figure 3.16 illustrates the back side of ATO in different views, highlighting the round shape of the capped tubes and the hollow inside.

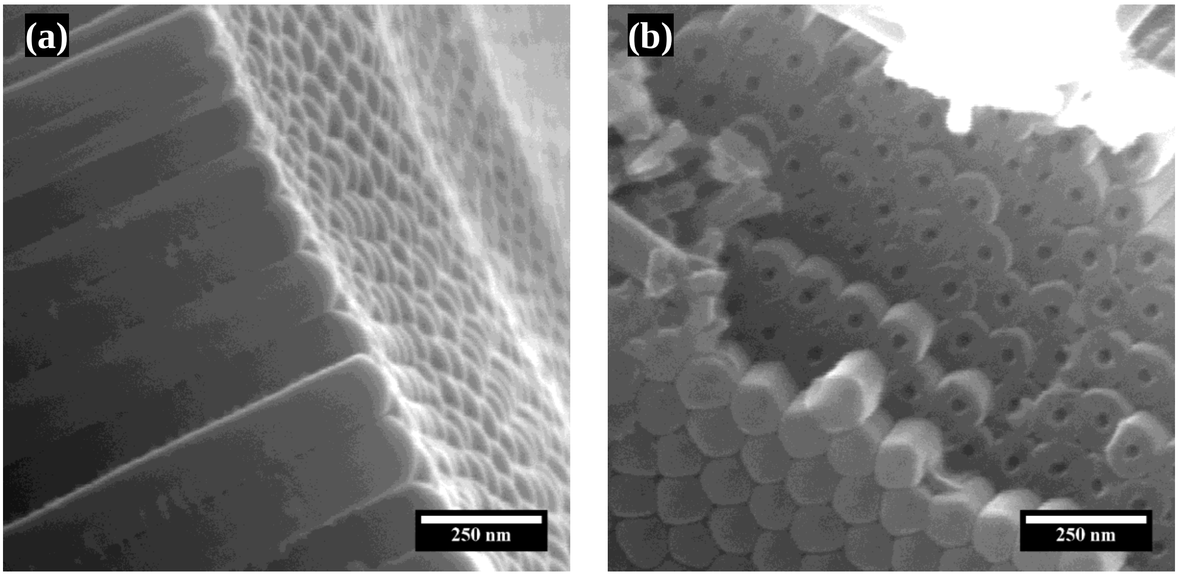

Figure 3.16: SEM images of the ATO back side (50 V, 2 h): (a) Pore bottoms as cross-sectional view with round-shaped caps and (b) bottom view of capped tubes and broken tubes showing the pores.

In literature, chemical etching is the predominating method. As etching agent, again only fluoride comes into consideration, and most often diluted solutions of HF are used. The following procedures were tested for their applicability: First, etching in 1 M H_2SO_4 containing 5 % NH_4F to form *in situ* HF was performed. Fang *et al.* obtained opened ATO membranes after 15 min of etching time.[88] Paulose *et al.* used a similar solution from H_2SO_4 and HF.[86] Second, the membranes were etched in 5 % aqueous HF solution according to Banerjee *et al.*[93]

For the tests, ATO layers of about 25 µm thickness, separated from the metal by the described reverse-bias method, were treated with the two etching solutions, but complete dissolution occurred within the first minutes. Further, a sub-10 µm oxide layer, kept floating backwards onto the 5 % HF solution, vanished even after 10 s. Consequently, the concentration of the etching solution was reduced to 2 % HF, and the result of the treatment was analyzed after only some seconds. Moreover, the ATO layers were brought backwards onto the solution to preserve the fluoride from unwanted etching of the front side. Even though several tests were made with oxide layers between 10 and 22 µm thickness, it was not possible to recapture only one single membrane as a whole. The surface tension of the solution always broke the weakened oxides, when they were removed from the solution. Further, SEM images documented the lacking suitability of this method. Figure 3.17 (a, b) shows the backside of an ATO membrane, produced at 60 V for 2 h, after floating for 15 s, respectively 30 s on 2 % HF solution. After 15 s, the tubes started to separate from each other, but the pores were not opened. After 30 s, the dissolution was proceeded so that nano grass formation became visible. Again, the tubes showed no sign of comprehensive pore opening. Moreover, even after this short etching time, the front side was much corroded too (see Figure 3.17 (c)). Cross-sectional images proved not only the strong diverging effect on the tubes, but an additional loss of lost of oxide layer thickness from originally 22 to only about 17 µm (see Figure 3.17 (d)).

Considering the surface area, it became clear that the front side of the ATO layers is more sensitive towards the etching in comparison to the back side. At the front side, very thin pore walls give a perfect starting point for the dissolution and complexation by the acidic fluoride solution. In contrast, the back side shows a compact, almost flat area (see also Figure 3.16).

A further reason for the resistivity of the barrier layer at the pore bottoms was its thickness. Figure 3.18 shows a transmission electron microscopy (TEM) image of the barrier layer for an anodization at 60 V. For the analysis, a piece of ATO was finely ground to provide thin fragments, which allowed electron transmission. The image clearly shows that the barrier layer is much thicker compared to the channel walls, here about 75 nm versus 45 nm. In order to prevent the ATO front side from wetting with etching solution, it was protected by a polymeric UV curing glue (approach similar to Lin *et al.*[91]).

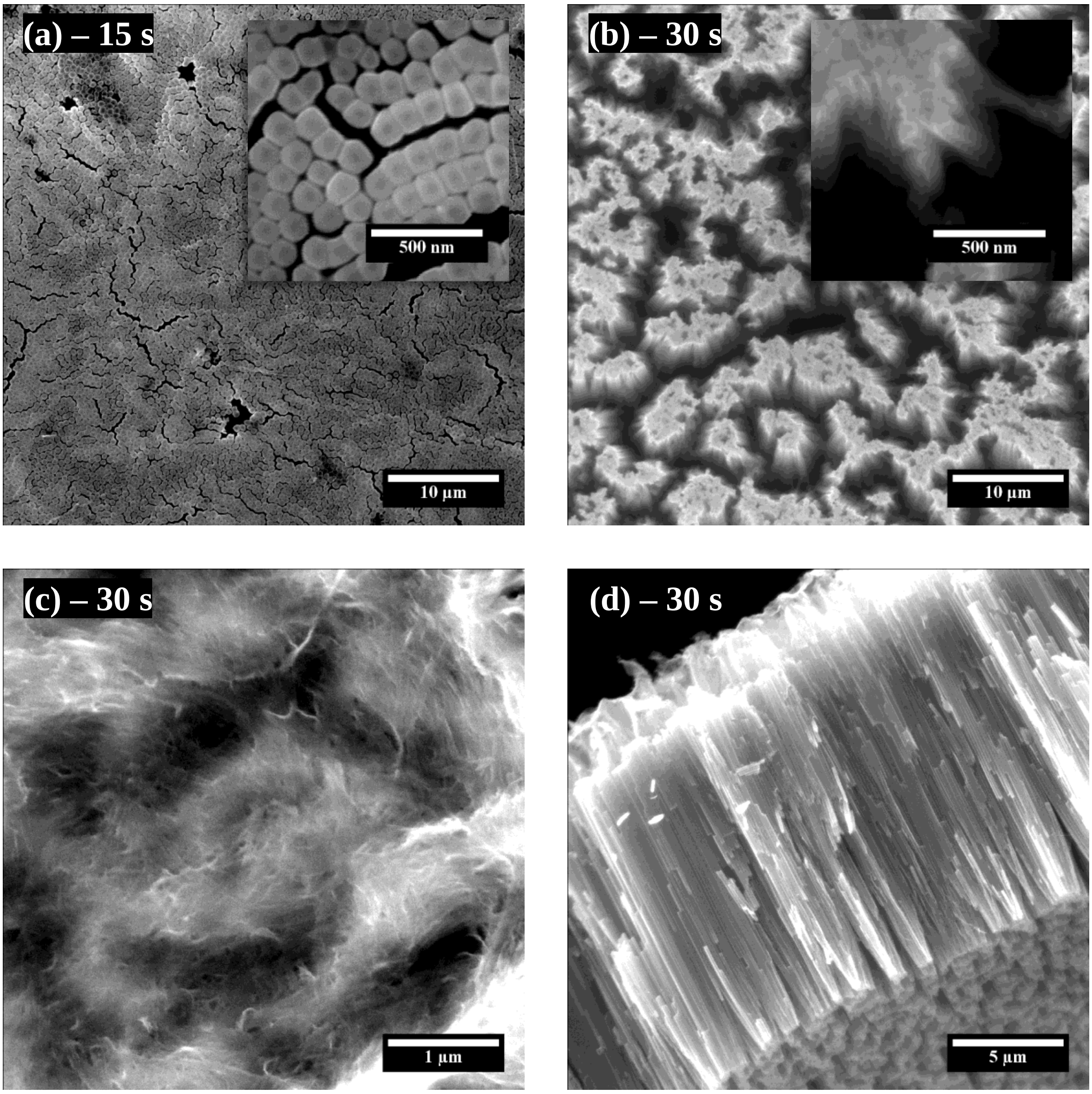

Figure 3.17: SEM images of an ATO membrane (60 V, 2 h) after floating back side down on 2 % HF solution: (a) Backside after 15 s etching showing diverging tubes, (b) backside after 30 s with tendencies of nano grass formation, (c) corroded front side, and (d) side view on reduced layer thickness after 30 s of etching. The insets show images with higher magnification.

Further advantage was the stabilization of the oxide layer against the curling upon drying. Thus, the oxidized titanium foils were washed directly after the anodization with organic solvents and covered with the glue in wet state. Therefore, the total and solely covering of the front side with the glue was guaranteed. After the curing process, the oxide, stabilized by the polymer, was beat out. The electrochemical reverse-bias method was not applicable with the protective layer. It was etched with diluted HF solution, whereas the concentration was reduced further to 1 % to ease the reaction control.

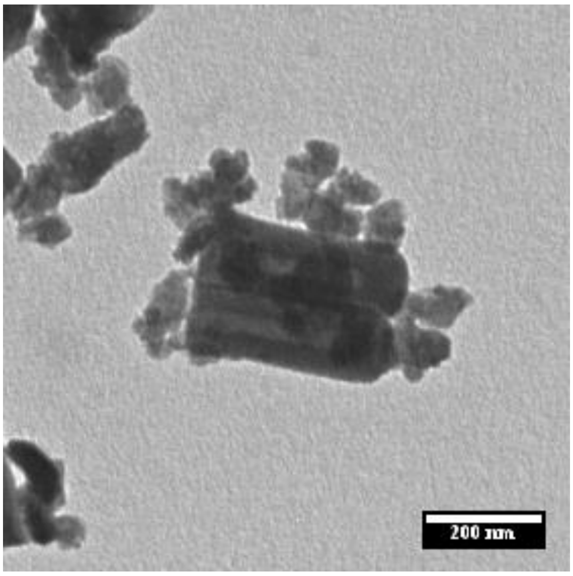

Figure 3.18: TEM image of ATO (60 V) tube bottoms showing enhanced barrier layer thickness (75 nm) compared to the tube walls (45 nm). The image was taken by [redacted] and [redacted].

Figure 3.19 shows the etching results for treatment periods between 1 and 10 min. Even though the used ATO layers were produced with anodization voltage of either 50 or 60 V, the images clearly show the separation process of the single tubes at the back side of the membranes increasing with time. Some tubes showed opened pores, but no quantitative pore opening was achieved. Moreover, the observed open tubes showed very small free diameters caused probably by a kind of melting process in the course of the oxide dissolution. In contrast, the protection process with the glue and its subsequent dissolution in organic solvent worked very well. The membrane's front sides were not affected and the ATO membranes could be recovered as a whole.

Alternatively to the immersing in HF containing solutions, the direct application of concentrated HF is described in literature.[86,91][89] For this reason, the ATO layers had to be mounted above concentrated HF solution, in a way, that its vapors might condensate at the bottom, where the barrier layer should be etched selectively. Even though certainly the reaction design varied, the indicated time until the pores became open was told to be about 30 min[89,94] up to 45 min[92]. Dry membranes had to be used for this approach, which were subjected to the curling.

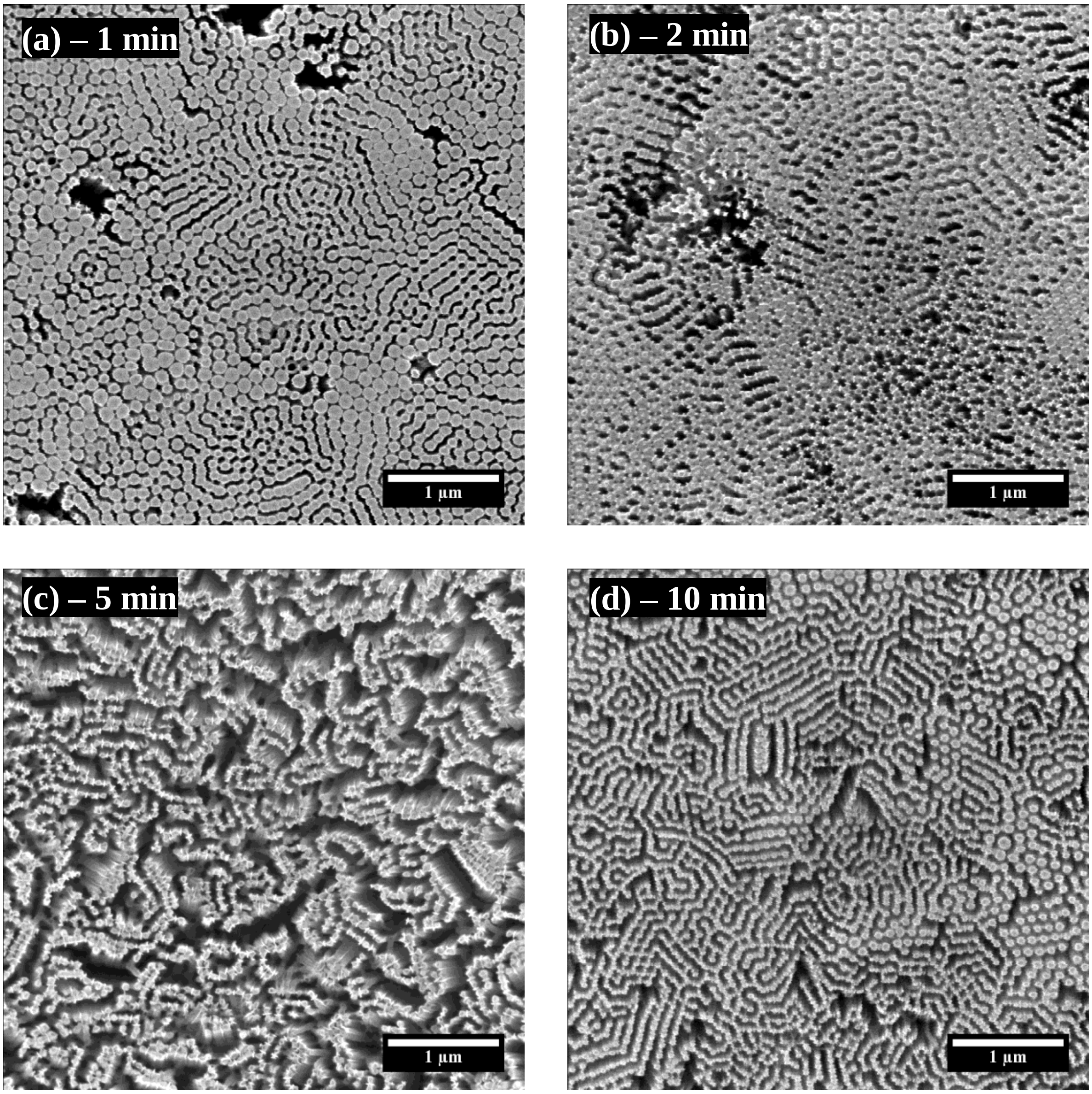

Figure 3.19: SEM images of ATO (50 or 60 V) membrane back sides after selective etching of the bottom with 1 % HF solution for a) 1 min, b) 2 min, c) 5 min, and d) 10 min.

However, several experiments with thick ATO layers were performed. The exposure to HF vapor for ony 5 min already led to corrugation of the oxide layer. The backside was etched likewise to the experiments with diluted HF solution. The former compact surface transformed into loose tubes, partially still closed, others already opened (see Figure 3.20 (a, b)). Obviously, the vapor treatment was very inhomogeneous as the coexistance of collapsing tubes proves (see Figure 3.20 (c)). An extended exposition to the HF caused the total dissolution of the oxide membranes after about 20 min.

Thus, the etching with HF did not provide completely porous ATO membranes in contrast to descriptions in literature. The back side surface was inhomogeneously etched by all applied treatments. A controlled pore opening process was not possible due to the formation of nano grass with extended reaction period.

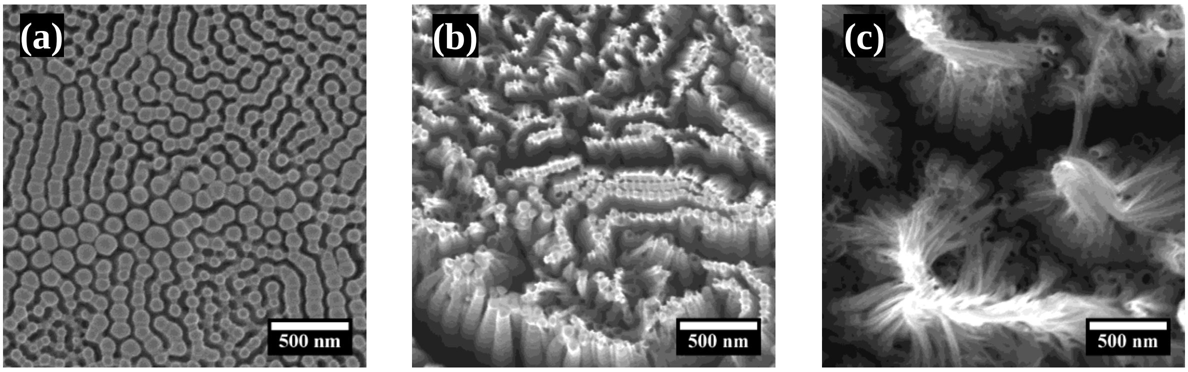

Figure 3.20: SEM images taken at different positions of the same ATO back side (50 V, 4 h) after 5 min exposition to HF vapor, showing different intensity of etching: (a) Separation of tubes, (b) partially opened tubes and first nano grass tendencies, and (c) collapsing tubes.

3.4.3 Electrochemical Pore Opening

Instead of using wet chemical etching methods, less common procedures for the pore opening were taken into consideration. These were not applied after the anodization and detachment, "*ex situ*", but were "*in situ*" finishing the anodization process. Common intention of the procedures was to disturb the pore order when the projected layer thickness was reached and to provoke a predetermined breaking point. Thus, ATO pore opening and detachment shall be achievable in one single step.

Since Kant *et al.* had a certain success by gradually reducing the voltage at the end of the anodization,[95] notably "potential shock" methods led to promising results in literature. Likewise, the anodization was thereby completed by a period of tenth of seconds up to some minutes, where the voltage was raised abruptly to a value some ten Volts higher than before: 120 or 150 V for some minutes after anodization at 60 V,[96] a potential shock of an extra of 40 V to the anodization voltage for tenth of seconds to minutes,[97] or an extra of some ten Volt for only some seconds[98] were favored with respect to various anodization conditions.

Furthermore, crystallization of the produced ATO by thermal annealing, followed by a continued anodization with changed voltage, was discussed.[99] The mentioned problems upon drying the produced ATO layers for this reason and the uncertain influence of the crystallization on the porous structure were exclusion criteria for this approach. Instead, at first a short voltage pulse of some seconds was tested subsequent to anodization experiments at 40 V. Limited by the power supplies available (for further details see Chapter 6.1.2), the height of the pulse was chosen to maximum 105 V. This short treatment did not show any effect, neither on the appearance of the back side, nor on the front side.

However, oxide layers produced at 40 or 50 V showed a positive response on applying a final potential of 80 V for about 10 min. Followed by a second reverse-bias impulse to detache the membranes from the metal, its back sides showed nicely opened pores (see Figure 3.21). With exception of smaller defects, the back side surface was homogeneously opened over the whole range of the oxide layer. Almost all tubes were open to a large extent. However, a reliable determination of the diameter of the created apertures was difficult due to the often observed irregular shape.

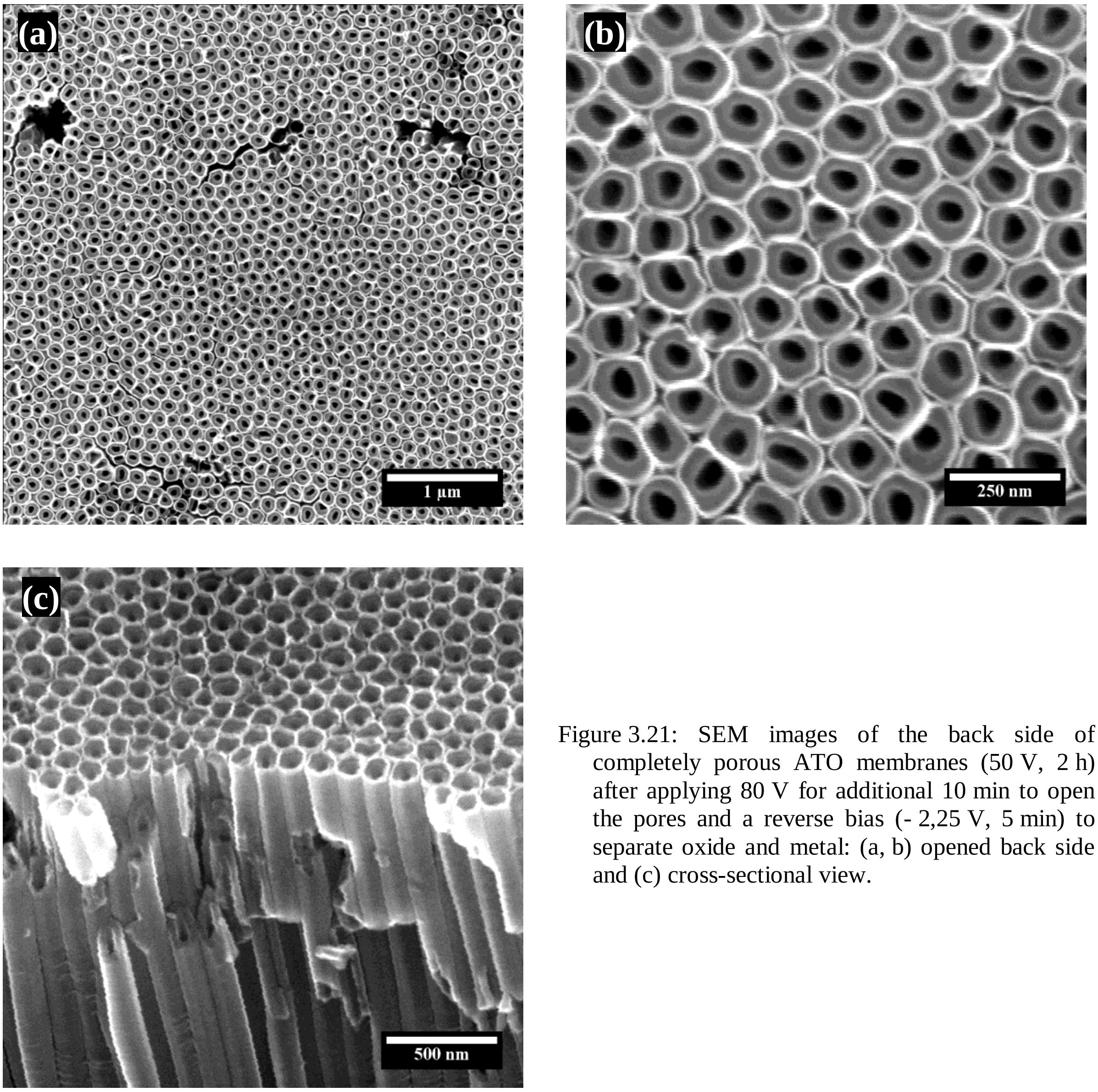

Figure 3.21: SEM images of the back side of completely porous ATO membranes (50 V, 2 h) after applying 80 V for additional 10 min to open the pores and a reverse bias (- 2,25 V, 5 min) to separate oxide and metal: (a, b) opened back side and (c) cross-sectional view.

By this relatively simple approach, completely porous ATO membranes of about 35 – 45 nm back side pore diameter, and with thicknesses between 10 and 20 µm, could be produced.

However, the curling still had to be overcome proceeding to applications of these membranes. Thus, ATO membranes were dryied at 200 °C between flat tiles on a hot plate. This treatment impeded the bending of the layers for some days.

Nevertheless, the mechanical instability as disadvantageous property of the ATO could not be rationalized. The tubular build-up of the membranes made them highly breakable, thus, an application with membranes of only some micrometers thickness rendered impossible. Literature applications of ATO used as a filter reveals in particular pressure-less diffusion studies. Even for this purpose, the used membranes are typically of the dimensions 100 to 200 µm or more.[86,89,94] The appearance of front and back side surface is rarely shown in detail, hypothesizing irregular surfaces and nano grass formation.

3.5 Conclusions and Outlook

Within this work, ATO membranes fulfilling a distinct set of filtration properties – thin, self-supporting, free from nano grass, highly porous, and sufficiently flat – have been produced for the first time.

The completely porous ATO membranes have been successfully created by adjusting the processes for the pore opening at the back side and in particular for the detachment of the anodic oxide from the metal. Applying an anodization voltage of 40 or 50 V, membranes with a minimum pore diameter of 35 – 45 nm and thicknesses in the range of 10 – 20 µm have been produced. Moreover, the almost inevitable curling of the dry thin membranes was controlled by a new heat and flattening post-treatment.

In the course of this work, the impact of the anodization voltage and reaction period on the obtained pore size and oxide layer thickness was explored in detail. A two-step anodization process, which operates with voltages of 30 to 50 V and led to high pore ordering, was used. For the pre-anodization, the reaction period was reduced to only 1 h though still resulted in a sufficient pre-structure. The second anodization for the formation of ATO membranes yielded oxide layers of 7 – 25 µm thickness within a reaction period of up to 3 h. A prolonged reaction often led to degradation through formation of nano grass. Surface ATO pore diameters of 30 – 90 nm have been produced, depending on the applied voltage and reaction period. However, a cross-section of the pores reveals them to have a conical shape across the oxide layer and their minimum diameter at the bottom is controlled only by the applied voltage and the efficiency of the back side pore opening.

The predominant procedure in literature for the latter is etching with HF, but it was found to give unreliable and non-uniform results, and therefore be inappropriate for application on thin ATO layers. Instead of opened pores, HF etching led rather to a separation process of the single tubes at the back side of the membranes and, with a prolonged reaction period, led to nano grass formation. In this work, it was found that a “potential shock”, an abruptly raised voltage, gave the best results in terms of uniformity and reproducibility.

However, ATO membranes are of a very fragile nature and need further stabilization to be useful as filtration membranes. There are approaches known to support the fragile ATO layers by saving a stabilizing metal grid from the oxidation.[100] Moreover, lamination between macroporous mesh can be imagined to provide the necessary mechanical stability. In order to avoid a complex filtration membrane design, it was logical to turn toward anodic aluminum oxide (AAO). By its porous, rather than tubular structure, this material would provide a higher mechanical stability. However, the knowledge to reliably produce membranes of AAO had been lacking in our research group.

4 Anodization of Aluminum

4.1 Introduction and Technical Implementation

As discussed in Section 2, which dealt with the general aspects of valve metal anodization, the anodization of aluminum does not differ greatly from the anodization of titanium, which was covered in Section 3. The two-step anodization, invented by Masuda and Fukuda, is favored in literature to produce anodic aluminum oxide (AAO).[17] In analogy to the presented results for the titanium anodization, it results in an enhanced order as well as homogeneity of the pores.

In contrast to the work with titanium foils, the anodization of aluminum had to be explored as a completely new research field. Hence, it seemed natural to rely on published results of Haberkorn *et al.* from a neighboring group in Mainz, which had used electrochemical setups similar to the PTFE Setup already introduced (for further details see Chapter 6.1.2).[101] Aluminum foil of 99.997 % high purity was used. As the foils were already very smooth and reflective as delivered, initial experiments were done without prior polishing. First experiments were carried out at a potential of 40 V and a temperature of 2 ºC, using the PTFE-Setup and a Pd sheet cathode. The fluoride-containing electrolyte for titanium anodization was changed to an aqueous solution of oxalic acid (0.3 M) was used, which is known to be a standard electrolyte to form AAO.

This simple approach did not work as the electric current died within seconds after starting the anodization. Obviously, stirring was necessary to keep the reaction running. This is in contrast to titanium, where non-stirred conditions are the norm. However, this difference is rarely treated in literature, and often no information about the employed setups, in particular about agitation of the electrolyte, is specified.

This raised the question how controlled and uniform stirring could be realized within the PTFE Setup. The common approach in chemical reactions to use a magnetic stir bar was not feasible with the available setups. Another conventional method is the use of an external laboratory rotary stirrer. The placement of a cathode *vis-à-vis* the sample, however, would necessitate a non-ideal, non-centered installation, if the constricted room enables this solution at all.

To avoid the mentioned problems, the applicability of the simpler setup construction previously mentioned in Section 2 was surveyed. However, even the typical approach with a glass beaker, equipped with two vertically aligned sheet-shaped electrodes and stir bar caused a lot of problems. It was difficult to keep the electrodes at a reproducible distance and to avoid back side attack of the aluminum foil. Moreover, the thin Al foil was exposed to strong vibrations in the violently stirred electrolyte, and the alligator clamps held the foil in an irregular way in the electrolyte.

Therefore, a solution based on our proven and tested setups was investigated. Instead of agitation by stirring, sonication became the focus. In literature, approaches favoring the sonication method are found, leading to a higher growth rate of the anodic oxide compared to stirring.[102]

In place of the temperature bath, an ultrasonic bath was tested with the PTFE-Setup. Unfortunately, the vibrations led not only to loosening of the bolting of the setup components, but also to even more serious heating of the aluminum foil. As the foil is locked on top of the copper contact, local heating was so strong that the foil deformed and burst. Alternatively, an ultrasonic homogenizer device (type Hielscher UP100H) was tested for its capability but found to be too weak. Finally, a new approach was pursued and found to be very advantageous. To the author’s knowledge, this method is unknown in association with anodizations. Stirring cathodes were introduced instead of immobile electrodes, representing the most elegant way to combine electrode character, stirring and a symmetric arrangement of all setup components. First attempts were made using a high-speed stirring electrode with platinum heading (for further details see Chapter 6.1.2). This professional equipment for electrochemical deposition was suitable to keep the current high. One disadvantage was the high motor speed necessary to obtain a sufficient stirring effect with the perfect circular rod-shaped electrode heading. A second was the impossibility of building more setups due to the high costs of such electrodes.

As an alternative, a conventional laboratory rotary stirrer was equipped with a sliding contact, the electrically conducting parts were insulated, and a cathode with stirring property was formed out of a titanium bar (for further details see Chapter 6.1.2).

Using this new construction in conjunction with the Cu-block Setup, which provides better access for the stirring electrodes, anodizations could be performed. However, results were poor and the reaction speed was very low due to the low temperatures. Temperatures between 0 and 5 °C are widely used to obtain AAOs in excellent pore order, but reactions are often 24 hours or longer because of the slow fabrication speed.

Few publications describe aluminum anodizations at room temperature with good quality. The first promising results were obtained by transforming reaction conditions described by

Sulka *et al.* to our setup. Sulka fabricated AAO templates using the already mentioned 0.3 M oxalic acid electrolyte and investigated the influence of potentials between 30 and 65 V and reaction temperatures of 20 to 30 °C on the pore size. Furthermore, it was found that the oxide growth was about 5 – 10 times higher compared to low-temperature anodizations.[103]

4.2 Electropolishing of Aluminum Foils

The general necessity for an adequate polishing (E) to prepare the metal surface for a high quality anodization result was already mentioned (see Section 2). Several literature approaches propose alcoholic solutions of perchloric acid for electropolishing, such as a 4:1 or 8:1 solution of EtOH or MeOH to $HClO_4$.[103,104][105]

The Cu-block Setup was chosen due to the positive results with the polishing of titanium and the anodization of aluminum. For an adequate material removal and to obtain the preferred high current of I > 100 mA, a relatively high potential of 40 – 50 V was necessary. Moreover, stirring was again required to prevent breakdown of the current. Both stirring electrode systems were found to be suitable, and the best polishing was obtained when stirring as fast as possible without mixing of air bubbles into the electrolyte. Figure 4.1 shows the surface of an untreated aluminum foil with clear manufacturing signs such as scratches from the roll-milling process.

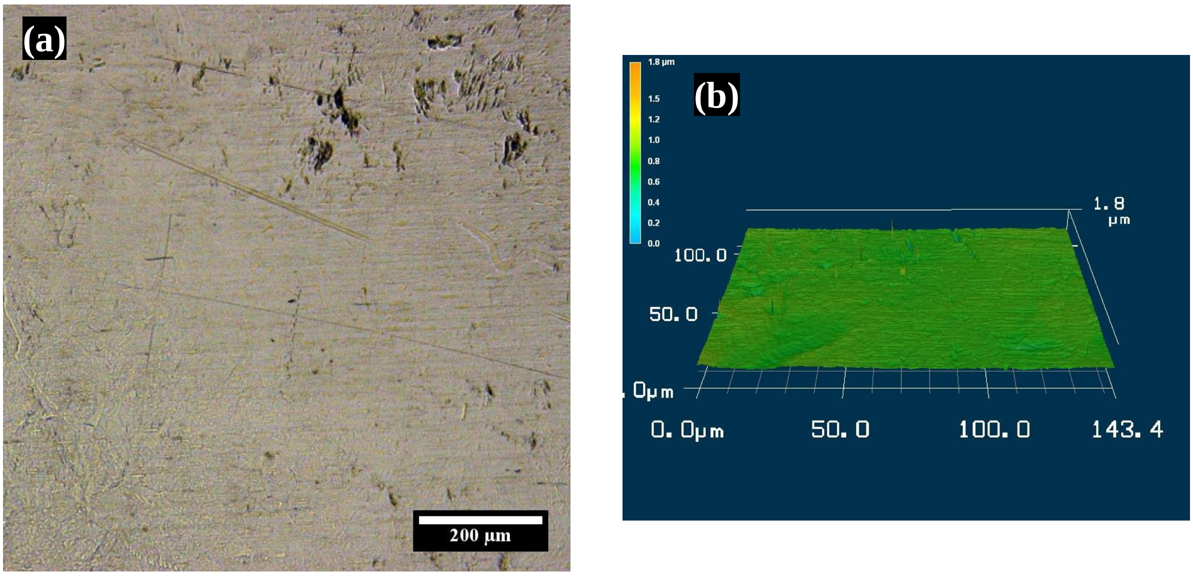

Figure 4.1: (a) Light microscopy image and (b) 3D topology laser scanning microscopy image of raw (unpolished) standard aluminum foil. The 3D image was extended 10-fold in z-axis.

The soft nature of the pure aluminum in combination with small foil thickness of 0.1 mm led to wrinkling of the metal after stamping. For better contact with the copper plate of the setup and especially a perfectly flat oxide product, the cut pieces were flattened with a hydraulic press. The pressing had no effect on the microscopic appearance of the surface. Degreasing of the foils was performed without sonication to prevent deformation of the foil.

Using the alcoholic 4:1 electrolyte, MeOH and EtOH were both suitable, and the homemade laboratory stirring electrode, a reasonably constant current of about 100 mA was obtained using a potential of 40 V. The surface roughness decreased with time and after 4 min a smooth surface was reached (see Figure 4.2).

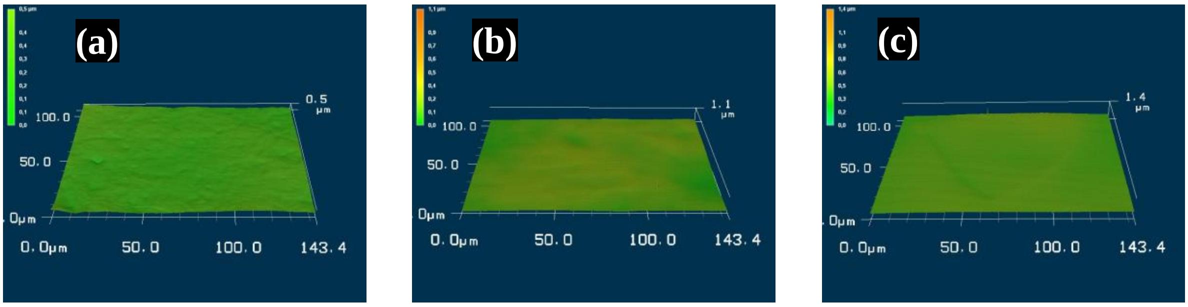

Figure 4.2: 3D topology laser microscopy images of aluminum surfaces polished with 4:1 alcohol/$HClO_4$ electrolyte using the homemade laboratory stirring electrode for (a) 1 min, (b) 2 min, and (c) 4 min. The 3D image was extended 10-fold in z-axis.

The total surface roughness measured with 3D laser microscopy decreased via $R_q = 0.090\ \mu m$ for 1 min polishing to reach $R_q = 0.045\ \mu m$. The polished metal foils exhibited a mirror-like finish, and light microscopy made grain boundaries visible (see Figure 4.3).

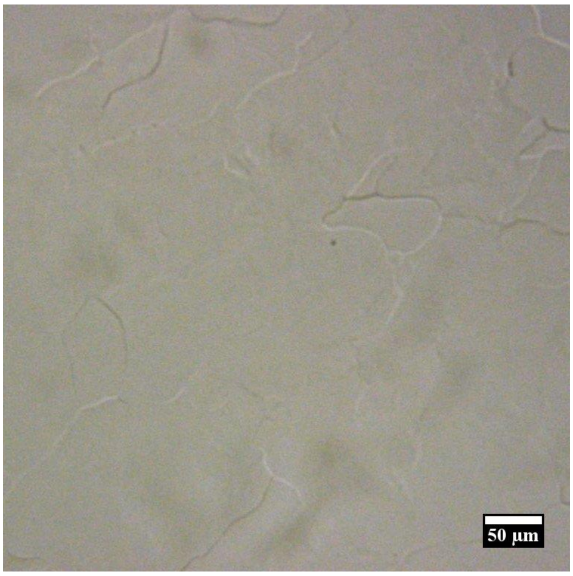

Figure 4.3: Light microscopy image of a polished aluminum surface showing grain boundaries.

However, using the high-speed stirring electrode for the polishing, the current flow was higher (150 – 200 mA), which seemed to be the reason for a further improved polishing result. To increase the current flow further, the distance between anode and cathode had to be reduced. Therefore, the base of the PTFE vessel was conically milled out to enable a closer installation of the rotating cathode to the metal foil (see Chapter 6.1.2). This setup modification finally led to the preferred high current of about 300 mA and very good, fast polishing results. Figure 4.4

shows the Al surface after 5 min of electropolishing in the standard PTFE vessel using the high-speed electrode in comparison to the result obtained using the modified vessel with only 2 min reaction time. It is evident that the modification enhanced the surface flatness, and this process became the standard for all polishings (E).

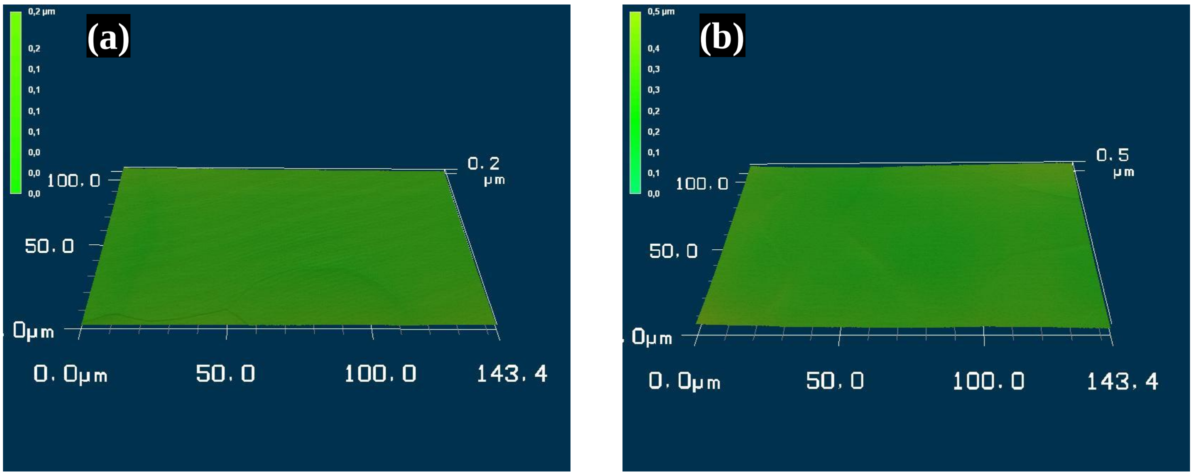

Figure 4.4: 3D topology laser microscopy images of aluminum surfaces polished with the high-speed stirring electrode (a) using the standard PTFE vessel for 5 min reaction period and (b) using the conically modified vessel and only 2 min reaction period. The 3D image was extended 10-fold in z-axis.

If it was necessary to prepare larger surfaces, of diameter > 15 mm, for the subsequent anodization (see Chapter 4.8.3), PTFE vessels with larger bottom apertures and standard cylindrical apertures were used (for further details see Chapter 6.1.2). For homogeneous polishing over the increased area, it was again necessary to choose a small electrode distance and to use the homemade stirring cathode with its larger surface area. Naturally, a higher current flow was observed. Sample diameters of 20 mm resulted in 450 – 500 mA, diameters of 30 mm to about 900 mA.

4.3 First Anodization and Dissolution of the Preliminary Oxide

According to Sulka *et al.*, a starting potential of 40 V and a reaction temperature of 25 °C were suggested to produce an oxide layer with pores of 30 to 50 nm.[103] Electropolished foils were anodized in the Cu-block Setup equipped with a rotating electrode (see Chapter 4.1). The measured current of about 16 mA indicated a considerable oxide growth compared to the ATO formation and, therefore, the reaction period was likewise set to 1 – 3 h. A transparent, as a function of reaction period colorless to yellowish-golden layer formed on top of the metal foil and broke when the foil was bent. The yellowish coloration of AAO formed in oxalic acid electrolyte is explained by the formation of $C_2O_4^{*2-}$ radicals by charge transfer between the low valency Al(I) ion and the oxalato ligand.[106]

Analysis with SEM showed irregular pores, very similar to the results obtained for the titanium A1 anodization. To prevent a strong charging effect of the non-conductive alumina, all samples had to be sputtered with a thin gold layer prior to electron microscopy analysis.

Figure 4.5 shows two different appearances of the formed porous oxide: Typically, pores were ordered along lines (see Figure 4.5 (a)), probably due to fine rolling marks resulting from production left even after the polishing step (E), but wavelike superstructures were also found (see Figure 4.5 (b)).

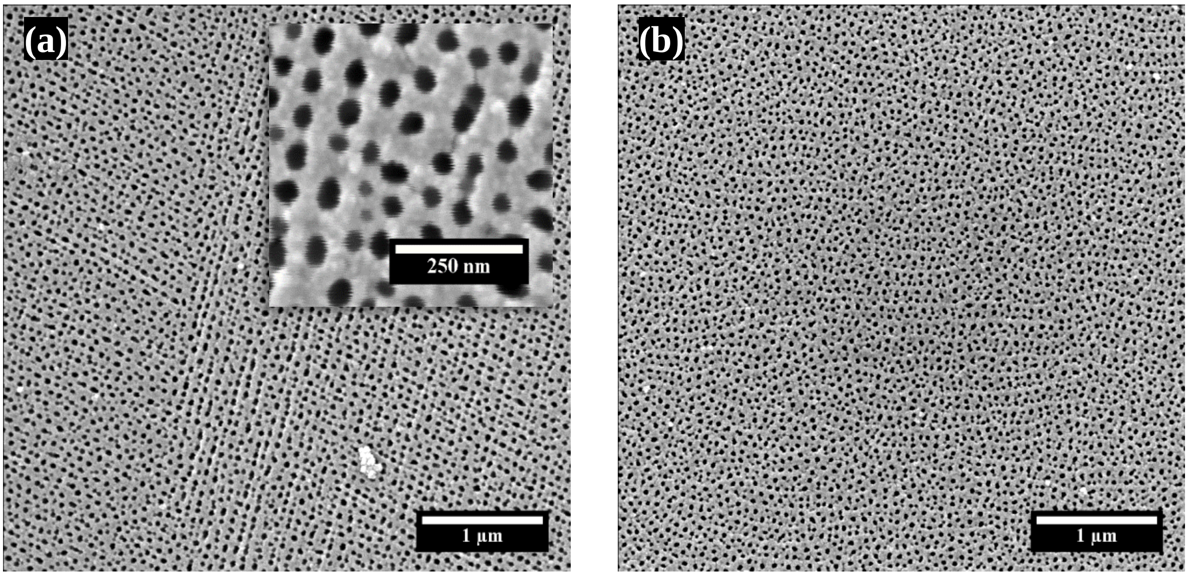

Figure 4.5: SEM images of porous aluminum oxide after the first anodization (A1) with 40 V for 3 h, showing irregular pores arranged in (a) lines and (b) along wave-like superstructures. The inset shows an image with higher magnification.

The different structures observed had nothing to do with their location in the center or close to the border of the exposed circular surface, because the electrolyte swirls with stirring. An explanation could be provided by the two different surfaces of the foil. Maybe slight differences induced by the milling process, e.g. concerning the crystal structure, could have an influence on the result. For polishing, the less scratched or damaged side of a cut blank was always used, and there was no further differentiation in former upper or lower side.

However, the appearance did not play any role in the outcome of the final oxidic membrane after a second anodization. The oxide produced in the first step (A1) just served as a template for a better order in the second anodization (A2).

The A1 oxide adhered strongly to the adjacent metal. Bending of the thin and soft aluminum foil led to shivering of the oxide, but no peeling. One method is mainly described in literature to dissolve the aluminum specifically next to the oxide: Treatment of the oxidized foils with

Cu^{2+} in an aqueous solution of hydrochloric acid.e.g.[107] Within some minutes, aluminum dissolved and metallic Cu was formed due to the standard potential in a redox reaction. A transparent slice of pure aluminum oxide remained, comparable to the one pictured in Figure 4.10 (see Chapter 4.4.1). The described method was favored over the use of toxic $HgCl_2$-solution, which was sometimes alternatively applied.e.g.[64]

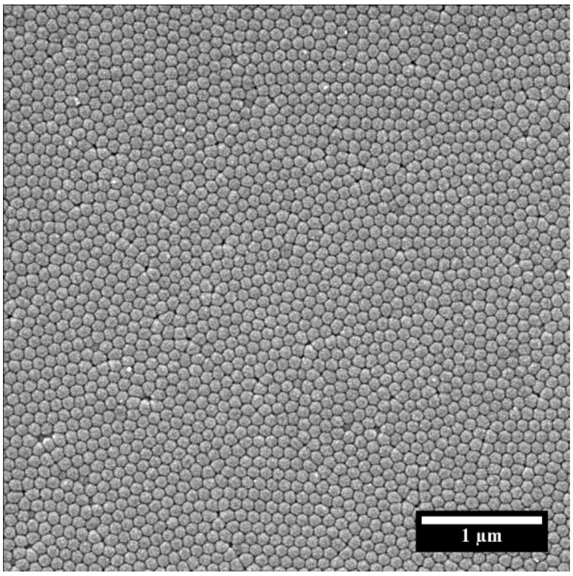

Figure 4.6: SEM image of the back side of porous aluminum oxide (A1, 40 V, 3 h) after dissolving the Al metal.

The back side analysis by SEM gave an image similar to by an ATO (see Figure 4.6). Even though it is easy to distinguish between tubular channels of ATO and porous channels of AAO in general (see Section 2), the honeycomb structure at the back side of AAO is reminiscent of a tubular character. The pores are closed due to the existence of the barrier layer on the pore bottoms. Anodization at 40 V resulted in a comb center-to-center distance of about 95 nm. In comparison with Figure 4.5, it is obvious that a high number of the small pores visible from the front side must have a dead end.

Even a relatively short pre-anodization of about 1 h showed a high degree of order on the back side. The order could not be measurably improved by extending the reaction time to some hours.

Dissolution of the aluminum was in fact not the desired subsequent step after the first anodic oxidation (A1). To prepare the foil for the final anodization (A2), the formed oxide had to be selectively dissolved to leave a pattern on the metal induced by the honeycomb-like barrier oxide layer. An established method is to immerse the oxidized foils in a so-called phosphochromic acid solution, where CrO_3 dissolved in diluted phosphoric acid.

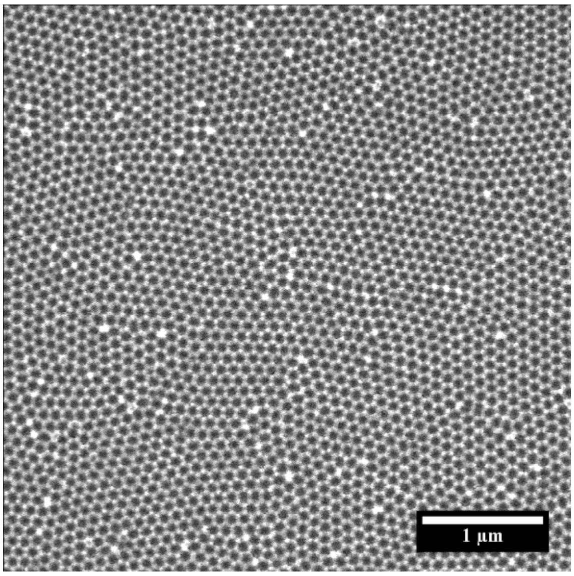

Figure 4.7: SEM image of the pattern left in the aluminum after dissolving the A1 pre-oxide.

Different reaction periods and reaction temperatures are found in literature,e.g.[107] naturally depending on the thickness of the oxide layer. We chose a treating time of either 3 h at elevated temperature of about 65 °C or immersed the foils at room temperature overnight.[101]

In doing so, the oxide layer was reliably completely dissolved, leaving behind a bright aluminum surface. Examination with SEM clearly showed a concave textured pattern on the surface of the aluminum substrate (see Figure 4.7). Anodization at 40 V led to imprints in the metal of about 65 nm, reflecting the expected high pore order of a second anodization under the same conditions.

4.4 Second Anodization and Examination of Reaction Parameters

4.4.1 Impact of the Potential on the Pore Size

On the first anodization, the formation of pores, which then leave an ordered imprint in the metal after dissolution of the oxide suggesting a monodisperse array, could be observed. The second anodization step A2 should lead to an ordered array of pores whose size should correlate directly with the applied voltage.

Based on the pre-anodization at 40 V, a second anodization was performed, resulting in well-defined, hexagonally-ordered pores across the whole sample surface (see Figure 4.8). The pore size was measured by SEM images to be about 35 nm with an inter-pore distance of about 100 nm.

The size of perfect domains with hexagonally-ordered pores was in the order of magnitude as it was observed for the imprint structure (see Figure 4.7). However, compared to the imprint pattern, the pores appeared much smaller (for an in-depth discussion of pore shapes see Chapter 4.5.5). The current-time curves showed the expected trend and follow the general explanations given in Section 2. Figure 4.9 shows typical curves for the first (A1) and second anodization (A2) at 40 V. Due to agitation, the current flow remained rather constant.

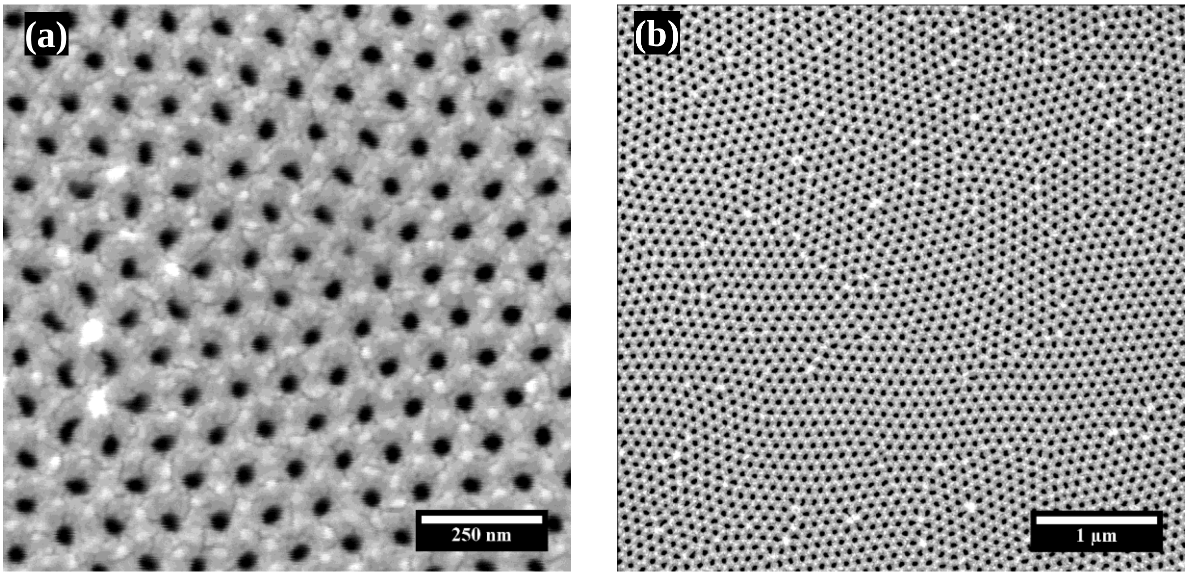

Figure 4.8: SEM images of porous aluminum oxide after the second anodization (A2) with 40 V for 2 h, showing monodisperse pores of about 35 nm.

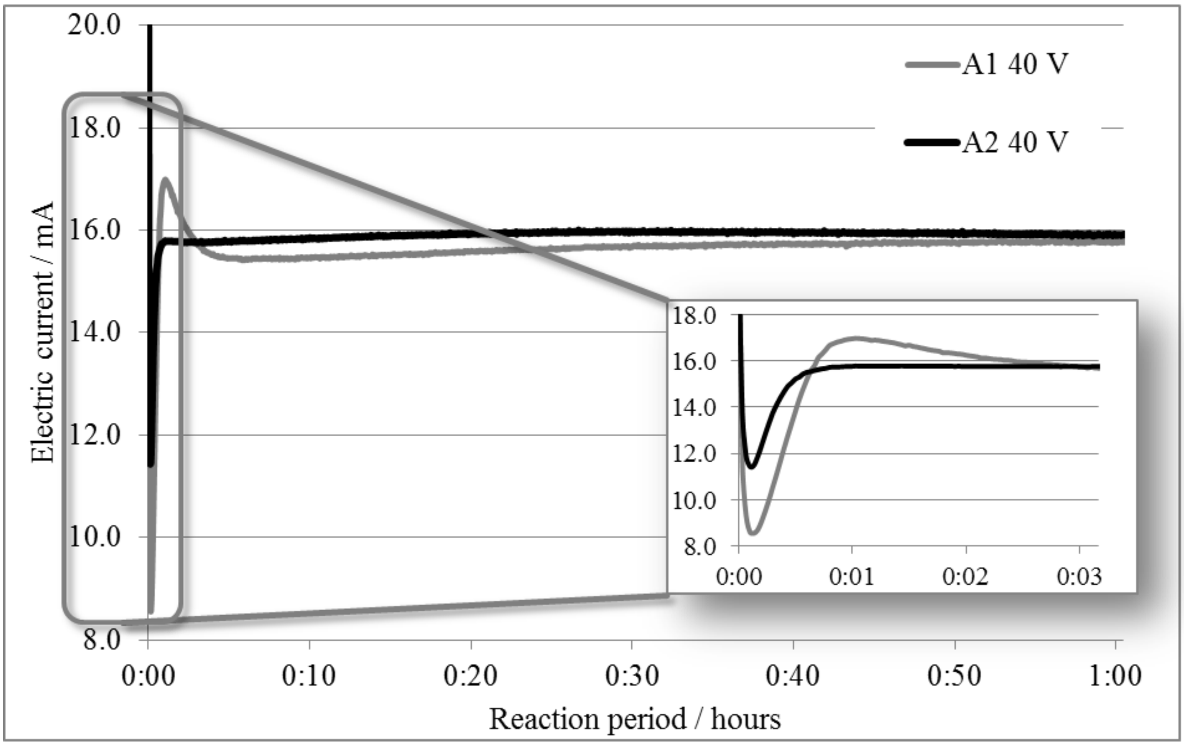

Figure 4.9: Current-time curves for A1 and A2 anodizations at a potential of 40 V. The inset shows the progress of within the first minutes when the pores start to form.

Comparing the curves of the pre-anodization with the subsequent curve, only small differences could be identified at the very beginning of the reaction. The current minimum, an indicator for the barrier layer forming, is reached for A1 and A2 after a few seconds, but the current drop at A2 is weaker because the pre-structured surface facilitates the pore formation.

The oxide layer on top of a polished foil should be thinner compared to the oxide on the imprinted surface after treatment with oxidative Cr(VI) solution. The maximum of the current in the A1 curve at the beginning of the pore growth may be explained by this. A2 current curves rarely ever showed this maximum and the time for reaching constant current was shorter compared to the first anodization. The explanation is again that no time is consumed for pore nucleation, as is required for the A1 step.[108] However, after about 5 min of reaction time, both curves showed a constant and comparable current.

The anodization at 40 V, for example, showed nearly no current drop, even after a 3 h reaction period. This was surprising when compared to the results with titanium, where slower diffusion through growing channels would decelerate the reaction. Obviously, this effect is less pronounced when using a stirred aqueous solvent as opposed to a glycolic non-stirred electrolyte.

Dissolution of the Subjacent Aluminum (DisA)

To yield a self-supporting and metal unsupported oxide sheet, the described dissolution process for aluminum (DisA, see Chapter 4.3) with Cu^{2+}/ HCl-solution was used.

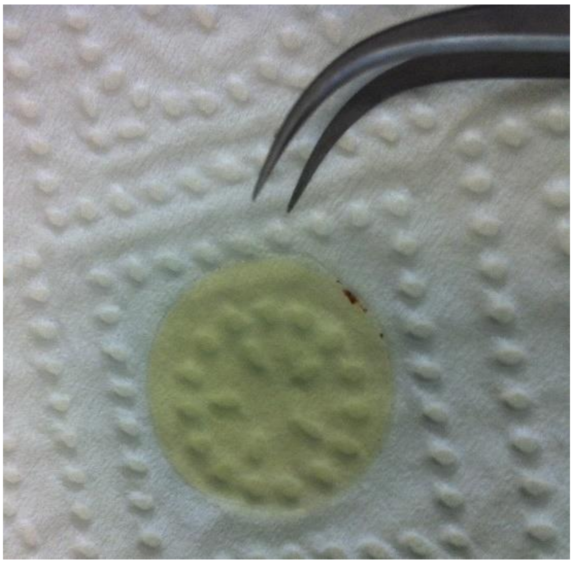

Figure 4.10: Photograph of an A2 16 mm oxide disc after the dissolution of supporting metal.

The treatment, applicable even for oxide layer thicknesses in the sub-micrometer range,[109] resulted in a disc of 16 mm diameter from aluminum oxide (see Figure 4.10). The sheet was homogeneous transparent, colorless to yellow (depending on thickness), and showed no curling effect. Handling it with tweezers reminded one of a thin plastic, but flexibility was low and bending resulted in long cracks. Only the sound when scraping on the material gave evidence to its solid, inorganic character.

Analysis of the thin AAO disc with SEM showed the expected result: well-ordered and undamaged pores at the front side and closed pores at the backside. Obviously, the short dissolution process also led to widening of the pores at the front side. The formerly 35 nm pores, produced with a potential of 40 V, were enlarged to about 45 nm (see Figure 4.11).

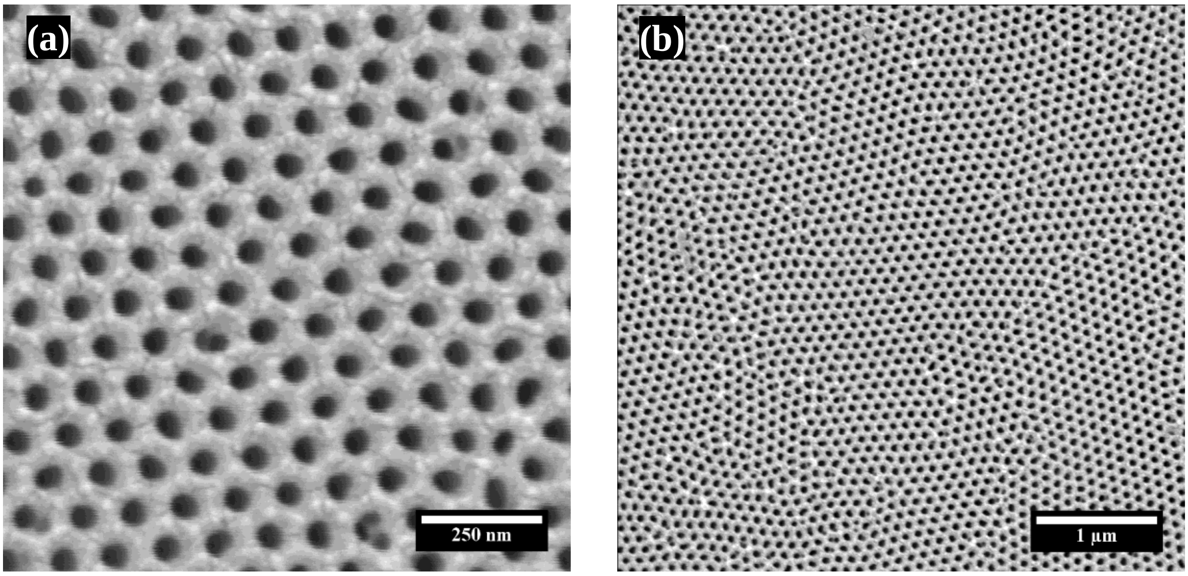

Figure 4.11: SEM images of porous aluminum oxide (40 V, 2 h) after the DisA process, showing widened pores of about 45 nm at the front side.

Because of its amphoteric nature, aluminum oxide slowly dissolves in strong acids. The question remained if this pore enlargement was only an effect at pore entrances or if the whole pore was affected. Figure 4.12 shows cross-sectional, electron microscopy images of porous oxide produced at 40 V. It is obvious that the pore openings are funnel-like, probably a result of the big “footsteps” left by the pre-anodization (see Figure 4.12 (c)). This makes it difficult to allocate a certain diameter to pores if measured from the front side. Chapter 4.4.3 deals with this problem in detail. A similarly difficult quantitative analysis of the cross-sectional view concluded that the channels were also widened from 30 – 35 nm before to 35 – 40 nm after the acid treatment.

A diagonal view to the pore bottoms in Figure 4.12 (a) clearly shows the barrier layer capping the pores. Figure 4.12 (b, c) indicates that the channels had an almost constant top-to-bottom diameter. This observation represented a further important difference to ATO tubular channels.

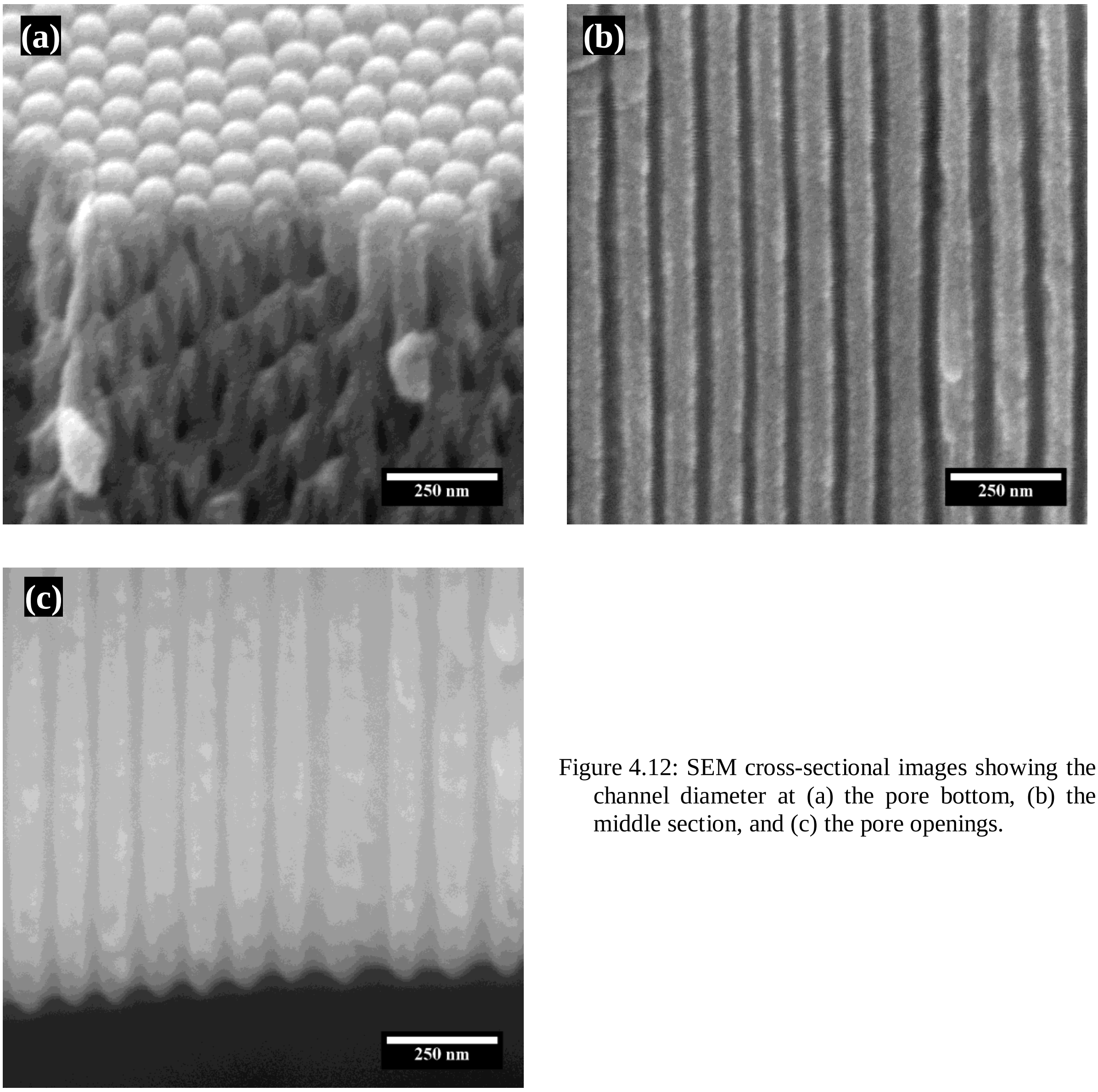

Figure 4.12: SEM cross-sectional images showing the channel diameter at (a) the pore bottom, (b) the middle section, and (c) the pore openings.

As previously mentioned, the anodizing voltage has a huge impact on the pore diameter of AAO.e.g.[13,19,110] General findings are that the pore diameter of AAO increases with the anodizing voltage in a quasi-linear relationship (compare Section 2). Because of interest in producing small pores, the anodization voltage was reduced as a start.

Anodizations with 35 or 30 V were found to give good and acceptable porous results, respectively (see Figure 4.13). Comparing the results, it is obvious that with 30 V the order of the pores was already significantly reduced, although a certain monodispersity was maintained. A reduction to 25 V degraded the homogeneity of the pores such that the AAO were no longer suitable as filtration membrane (see Figure 4.14 (a)). The pore size distribution became wide and a reasonable pore diameter could not be stated. Therefore, even lower electrical potentials were not tested.

Because of the slow reaction rate, the anodization time had to be extended. This resulted partially in nano grass formation, promoted by the thinning pore walls with lower anodization voltage (see Figure 4.14 (b)). From literature it is known that pores do not form at all below an anodizing voltage of about 5 V, independent of the electrolyte used.[54]

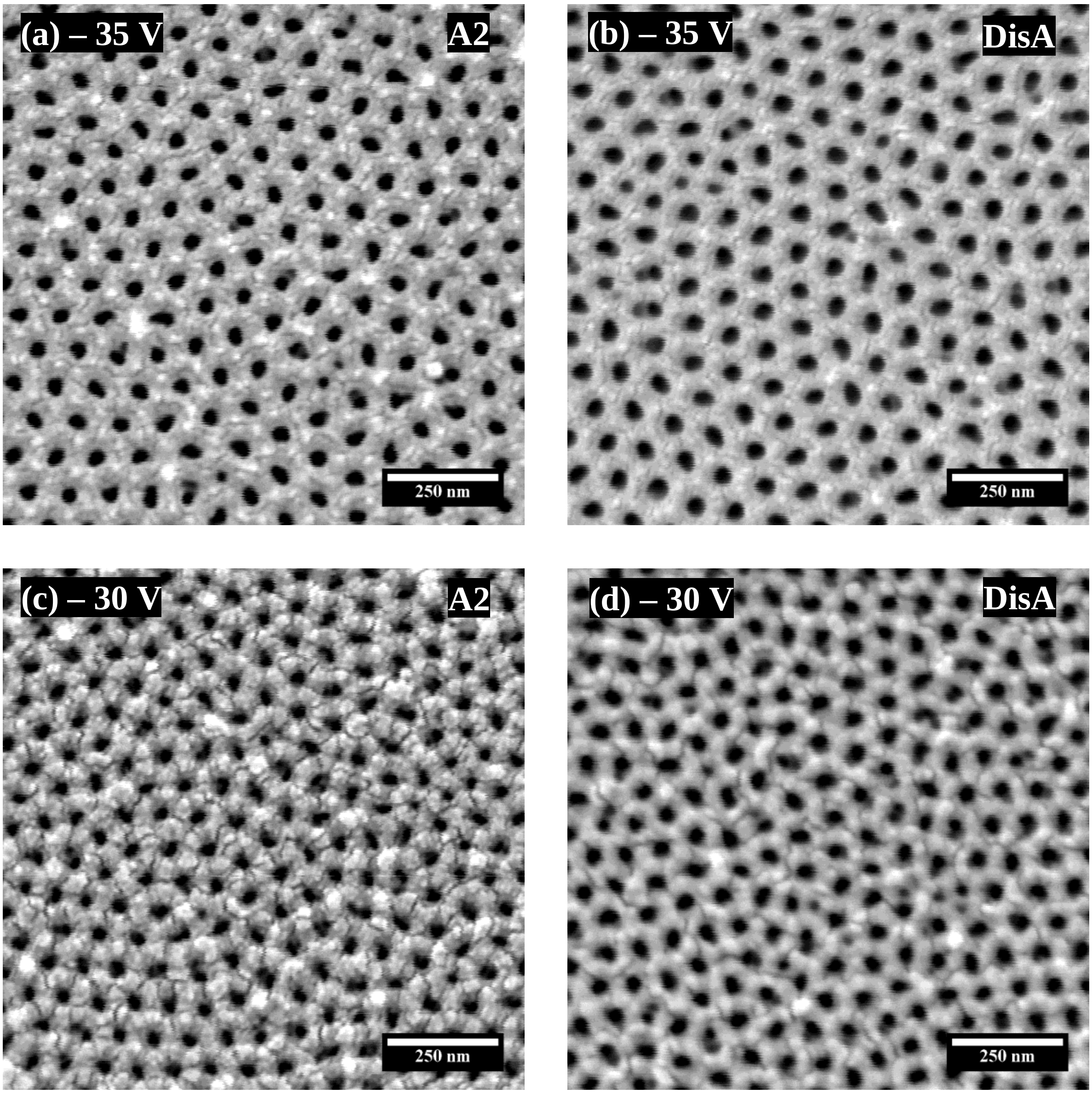

Figure 4.13: SEM images of AAO formed at 35 V (a, b) and 30 V (c, d), after A2 (a, c) and after dissolution of the metal base (DisA) leading to widened pores (b, d).

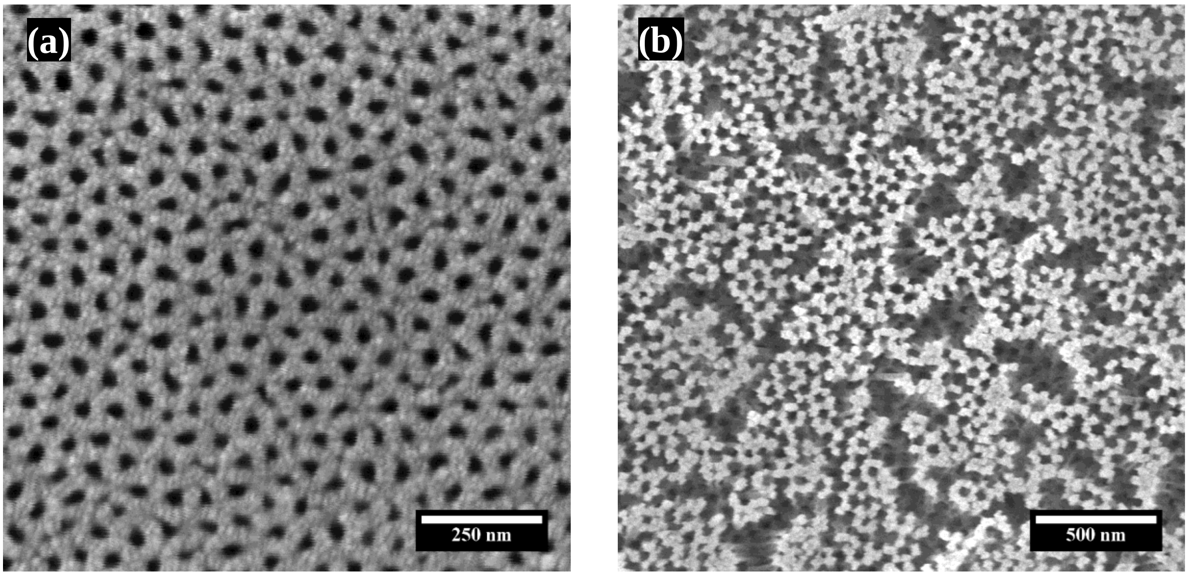

Figure 4.14: SEM images of AAO formed at (a) 25 V and (b) its partially degeneration to nano grass due to extended reaction time.

The measured pore size after A2 dropped from about 35 nm for the 40 V products to 20 – 25 nm for the 25 and 30 V cases. The dissolution step (DisA) expanded the pore sizes by about 5 nm in each case. The inter-pore distance also decreased with lower voltage, resulting in a higher number of pores per area. Table 1 summarizes the results of the interpretation of the scanning electron micrographs.

Table 1: Measured pore diameters (front side by SEM) and inter-pore distances after anodization (A2) and metal dissolution (DisA) for low anodization voltages.

	A2 pore diameter	DisA pore diameter	Inter-pore distance
25 V		25 nm	70 nm
30 V	20 – 25 nm	25 – 30nm	80 nm
35 V	30 nm	35 nm	85 nm
40 V	35 nm	40 – 45 nm	105 nm

Variations in the anodization period within the limits of 1 to 4 hours had no significant effect on the pore size. With longer reaction periods, slight pore widening could be detected, while very short reaction times led to smaller pore diameters. However, for the chosen reaction periods in this work, the effect was negligible.

Su and Zhou analyzed the relation between pore size and anodizing voltage by a theoretical model that was confirmed by experiments using 0.3 M oxalic acid as electrolyte as well. They concluded that a possible maximum value for the pore diameter could be obtained at an anodization voltage between 70 and 80 V.[111]

Increasing the anodization voltage to 50 V resulted in a good pore order and an increased pore diameter of 40 – 45 nm, which enlarged to 45 – 50 nm after DisA (see Figure 4.15).

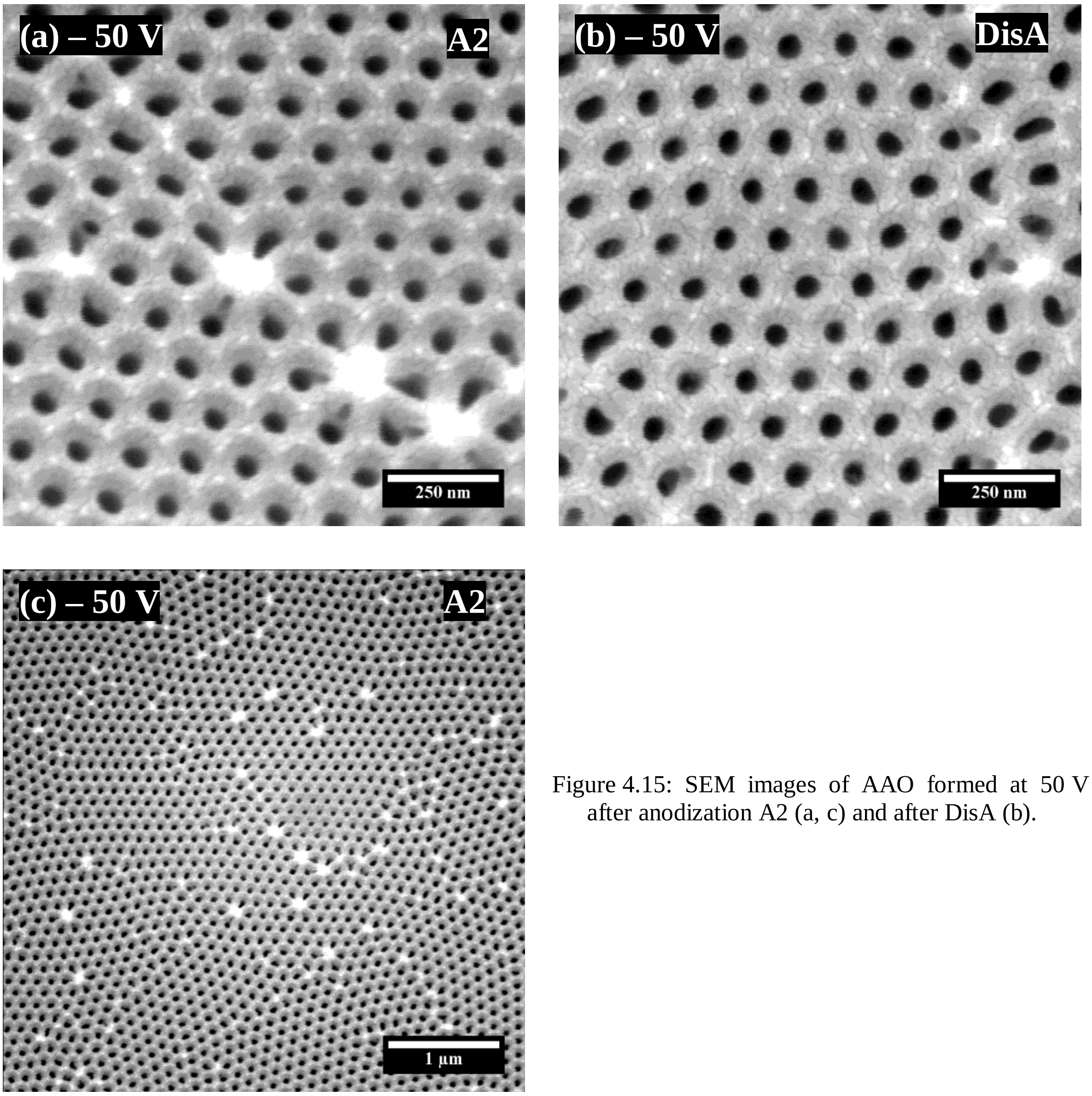

Figure 4.15: SEM images of AAO formed at 50 V after anodization A2 (a, c) and after DisA (b).

Increasing the voltage above 50 V led to disruptions in the pore order and pore size distribution: Mainly „twin-“ and „triplet-pores“ were observed, sharing a place where usually just one pore should be. The prevention of an adequate self-ordering at higher potentials, however, seems not to be a consequence of the comparatively warm reaction temperatures. At lower anodization temperatures, grid-like superstructures are also reported.[112]

Figure 4.16 shows the result for a 60 V, 70 V and 90 V anodization after dissolution of the aluminum (DisA). With increasing potential, the number of pores “sharing” one spot in the superstructure rose. Due to this “multiplet” pore structure, the single pore diameters could hardly be enlarged by choosing higher voltages. However, the average pore size seemed to indeed drop when comparing the results of 70 V and 90 V (see Figure 4.16 (b, c)).

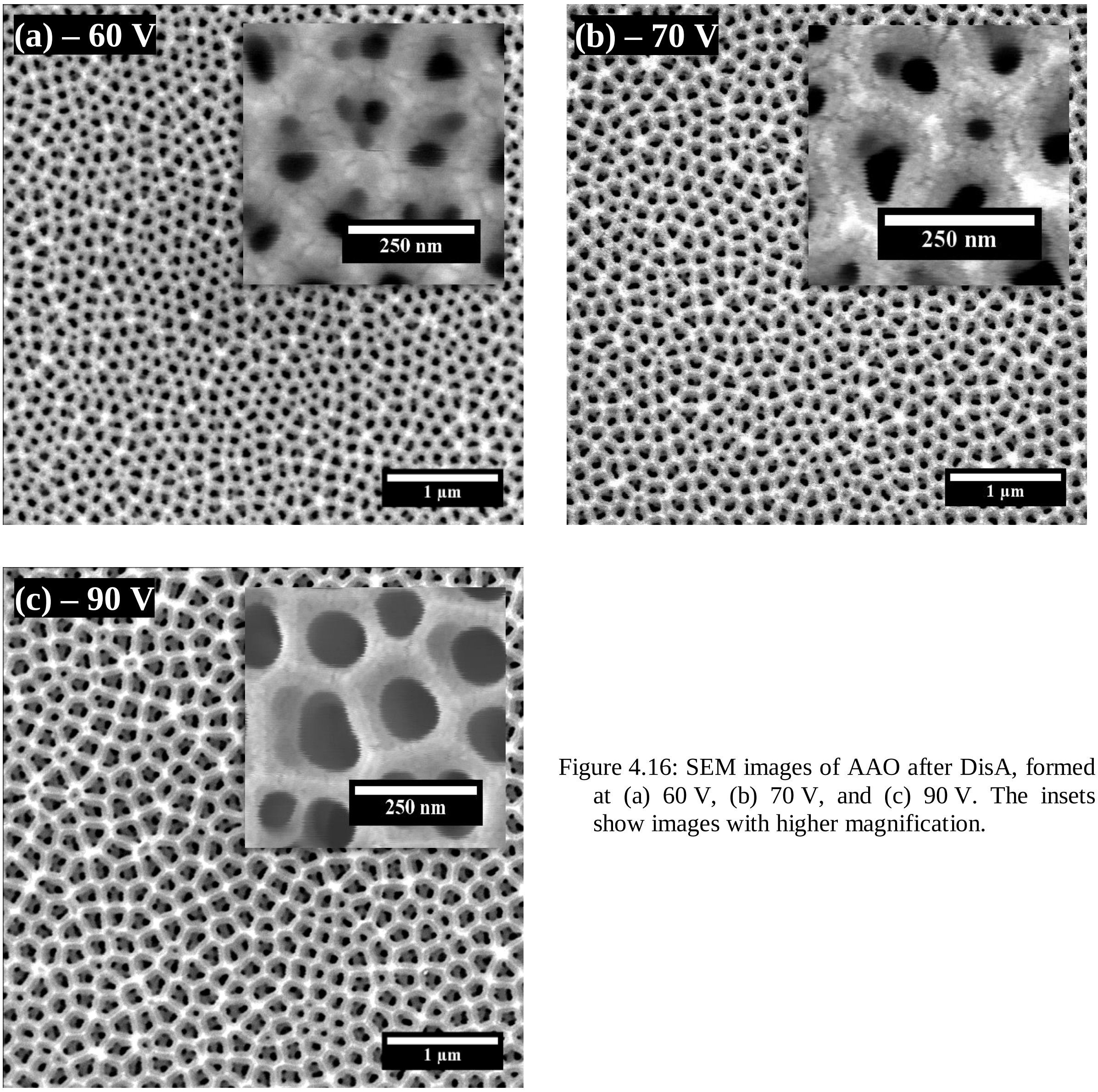

Figure 4.16: SEM images of AAO after DisA, formed at (a) 60 V, (b) 70 V, and (c) 90 V. The insets show images with higher magnification.

Figure 4.17 provides an overview of measured pore diameters and the inter-pore distance at the oxide layer surface as a function of the anodization potential. As expected, both curves show a linear trend for an anodization voltage below 60 V. Above this voltage, the inter-pore distance is expressed rather as the cell size, measured at the back side of the membrane. It shows a huge distribution, indicated by the arrows in the graph, due to the weak self-ordering forces.

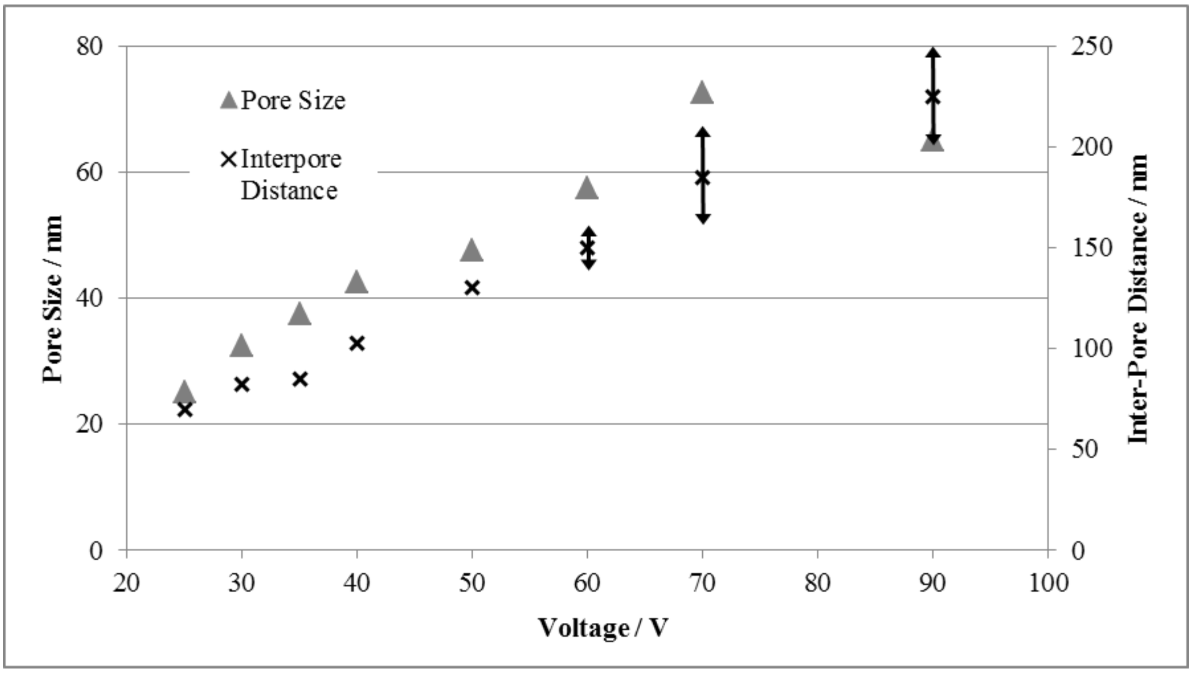

Figure 4.17: Plot of pore diameters (measured at the front side by SEM) and inter-pore distances after metal dissolution (DisA) as a function of the anodization voltage. The inter-pore distance for 60 V, 70 V, and 90 V is replaced by the cell size (measured on the back side). The arrows indicate the huge distribution of measured values.

The distribution of achieved pore sizes between about 30 nm and 50 nm was consistent with the requirements for application as a filter membrane (see Chapter 1.3). For this reason, further variations of the electrolyte concentration to alter pore size were not pursued.

In Figure 4.18, a selection of SEM back side views are presented. The order of the combs decreased strongly at the low potential of 30 V or the high potential of 60 V. In between long-range hexagonal order was observed.

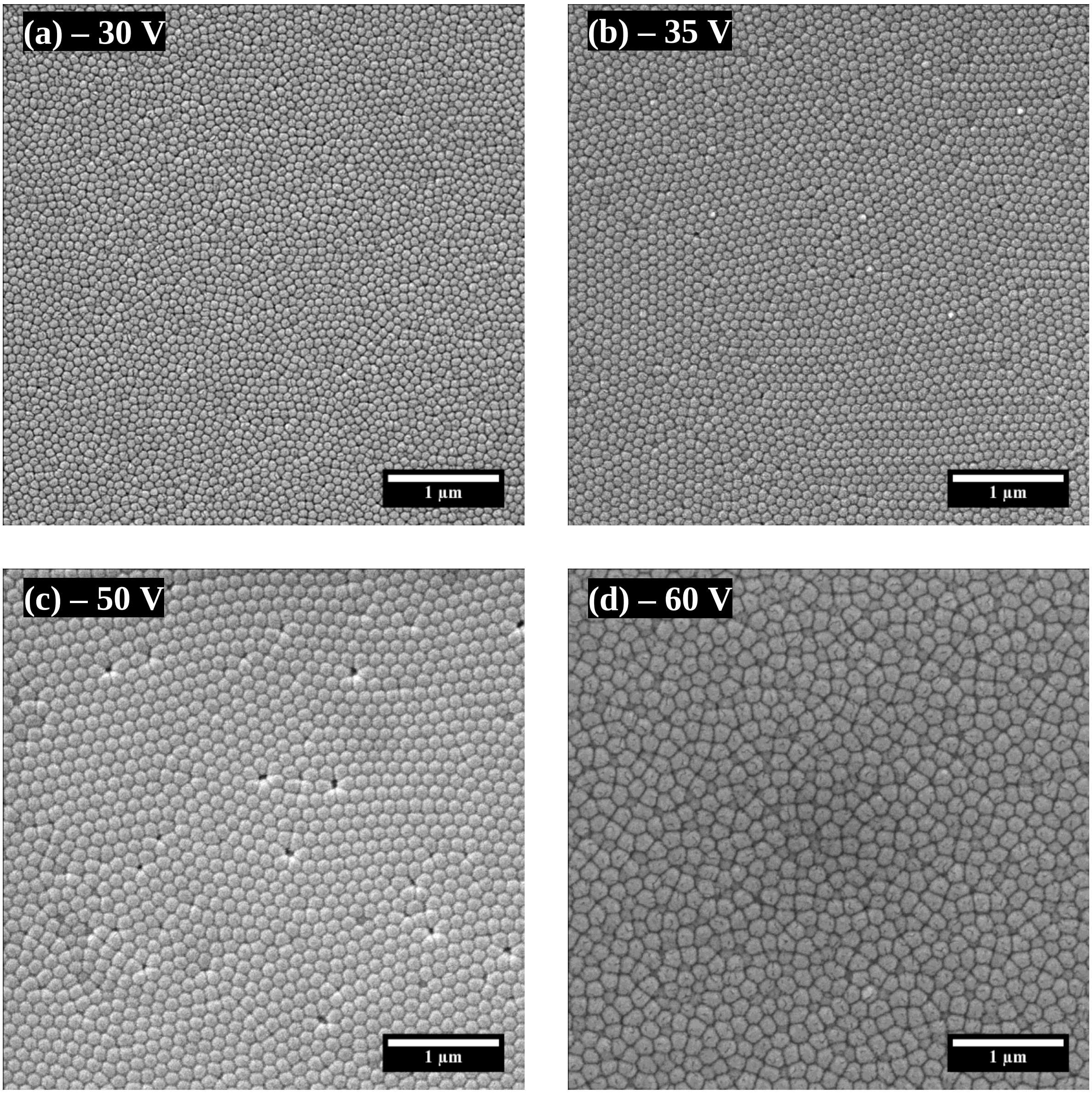

Figure 4.18: SEM images of AAO back sides with closed pores (combs) formed at (a) 30 V, (b) 35 V, (c) 50 V, and (d) 60 V.

Figure 4.19 shows the typical exponential trend[103] of the (steady) current measured with increasing anodization potential. Deviations up to about 10 %from the given values were not unusual and had multiple possible reasons, such as minor variations in temperature, electrode distance, or agitation speed. Current densities could easily be calculated with respect to the 16 mm oxide disc area of 2 cm^2.

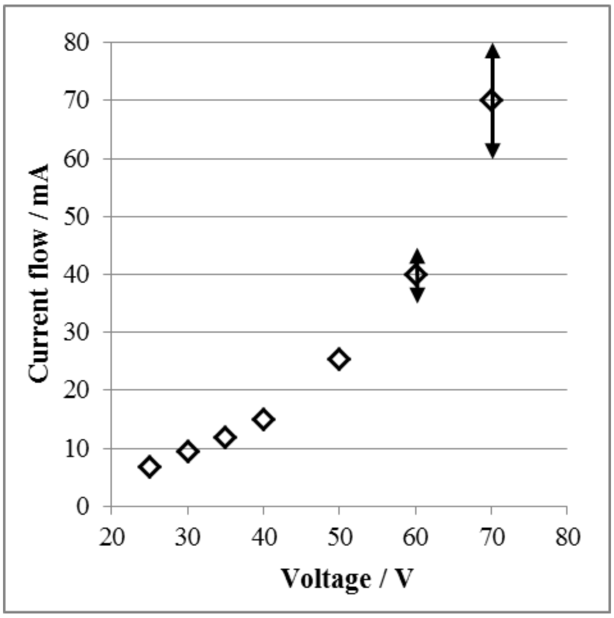

Figure 4.19: Plot of steady current values measured for standard anodizations (16 mm sample diameter) against the anodization voltage. The arrows at higher voltages indicate the non-uniform current obtained.

The values were stable to some degree over the reaction time (as previously discussed, see Chapter 4.3), but with rising potential, the values eventually dropped, at an earlier point with correspondingly higher chosen potentials. An anodization period of more than 3 h at 50 V, for example, led to a decrease in current from about 25 – 26 to 21 – 22 mA. A reason for the decrease is the diffusion limiting thickness of the oxide layer, which grows much faster at higher voltages. Anodizations with more than 50 V showed a very high current and a fast decay, sometimes within a one-hour reaction period.

4.4.2 Factors Influencing the Oxide Layer Thickness

So far, pore sizes (measured at the porous surface) were discussed in relation to the applied voltage. It was also mentioned that the measured current increased with the potential. Of course, the oxide layer thickness is a function of the total current flow during the electrochemical oxidation (according to Faraday’s law). Extending the reaction time will lead to thicker oxide layers, as will anodizations at higher compared to lower potentials, if the reaction period remains constant.

Figure 4.20 shows self-supporting oxide layers produced with the same voltage for different reaction periods. The color increase of the AAO in Figure 4.20 (b) indicates an increased thickness for the long-term experiment.

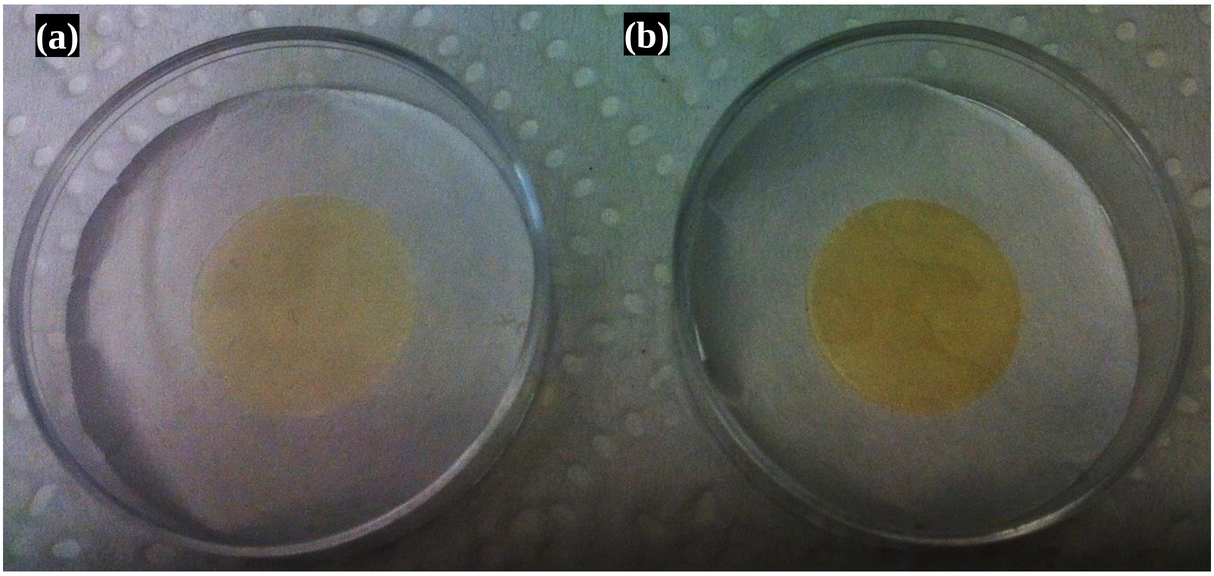

Figure 4.20: Photograph of two AAO after DisA, anodized at the same voltage for (a) a short and (b) a prolonged reaction period.

Reaction period and layer thickness should correlate proportionately, simply because the current flow over the time remained approximately constant. In practice, this relation was found to be true. There also was no difference in layer thickness between the first (A1) and second anodizations (A2), if voltage and reaction period were the same.

Figure 4.21 shows cross-sectional studies on the time-dependent thickness of the oxide layer, all formed at a potential of 40 V. The oxide layer thickness increased from about 12.5 – 13 µm for 1 h to 46 – 48 µm for 4 h, following a linear trend.

The current flow in single experiments was sometimes much lower compared to the average. Usually, abrasion of the sliding contact at the rotating electrode was identified to be responsible for insufficient conductivity. Surprisingly, the lower current generally had no negative influence on the layer thickness, indicating a moderate efficiency of the electrochemical process.

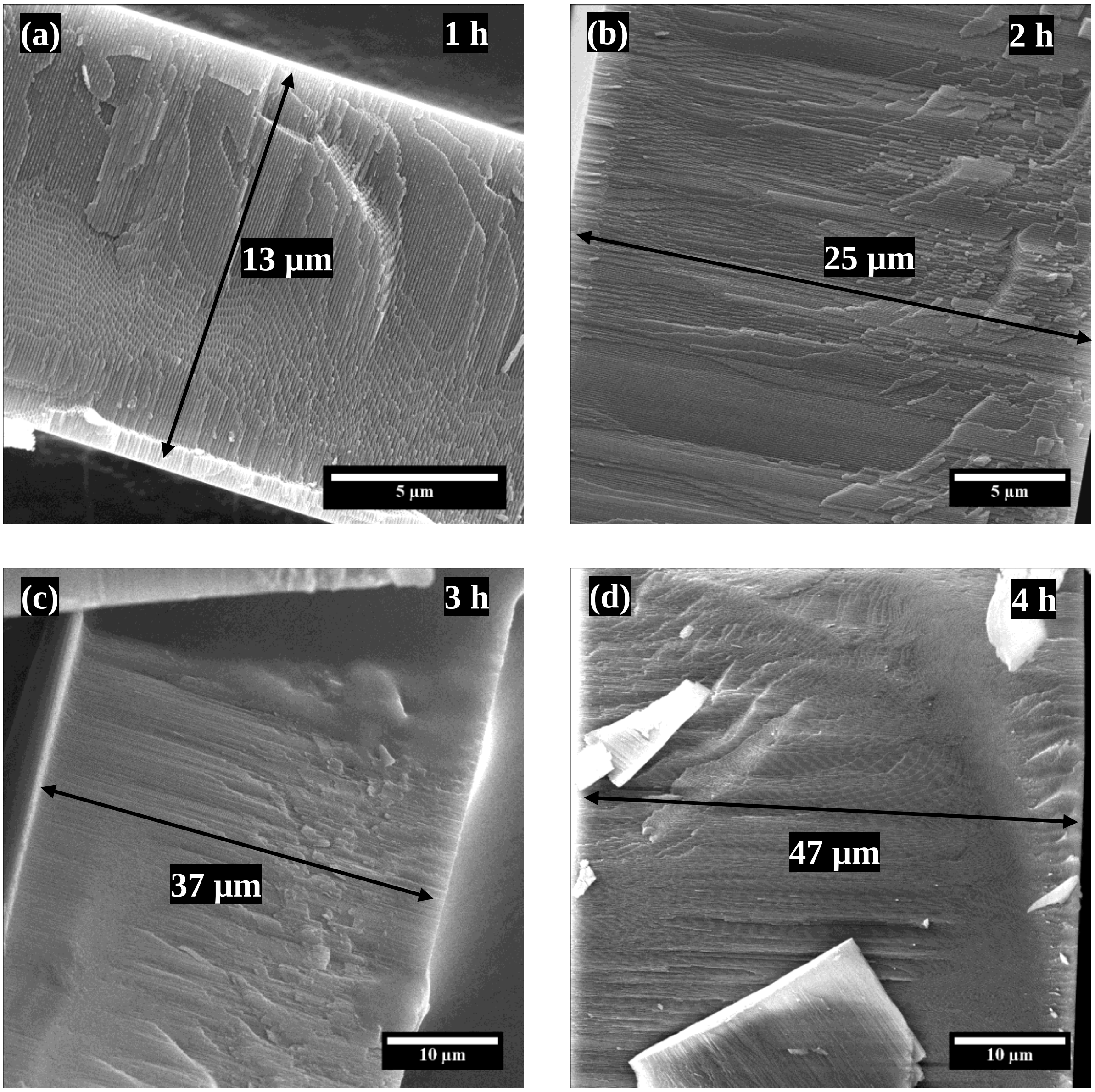

Figure 4.21: SEM cross-sectional studies of AAO produced at 40 V for 1 to 4 h (a-d).

Because the current density increases with the applied potential, the oxide layer thickness grows likewise. Figure 4.22 gives a comparison of three self-supporting AAO formed after a reaction period of 2 h at 35, 40, and 50 V, respectively.

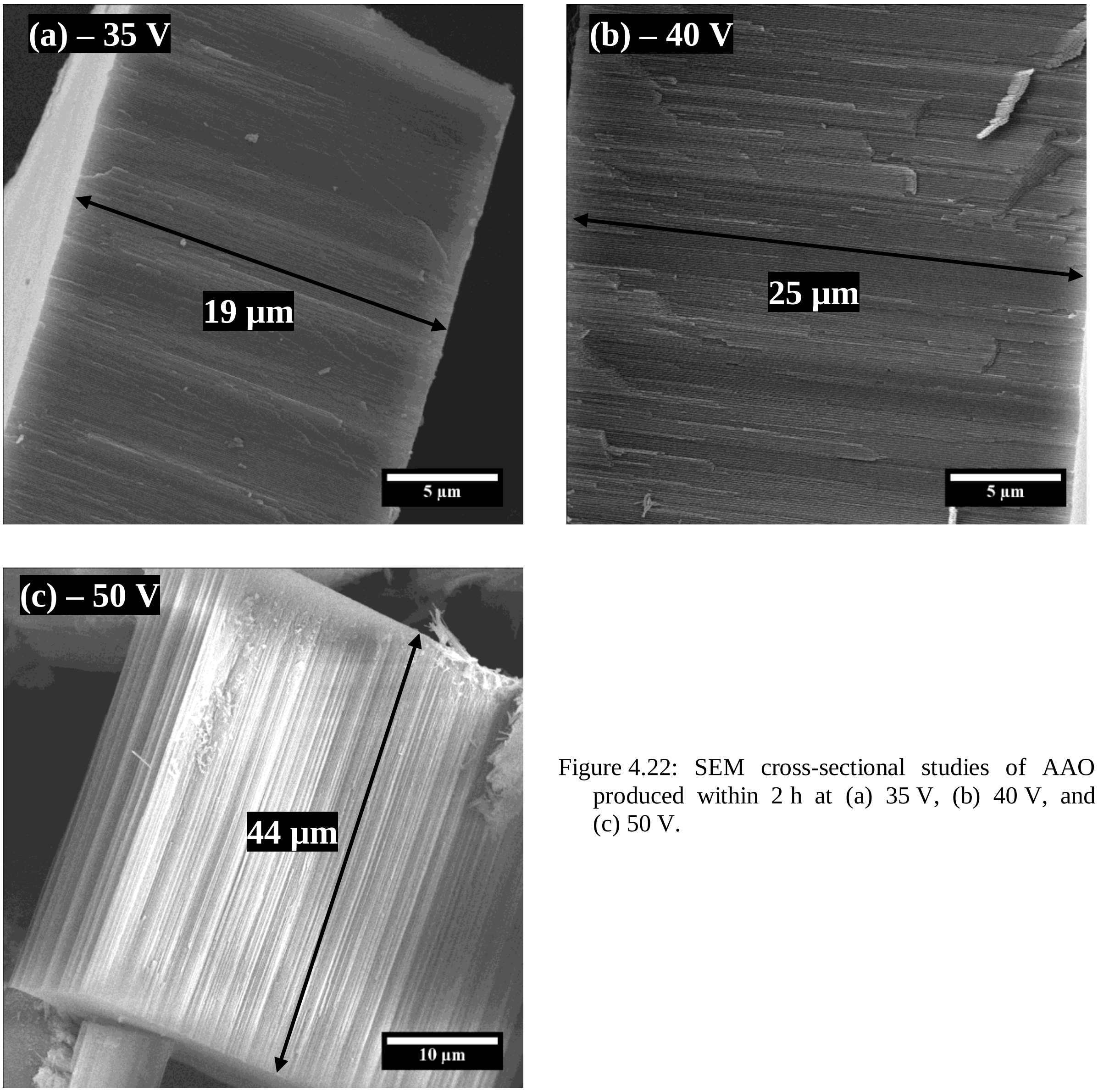

Figure 4.22: SEM cross-sectional studies of AAO produced within 2 h at (a) 35 V, (b) 40 V, and (c) 50 V.

Figure 4.23 shows the correlation between anodization period and layer thickness with dependence on the voltage. The linear relationship between oxide thickness and reaction period becomes clearly visible. As discussed earlier, with longer reaction periods or at higher potentials the increase in thickness became disproportionately low. Generally, the growth rates for the AAO were comparable to the ones published by Sulka *et al.* for 25 °C.[103]

The indicated values for the membrane thickness are suitable as guidelines. Usually, an attempt was made to analyze the layer thickness by SEM in the approximate middle of the macroscopic oxide disc. It was assumed that the oxide layer thickness over the whole sample diameter is not perfectly constant, due to edge and agitation effects during production.

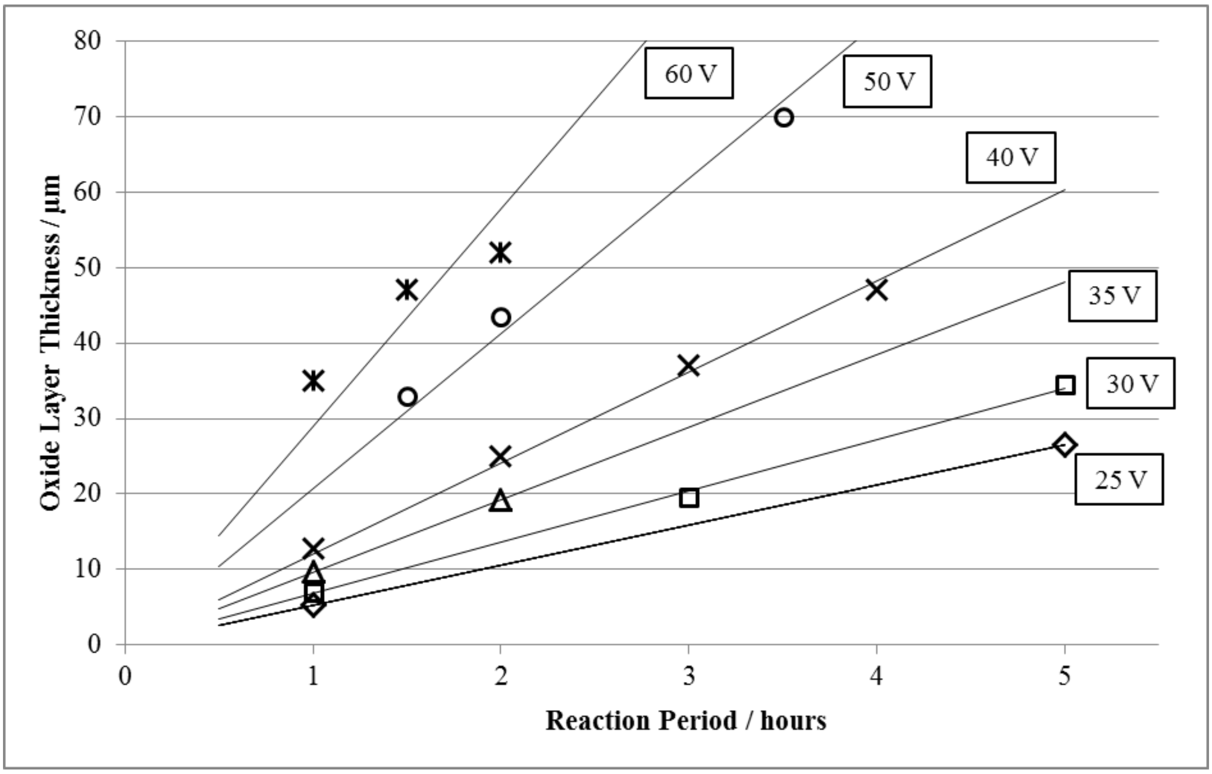

Figure 4.23: Plot of the oxide layer thickness against the reaction period for different anodization voltages.

In general, maximum layer thicknesses of about 70 µm could be produced when a relatively short pre-anodization was applied. The only reason for this limit was the use of an aluminum foil with a thickness of 100 µm as a standard. However, a complete oxidation of the foil by anodization was unfavorable and consequences thereof will be discussed in a different context in Chapter 4.8.5. For the minimum layer thickness, no defined limit was examined because of the demand for a mechanically stable membrane. The dissolution process of aluminum led to a high emission of bubbling hydrogen gas, exerting force on the brittle samples. Completed membranes with opened pores on the back side were produced down to a layer thickness of 7 µm (see Chapter 4.5.3).

If the diameter of the channels was analyzed close to the front side (where measurements are usually performed by SEM top views), halfway in the middle of the oxide layer, and close to the capped ends of the channels, the pore diameter remained strikingly constant. The example in Figure 4.24 shows an A1 oxide layer (40 V, 2 h) with about 45 nm channels. Figure 4.24 (a) reveals that after only some 100 nm of anodically grown oxide, regular ordered channels had formed, with a diameter surpassing that of the initial, unordered pores (see Figure 4.5).

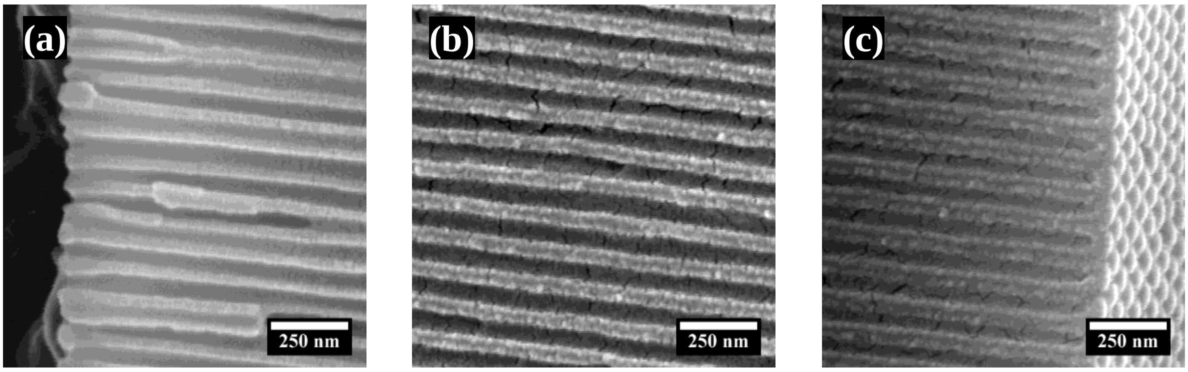

Figure 4.24: SEM cross-sectional study of AAO channels (A1, 40 V, 2 h) along the whole oxide layer thickness: (a) front side, (b) middle section, and (c) bottom side.

4.4.3 Exact Pore Size Determination: An Excursus

So far, pore sizes measured on top of the AAO with help of electron microscopy pictures, as well as channel diameters inside the porous structure were discussed. To draw the right consequences for the reaction planning from the observed results and to compare and rank them with literature results, a closer look at the pore measurement process should be taken.

Very often in literature, meticulous pore size distributions are presented, assuming a high accuracy in synthesis and analysis. In the publication of Sulka *et al.*, herein already often cited, one can read that “the average pore diameter of anodic alumina based on 1000 independent measurements, was estimated from FE-SEM top-views for various anodizing potentials and all studied temperatures”.[103] In terms of statistics, this is a powerful statement, but what about, for example, systematic errors?

Usually, three analytical methods are used for the determination of pore sizes: Atomic force microscopy (AFM), transmission electron microscopy (TEM), and, of course, SEM.[113] With AFM only the AAO surface can be scanned, but therefore no requirement on the conductivity of the samples is necessary. TEM can be used to observe the cross-sections by slicing and thinning the macroscopic oxide layers, but the pretreatment is complicated and time-consuming. SEM, a by far easier method, is more widely used and is also the predominant analysis method in this work.

Images taken by SEM, however, should be regarded with a critical eye and a comparison with foreign data is problematic. First of all, the acceleration voltage used has a high influence on the images recorded, but it is rarely reported. Figure 4.25 shows images of the opened back side (see Chapter 4.5.3) of an AAO produced at 50 V, taken with 15 kV, our standard settings, and 30 kV. The faster electrons at 30 kV penetrate deeper into the material, thus the detected secondary electrons contain more depth and less surface information. In this case, the apparent pores obviously seem to be narrower in Figure 4.25 (b). In fact, the pores do are narrower compared to their surface appearance.

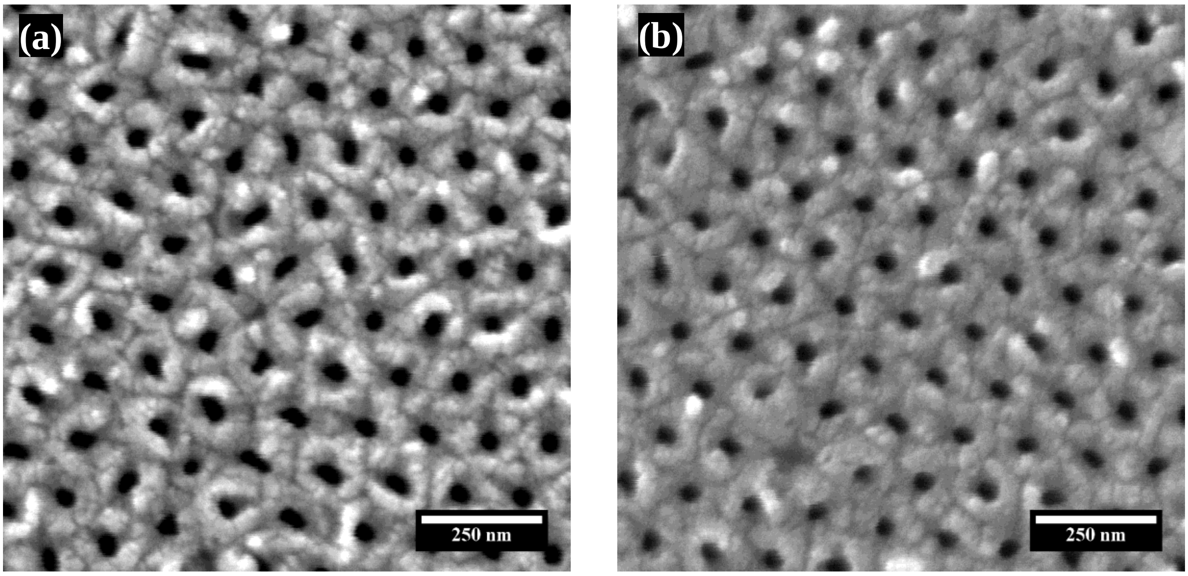

Figure 4.25: SEM images of the same AAO surface (50 V, back side with opened pores), taken with (a) 15 kV and (b) 30 kV acceleration voltage.

A further possibility of unintended manipulation are the contrast and brightness settings of the control software. Because the pores had a funnel-shaped aperture, the transition from pore wall to pore channel is smooth and allows a different view on the same sample.

However, the most worthy discussion factor is the sputtering of a conductive layer (typically gold) on top of the insulating AAO, not only covering the surface microstructure, but maybe even reducing the real pore sizes. For high-resolution SEM, this process was absolutely necessary, in contrast to the results shown for semi conductive ATO in Section 3. To keep the influence of an extra layer on top of the sample as small as possible, only 7.5 nm of gold were deposited on the as-prepared AAO. However, the diameter of the created pores was only one order of magnitude higher. Therefore, it had to be determined if the sputtered porous AAO appeared smaller in diameter on SEM images because of the gold topping.

To analyze the effect of gold sputtering, thin layers of AAO on stabilizing aluminum foil were produced. Figure 4.26 shows a surface anodized for only 10 min at 50 V with and without gold layer. The gold is clearly visible, covering the surface fine structure of hexagonal cells surrounding the round shaped pores. Even though the pores are very small (30 – 35 nm) due to the very short reaction time and the missing dissolution step (DisA), no clear reduction of pore size or even plugging is visible. However, without gold, even this thin oxide layer was insulating enough such that initial charging effects were observed while using the SEM.

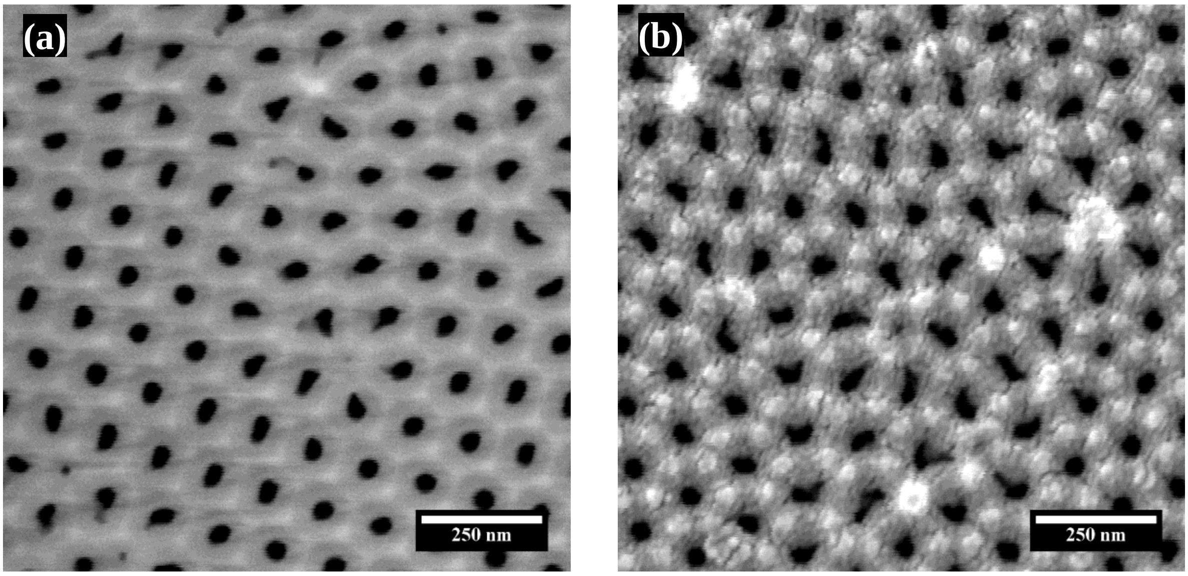

Figure 4.26: SEM images of the same AAO surface (50 V, 10 min) (a) without gold layer and (b) with conductive gold layer of 7.5 nm.

In summary, it is disputable how AAO pore sizes can be published accurately down to single nanometers (as often claimed), disregarding effects like electron microscope resolution, undefined pore contours on the surface, and surface changes due to sputtering. For this reason, all presented specification in this work are error-prone, which is taken into consideration by indicating size ranges of typically 5 nm. Just the top view of the sample does not tell much about the pore diameter in the material, which will be discussed intensively in Chapter 4.5.5.

The non-sputtered image (see Figure 4.26 (a)) showed hexagonal cells declining into the “real” pores. Cross section views of the first nanometers of an oxide layer show the funnel-like character of the pore entrances (see Figure 4.27). This structural effect might be induced by the “oversized” imprint after the pre-anodization (see Figure 4.7) or be an effect of chemical attack of the acidic electrolyte. It reduces the informative value of the top view considerably, even though it is the most common value in literature.

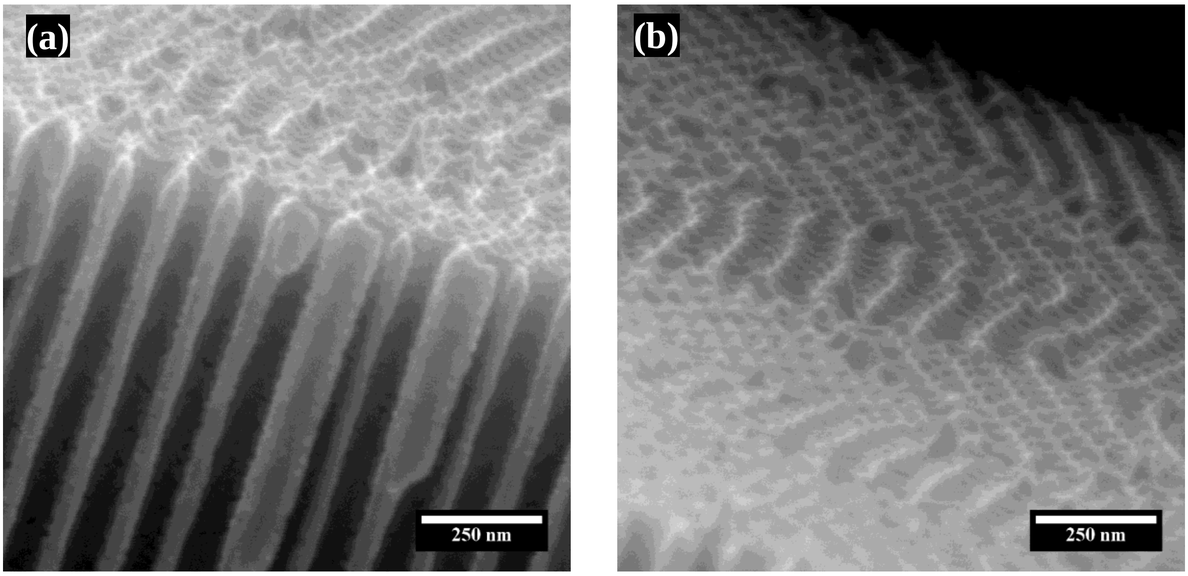

Figure 4.27: SEM cross-sectional studies showing (a) the funnel shaped pore apertures at the front side of AAO surfaces and (b) the resulting nano-structuring.

More significantly, especially if application as a filtration membrane or template is planned, the measurement of pore channels from cross section images is favorable. But in this case other problems arise: Sputtering with gold will still have more influence on the observed channel structures because of its shallow depth. Moreover, a certain number of straight-lined broken oxide pieces with several parallel channels of the same size have to be found for a reliable analysis. In addition, if the cross-sectional area is orientated only slightly diagonal to the scanning beam, all channels are measured smaller than they actually are. Altogether, the informative value of a random sample becomes small compared to the unlimited possibilities of finding nicely ordered pores on the front side of a square-centimeter-sized sample.

4.5 Creation of Self-Supporting Membranes (Pore Opening Procedure)

4.5.1 Conventional Wet Chemical Etching Approach

Of high importance, with our application in mind, was the transformation, or one could even say “metamorphosis”, of only a porous oxide into a membrane with open and continuous channels. The only barrier to this goal was represented by the tellingly so-called “barrier layer” of just some ten nanometers. As well as the thickness of the pore walls, a result of the self-ordering of the pores, the barrier layer grows with applied anodization potential. Figure 4.28 shows the barrier layer of about 55 nm of AAO formed at 40 V.

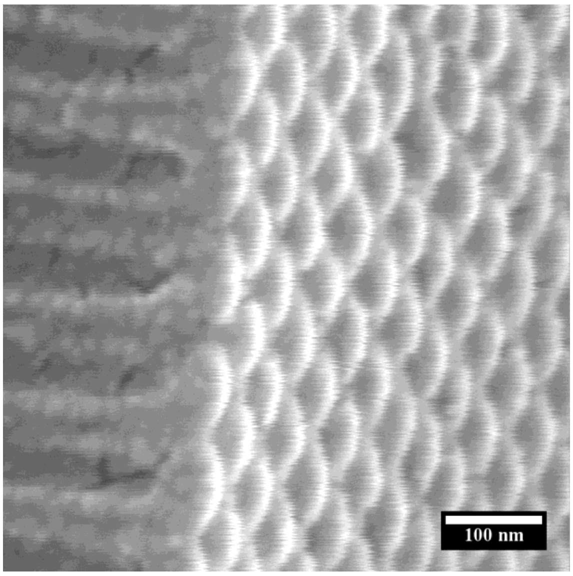

Figure 4.28: SEM image of the barrier layer formed by anodization at 40 V.

For certain template applications, and in particular the filtration, the barrier layer has to be removed. Membranes with barrier layers were proven to be totally impermeable, even to hydrogen gas.[114]

The difficulty lay in selectively removing the bottom part of the oxide disc without damaging the general pore structure. That is why it is described as the “most critical step in the fabrication of anodic alumina oxide with through-hole pore morphology”.[115]

The most popular and particularly widely-used approach is wet chemical etching with phosphoric acid.e.g.[104,116–118] The disadvantage of the wet chemical etching is that the process of pore opening is mainly controlled by the etching time, usually 50 to 90 min. Different etching conditions, such as concentrations of H_3PO_4 from 5 to 10 % and temperature from 25 to 50 °C, have been reported for the pore opening of AAO.[115] Starting from the oxide discs without an aluminum base, the AAO layers are merely immersed in diluted acid, and the barrier layer should dissolve without damaging the remaining membrane.

Usually, the “conventional” wet chemical etching step is performed with 5 % H_3PO_4 at room temperature. Membranes generated at 50 V were reported to lose their barrier layer within 45 – 55 min.[119] Xu *et al.* found the rate of dissolution of the barrier layer at 30 °C to be approximately 1.3 nm/min.[117] 30 µm-membranes were reported to have been produced by treatment with 0.1 M H_3PO_4 for 1.5 – 2 h at room temperature.[118]

Thus, experiments with 5 % H_3PO_4 at room temperature, or a slightly elevated temperature of 30 °C, were performed with the as-prepared AAO discs. Within a short reaction time of some ten minutes, no effect on the structure was observed. The closed pore ends were not affected. Extension of the time to almost 1 h or even 2 h always led to the same observation: The acid attack on the 16 mm discs was irregular. Edges were dissolved much faster than the middle part of the disc. In any case, the whole disc was recovered, and often perceivable maceration appeared.

Depending on exactly which part of the disc was analyzed with SEM, different phases of etching could be documented. There were parts where the desired results occurred. Figure 4.29 shows SEM front (a) and back side (b) images of AAO produced at 35 V for 2 h after treatment with H_3PO_4 for 1 h.

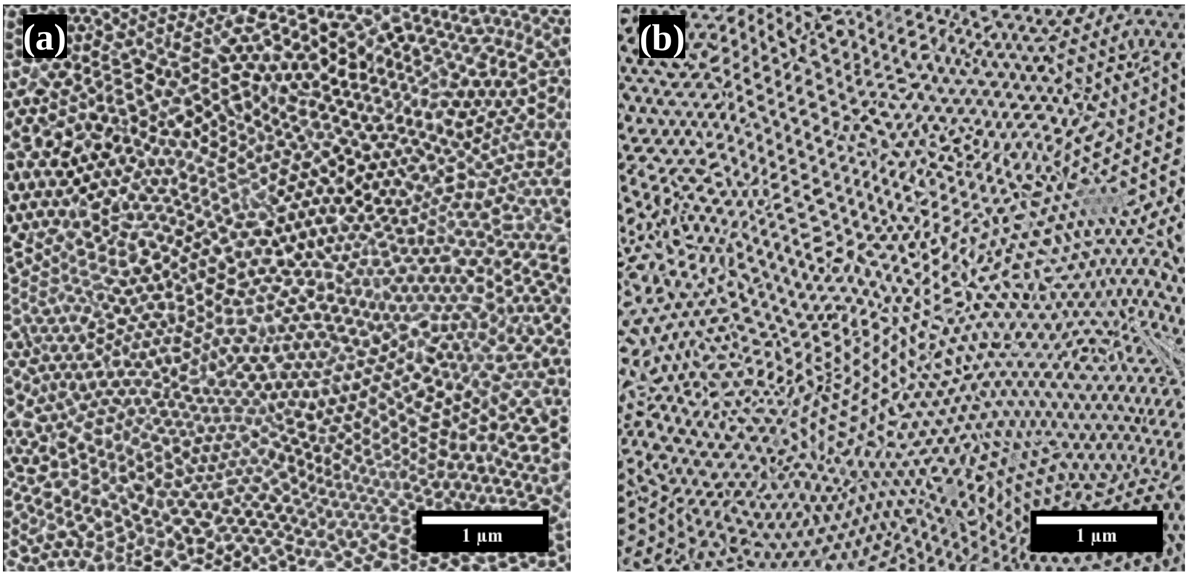

Figure 4.29: SEM images, not representative, of AAO (35 V, 2 h, DisA) after treatment with 5 % H_3PO_4 for 1 h: (a) front side with widened pores and (b) back side with opened pores.

The front side shows an enlargement of the pore diameter from typically about 35 nm (see Table 1) to about 55 nm. This is inevitable because the attack on the oxide reduces the thickness of the pore walls.[120] Figure 4.29 (b) shows an area of the back side where the barrier layer was completely dissolved and the pores became visible (pore sizes were about 45 nm).

Figure 4.30, however, gives a totally different impression by showing another part of the same oxide disc. Due to massive acid attack, the surface of the oxide membrane started to be transformed into nano grass structures (as already observed with ATO). Whatever combination was tried by variation of temperature, reaction period and acid concentration, no homogeneous results were achieved.

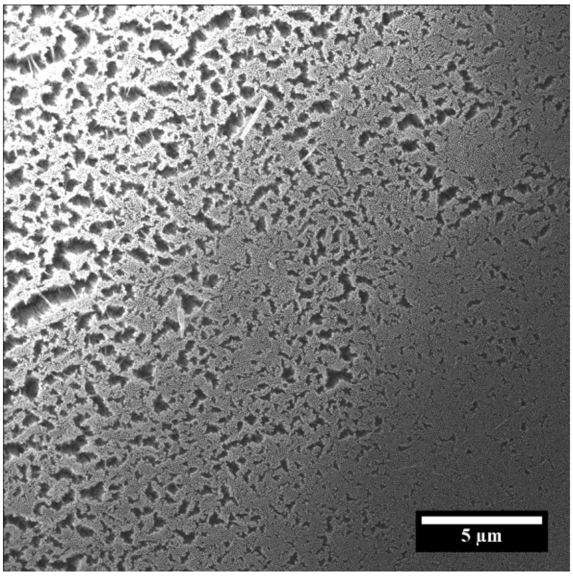

Figure 4.30: SEM image of a corroded part of an AAO layer (35 V, 2 h, DisA) after H_3PO_4 treatment.

Always areas were found where pore walls became too thin and weak, resulting in a sequential folding of collapsing pores (see Figure 4.31 (a, b)). Further thinning of the structures led to a complete destruction of the surface as Figure 4.31 (c, d) impressively shows.

The front side of the membrane was mainly attacked where the high surface of the open pores accelerated the dissolution. These as-treated samples were of course not useful for filtration applications. Often the front side was destroyed before only a single channel was freed from the back side barrier layer.

This lack of control is a frequently mentioned, but often ignored, fact in common literature. The observation of Schneider *et al.* while working with comparable AAO illustrates the difficulty: After 45 min treatment with H_3PO_4 many pores were partially opened at the back side. After a further 5 to 10 min, all pores were found to be opened, but some pores were also already connected to neighboring pores.[119]

The suggestion, often found, to float oxide layers back-facing on the phosphoric acid, would intuitively help to prevent the attack of the front side and to intensify the impact on the back side. However, results with as-prepared AAO layers did not differ at all from those described above. Probably wetting of the front side of the oxide discs occurred anyway, especially at the edges of the disc. Moreover, after a given period of time, the discs sometimes sank into the solution of H_3PO_4. Taking this moment as the ideal breakpoint did not prove to be feasible, as sinking due to soaking was not indicative of completely opened pores.

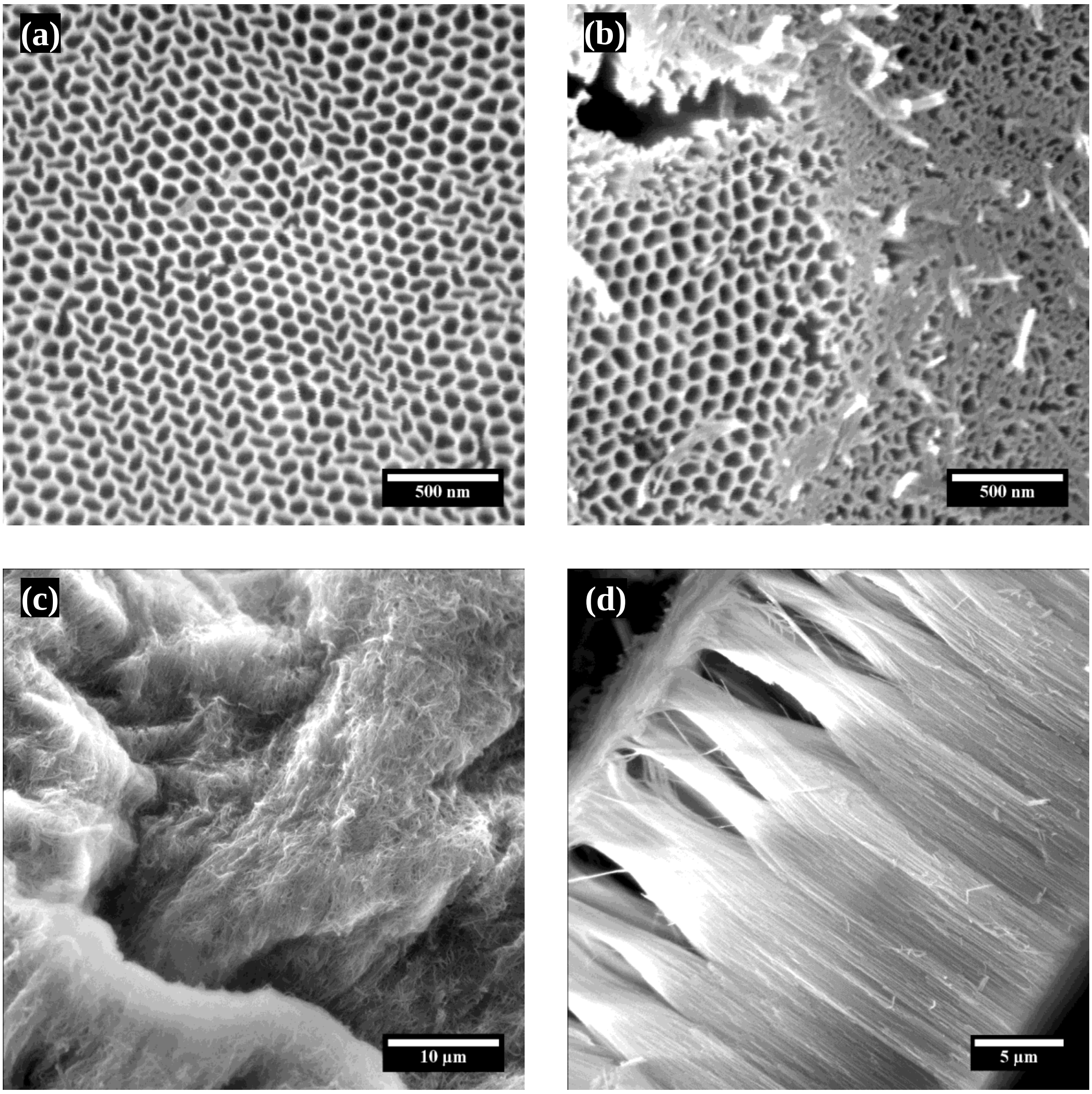

Figure 4.31: SEM images of different stages of degradation due to H_3PO_4 treatment: (a, b) Collapsing pore walls and (c, d) nano grass formation from top and cross-sectional view.

Instead of using acids to dissolve the barrier layer, sodium hydroxide solution is a reported alternative.[121] According to Chen *et al.*,[122] experiments were performed in 0.2 % NaOH solution for 1 to 4 h with application of the “floating” technique. Analogous to results obtained for phosphoric acid, the front side showed corroded and fused pores (see Figure 4.32 (a)). At the same time, the back side was only partially opened, even after about 2 – 3 h (see Figure 4.32 (b)) and the thickness of the oxide discs was always reduced by tenths of micrometers, as cross-sectional studies revealed (see Figure 4.32 (c)).

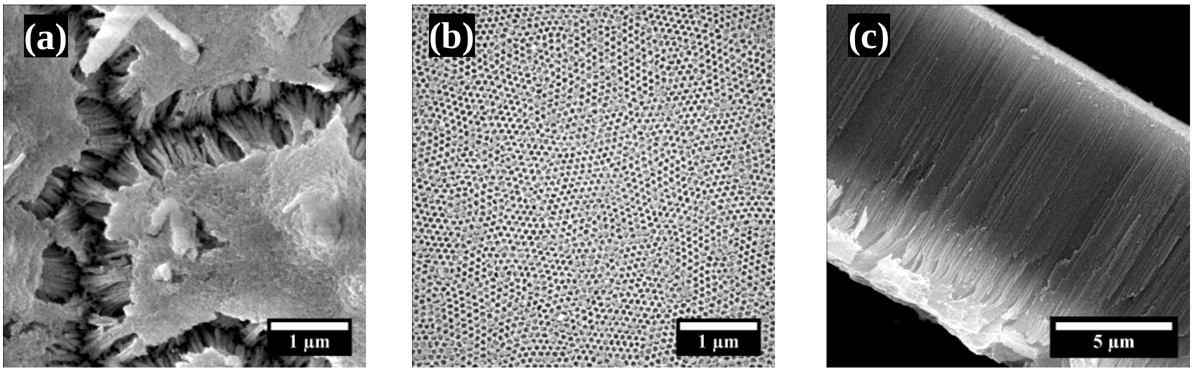

Figure 4.32: SEM images of AAO (35 V, 2 h) after treatment with 0.2 % NaOH solution for 1 h: (a) Corroded front side, (b) back side with partially opened pores, and (c) cross section showing initial nano grass formation.

4.5.2 Modified Wet Chemical Etching Approach

In conclusion, for the acidic and the basic approach, it was noted that immersing in the solution did not allow for a pore opening over a large area. Capillary forces help the etching medium to penetrate into the pores and thin out the walls from the inside. Floating the disc's backside on the solution theoretically had the potential to improve the results, but an improvement of the procedure was necessary, because wetting of the front layer could not yet be excluded.

To counteract sinking of the samples into the solution and front side wetting, increase in the density and viscosity of the etching solution by the addition of a thickener was explored.

Experiments were performed with 0.4 % NaOH solution in which PEG 20000 was dissolved. The PEG had the advantage that it was already soluble in the cold solution and was miscible with water in every ratio. Therefore, it was easy to wash the sample after the treatment to clean it from polymer. A 1:1 weight ratio of NaOH solution/ PEG resulted in a honey-like gel that fulfilled the demands. Experiments for 45, 90 and 180 min confirmed that the oxide discs were adhering in a good manner to the gel but did not sink. SEM analysis showed that on the one hand, the front side was not attacked at all (see Figure 4.33 (a)), but on the other, the back side pore bottoms were not opened. Instead, it was seen that crack formation occurred along the borders of the hexagonal cells (see Figure 4.33 (b)). The extension of the reaction time only increased the size of the cracks, but did not result in pore opening over a large area. This was already observed for titanium (see Figure 3.17 and Figure 3.19), but it was nevertheless very surprising for the porous-type aluminum oxide. Once again, structural similarities between ATO and AAO become evident.

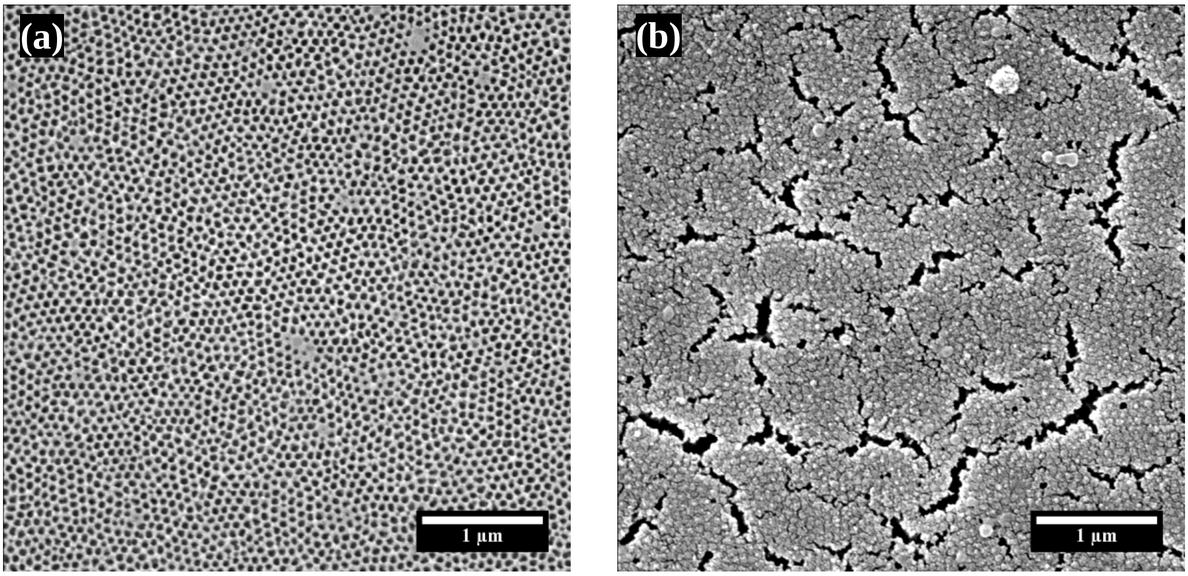

Figure 4.33: SEM images of (a) front and (b) back side of AAO (30 V, 3 h) after back side floating on NaOH-PEG for 90 min.

Several variations were tested to dissolve the barrier layer through a more concentrated etching gel. Increasing the concentration of the NaOH in the solution to 1 % did not improve the result; 2 % already led to a strong dissolution of the oxide disc, which became soft and started curling. Because a replacement of the base by phosphoric acid yielded no improvement, and often residues of PEG were found on the oxide even after intense washing, the general idea was discarded.

Another solution for preventing front side attack with wet chemical approaches discussed in literature is the protection of the front side of the AAO with polymeric adhesives before etching (as is also suggested for ATO, Chapter 3.4.1). In 1996, Masuda and Satoh had already used a protective layer composed of a mixture of nitrocellulose and polyester resin in ethyl acetate, butylacetate, and heptane.[36] Using 5 % H_3PO_4 solution at 30 °C, it is reported that the level of pore opening is directly controllable by the reaction time.[104]

A more convenient method was reported using just nail polish, coated on the oxidized foil before removing the Al and peeled off after the H_3PO_4-treatment using tweezers.[107]

All of these approaches have the disadvantage that two more steps are required: protection before and deprotection after the etching. The coating with a polymer layer requires an accurate covering of only the front side and the ability to easily dissolve the protective layer after the process, leaving no residues. However, alternatives reported, like adhesion of the front side of the AAO to microscopic slide glass[105] or mounting of the AAO in a setup that allows just back side etching,[115,123] seemed to be uncertain and technically demanding, respectively.

For the experiments, in addition to standard nail polish, a polymeric UV-curing glue already used with ATO was found to be suitable to adhere to the oxide discs. Both substances could be precisely applied to the oxidized foils right before dissolving the aluminum. This method guaranteed a covering of the whole front surface without contaminating the back surface. Moreover, thin oxide discs were mechanically stabilized, and a further advantage was that the polymeric layer safely floated on the etching solution, always keeping the surface to be attacked in contact with the solution. After the etching, the polymer layers were dissolved in toluene.

Both polymer layers protected the front surfaces reliably, but etching with H_3PO_4 or NaOH solution still led to the described problems on the back side. The approach with NaOH, in particular, continued to give inhomogeneous results. The barrier layer was insufficiently dissolved in one region, while collapsing of the pores had already started in another. In spite of the protective polymer, the discs lost shape when dissolved from the edges.

With phosphoric acid, the best results with the wet chemical etching method were achieved. Figure 4.34 shows SEM images of an AAO (35 V, 2 h) that was protected with nail polish and subsequently treated with 5% H_3PO_4 for 90 min. Due to the protective layer, the front side stayed intact, apparent also from the cross-sectional view, and the back side showed a high degree of opened pores. The typical pore size for 35 V AAO of about 35 – 40 nm was enlarged to about 55 nm on both sides by the acid. Within the channels, 45 – 50 nm were measured (see Figure 4.34 (d)). Figure 4.34 (b), however, still shows some unopened pores and the oft-described tendency of over-etching at the edges of the discs, destroying the integrity of the whole membrane, remained. The nature of the anodic oxide made the whole etching processes hard to control. A to-the-minute procedure with respect to different barrier layer thicknesses or even small room temperature variations would be necessary. For this reason, a monitoring of the pore opening process by measuring electric current through AAO using an electrochemical permeation cell had been previously proposed to hit the desired time window of about 5 min.[115]

Therefore, it was analyzed if the AAO could be made more resistive against the chemical attack and if the results could be improved by extending the time window in which pore opening without over etching was possible. As already mentioned (see Section 2), anodic oxides in general are of an amorphous nature. X-ray diffractograms taken of our AAO (not shown here) confirmed this general finding, showing an amorphous background scattering without sharp reflexes that might be allocated to any phase of Al_2O_3.

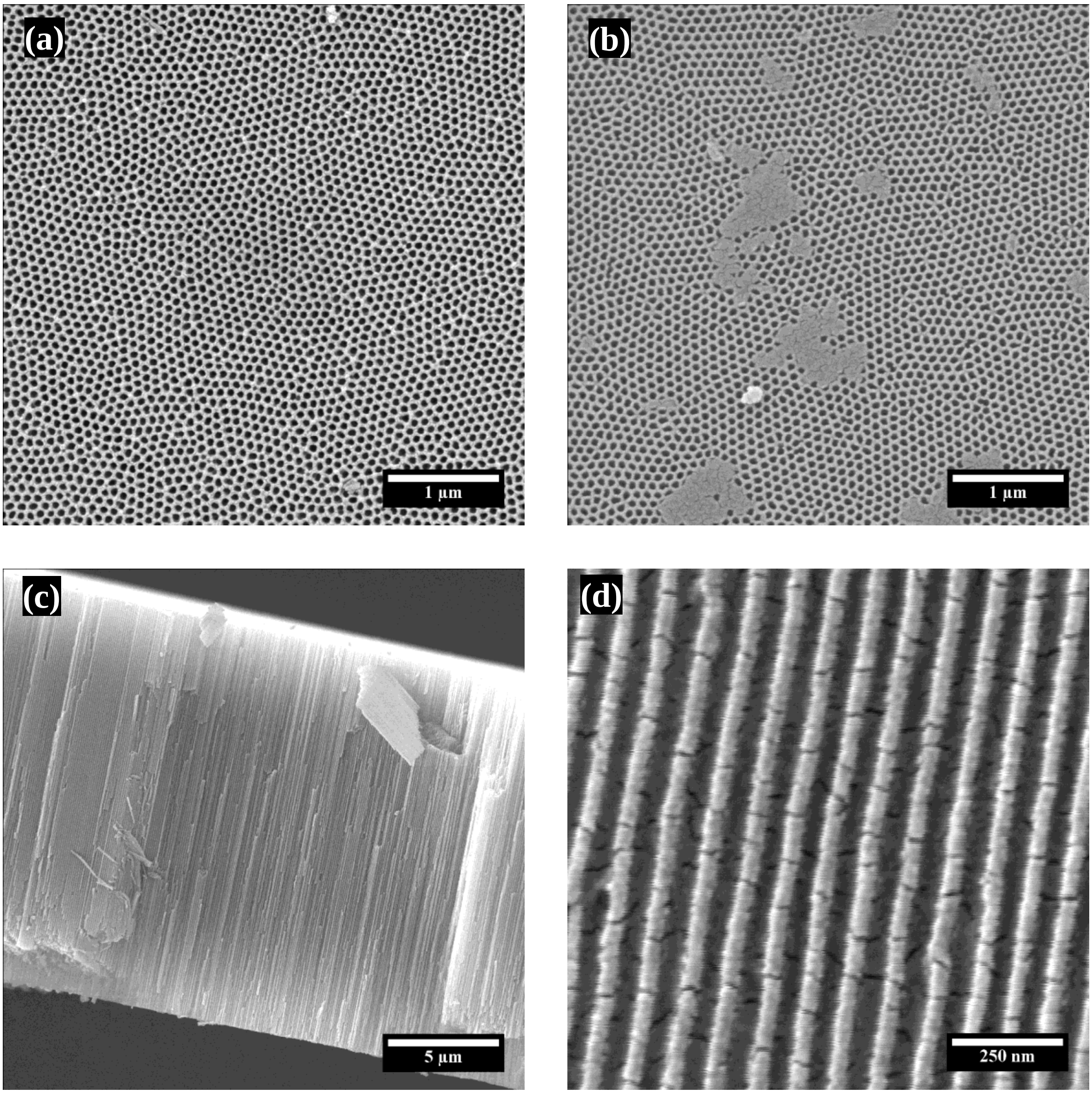

Figure 4.34: SEM images of AAO (35 V, 2 h) have been protected with nail polish and subsequently treated with 5% H_3PO_4 for 90 min: (a) front side after dissolution of the nail polish, (b) back side, (c) cross-sectional study, and (d) channel structure.

Amorphous materials can be characterized as more reactive compared to crystalline materials due to a higher number of defects in the structure. Heat treatment of the amorphous oxide should reduce those defects and finally lead to crystallization of the material. In Chapter 4.8.1.1, this topic is discussed in detail.

AAO discs were annealed at 650 °C where crystallization had not yet occurred (proven by XRD). The only observed difference was that the eventual yellowish coloring of organic residues and oxalate had vanished and the discs had become highly transparent. To prevent curling of the discs, they had to be weighed down by a thermally stable tile. SEM analysis showed that the nanoporous appearance was not changed by the heat treatment (see Figure 4.35 (a)).

Indeed, the resistivity of the front side against etching with phosphoric acid or sodium hydroxide solution was improved, and results for back side pore opening were acceptable.

Unfortunately, even in combination with protective steps for the front side or using the PEG-gel approach, no perfect open membranes could be produced (see Figure 4.35 (b, c)) without corroded sections, especially at the disc's edges.

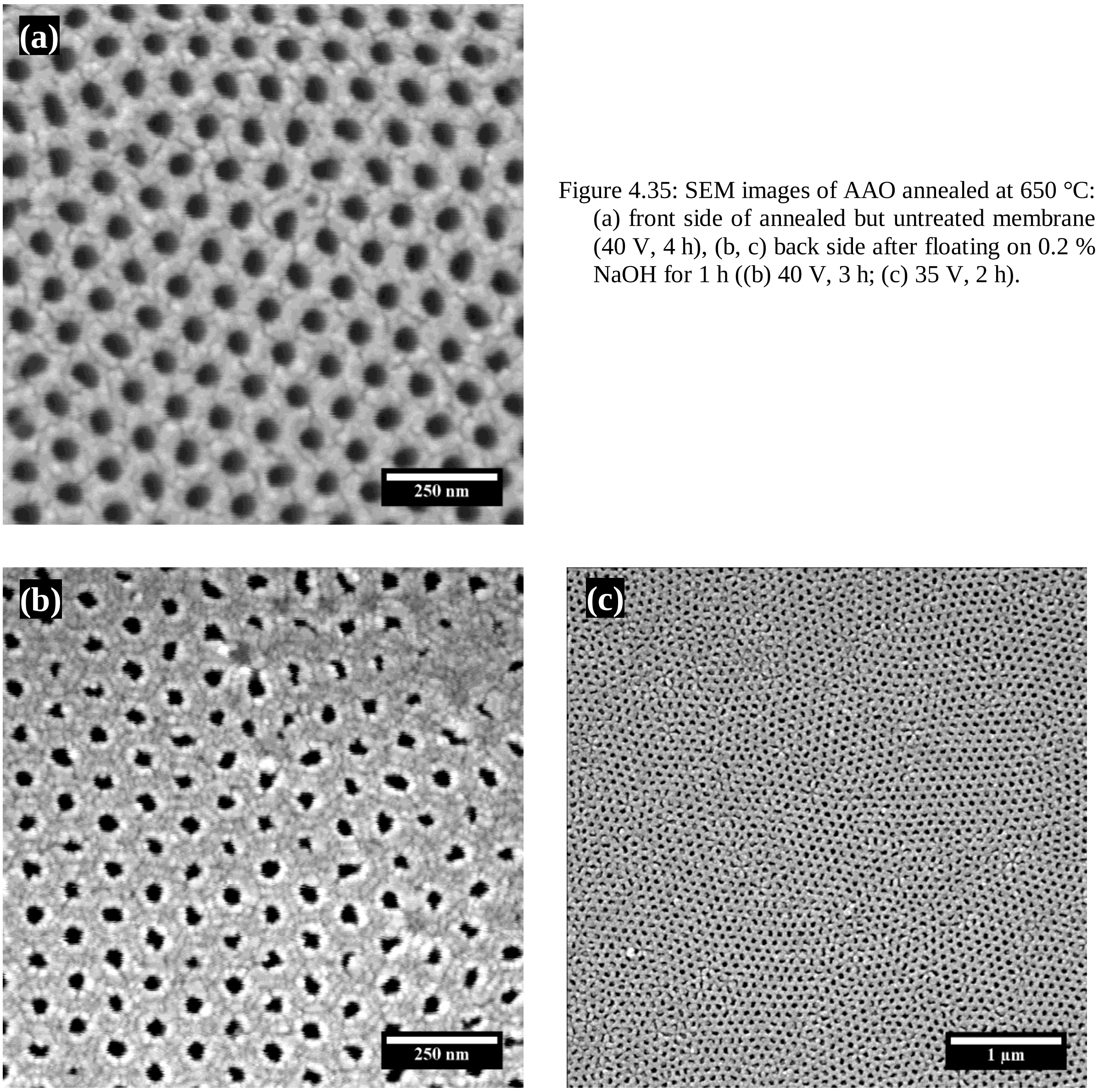

Figure 4.35: SEM images of AAO annealed at 650 °C: (a) front side of annealed but untreated membrane (40 V, 4 h), (b, c) back side after floating on 0.2 % NaOH for 1 h ((b) 40 V, 3 h; (c) 35 V, 2 h).

4.5.3 Voltage Pulse Method

The conventional chemical etching methods gave rise to imperfect results. Even though it might have been possible to better control the etching process, e.g. by varying further the concentrations, for every individual anodization potential a matching procedure had had to be found. Oxide discs exhibiting different pore sizes, and thus different pore wall and barrier layer thickness, would require individual reaction periods too.

It shall not be concealed that there are some more rather “exotic” processes of dry etching described in literature that probably work well. Ar^+ ion milling was found to open the closed nanopores in a controlled way, nanometer by nanometer.[124–126] Performing likewise, Ga^+ ions were introduced,[115,127] as well as reactive ion etching with BCl_3 and CF_4.[128–130] All these techniques require an expensive and sophisticated equipment and are very time-consuming. From this point of view, they were considered inappropriate for an efficient AAO filter production.

Furthermore, a most elegant electrochemical approach was found in literature, which was described in detail by Lira and Paterson in 2002[131] and in particular by Yuan *et al.* in 2004.[105] Anodically oxidized aluminum sheets were again being anodized in a solution of concentrated perchloric acid and butane dione, at a voltage of 5 V higher compared to the voltage used for the anodization. After only 3 s, oxide and aluminum would separate immediately. Even a reuse of the remaining aluminum template for further anodizations should be possible.[108]

First experiments failed just for the reason that butane dione is not very oxidation stable. Mixing with perchloric acid led to an exothermic reaction, resulting in a brownish, viscous product. However, the short voltage pulse led to the desired separation if this unsavory mixture was used as electrolyte together with the Cu-block Setup, containing the oxidized foil and a Pd counter electrode. In fact, the two parts did not fall apart, but an air bubble became visible, captured between oxide and aluminum (see Figure 4.36). The reason for the adhesion can be found in the setup geometry, where a sealing prevents anodization of the whole metal foil. At this interface, no detachment is induced.

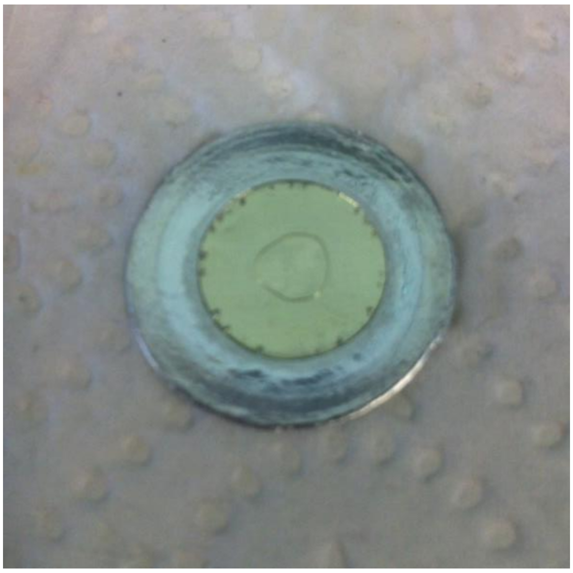

Figure 4.36: Photograph of AAO separated from the underlying Al metal by a voltage pulse, exhibiting a bubble formed between oxide and metal.

The oxide disc could be separated from the aluminum by compressed air, but broke due to the induced mechanical stress. Apart from breaking, no inhomogeneity in shape or color were detectable. The disc had a similar appearance compared to non-opened ones (see Figure 4.10). SEM examination confirmed the existence of continuous channels. Figure 4.37 shows images of an AAO formed at 35 V for 2 h, which was treated at 40 V for 3 s. The membrane's back side showed small but opened pores, partially covered with debris (see Figure 4.37 (b)). The debris observed was in line with images provided in the original literature.[108] Obviously, the short contact with aggressive perchloric acid neither resulted in a pore widening at the front side nor inside the pores.

As improvement, dissolution of the aluminum (DisA) was used to release the oxide disc as a whole after the electrochemical pore opening process (PO). H_2 gas evolution between oxide and metal indicated the missing barrier layer when the metal was dissolved. The treatment with HCl/Cu^{2+} had the advantage that the back side was cleaned from debris and that the channel entrances were now fully opened. Figure 4.38 shows the front and back side of an AAO membrane with homogeneous through-hole morphology, comparable to that in Figure 4.37. Tidied surfaces exhibiting highly ordered pores had been achieved on the whole sample area. The two surfaces of the AAO membrane produced at 35 V were very similar in appearance and exhibited pore diameters of about 35 nm on the front side as well as about 30 – 35 nm on the back side.

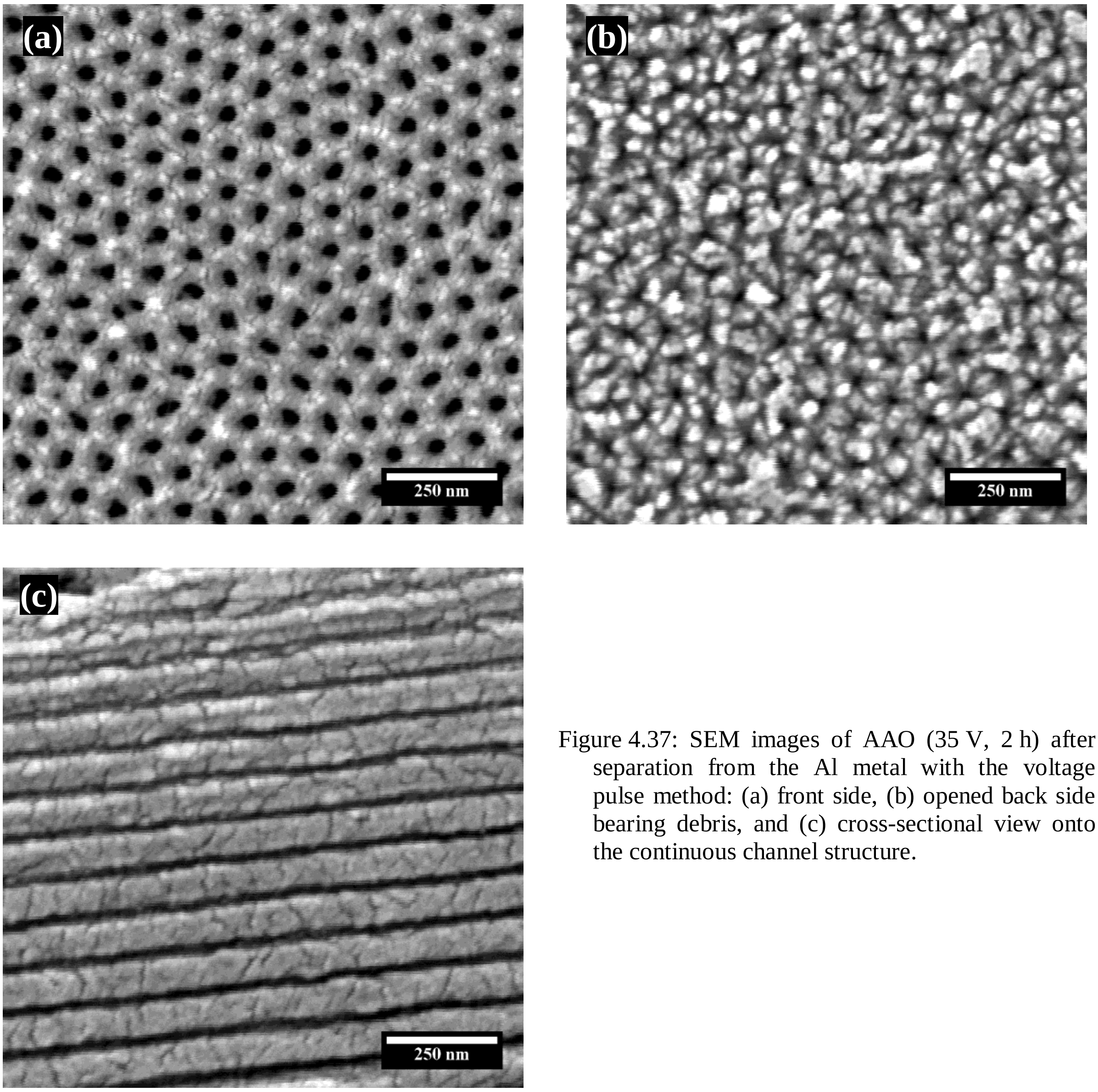

Figure 4.37: SEM images of AAO (35 V, 2 h) after separation from the Al metal with the voltage pulse method: (a) front side, (b) opened back side bearing debris, and (c) cross-sectional view onto the continuous channel structure.

A differentiation of the two surfaces was possible by small distinctive features. At the front side, light bumps were observed on the walls between the pores, which were never found at the back side. In contrast, the back side exhibited defects in form of slit dimples. Moreover, the pores appeared more oval formed and little smaller. However, the regimes of perfect hexagonally order at the back side were larger compared to the front side The described characteristics are highlighted in Figure 4.39.

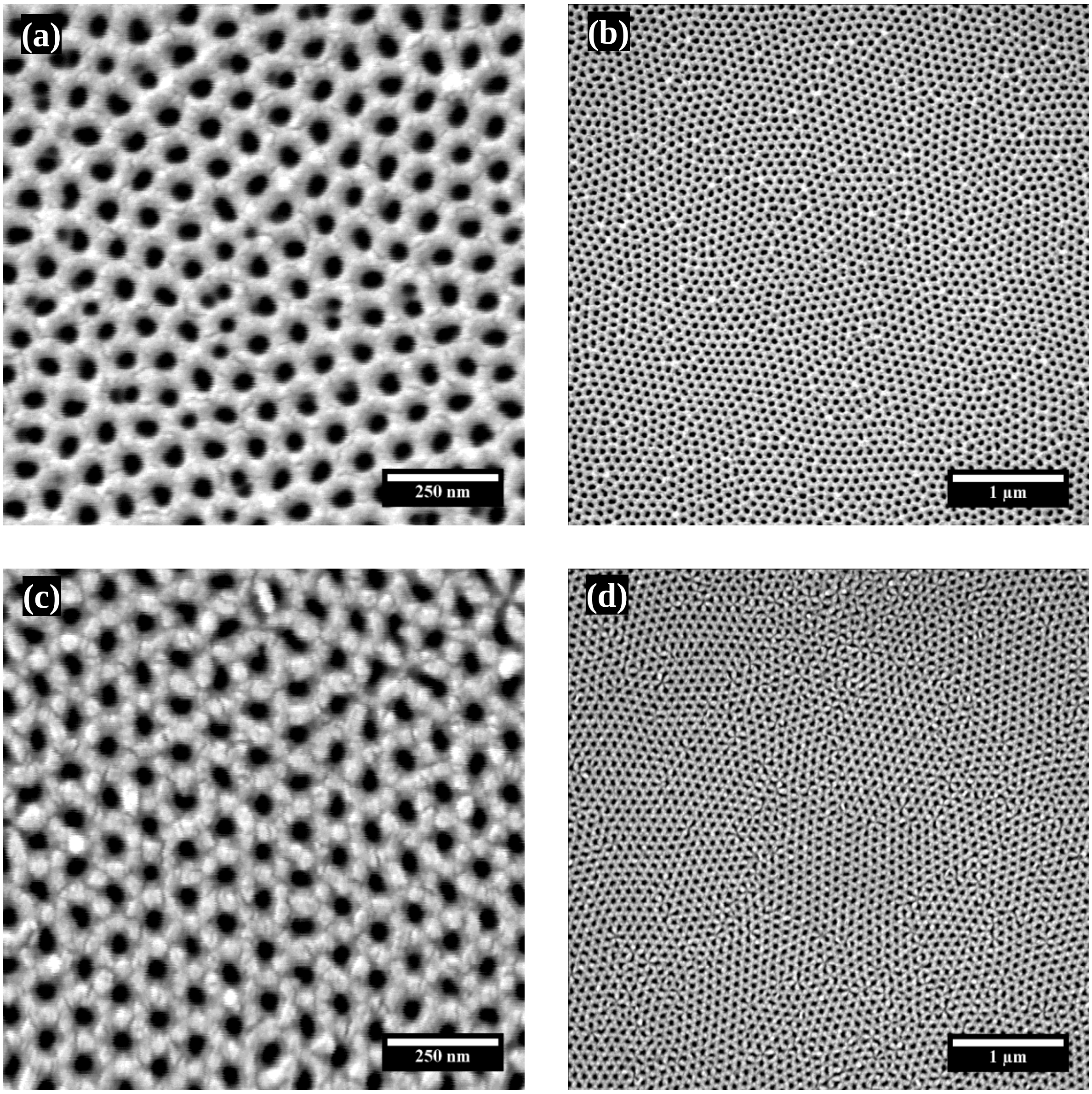

Figure 4.38: SEM images of an AAO membrane (35 V, 2 h) after separation from the Al metal with the voltage pulse method (PO) and subsequent dissolution of Al (DisA): (a, b) front side and (c, d) opened back side.

The advantages of the electrochemical voltage pulse method (PO) over the wet chemical pore opening are obvious: First, there is no pre-preparation, e.g. protection of the sample's front side, necessary. Second, there is no further pore enlargement by the electrochemical pore opening process. However, this is not valid for the subsequent aluminum dissolution process as discussed earlier. Third, the electrochemical pore opening process is very fast. Fourth, the required electrochemical equipment is present anyway. The process follows directly on the anodization (A2) without dismounting of the oxidized foil in the meantime.

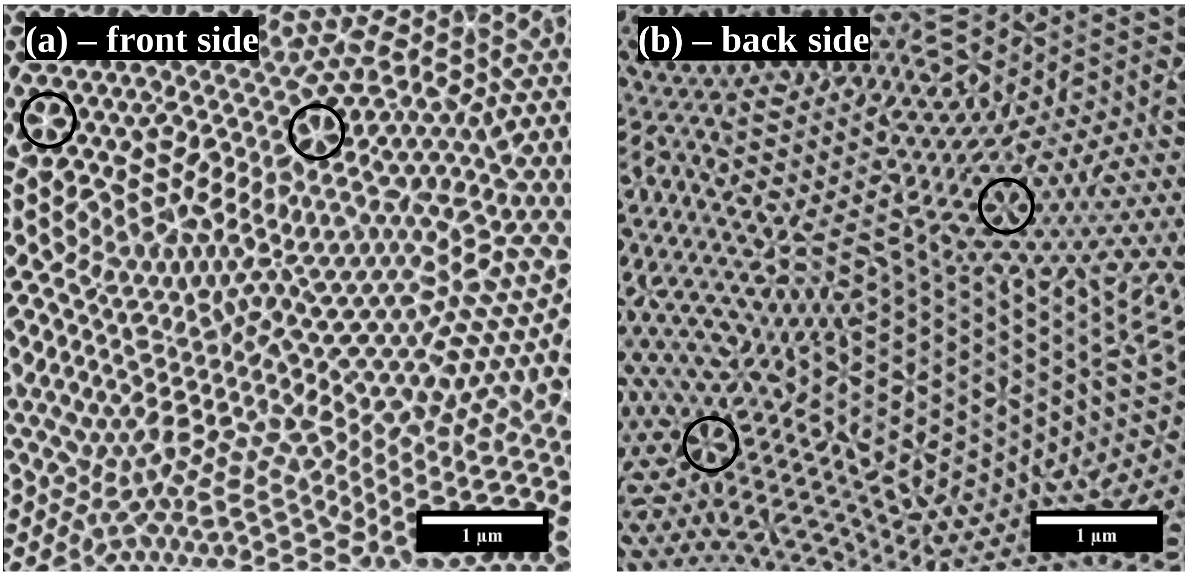

Figure 4.39: SEM images of an AAO filtration membrane with highlighted distinctive features for (a) front and (b) back side.

Butane dione, being expensive and foul-smelling, showed the disadvantage that its mixture with perchloric acid turned more viscous and brown with time. Sometimes solid decomposition products contaminated the produced membrane. However, the PO process can be imagined as an intense electropolishing of the barrier layer across the pores that are opened to the front side. As in electropolishing electrolytes, the active ingredient should be perchloric acid. Therefore, Yuan *et al.* tested different $HClO_4$ containing mixtures to find many of them suitable. Using a 3 s pulse of 5 – 10 V higher voltage, e.g. EtOH instead of the butane dione worked in the same manner.[132] In ignorance of the improvements by Yuan *et al.*, recently, several researchers re-invented the findings.[133–135]

In experiments, also the replacement of ethanol by acetone did well as a component of the electrolyte. However, the ethanolic mixture became standard for all pore opening processes because almost no degradation was observed. Therefore, the electrolyte could be prepared in advance and several times reused. Finally, continuously porous membranes could be obtained for any oxide layer thickness, with pore sizes with respect to the anodization voltage. The limits of the PO process in terms of oxide membrane's thinness was not explicitly tested. Definitely, a 7 µm oxide layer (30 V, 1 h) was successfully opened and the aluminum dissolved. However, the resulting membrane was so weak, that the surface tension of water was strong enough to break the oxide layer.

The current flow during the short 3 s pulse gave additional valuable information about the intactness of the oxidized foil. Usually, the current started with a set maximum value of 1 A and dropped rapidly to values of about 100 mA. The exact values were depending on the used voltage and disc area. Tiny, invisible holes or cracks present in the oxide layer prevented the current flow to drop below 200 – 300 mA. Holes appeared rarely due to fully anodization of the metal base in single spots whereas cracks could be induced by mechanical force.

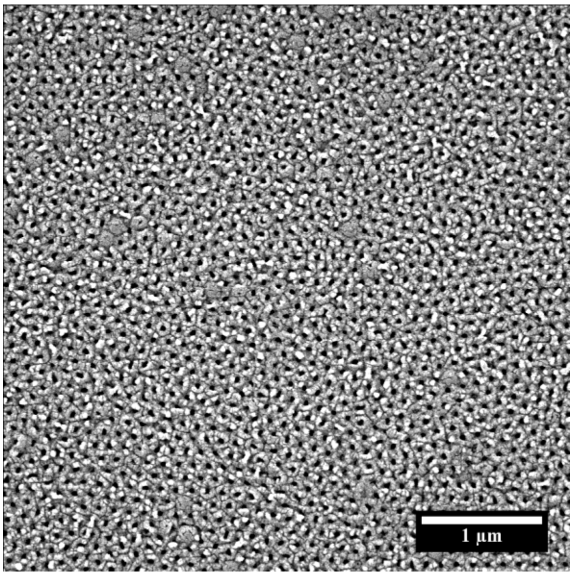

Figure 4.40: SEM image of an AAO (produced at 50 V for 2 h) back side, incompletely opened with a short 55 V-3 s-voltage pulse.

The electric pulse had to be extended from 3 to 5 s for AAO that had been anodized at 50 V or more, similar if the A2 reaction temperature was raised (see Chapter 4.6). In both cases, an increased barrier layer thickness would else prevent a complete back side pore opening. Figure 4.40 shows the backside of an AAO membrane produced at 50 V, exhibiting partially capped pores after a short pulse of only 3 s.

It was analyzed if a prolonged pore opening procedure could generally further increase the pore size generated at the back side. Apart from the improvements described, there was no positive impact observed if the electrochemical etching was extended to 10 or even 30 s. In contrast, the prolonged reaction period enhanced the etching of both membrane surfaces, leading to altered, blurred pore walls.

In literature (see above), instead of an extra voltage of + 5 V sometimes + 10 V were preferred. The hope was that maybe the narrow back side pore apertures could be further enlarged by using a stronger pulse. Experiments with AAO produced at 50 V however resulted in a non-complete pore opening, neither if the pulse was 3 nor 5 s long (see Figure 4.41).

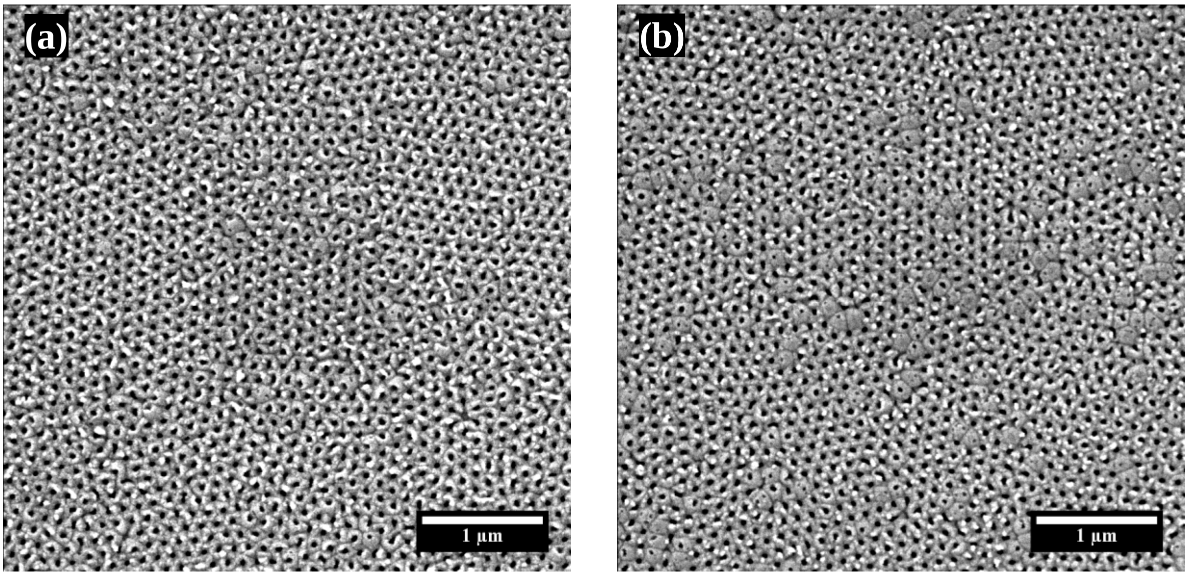

Figure 4.41: SEM images of AAO (50 V, 2 h) after applying a + 10 V-pulse for (a) 3 s and (b) 5 s instead of the usual + 5 V-pulse to open electrochemically the back side pores.

A further previously mentioned advantage could have been to reuse the remaining aluminum for another anodization. Here, the final separation from the oxide would have to be done mechanically and not by dissolution of the metal. However, when a further, third anodization with conditions of the second was tried, the result was disorder (see Figure 4.42). There was obviously no reusable nanoindentation left on the metal and the surface appeared similar to a pre-anodization A1 oxide. From the backside view obviously a good order could have been build up in a further (fourth) anodization, but this seemed not to be advantageous any more. Consequently, separation was consistently done by dissolution of the metal part.

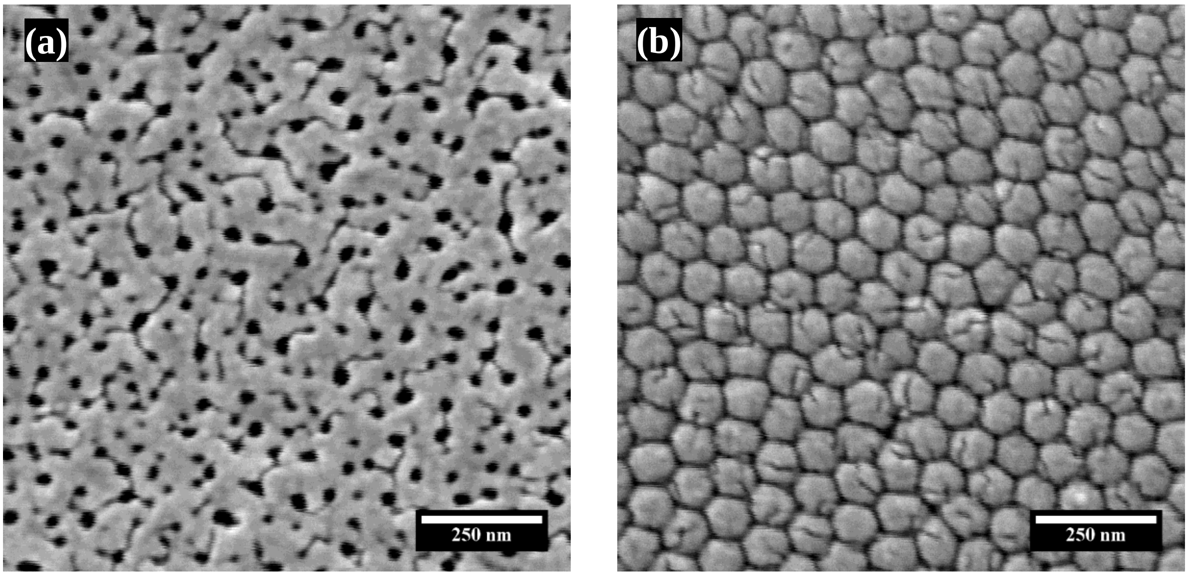

Figure 4.42: SEM images of AAO (35 V, 2 h, A3), produced on reused Al after the voltage pulse detachment (PO) of the A2 oxide and mechanical separation of oxide and metal; (a) front side and (b) back side.

4.5.4 Pore Widening and Porosity Improvement

As already described in Chapter 4.4.1, the dissolution process of the aluminum resulted in pore enlargement. The question was to what extent this chemical etching could be used to increase the porosity of a filtration membrane and, therefore, its potential flow rate. The pore widening after the anodization is interesting because pore sizes can be affected without changing the inter-pore distance. The latter would occur if the voltage would be adapted.

The prolonged exposition to the HCl/Cu^{2+}-solution resulted in an overall enlargement of the pore channels and therefore an increase of the porosity too. Figure 4.43 shows images of an AAO produced at 40 V and left in the etching solution for more than 1 h. The pore size measured on the front side increased from 40 – 45 nm to about 65 nm, the channel size was increased from 30 – 35 nm to about 55 nm.

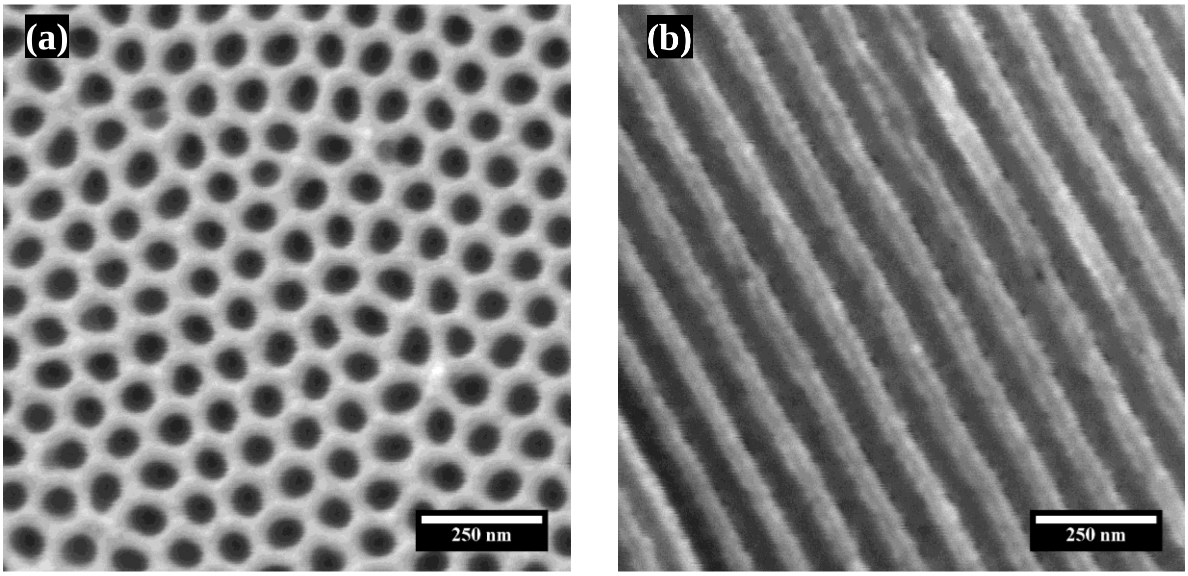

Figure 4.43: SEM images of AAO (40 V, 3 h) left in HCl/Cu^{2+}-solution (DisA) for more than 1 h after the pore opening procedure; (a) front side and (b) cross-sectional channel view.

The porosity of AAO can be calculated if the assumption of a perfectly hexagonal pore order is made. Coming from the equilateral triangle with edge length of the inter pore distance d_I and comprising 3 × 1/6 pores of diameter d (see Figure 4.44 and Figure 2.3), the following formula (eq. 4.1) may be used to calculate the porosity P:

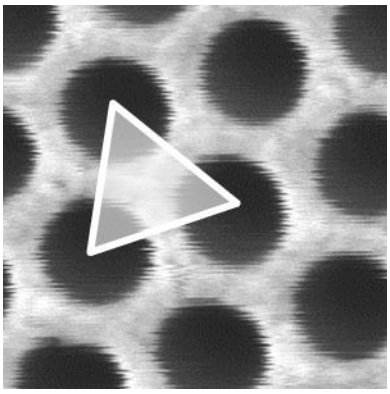

$$P = \frac{\text{area of pore x-section}}{\text{total area}} = \frac{\frac{3}{6}\pi\left(\frac{d}{2}\right)^2}{\frac{\sqrt{3}}{4}\,d_I{}^2} = \frac{2\,\pi\left(\frac{d}{2}\right)^2}{\sqrt{3}\;d_I{}^2} \tag{4.1}$$

Figure 4.44: Equilateral triangle and formula to calculate the porosity of AAO.

For anodizations at 40 V, the inter-pore distance was determined to be 105 nm. If a pore diameter of 45 nm on the front side before and a diameter of 65 nm after pore widening (PoWi) is considered, the surface porosity increased from 16.7 % to 34.8 % for the example of Figure 4.43. However, a porosity value for AAO of 10 % is generally accepted, independent of the used anodization potential.[120] This value is calculated exactly if the channel diameter of 35 nm is considered instead of the front side diameter (see Figure 4.43 (b)). It has to be differentiated between the obvious surface porosity, which is affected more strongly by etching processes, and the actual porosity of the membrane as a whole. In the chosen example, the latter was enhanced from 10.0 % to 24.9 %.

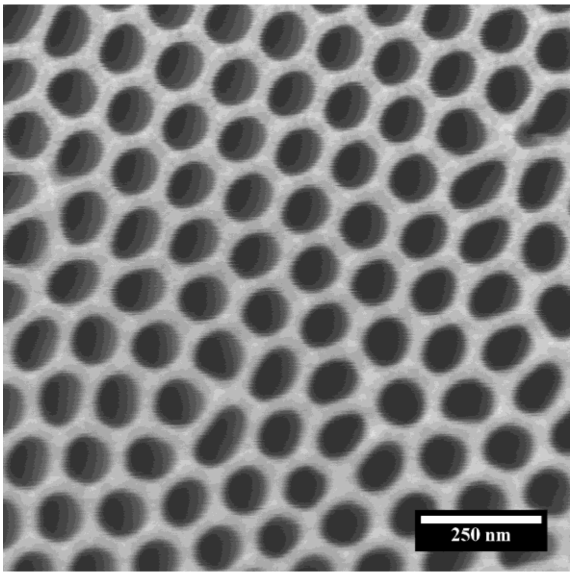

Figure 4.45: SEM image of AAO (50 V, 2 h) front side after a pore widening procedure for 3 h with HCl/Cu^{2+}-solution.

HCl/Cu^{2+}-solution was tested systematically for the pore widening (PoWi), subsequent to the DisA step. As a maximum value, a surface porosity of almost 45 % was achieved with membranes produced at 50 V and subsequent PoWi of 3 h (see Figure 4.45).

However, the stability of the membranes decreased with increasing porosity as a result of material loss. Extended treatment could even lead to dissolution of the whole membrane. Therefore, typically etching periods of 1 or 2 h were not exceeded.

As it was mentioned before, the frontal surface pore diameter is a value that does not describe an AAO membrane best. The channel size inside are usually smaller and finally the point of narrowest pore diameter within a filtration membrane decides about the flow.

Figure 4.46 shows SEM images of a 50 V-AAO before and after a pore widening step. Before the treatment, the pore sizes at the surfaces were about 50 and 45 nm, respectively. After 2 h in the HCl/Cu^{2+}-solution, it changed to 85 – 90 nm for the front side and 70 – 75 nm for the back side. The increased difference in diameter between the two surfaces indicates that the smaller apertures on the backside were not as much attacked compared to the major ones at the front side. An explanation could be the limitation of diffusive transport processes in the narrower environment. Most important is the fact that the channel size changed as well from about 45 – 50 nm (see Figure 4.46 (e)) to a value of about 80 nm (see Figure 4.46 (f)). The pore size measured from the top, and all calculations of porosities thereof, plays a minor role for applications as filtration membrane because the measured channel size was always smaller. Usually, it had to be considered that asymmetries in the channel shape (wide front side, narrow back side) were intensified with the pore widening process and that more sophisticated methods would have been necessary to end up with almost cylinder shaped pore channels. A detailed discussion of the shape of the overall pores will follow in Chapter 4.5.5.

In literature, usually H_3PO_4-solution is used for the widening[11] as result of the common wet chemical pore opening procedure (see Chapter 4.5.1). In experiments, H_3PO_4 was not found to work different from the acidic Cu^{2+}-solution. Quite contrary to the experiences made with HCl/Cu^{2+}, it was reported that the AAO layer thickness is reduced upon pore widening with H_3PO_4.[9]

Another imaginable possibility to increase the porosity is reducing the inter-pore distance without changing the pore sizes. The eventual disadvantage of the pore widening process to influence the two unequal channel apertures in a different way maybe could be avoided.

There are several approaches known from literature where a pattern was provided with mechanical methods (instead of a pre-anodization) to encourage pore formation at specific sites: imprinting by stamps,[17,18,136] using various lithographic processes,[137–140] and plasma etching.[141]

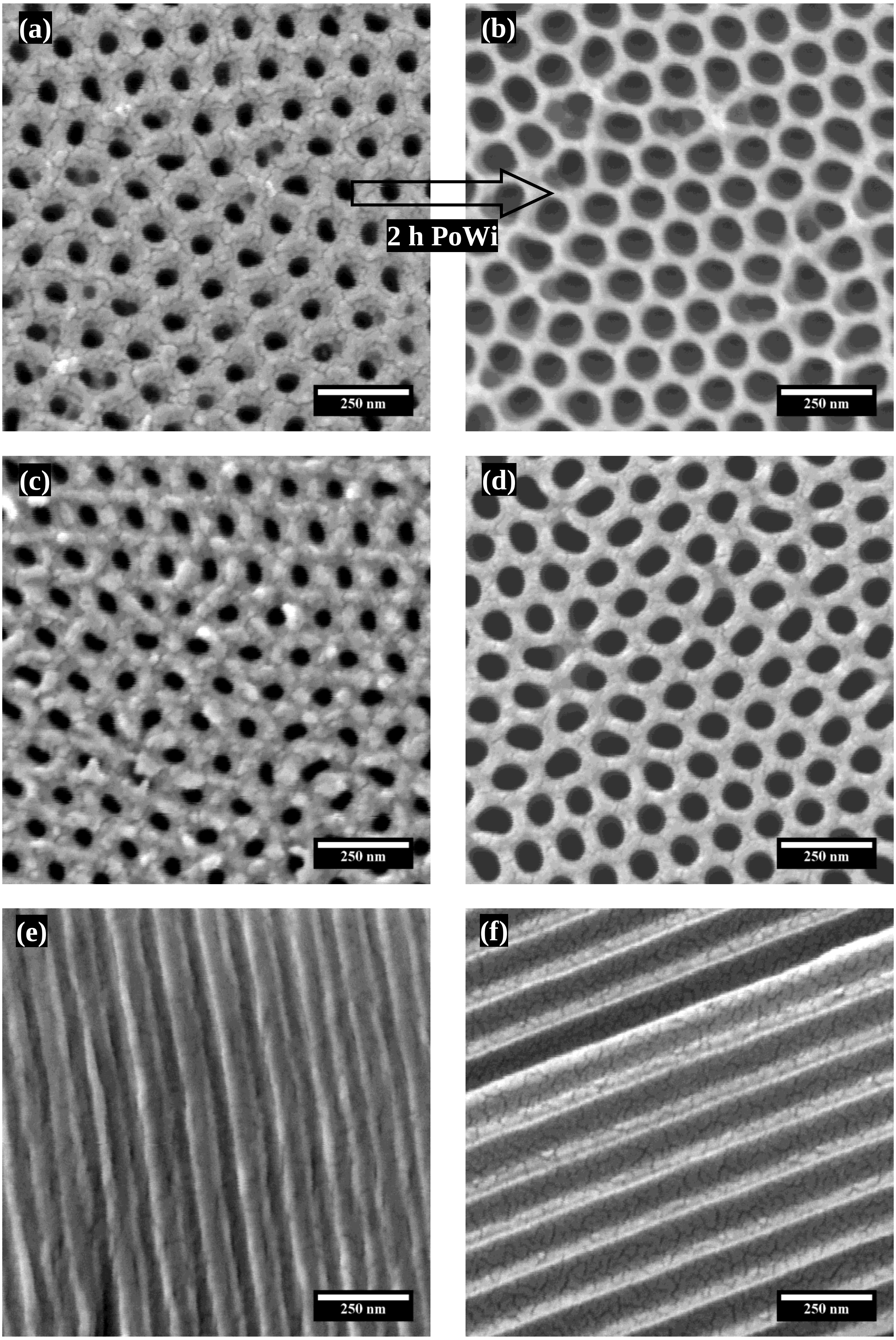

Figure 4.46: SEM images of AAO membrane (50 V, 2 h) without (a, c, e) and after pore widening step for 2 h (b, d, f) of the front side (a, b), the back side (c, d) and cross-sectional channel view (e, f).

Of course, the pore array could be no longer described as self-ordered, and usually the application of the described technical measures reduced the porosity process rather than it was enhanced. Most of the described methods are also costly and time consuming. Moreover, usually only small AAO areas are accessible. Another limitation is the thickness of the achieved oxide layers. The longer the anodization lasts, the higher is the probability that the self-ordering forces start to reorder the structure.

In contrast, it was thought to modify (reduce) the inter-pore distance just a little by a combination of different anodization voltages in the first A1 and second A2 anodization to increase slightly the porosity. If the difference would be small enough, maybe the hexagonal order and monodispersity of the pores could be preserved.

Experiments were performed with A1 anodization of 35 V to produce a relative small inter-pore distance, followed by A2 of 40 V to induce the bigger channel size. Unfortunately, the changed pre-structuring had no effect on the result, an inter-pore distance of 95 – 100 nm was observed (instead of the desired 85 nm). Because even hexagonal order of the pores was achieved, probably the nanoindentation was too weak to induce a decrease of the inter-pore distance. Only the other way around, a pre-anodization at 50 V followed by a second at 40 V, resulted in a curious image of the two membrane surfaces (see Figure 4.47).

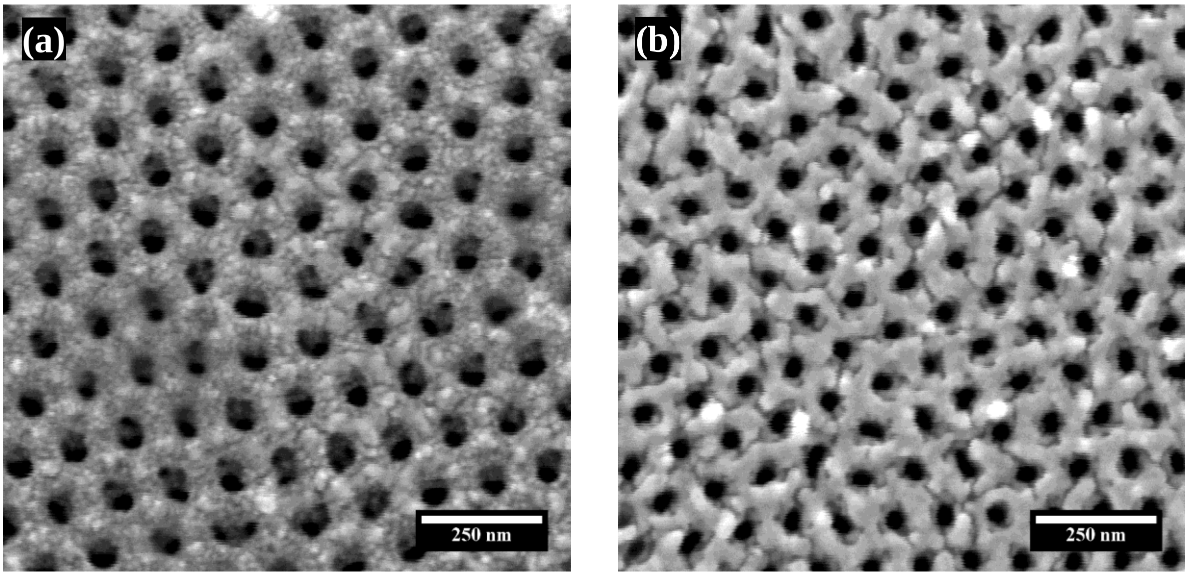

Figure 4.47: SEM images of AAO pre-anodized at 50 V (A1) and afterwards anodized at 40 V (A2) showing (a) characteristics of a 50 V-anodization at the front side and (b) of 40 V-anodization on the back side.

The front side had the inter-pore distance of a 50 V anodization (130 nm) and was of a good order, even though multiple pores seemed to grow in only one dimple. The back side however showed the characteristics of a 40 V anodization (inter-pore distance 105 nm), but the order was just moderate. The results showed that there was probably no way to use a modified pre-anodization.

4.5.5 Impacts on the Channel Shape

In previous chapters, it was often discussed that the pore diameter measured on the surface, typically on the front side, is not crucial for applications e.g. as filter. Herein the shape of the pore channels is discussed in detail.

When doing a couple of reactions with identical anodization conditions, it attracted attention that especially the appearing diameter of the pores on the front side could vary strongly. Before pore opening PO and dissolution of the aluminum DisA, both by aid of strong acids, the pores appeared relatively small (see Figure 4.48 (a)). As soon as a self-supporting, flow-through membrane was produced, the channels were enlarged a little small (see Figure 4.48 (b)). Especially the frontal pore openings showed a distinctive broadening, usually much more compared to the channel diameter some 100 nm underneath which can be determined to be allover about 40 nm (see Figure 4.48 (c – e)). An explanation was easy to find while the front side had the longest contact to the acids without diffusion restriction as within the channels. Maybe the large pre-pattern, result of the first anodization A1 (see Chapter 4.3), had a little influence on the oversized front pores, too.

Even the amplitude of measured front side diameters can be explained with different treatment time and temperature: Between filling the setup with half-concentrated $HClO_4$ and turning-on of the current for the electrochemical pore opening procedure, sometimes little more or less time lapsed. Moreover, mainly the treatment to dissolve the aluminum could influence the result. Little variations in solution volume would lead to a different overall heat capacity and therefore reaction temperature on the one hand, the time until the aluminum was dissolved was of course never exactly identical on the other hand. Finally, the process ended up in formation of a more or less distinct funnel-shape aperture (see Figure 4.27 too).

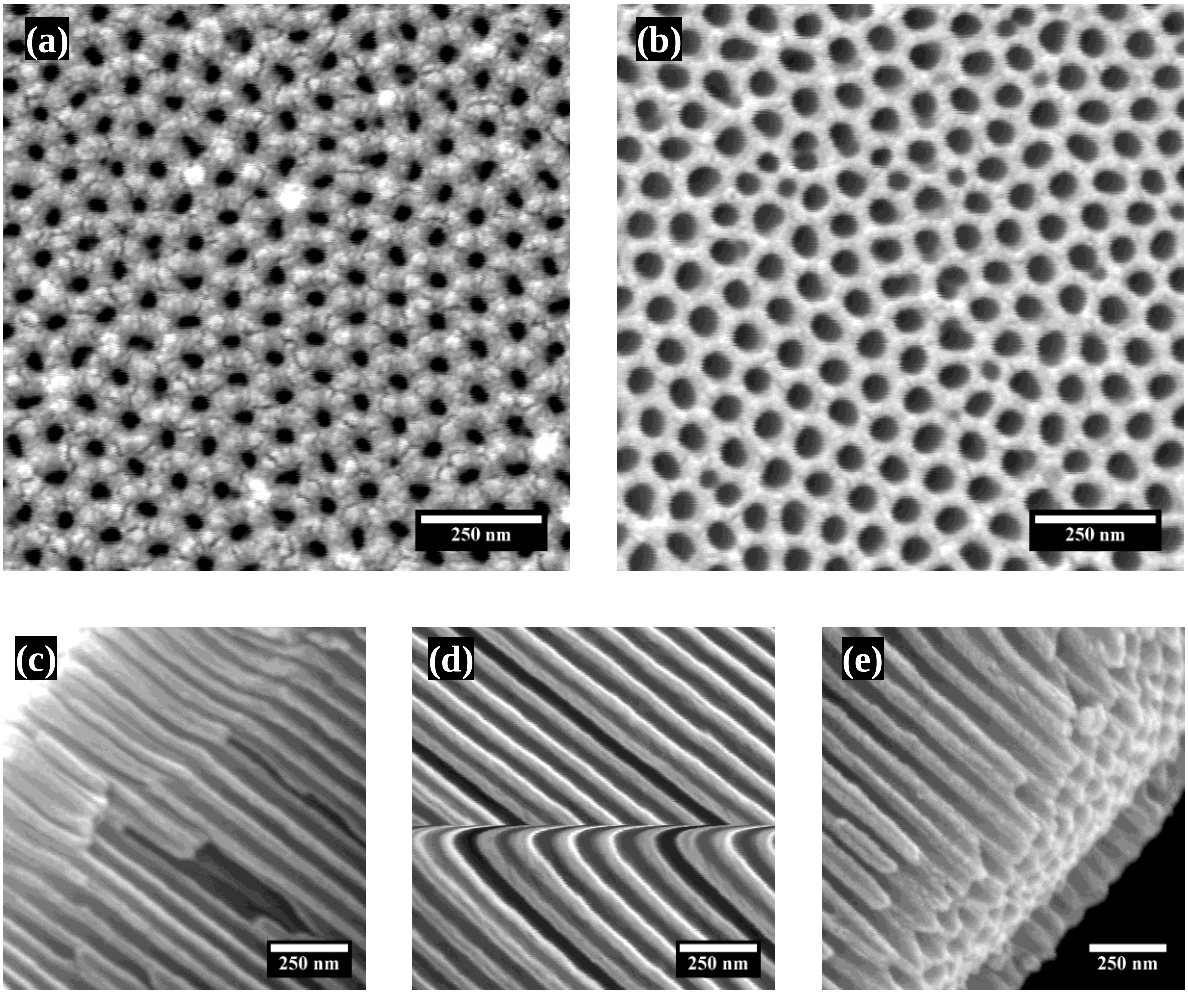

Figure 4.48: SEM images of an AAO (35 V, 2 h) membrane: (a) front side after A2 (on the metal), (b) front side after DisA, and (c – e) cross-sectional studies along the channels after DisA ((d) shows scanning artifact).

Another aspect, which seemed to be worth to be explored, was the dissolution process of the preliminary oxide (DisO) with phosphochromic acid. In Chapter 4.3, simply general etching conditions were chosen being harsh enough to dissolve oxide layers of any thickness within the reaction time of 3 h at elevated temperature or 12 – 24 h at RT. There was never a difference observed in the samples either if they were treated the one or the other way. The phosphochromic acid removed the A1 oxide reliably, but how was the pattern of oxide affected as soon as the anodic oxide was dissolved? Experiences made with other etching solutions used to dissolve either the aluminum or the oxide (NaOH, H_3PO_4, HCl/Cu^{2+}) hypothesized, that the selectivity of the phosphochromic acid could be maybe low. Over-etching could lead to a flattening of the pattern and larger funnel-shaped pore openings in the A2 oxide, or a reduced order could be the result. To control this aspect, a set of experiments was designed where typical A1 oxide layer were produced and subsequently subjected to the phosphocromic acid. The progress of dissolution was controlled in warm acid after 0.5, 1, and 2 h, in room temperature solution after 2, 4, and 6 h.

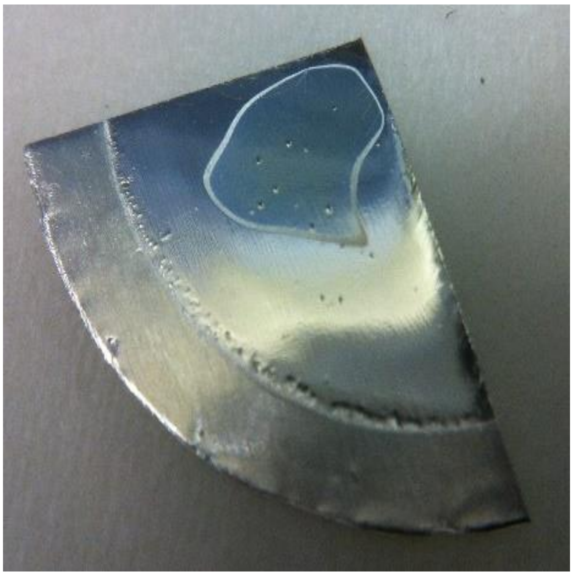

Figure 4.49: Photograph of a piece of Al foil bearing a residue of A1 oxide (white spot) after 0.5 h treatment with phosphochromic acid.

Typically, the evident appearance of polished foils, shortly pre-anodized foils and pre-structured foils (after DisO) was very similar, blank and shiny. A1 foils treated at room temperature with the phosphochromic acid for some hours however became milky. In warm solution, initially (after 0.5 h) sometimes white spots were visible (see Figure 4.49), but longer exposure to the solution showed completely blank foils. The dull and milky appearance indicated an inhomogeneous surface, scattering the in-coming light. This observation had already been made before as soon as nano grass had been formed.

Analysis of SEM images of the foils treated at room temperature confirmed the assumptions made. The previously described porous surface structure after the pre-anodization (see Figure 4.50 (a)) was firstly etched from the top, exposing more regular pores after 2 h etching. Clearly dead-end pores were recognized, no hexagonal order at all had been formed yet, but the pore diameter was already the expected 45 to 50 nm at a voltage of 50 V (see Figure 4.50 (b)). After 4 h, the homogeneous oxide layer started to get fractured and pore walls vanished leaving behind first growing holes (see Figure 4.50 (c)). After further 2 h, no more porous oxide was visible. The surface was completely covered with nano grass or needle-like structures spread like pick-up sticks on top of the emerging hexagonal imprint pattern (see Figure 4.50 (d)).

Consequently, foils treated at room temperature had to stay there more than 6 hours to lose a “typical” oxide layer after the pre-anodization, the procedure “overnight” was applied.

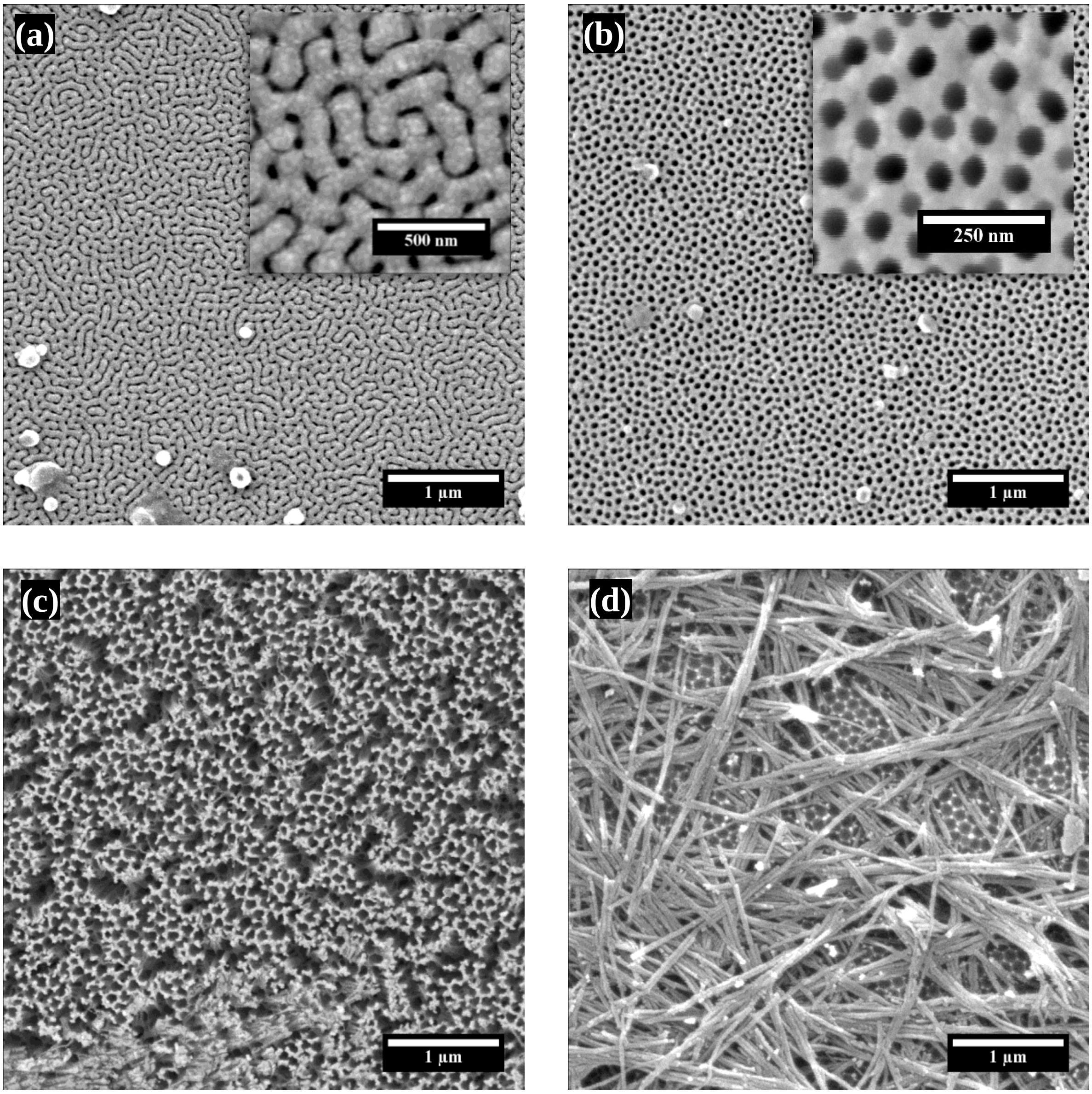

Figure 4.50: SEM images of A1 oxide (50 V, 1 h) without treatment (a) and after etching in phosphochromic for 2 h, 4 h, and 6 h at RT (b – d). The insets show images with higher magnification.

The observation made with the foils having been suspended in the phosphochromic acid at elevated temperatures indicated a completely different reaction speed. Independent of the A1 oxide layer thickness produced between about 10 to about 40 µm, after 1 h treatment the bare hexagonal pattern became visible free from nano grass. When having only a very thin oxide layer, even 0.5 h was enough to dissolve the oxide, even though the solution had to warm up within the first minutes to finally reach about 65 °C. The white spots observed (see Figure 4.49) were, as expected, just a "melting" residue of porous oxide.

Keeping the pre-patterned surfaces longer than necessary in the etching solution was surprisingly absolutely equal. Figure 4.51 shows the pre-structured foil after exposition for

0.5, 1, and 2 h. The quality of the pattern did not change, not even the number of oxide residues (white) was reduced with longer etching time.

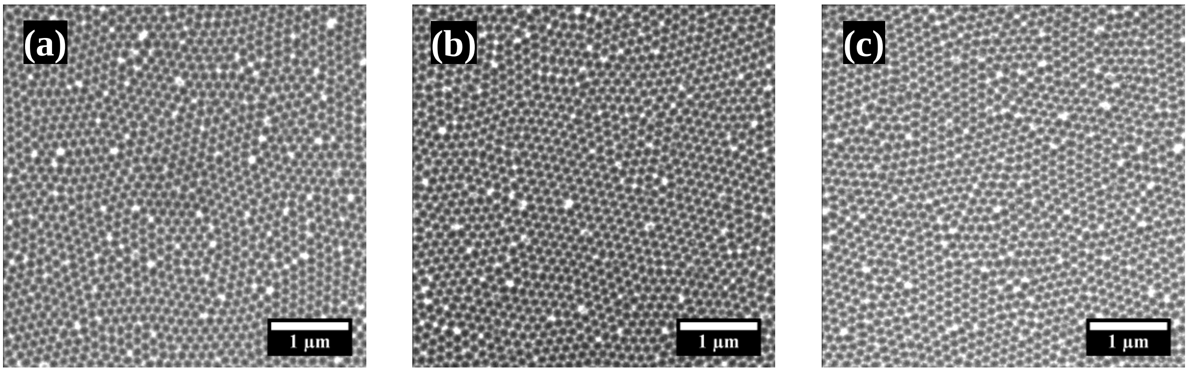

Figure 4.51: SEM images of a pre-pattern (50 V) left after etching the AAO with phosphochromic acid for (a) 0.5 h, (b) 1 h, and (c) 2 h at a temperature of about 65 °C.

The conclusion of the test series was rather that the process of dissolving the first oxide layer could be accelerated by reducing the impact time in hot solution from 3 to about 1 hour without compromise in quality. This means a serious potential saving of the overall production time for a membrane (see Chapter 4.8.6).

Figure 4.52 shows a scheme of the typical pore's shape across the oxide layer thickness. The narrowest part of the membrane was always the aperture on the back side of the membrane d_1. The pore opening process probably did not dissolve the whole bottom of the pores completely, leaving a bottleneck. The pore channel above was usually bigger in size and, independently if only some micrometers or tenth of micrometers long, remarkably constant in diameter. The variation of channel diameters close to the front d_2 and close to the back d_3 usually did not exceed more than five nanometers absolute along the height h. These observations are not completely in line with published results and explanations. It is reported that the difference in the diameter at the front side d_1 compared to that near the barrier layer d_3 increases with prolonged reaction period.[111] However, this effect played only an underpart within the relatively short reaction periods of below 3 h used.

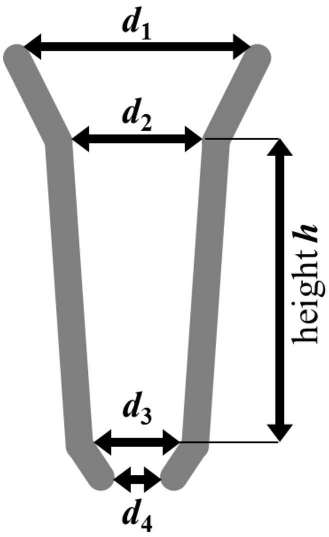

Figure 4.52: Scheme of an AAO pore exhibiting four distinctive diameters $d1$-$d2$ across the oxide layer thickness in deviation of a perfect cylindrical shape.

It was thought that the undirected pore widening process would just dissolve very slowly the walls of the pores homogeneously, that potentially even the narrow back side aperture good to access would be adapted to the mean diameter of the channels. However, it turned out that the front side of the membrane was attacked more intensely compared to the back side. Maybe thinning of the pore walls on the front side was preferred due to higher corrosion surface or even due to higher resistivity of the barrier layer residues.

Figure 4.53 represents the results of a study made with AAO (40 V, 3 h) and subsequent pore widening for either 30 or 60 min. Starting from a relatively large frontal 55 nm pore diameter, the pores became 65 – 70 nm after 30 min and 70 – 75 nm after 60 min. Due to the high pore size right from the beginning, already after 60 min treatment first pore walls got perforation connecting pores. At the back side, the pore growth was much less pronounced, 50 nm became only 60 nm after 60 min, increasing the disparity between the two surfaces. In analogy to the back side also the channel size increased to about 60 nm.

It was found that membranes having overall large pore diameters, e.g. due to a higher anodization voltage, showed a very pronounced difference in front and back side pore diameter after pore widening. Consequently, pore widening was just applied to enhance the possible flow through the membrane. Limitation was the decreasing stability of the membranes with thinning of the pore walls, and finally at the worst nano grass formation on the front side.

Two more methods to enlarge the channel diameter will be discussed in the next chapters. On the one hand, it was tested if the pore widening could assist in making anodizations with more than 50 V useful. On the other hand, the anodization temperature was raised to accelerate the reaction.

To guide the etching force in particular to the back side of the AAO membranes, an idea was reapplied that was tried when searching for a way to implement a chemical pore opening procedure (see Chapter 4.5.2). A thickener was used in combination with the etching agent to float the membranes back facing on the solution and, therefore, prevent an attack of the front side. In a series of experiments with AAO produced at 50 V for 2 h, two different concentrations of PEG 20000 as additive were tested with different impact times. Floating of AAO membranes on the gel formed by the PEG indeed reduced the attack onto the front surface, but the etching of the back side was slower likewise. Figure 4.54 shows the result of a back side pore widening on a gel, formed by 1.5 g PEG on 5 mL HCl/Cu^{2+}-solution, for 2 h.

Even though the front side was not wetted, the pore size was enlarged from about 45 nm to 55 nm there too, while at the back side the diameter changed from about 40 nm to 45-50 nm.

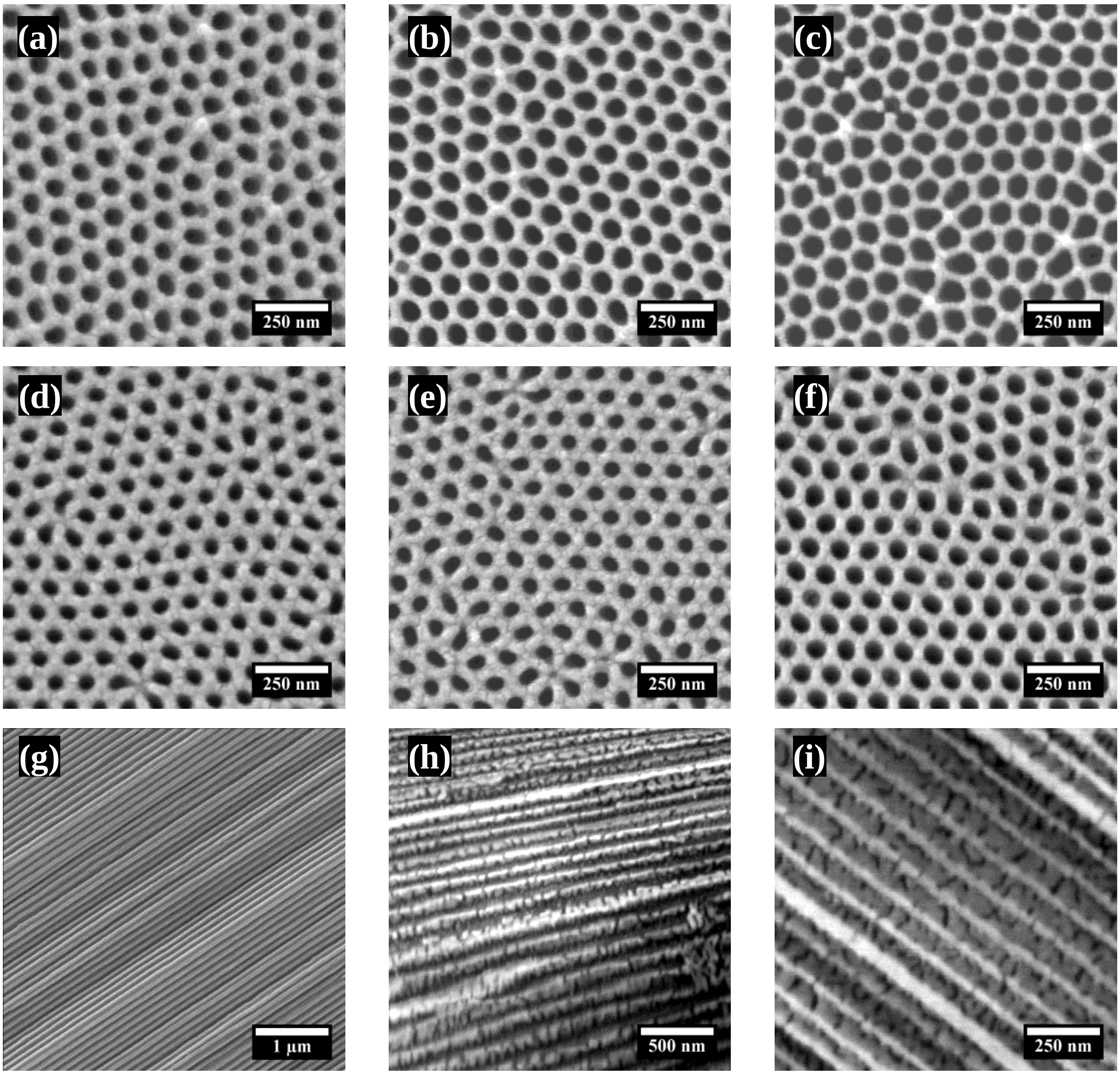

Figure 4.53: SEM images of AAO membranes (40 V, 3 h) showing (a – c) the front side, (d – f) the back side, and (g – i) a cross-sectional channel view, (a, d, g) without pore widening step (PoWi), (b, e, h) after 30 min PoWi, and (c, f, i) after 60 min PoWi.

An extended floating time of 4 h led to a higher impact on the front side compared to the back side. The increase of the PEG concentration also did not change the described tendency. Obviously, the chemical resistivity of the back side, the pore bottom side, is exceptionally high as a result of the barrier layer forming. To overcompensate the thinning effect of the added PEG, gels with HCl/Cu^{2+}-solution of doubled concentration were prepared and tested in equal measure. The higher concentration however did not result in an accelerated attack of the back side in comparison to the front side, which is affected by the etching agent only via capillary forces in the channels. Within 2 h floating, the pore size was increased on both sides strongly (80 respectively 65 nm), but disadvantageous was that the pore shapes already showed signs of fringes by the heavy acid attack (see Figure 4.55).

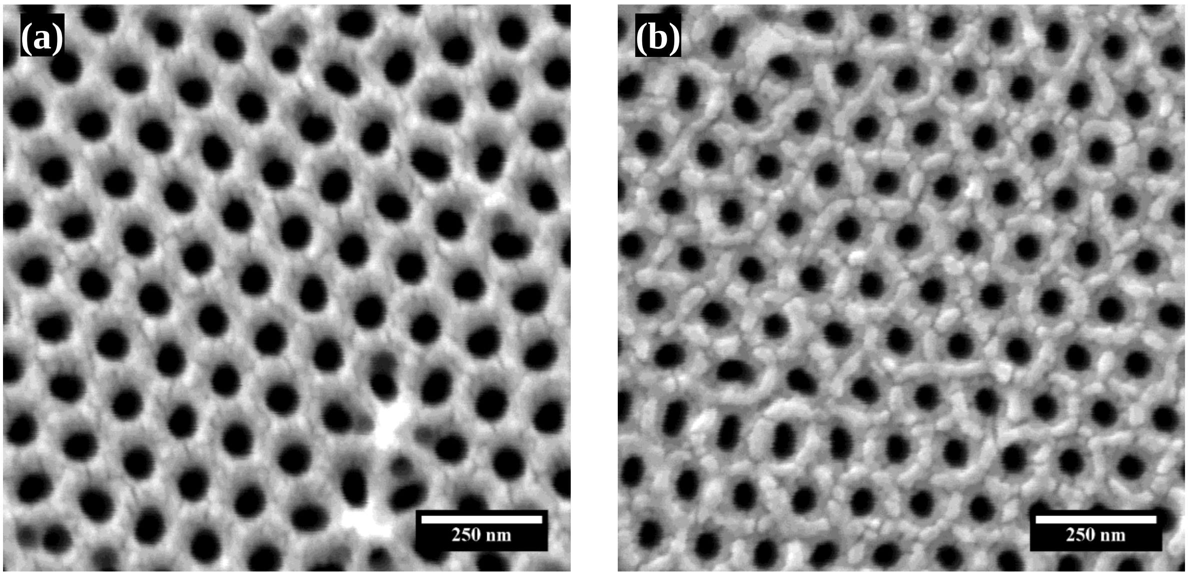

Figure 4.54: SEM images of AAO (50 V, 2 h) after floating on HCl/Cu^{2+}-gel for 2 h, (a) front side and (b) back side.

Thus, the additional experiments gave further hints that the creation of perfect cylindrical channels with constant diameter was not practical using wet etching methods. To understand the resistivity of the AAO back side, further investigations on chemical and physical state of this layer have to be made.

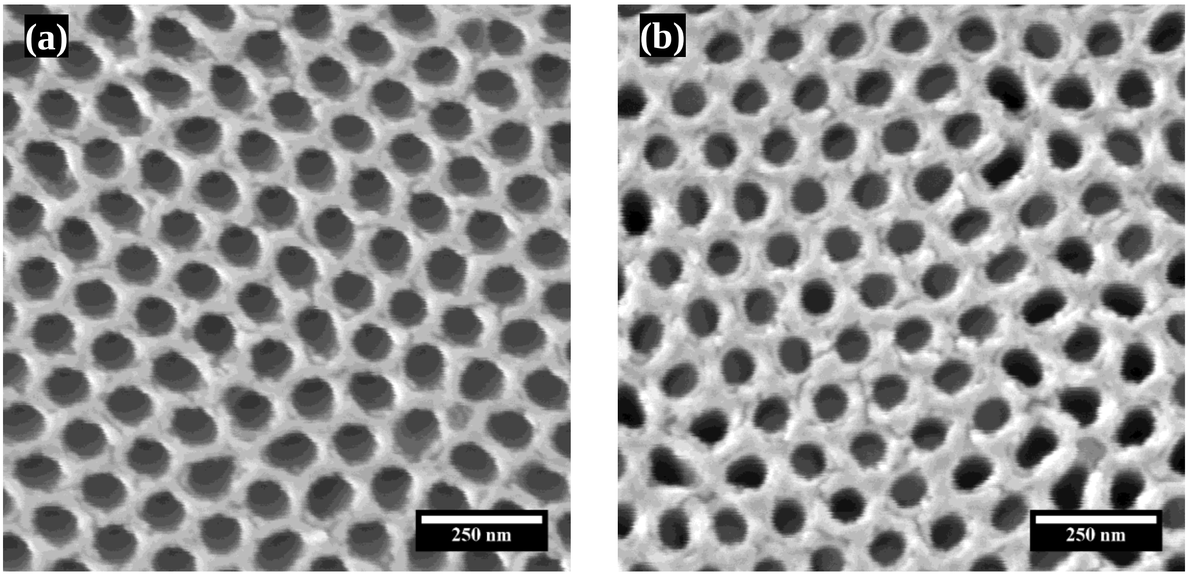

Figure 4.55: SEM images of AAO (50 V, 2 h) after floating on a concentrated HCl/Cu^{2+}-gel for 2 h, (a) front side and (b) back side.

4.5.6 Improvements toward Pore Shapes of Membranes Produced at Higher Voltage

In Chapter 4.4.1, it was declared that in the chosen system (electrolyte concentration, reaction temperature…) anodizations with more than 50 V were meaningless because of inhomogeneity of the porous surfaces. Instead of yielding growing pore sizes and inter-pore distances, more than one pore started growing in one dedicated place, resulting in disturbances of the order and relatively small pore openings. Anyhow, anodization at high voltages has the advantage of short reaction times (fast oxide growth) and for first tests of membrane performance with filtrations, a preferably big pore diameter was desirable.

Even if anodizations were performed in the potential region of 35 to 50 V of high self-ordering, sometimes "twin pores" were also found as little defects on otherwise well-ordered surfaces (see Figure 4.56 (a)). Application of the pore widening procedure, resulting in a certain over-all etching of the oxide surface, made visible, that one of the multiple pores prevailed mostly right still close to the surface (see Figure 4.56 (b)).

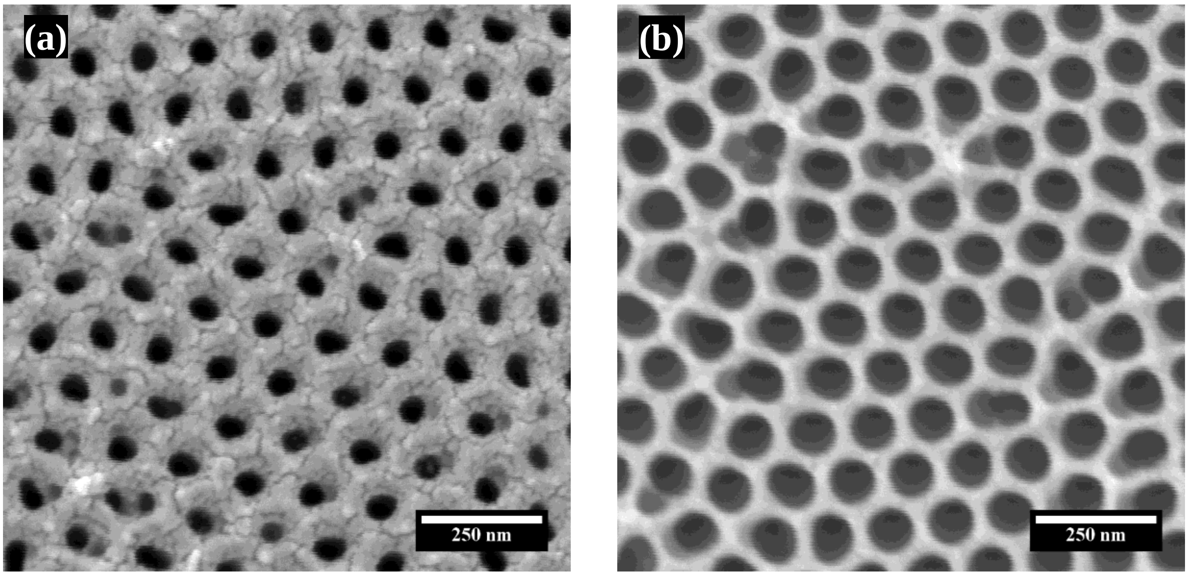

Figure 4.56: SEM images of AAO (50 V, 2 h) front side, showing several „twin pore" defects; (a) without and (b) with 2 h pore widening.

Membranes produced at 60 V showed usually already a certain disorder on its front side. The back side was much more homogeneous considering the pore size distribution, however the appearance on the back side was rather tube- than pore-like. The growing thickness of the barrier layer with voltage resulted in increasing difficulties to open the pores accurately with the described electrochemical process (PO). The impact time was elongated from 3 to 5 s improving the success (see Chapter 4.5.3). Figure 4.57 documents how the pore widening impacts on a 60 V-AAO.

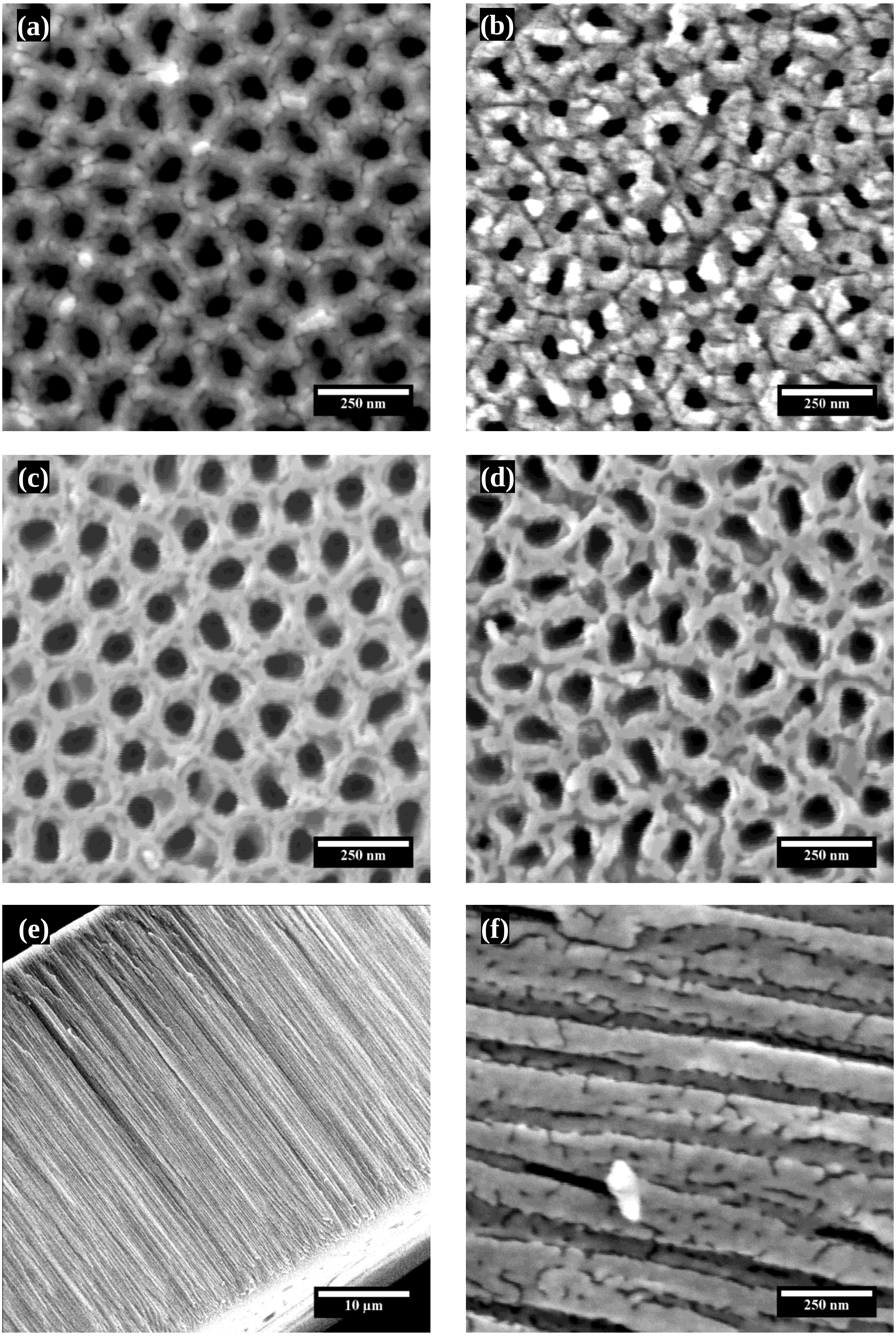

Figure 4.57: SEM images of an AAO (60 V, 2 h) membrane (a, b) before and (c – f) after a pore widening procedure for 2 h; (a, c) show the front side, (b, d) the back side, and (e, f) show cross-sectional studies.

Figure 4.57 (a) shows a typical front side view of low ordered pores and frequent deformations or twin-pore generation. Figure 4.57 (b) shows the back side after 5 s pore opening procedure, all pores are open but residues of the barrier layer capping are still obvious, leading to the tube-like appearance. After 2 h of pore widening, both surfaces were affected and the pore sizes were enlarged (see Figure 4.57 (c, d)). However, the pore size distribution was still high so that a specific value for the diameter was difficult to determine (front side from 55 – 60 nm to 80 nm, back side from about 40 to 65 nm). The irregularity in pore order had also an effect on the homogeneity of the whole channels. Even though the anodization resulted in an oxide disc of about 47 µm thickness (see Figure 4.57 (e)) with normal appearance, analysis of the channel structure gave evidence of non-parallel and uncontinuous pores of various size (see Figure 4.57 (f)).

Application of the pore widening procedure led to occasional impressive results regarding the front side. Figure 4.58 shows its effect on a 70 V surface with noticeable thick pore walls between the combs containing usually more than one pore aperture. The pore widening procedure (2 h) indeed resulted in almost uniform pore aperture sizes which grew from about 60 – 65 nm to more than 100 nm.

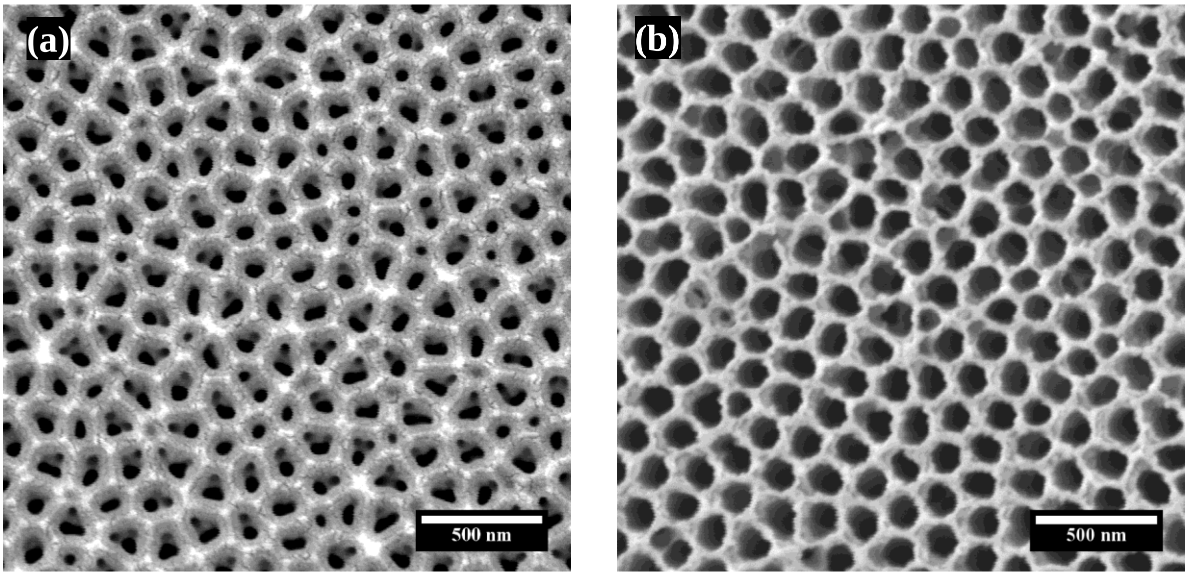

Figure 4.58: SEM images of AAO (70 V, 1.5 h) front side (a) before and (b) after 2 h PoWi.

However, further investigations on the value for applications as filters were suspended because of several reasons: At first, the pore opening process (PO) would have to be optimized to yield sufficient opened pores. Even after the pore widening step the back side apertures remained rather small compared to the front side pores. Figure 4.59 shows the extreme case for a 90 V anodization.

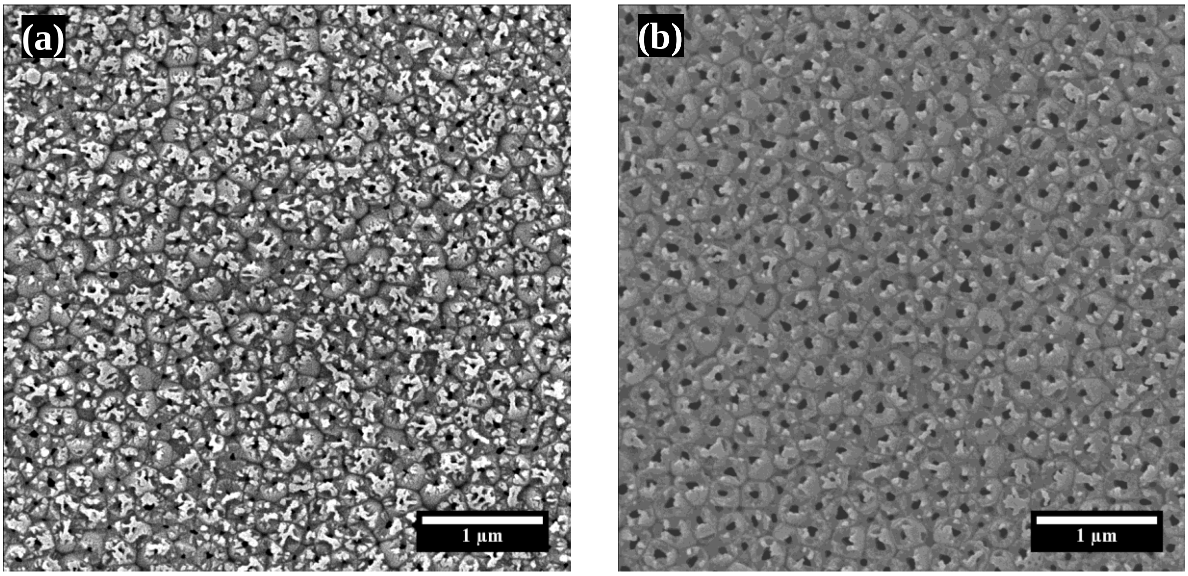

Figure 4.59: SEM images of an AAO (90 V, 0.5 h) membrane showing the back side (a) before and (b) after the pore widening procedure applied for 2 h.

Moreover, the use of potentials of 70 V or more led to starting currents for the anodization of minimum 100 mA (fast dropping), meaning a high energy input related with heat generation that probably cannot be dissipated sufficiently. The reaction control by means of reproducibility was therefore low and the speed of oxide growth allowed just very short reactions limited by the thin aluminum foil used.

Overall, it could be concluded that the advantage of high voltage anodizations for our purposes was low and that the problems predominated. To yield reliable and highly reproducible results, the anodization voltage was kept between 35 and 50 V for applications.

If pore sizes of about 100 nm or larger would have been necessary, switching to another electrolyte would have been the favored solution.[142]

A future work might be the analysis of the effects leading to the multiple pores and missing order. If a lower temperature would help or to ramp the voltage at the beginning of the anodization to give the system time to come into the thermodynamic equilibrium.

4.6 Variations in Reaction Temperature

As a last parameter, the impact of the reaction temperature was explored. In literature, usually low temperatures of 0 – 5 °C are preferred with anodizations in oxalic acid, leading to high pore order but a slow reaction rate. The oxide growth rates for anodizations performed at 20 °C are almost seven times higher than the growth rates at 1 °C.[105]

Two different goals were pursued with a change in reaction temperature. On the one hand, it should be analyzed if lowering the reaction temperature should provide a positive effect on the monodispersity and order of the pores. On the other hand, the influence of a temperature raise should be examined. Upon an increased oxide growth rate, it was assumed that the pore size would be affected due to an enhanced chemical dissolution rate of the formed Al_2O_3. The inter-pore distance, however, should stay rather constant.[105]

To analyze the possible positive effect of a lowered reaction temperature, two types of experiments were chosen: On the one hand, in a typical standard anodization the temperature was changed to 5 °C (implicating a very low reaction speed and therefore a thin oxide layer). On the other hand, the low reaction rate was planned to be overcompensated by choosing a higher potential for the anodization. In the previous chapter it was speculated that maybe a slower reaction could improve the disordered results received at higher voltages.

Figure 4.60 (a, b) shows the results for an anodization at 50 V (5 °C) and a current flow of about just 10 mA (instead of usual 25 mA). The result of 3 h reaction time was a thin 20 µm membrane showing a good pore order and a similar size of front and back side pores. With about 50 – 60 nm diameter they were at least of the same size compared to the room temperature anodizations (for usually shorter reaction time). However, the quality and order of the pores was not better and the oxide growth rate was lowered by a factor of about 3.

The second approach using a higher voltage of 80 V indeed resulted in a 30 µm membrane of dark yellow color with just 1 h reaction time. However, the SEM analysis showed the typical problems of structures produced at higher voltage: Misorder and superstructures with multipores on the front side and incomplete opened pores on the back side (see Figure 4.60 (c, d)). In conclusion, no significant advantages could be taken from choosing lower temperatures. Solely the indications pointing towards remarkably cylindrical shaped channels at low temperatures should be further investigated in the future.

Our attention was turned to the possibility of a positive influence on the oxide growth rate by testing higher temperatures. Sulka *et al* [103] observed just gradually changes in pore diameter and inter-pore distance varying the reaction temperature between 20 and 30 °C. But particularly the inner channel size and the pore size at the back side were not considered, values that are of high interest for our application in mind.

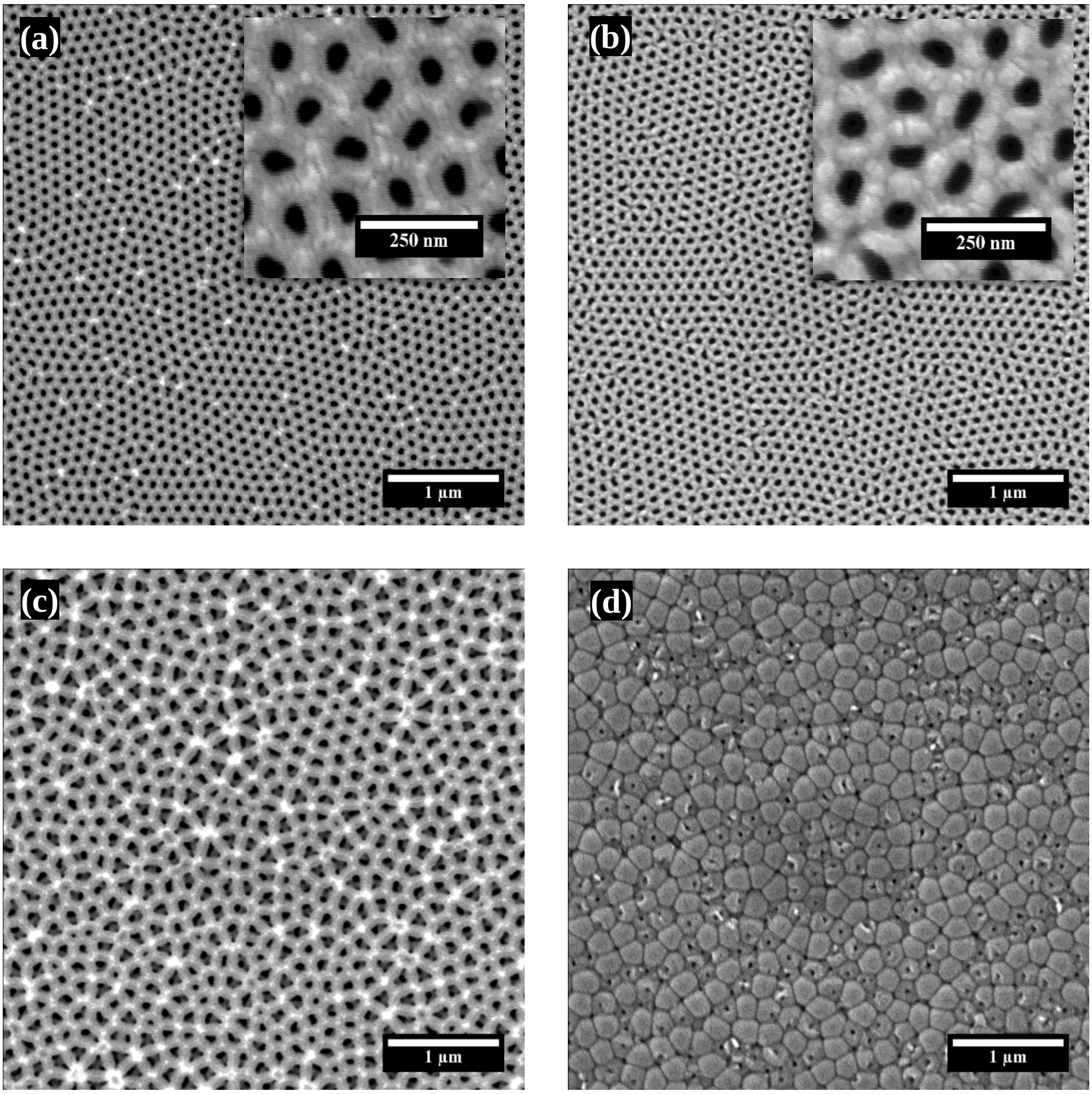

Figure 4.60: SEM images of AAO membranes (after PO) anodized at 5 °C: (a, b) front and back side of AAO anodized at 50 V for 3 h and (c, d) front and back side of AAO anodized at 80 V for 1 h. The insets show images with higher magnification.

It was decided to elevate the reaction temperature by 10 °C to 35 °C for a start and compare with anodizations at potentials of 35 V and 50 V. Figure 4.61 shows the results of a 2 h anodization respectively. Homogeneity of the surfaces were not reduced by the higher temperatures as it is obvious from the SEM images. But in comparison to anodizations performed at 25 °C the front side pores are enlarged, an effect that is reported to increase with prolonged anodization time.[103] This can be explained by the higher corrosiveness of the warmer acidic electrolyte leading to dissolution.

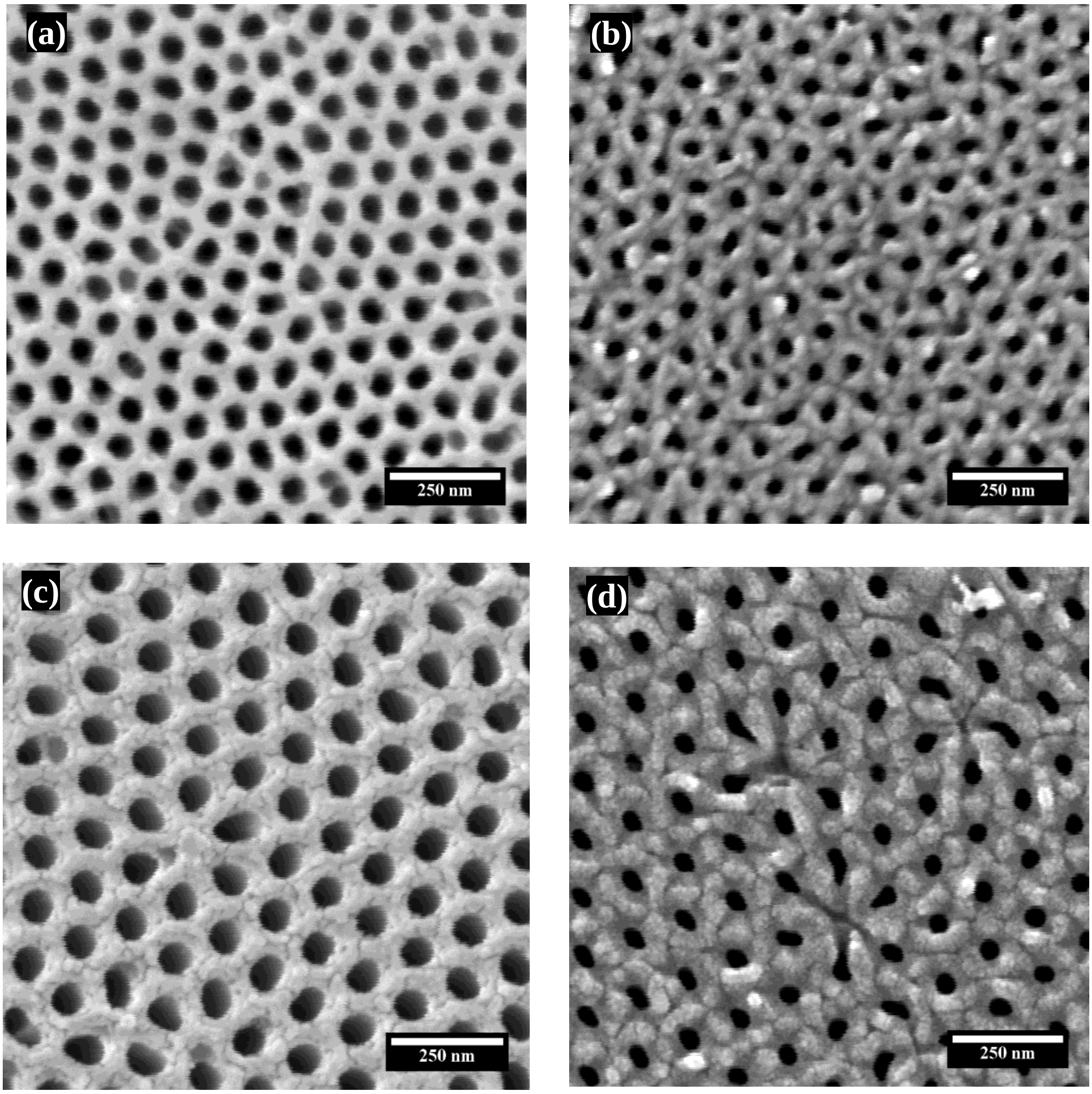

Figure 4.61: SEM images of AAO anodized at 35 °C (after PO): (a, b) front and back side of AAO anodized at 35 V for 2 h and (c, d) front and back side of AAO anodized at 50 V for 2 h.

Table 2 lists important measured parameters in comparison to typical values achieved for standard 25 °C reaction temperature.

The size of the back side pores seemed not to be influenced as long as the PO process was extended to 5 s. At higher temperature, the ion mobility and reaction rate was increased as it was indicated by the higher current flow. As a result, the thickness of the oxide layer was increased by about 50 % in comparison to the standard 25 °C temperature.

Table 2: Measured parameters for 35 °C anodizations and 2 h reaction period in comparison to (standard) values for anodizations at 25 °C.

Anodization conditions	**35 V, 2 h 35 °C**	35 V, 2 h, 25 °C	40 V, 2 h, 25 °C	**50 V, 2 h, 35 °C**	50 V, 2 h, 25 °C	60 V, 2 h, 25 °C
Pore size front / nm	**40 – 45**	35 – 40	40-45	**60 – 65**	45 – 50	55 – 60
Pore size back / nm	**30 – 35**	30 – 35	35-40	**35 – 40**	35 – 40	40 – 45
Inter-pore distance / nm	**85**	85	105	**130**	130	150*
Current / mA	**16 – 17**	12	15	**37 – 38**	26	35 – 45
Membrane thickness / µm	**29**	19	25	**65**	43	55

* estimation by back side cell diameter

Regarding the front side pore diameter, the current flow, and the layer thickness, the anodization at 35 V and 35 °C was rather comparable to a 40 V-25 °C-anodization and 50 V-35 °C matched with 60 V-25 °C. Because changing to higher temperatures seemed to be a suitable method to increase the rate of production for filters, the combination with the pore widening procedure was tested (see Figure 4.62).

As already discussed in Chapter 4.5.4, this etching step once more enlarged the bigger front sides more than the smaller back sides. For the 35 V-anodization the front size pore diameter increased by 1 h pore widening from 40 – 45 nm to 55 – 60 nm, the back side apertures were enlarged to about 40 nm. Anodization at 50 V with subsequent 2 h-pore widening led to a strong increase of the front diameter to 80 – 90 nm, the back side enlargement was weaker (50 – 60 nm). The conclusion, that pore widening increases the difference between front and back side diameter the stronger the bigger the pore sizes had been, was again found to be true. The channel diameters within the membrane were rather constant with usually 5 nm front-to-back size difference. Narrowest part of the membrane was still the pore aperture at the back side.

The anodization at 35 °C showed overall a high number of similarities to the conventional 25 °C reaction. Both reaction conditions were suitable to form membranes for a filtration approach and were basis for the separation experiments described in Chapter 4.8.4.

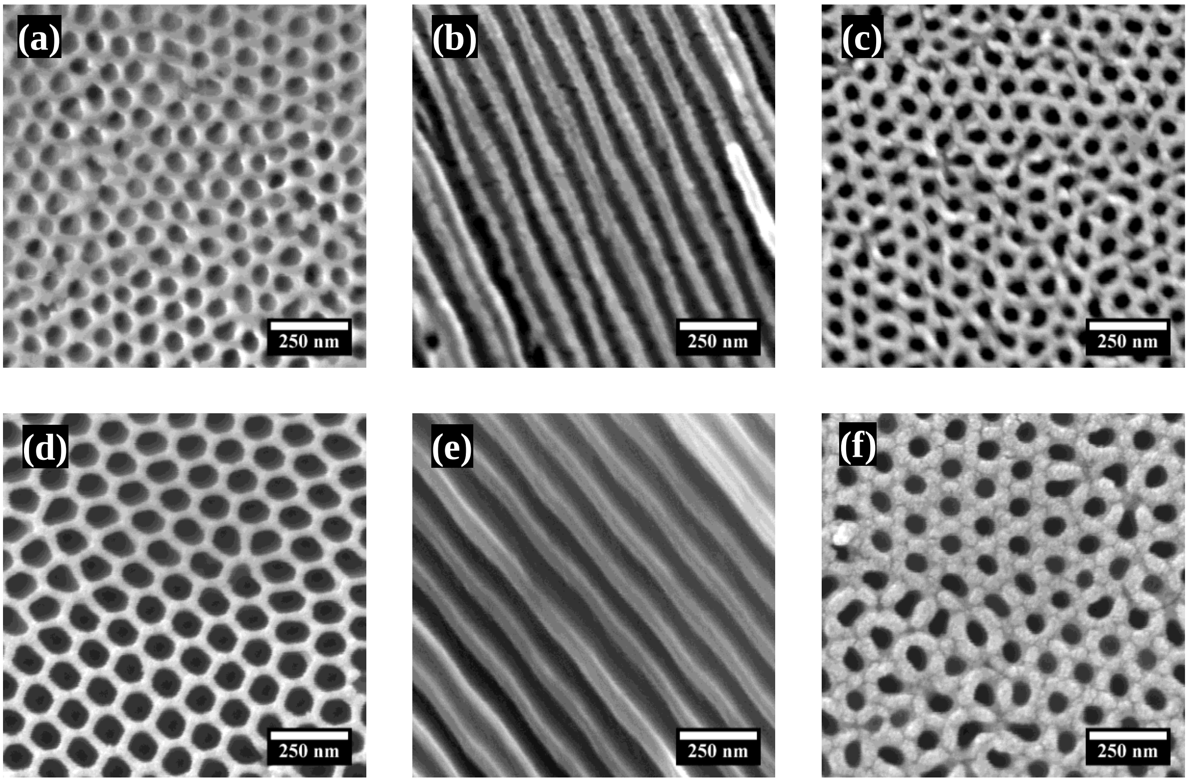

Figure 4.62: SEM images of AAO anodized at 35 °C: (a – c) front side, cross section and back side of AAO anodized at 35 V for 2 h and 1 h pore widening; (d – f) front side, cross section and back side of AAO anodized at 50 V for 2 h and subsequent 2 h pore widening.

Exploring the possibilities for a further temperature increase, also reactions at 50 °C were performed. Anodization temperatures above 60 °C were found in the past to be not suitable any more, leading only to a thin, soft and non-protective porous oxide layer.[143] Zhu *et al.* reported the formation of nano grass anodizing aluminum at temperatures of 50 to 70 °C in 0.3 M oxalic acid.[113]

Because of the temperature increase, partial surface corrosion as a result of overetching was also observed here when anodizing at 50 V for 1.5 h (see Figure 4.63 (a)).

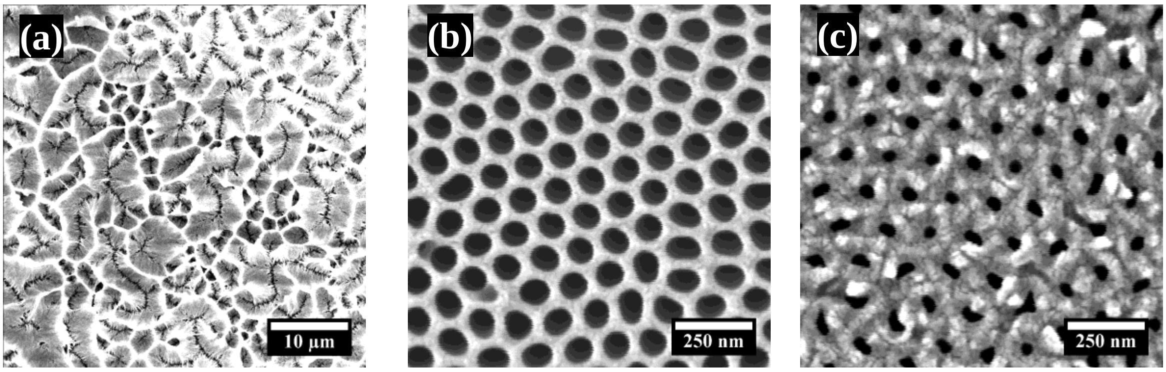

Figure 4.63: SEM images of an AAO membrane produced at 50 °C (50 V, 1.5 h) showing (a) partially front side corrosion, (b) front side pores, and (c) back side pores.

Only in some parts of the disc regular pores on the front side were found, just very short reaction times maybe would completely avoid the nano grass formation. On the backside always regular pores were found but with very small apertures using the described PO process (see Figure 4.63 (b, c). Even though the high current flow of about 65 mA at 50 V led to an oxide growth rate of more than 40 µm/h, the high discrepancy between the front and back pore sizes anticipated a high value of 50 °C-reactions for the filter production.

4.7 Surface Functionalization of AAO

As it was already discussed in the introduction (see Chapter 1.3), the easy access to AAO, or ATO respectively, surface functionalization was an important reason to choose this system for the development of filtration membranes. The surface properties of AAO are determined by hydroxyl groups, forming the unsaturated finish of the aluminum oxide.[144] The OH-groups on the AAO surface allow an easy modification with oxygen affine molecules of desired functionality. The hydrophilic surface can be reversed into hydrophobic or even special designed host molecules can be coupled to the surface to enable specific interactions to guest molecules.

Due to its porosity, AAO membranes have a large surface that can be determined by BET, Brunauer, Emmett, and Teller, measurements. Typically, nitrogen is adsorbed as a monolayer onto the surface to be analyzed and its area can be calculated. For the measurements, discs produced at 35 V for 2 h were used without subsequent pore opening step. The surface, calculated by the BJH-method (see Chapter 6.2), was determined to be narrow 29 m^2/g. From the adsorption section of the isotherme, a pore size distribution was calculated with a maximum at 48 nm.[a] This is little more than typically measured by SEM images, but it is in line with the assumptions made in Chapter 4.4.3.The isothermes and the calculated pore size distribution is found in the appendix (Section 7).

The most simple way to change surface properties is by wet chemical synthesis which is easy accessible and has no need for special technical equipment. Most common method is the silanization,[e.g.[145][118,146–150]] but the broad range of possible chemical functionalizations includes also e.g. the reaction with phosphate derivatives,[151] catechol anchors,[152] or even terminal alkynes.[153]

---

[a] BET measurements were performed by [redacted].

Even though our main focus was in providing a basic AAO filtration membrane and specific functionalization was the task of our cooperation partners (see Chapter 1.3), the ability of our electrochemical product for that purpose was surveyed. For the mentioned reasons alkoxy silanes for the testing with the membranes were chosen. A whole class of substituted silanes is commercially available and they are known to bind covalently in a high density to AAO surfaces.

The popular (3-aminopropyl)triethoxysilane (APTES), bearing an amino-function to couple easily further functionalities, was selected as well as the octadecyl-trimethoxysilane (18-TMS), an alkyl silane bearing a long organic chain providing hydrophobic properties when linked to the membranes. Both molecules are very small and should be able to reach via diffusion also the inner surface of the membranes (the surface of the channels) and not only the outer surface.

The APTES was first of all used to proof the success of the coupling reaction. Surface functionalizations are in general difficult to detect with analytical methods because layers of about just one molecule width represent only a tiny part of the whole material. Bulk analytical methods usually are not even sensitive enough to identify the layers, least of all a space-resolved detection is possible. A method which could give hints on the success is the highly surface sensitive XPS analysis (described in Chapter 5.3), but no evidence about the inner surface would be possible.

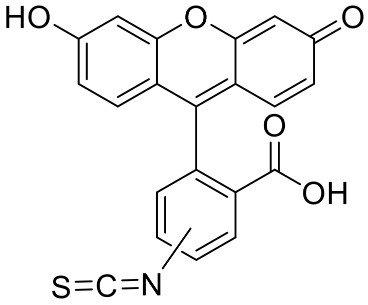

Figure 4.64: Structural formula of fluorescein isothiocyanate (FITC).

For this reason, commonly an indirect approach is preferred. Dyes can be detected due to strong absorption and emission (or fluorescence) bands even in lowest concentrations and conventional laser scanning microscopes are able to excite and detect the dye molecules. A popular, commercial available dye specially designed for the coupling to amino-groups is the fluorescein derivative FITC (see Figure 4.64). The isothiocyanato group is highly amino reactive, building a thiourea bond.

An AAO membrane was treated with a solution of APTES in acetone and subsequently exposed to a solution of FITC in anhydrous DMF. The orange solution discolored very fast, concentrating the dye on and/or in the membrane. After intense washing, the membrane kept an orange color and it was controlled with SEM that the porous surface of the AAO was still intact. The images showed no abnormality at all (see Figure 4.65), potential polycondensation reactions of APTES molecules did not lead to constriction or even blockage of the pores.

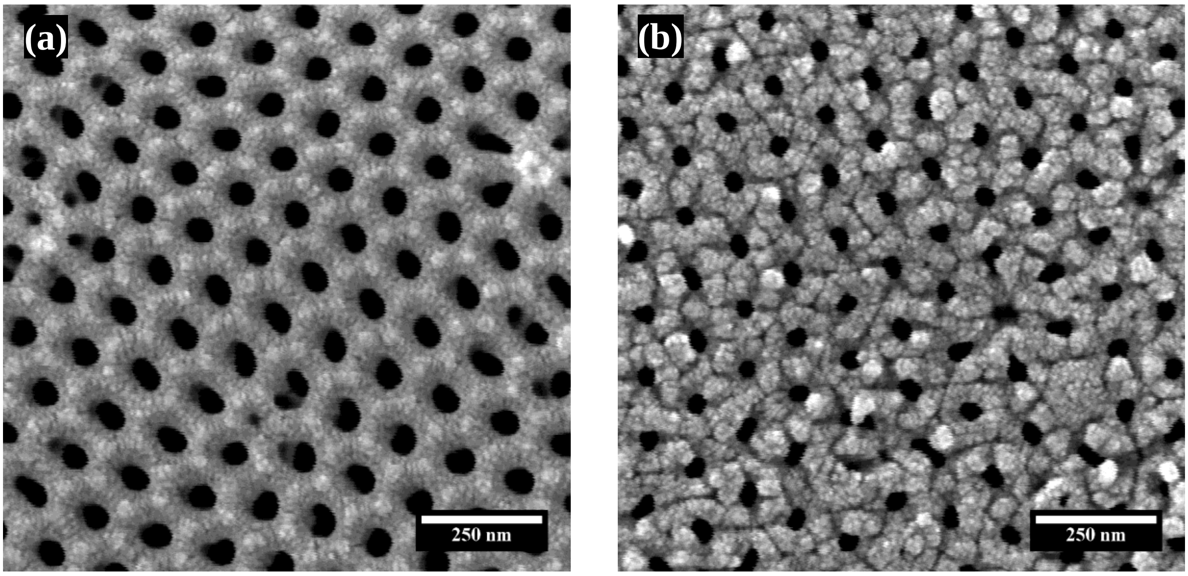

Figure 4.65: SEM images of AAO front and back side (50 V, 2 h) after functionalization with APTES and FITC.

A freshly broken edge of the stained membrane was analyzed with confocal laser scanning microscopy (CLSM), showing a characteristic emission (see Figure 4.66 (a)). The green fluorescence from the dye was visible all over the side view of the membrane. In reflective mode, the red laser light gave an impression of the anisotropic nature of the material, even though the single channels cannot be resolved with visible light, of course (see Figure 4.66 (b)). The stronger fluorescence from the two surfaces of the membrane could be easily explained by the high amount of dye coupled to the outer surfaces. Moreover, the emission is not reduced by any absorption effects of the AAO. If it is considered that the cross section shows a high ratio of non-emitting aluminum oxide, the considerable fluorescence therefrom argued for a probable functionalization of the inner surface too. However, contribution from the outer surfaces by light conducting properties of the aluminum oxide was possible.

Blank samples of same pore size and thickness were produced to study the affinity of FITC to non-functionalized surfaces without previous APTES treatment. FITC showed a preference for the AAO surface too. However, washing of the membranes after the treatment resulted in intense leaching of the dye. Less stained but no complete discolored membranes were obtained. Regarding the differences in color intensity and the behavior under the washing, a functionalization of the membrane by APTES was most likely.

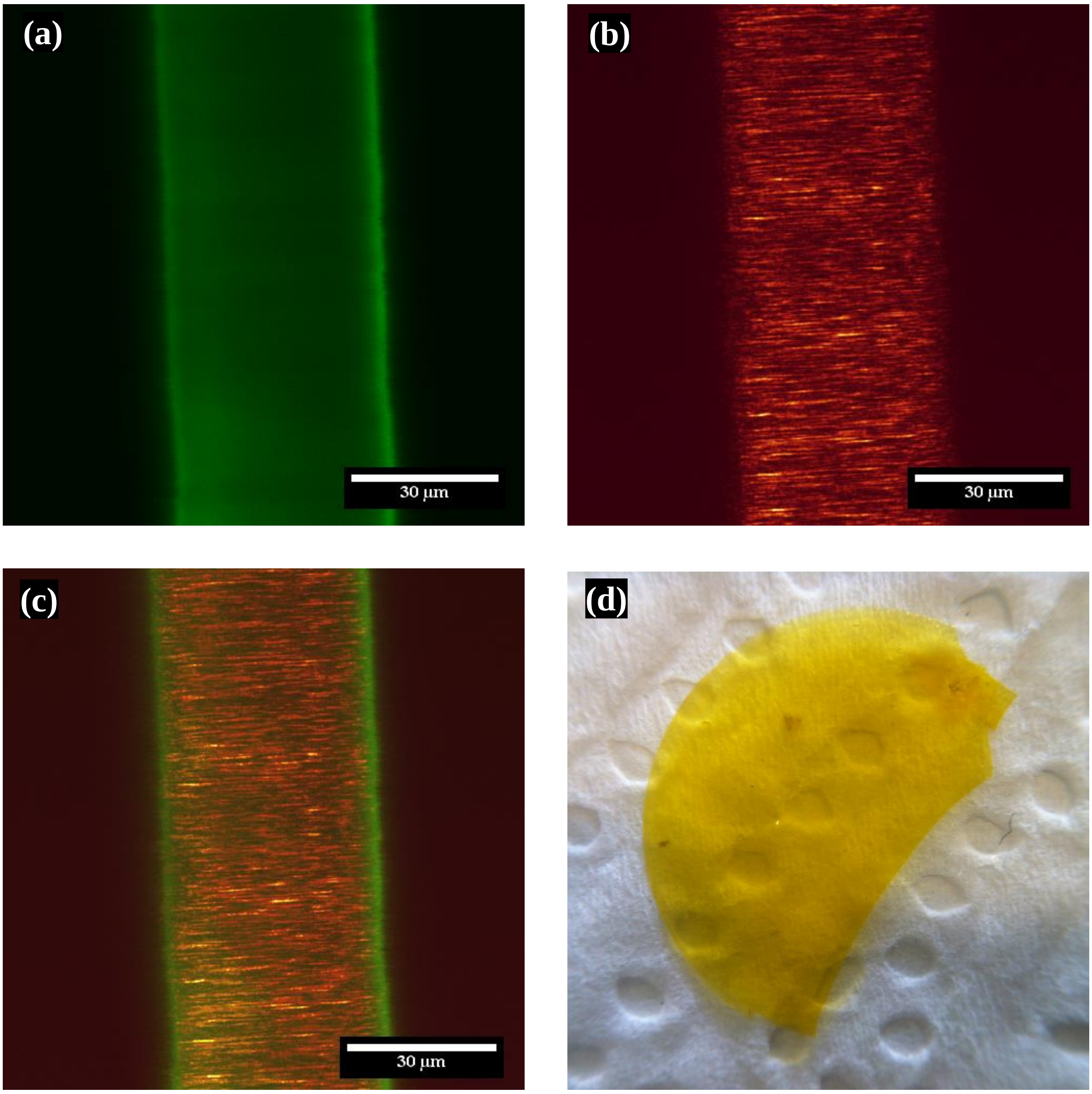

Figure 4.66: (a – c) CLSM images of FITC-functionalized AAO (50 V, 2 h) in cross-sectional view, (a) green emission of the dye (excitation 488 nm, detection bandpass 500 – 535 nm), (b) red reflection of the laser excitation (633 nm), and (c) overlay of emission and reflection (all three images taken by [redacted]); (d) photograph of a functionalized membrane.

The treatment with the alkyl silane 18-TMS instead of APTES likewise did not influence the appearance of the membranes in SEM images and the pores were still unblocked. Membranes treated by this alkyl silane showed enhanced hydrophobic properties.

4.8 Completed Synthesis of Testing Membranes

Within the previous chapters, different steps of AAO filtration membrane production were discussed. As few approaches did not lead to optimal results, the optimized synthesis procedure to yield perfect suitable oxide discs shall be shortly concluded in the following. Figure 4.67 shows an illustration comprising the single steps including their introduced abbreviations.

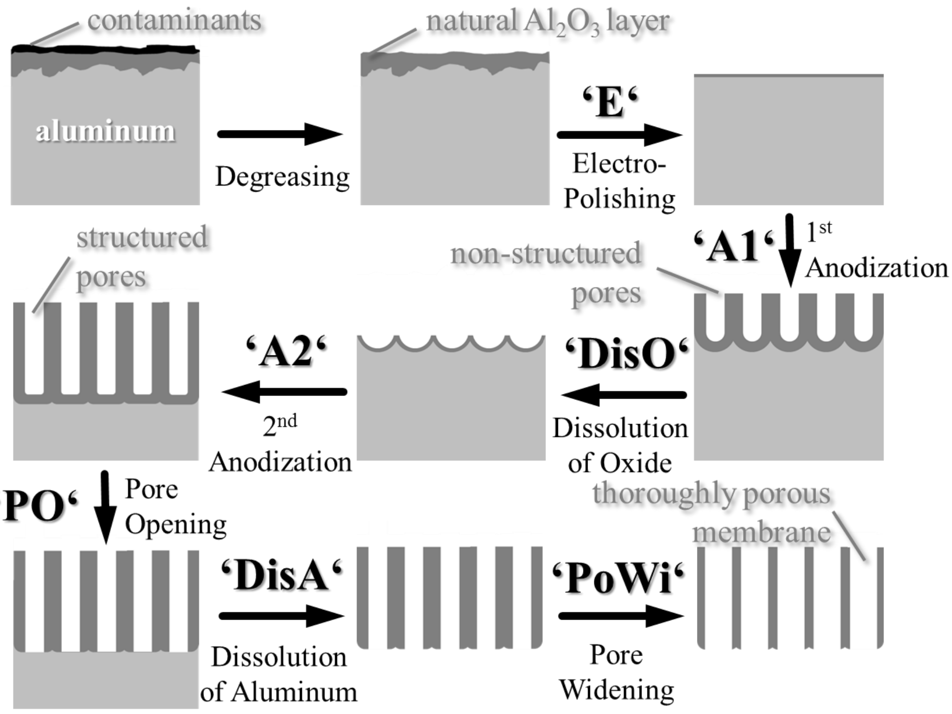

Figure 4.67: Scheme of the complete AAO synthesis route to prepare suitable filtration membranes.

The process was started by preparation of a bare circular aluminum foil including the cutting, pressing, and degreasing. It was followed by an electropolishing (E) in alcoholic perchloric acid with agitation by a stirring electrode. Subsequent pre-anodization (A1) in oxalic acid solution at distinct conditions determined the pore diameter and inter-pore distance. This provided an ordered pattern on the foil after dissolution of the preliminary oxide (DisO) with phosphochromic acid. The second anodization (A2) at the same voltage resulted in the final porous oxide layer. Its thickness was controlled by the reaction period and reaction temperatures of 25 or 35 °C. Subsequent electrochemical pore opening (PO) with perchloric acid and uncovering of the oxide by metal dissolution (DisA) in acidic Cu^{2+}-solution produced the self-supporting, flow-through filtration membrane. Optionally, the process was completed by a pore widening (PoWi) step. The performance tests and filtration experiments, described in the following, utilized AAO oxide discs produced that way.

4.8.1 Screening of Membrane Parameters for the Subsequent Filtration Tests

4.8.1.1 Physical Performance Tests

Handling experiences with tweezers manifested a certain stability of the transparent oxide discs, but also a sensitivity for punctual, abrupt pressure. The mechanical stability of a self-supporting AAO layer was not only dependent on its thickness, but also of its porosity and structural homogeneity. A membrane produced at 25 V for 5 h exhibited a thickness of about 25 µm and was comparable to a 40 V-2 h-membrane regarding this aspect. With the former, however, breaking appeared very easily due to weaker pore walls and a reduced pore order. Bending of the brittle oxide was only possible within a very small range. Generally, the moderate flexibility of AAO can only be demonstrated with large-scale layers.[119] Thus, versatile examinations were performed to judge the potential as well as the limits of the as-prepared discs in the planned filtration application.

Ultrasonic cleaning could not be used for the membranes at any point of the synthesis until the membrane became free from the Al metal. The aluminum foil was too thin to withstand the high energy input of the sound waves. Strong local heating when touching the wall of the container resulted in destroyed or flexed foils with broken layers of anodic oxide. However, all tested AAO membranes, even thin discs of about 10 µm, turned out to be sonication stable.

Prior to first filtration tests, it had to be examined which pressure level could be applied. Therefore, a steady, slowly increasing pressure brought to the membrane discs should be applied. This was implemented by a hydrostatic pressure setup, in which an increasing liquid column slowly enhanced the force on the filtration membrane. A split filter holder with two O-ring seals should realize the tightening of the membranes. However, commercial filter holders are available in sizes of 13 or 25 mm diameter only. Thus, it was started with water-tap connecting parts having the optimal inner diameter to hold the 16 mm oxide discs (see Figure 4.68). A drawback was the fastening as it was a tightrope walk in between breaking the brittle material and screwing the holder tight enough to seal the membrane.

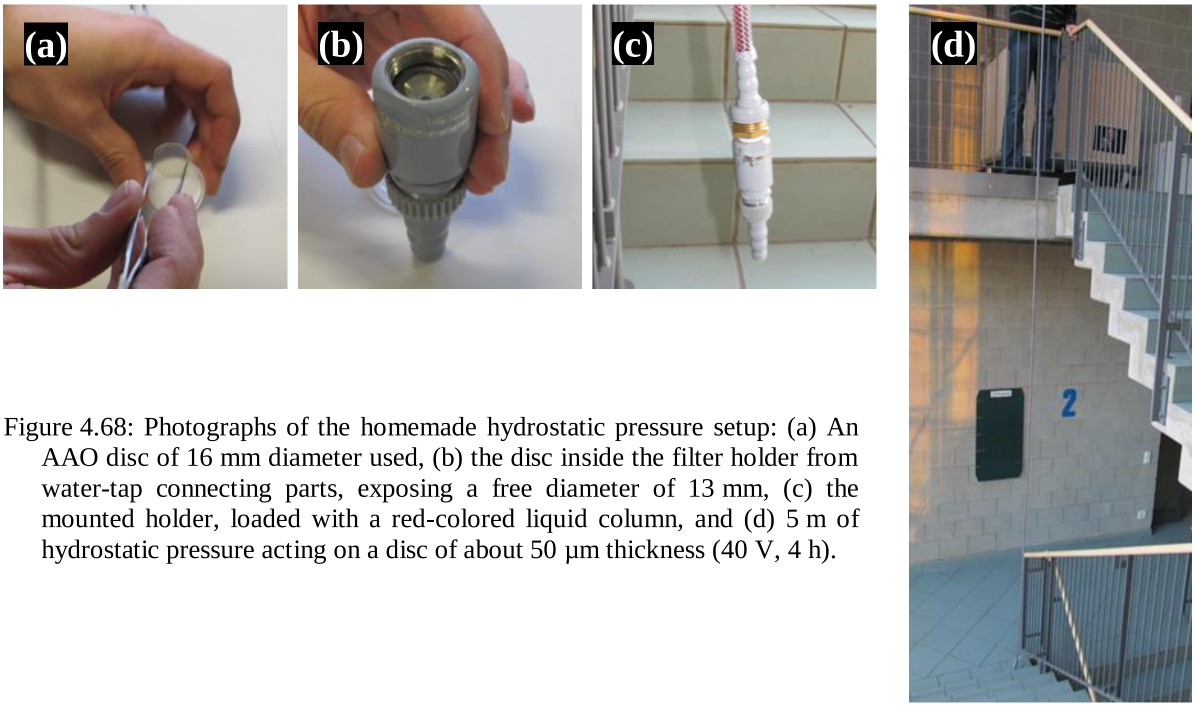

Figure 4.68: Photographs of the homemade hydrostatic pressure setup: (a) An AAO disc of 16 mm diameter used, (b) the disc inside the filter holder from water-tap connecting parts, exposing a free diameter of 13 mm, (c) the mounted holder, loaded with a red-colored liquid column, and (d) 5 m of hydrostatic pressure acting on a disc of about 50 µm thickness (40 V, 4 h).

The load tests allowed the 16 mm discs to be mounted with a non-supported diameter of 13 mm (see Figure 4.68 (a, b)). This area of about 1.33 cm^2 had to withstand a liquid column set on the disc by a flexible tube (see Figure 4.68 (c, d)). Using the described construction, discs of about 19 µm thickness (35 V, 2 h) sustained a liquid column of 2 m, meaning a hydrostatic pressure of 200 mbar. Discs of 45 – 50 µm (40 V, 4 h) resisted a 5 m liquid column equal to 1 bar pressure. Alternatively, instead of an overpressure load, low pressure of 60 mbar was applied by a membrane vacuum pump to those membranes without rupture. The unconventional filter holder construction with many single parts and sealings did not allow monitoring liquids passing the filtration membranes. A more professional approach will be discussed in the following Chapter 6.1.2.

4.8.1.2 (Bio-)Chemical Stability Tests

For the application of the produced AAO in medical devices its potential toxicity is an important factor. AAO shows in general a positive effect on cell growth, e.g. osteoblasts, and on the cultivation of many other microorganisms.[11,154] However, aside from the membrane’s toxicity itself, the heavy metals copper and chromium were used in the synthesis route. For this reason, membranes were cleaned by short sonication in water and subjected to a standard

WST8-Assay, a viability assay with Caki-1 cells[a]. From the results concluded in the appendix (Section 7), it was evident that the membranes did not behave cytotoxic.

A further aspect is the chemical stability of amorphous AAO. The as-prepared membranes were limited in applications by their susceptibility to both acid and base attack. Figure 4.69 shows the etching effect of an ammoniac solution on the surface of an AAO membrane. Mardilovich *et al.* found that amorphous AAO membranes are totally dissolved in solutions of $pH < 4.2$ or $pH > 9.9$. Furthermore, at pH 5.0 and respectively pH 8.2, first etching could be observed. In contrast, if AAO is transformed into a polycrystalline material, no release of Al(III) was detectable in a pH range from 4.7 to 9.0.[144]

This is in line with findings that amorphous AAO is instable in deionized (DI), acidic water, but that annealing between 600 and 700 °C enhances its stability.[155] In Chapter 4.5.2, it was already reported that a heat treatment at 650 °C improved the resistivity of the porous AAO surfaces against H_3PO_4. Further, the impact of DI water of pH 4.5 could be confirmed in long-term studies: The as-prepared membranes became soft and milky within 4 weeks, sign for dissolution processes, independent of annealing at 650 °C. However, in pH-neutral isotonic sodium chloride solution, no alteration was observed at all.

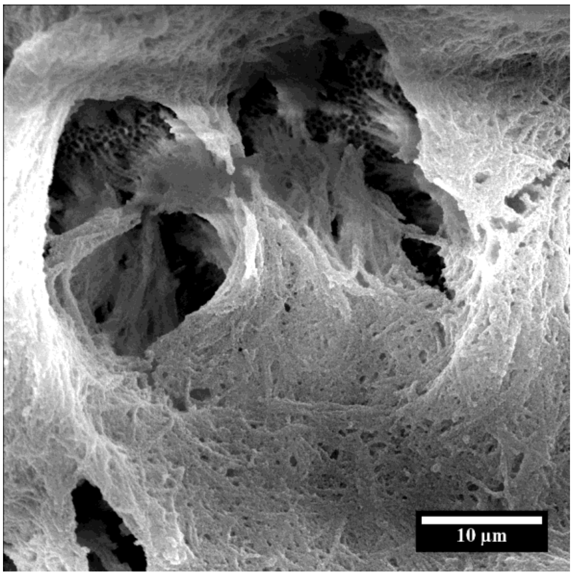

Figure 4.69: SEM image showing the surface of an AAO membrane after impact by a solution of pH 11 for 1 h.

Contemporaneously with the conversion to crystalline material, already discussed earlier, structural changes are reported in literature: Curling or even breaking of the membranes is observed,[155,156] but also slight changes in the nanostructure affecting e.g. pore sizes.[144,157]

Exceeding a temperature of about 850 °C, AAO starts to crystallize. In dependency of the temperature, γ-, δ-, θ-, and α-Al_2O_3 are formed between 900 and 1200 °C.[144]

Crystalline membranes are more robust against acids and bases, their stability against 1 M H_2SO_4 or NaOH is reported.[157] However, they are mechanically less flexible.[144] Further, annealing procedures at high temperatures are disadvantageous as they reduce the number of defect sites on the oxidic surface. It can be suggested that functionalization methods, which avail of hydroxyl groups on the surface, show reduced

---

[a] The cytotoxic test was performed and analyzed by [redacted].

activity with annealed surfaces, especially if a transformation from amorphous into a crystalline state is involved. Thus, it was found for anodic titanium oxide (ATO) that monolayers of silanes are denser on amorphous than on crystalline layers.[158] Regarding the different aspects, it was decided to work with the amorphous AAO and without a subsequent heat treatment.

4.8.2 Evaluation of Different Filtration Set-Ups

The use of the homemade Cu-block Setup had the advantage of ejecting perfectly round shaped oxide discs. More simple approaches, often found in literature, do not allow a precise shape control of the resulting oxide. Unfortunately, the obtained discs of 16 mm diameter were not compatible with commercially available filter holders. As it was impossible to break the brittle membranes down to exactly the 13 mm size, 25 mm holders were tried (see Figure 4.70 (a)). Therefore, the sealing rings were exchanged to provide an overlap with the smaller membranes.

A membrane pump was used to suck liquids through the membranes. Either pure water or mixtures with ethanol were tried to reduce the surface tension. Alternatively to the membrane pump, a syringe pump was used to apply a controlled pressure to the membrane. Furthermore, different rubbery materials were tested, but leak tightness could not be solved satisfactorily. Attempts to firmly tight the two parts of the holder together damaged the used membranes of about 40 µm in thickness (50 V, 2 h). Thus, it was assumed that the distribution of the applied pressure when screwing the holder was nonuniform, mainly caused by the broad flexible rubber material.

A new holder was constructed from aluminum to hold 16 mm discs (see Figure 4.70 (b)). In contrast to the commercial plastic holders, aluminum provides chemical resistance against organic solvents. As a further action, PTFE vessels of anodization setups were modified to yield discs in adaptation to commercial filter holders. The synthesis of AAO discs in deviation the 16 mm size is discussed in the following Chapter 4.8.3.

But the new filter holder brought no improvements regarding leak tightness and breaking filters. Contrary to expectations, the problems in handling occurred the same way for commercially available Whatman® Anopore™ membranes (see Chapter 1.3). This was surprising as these membranes are dedicated to the application with filter holders.

Figure 4.70: Photographs of tested filter holders: (a) Commercial 25 mm plastic filter holder (Whatman), (b) reproduction from aluminum for 16 mm discs, and (c) manufactured holder with device against twisting.

Most membranes broke directly at the edge to the sealing support when screwing the holder tightly. To exclude twisting forces as a last error source, a new filter holder was constructed. A bolt and a tubing with external thread guaranteed a tight connection without provoking forces parallel to the membrane’s surface (see Figure 4.70 (c)). However, this construction did not solve the sealing problem either, so that further approaches were tried.

Within the new construction, the sealings were replaced by adhesives. Replaceable inserts allowed the application to membranes with different sizes and the tightening was realized by glue (see Figure 4.71 (a, b)). As a consequence, the membranes could be hardly recovered non-destroyed and many typical organic solvents were incompatible with any kind of adequate adhesive. In order to increase the resistivity of the oxide discs to pressure, aluminum grids were glued in place with the discs as well (see Figure 4.71 (c)).

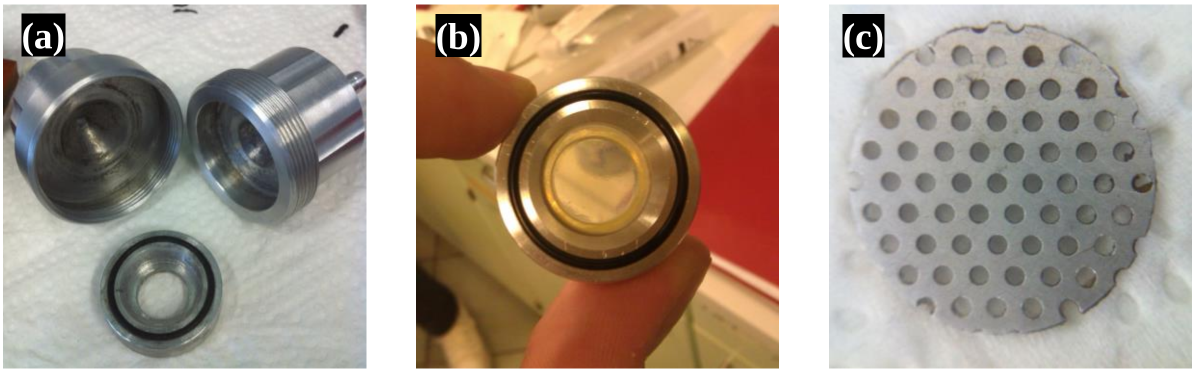

Figure 4.71: Photographs of (a) the used filter holder with replaceable insets to glue in membrane discs of different sizes, (b) an AAO membrane fixed in an inset, and (c) the stabilizing Al grid with 1 mm apertures.

Different types of adhesives were tested, which had to connect the oxidic membrane and the grid with the aluminum holder and to seal both parts completely. By means of viscosity and applicability, an acrylate and a silicone glue were identified to work best. The membranes were tightly fixed and showed a certain resistivity against a low-pressure flow of N_2 gas of about 100 – 200 mbar.

Prior to a filtration process, the flow of liquids through the membranes had to be ensured. Flexible tubes were connected to the filter holder equipped, with a stable membrane of about 50 nm free pore diameter (see Figure 4.72). The feeding side was filled with an aqueous dispersion of a red ruthenium dye (N719 with low solubility in water) and connected to a N_2 pressure line. On the efflux, little water was used as bubble counter. When applying an overpressure of about 100 – 200 mbar to the colored liquid column, its level started sinking immediately. The residual air in the holder was pressed through the membrane and bubbled out. The process came to an abrupt end when the liquid itself reached the membrane. Keeping the pressure on the liquid, filtrate permeated very slowly. After 8 h, an amount of about 5 mL was recovered.

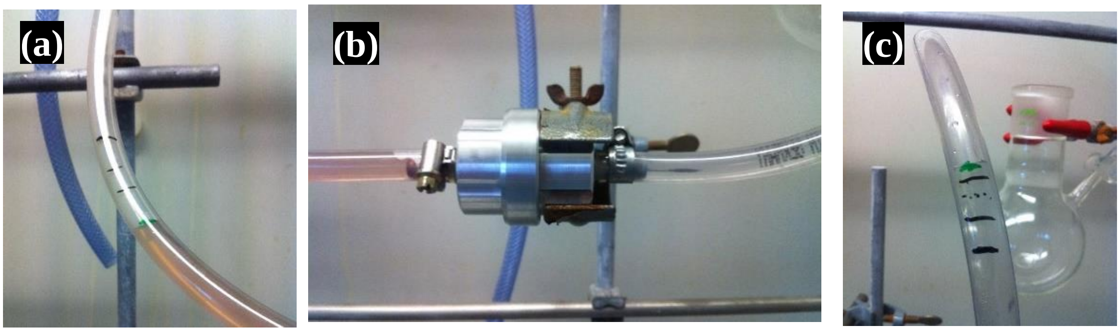

Figure 4.72: Photographs of the filtration setup showing (a) the feed liquid column containing red dye, (b) the filter holder including the AAO filtration membrane, and (c) the efflux.

The first fraction was colorless, with further progress also the red color of the dye became visible. This result showed clearly a significant separating capacity of the membrane. The water molecules moved much faster through the pores while the dye molecules and also particles were hindered to follow with the same velocity. As a secondary effect, the retention of the dye certainly proved the tightness of the construction. Subsequent to the experiment, the membrane showed intense staining with the dye (see Figure 4.73 (a)). Analysis by SEM showed precipitate also on the back side of the membrane originating probably from the dye (see Figure 4.73 (b)). As an intermediate result, a basic material for the development of a filtration membrane was developed, which offered the possibility for further surface functionalization (see Chapter 4.7).

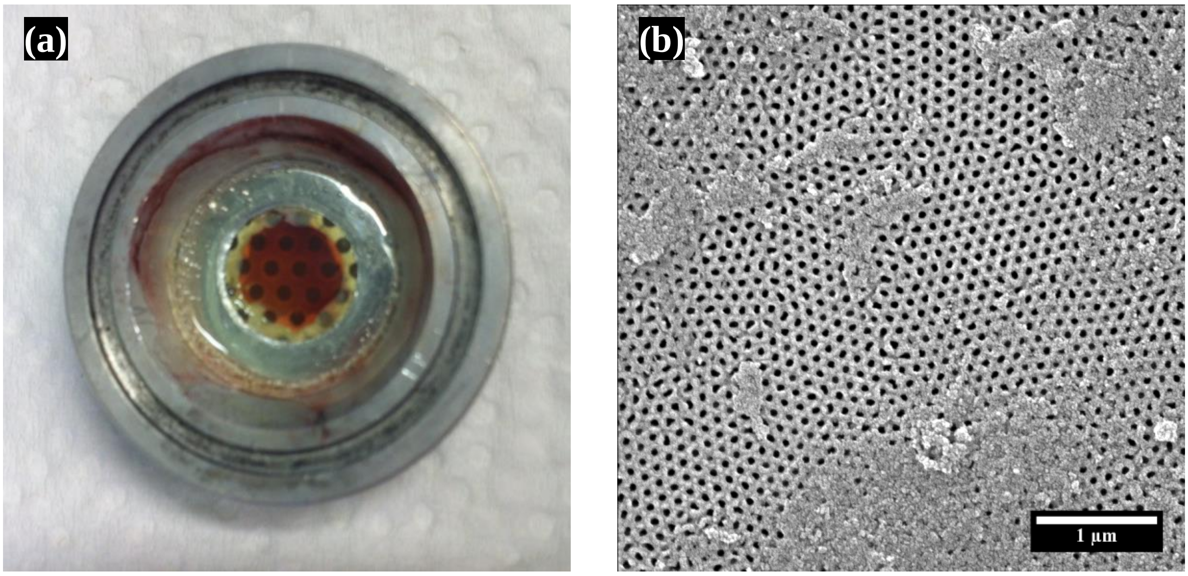

Figure 4.73: (a) Photograph of the stained AAO membrane in the filter inset and (b) SEM image of the AAO backside showing residues of the dye.

4.8.3 Production of Alternative Filter Disc Sizes

The standard diameter of produced oxide discs was 16 mm (see Chapter 6.1.2). By means of the use of the AAO membranes in filter holders, the membrane size needed to be adapted to the sizes of commercially available 13 or 25 mm filter holders.

Moreover, it was explored whether an up-scaling of the disc size was possible without causing problems in synthesis, nanoscopic appearance, and subsequent handling. Attempts to reduce the active area in the 16 mm setup to 13 mm failed by use of broad sealings, adhesive tape, or isolating paint. Therefore, new PTFE vessels were constructed with apertures of 13, 20, and 30 mm diameter to take up different foil sizes.

The smaller 13 mm discs were produced in the same way as the standard size. Generally, the polishing as well as the pre-anodization step were performed in the standard setup. The final anodization (A2) as well as the pore opening procedure took place in the 13 mm setup. Many combinations of anodization voltage, time, and reaction temperature were tested. Figure 4.74 shows SEM images of a membrane produced at 50 V with a reaction period of 3 h and a subsequent pore widening step.

The measured pore sizes on front and back side, about 90 and 75 nm, respectively, coincided with values obtained for the standard diameter of 16 mm. The same was valid for the thickness of the oxide layer of narrow 60 µm. However, the comparison revealed slightly bigger pores for the smaller discs, which was explained as influence of the DisA process. In both cases, Al foil discs of 20 mm were used as starting material. The smaller anodization area of only 13 mm resulted in more aluminum left to be dissolved. Because the amount of acid used for the DisA was about the same, higher temperatures caused by the more intense dissolution reaction enhanced the etching of the pore walls.

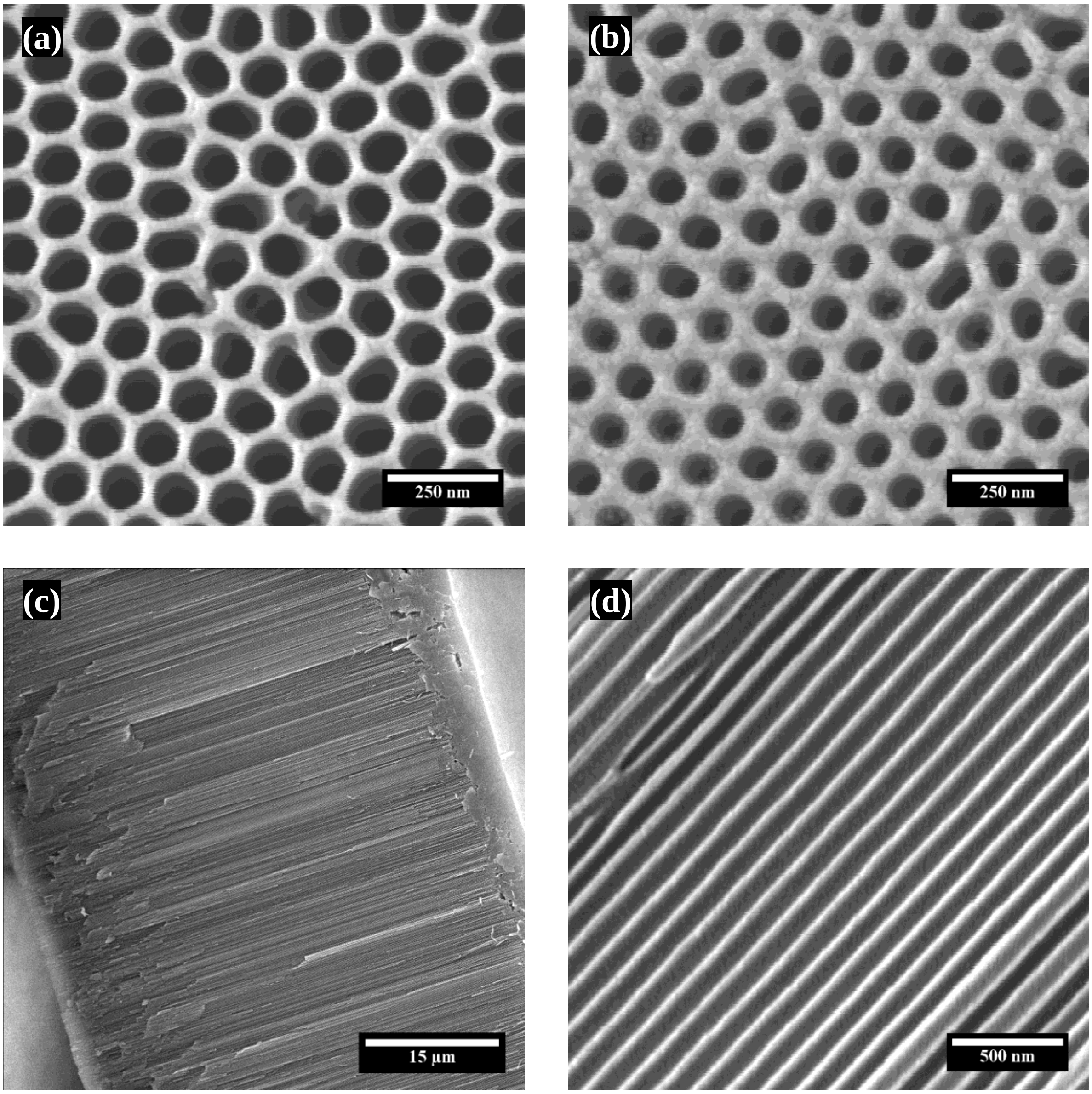

Figure 4.74: SEM images of a 13 mm oxide membrane (50 V, 3 h) after 2 h pore widening: (a) front side, (b) back side, (c) cross-sectional view, and (d) close view to the channels.

Further similarities with the 16 mm standard were also observed concerning the calculated oxide growth rate, but the efficiency of the electrochemical oxidation process was different. In this regard, Table 3 provides an overview and a comparison of measured and calculated values for both disc sizes.

Table 3: Comparison of current flow and density, oxide growth rate, and efficiency of the electrochemical oxidation process for 13 mm and 16 mm disc anodization at 25 °C and 35 °C.

		13 mm disc size			16 mm disc size		
Reaction Temperature	Voltage / V	Current flow / mA (current density / mA cm^{-2})	Growth rate / µm h^{-1}	Efficiency / mm^3 oxide mAh^{-1}	Current flow / mA (current density / mA cm^{-2})	Growth rate / µm h^{-1}	Efficiency / mm^3 oxide mAh^{-1}
25 °C	35 V	5 (4)	8	0.19 – 0.21	12 (6)	10	0.16 – 0.17
	40 V	8 (6)	13		15 (8)	13	
	50 V	14 (11)	20		26 (13)	23	
35 °C	35 V	10 (8)	15	0.20	17 (9)	15	0.16 – 0.18
	50 V	20 (15)	30		38 (19)	32	

It is obvious that the growth rates were independent of the active area for 25 °C and 35 °C, in respect of the voltages. However, the use of the setup with smaller apertures showed a higher efficiency. For the calculation, the current flow, being proportional to the number of electrons flowing, was related to the amount of oxide created. The lower energy conversion at the smaller surface led obviously to minor loss in terms of side reactions.

To produce larger oxide discs of > 16 mm, several adjustments to the standard procedure were necessary: First, all electrochemical steps had to be performed in the setups with corresponding aperture size. However, the anodization of discs with larger diameter was more error-prone with regard to pitting corrosion. Small holes in the metal foil, sometimes occurring close to the sealing with the vessel, were fixed with nail polish to maintain the functionality of the membrane. Second, for the electropolishing (E) it was essential to use the homemade stirring electrode out of titanium. The effect of the larger titanium stirrer was superior, when used with the bigger sample areas. By this adaptation, the quality of polishing was comparable to the standard procedure. Third, the pore opening procedure (PO) worked better using the longer reaction period of 5 s. Fourth, the process of dissolving the aluminum (DisA) could not be executed by just immersing the oxide bearing foil in the HCl/Cu^{2+}-

solution. As mentioned before, the acid diffused immediately through the opened pores in the gap between metal and oxide and started to dissolve Al by hydrogen evolution. The pressure brought to the oxide layer by the forming gas usually sufficed to break open the oxide layer of larger membranes. For this reason, the foil was treated only at one edge until the oxide layer became free and provided a gas outlet.

Figure 4.75 shows SEM images of a membrane produced at 35 V with a reaction period of 2 h. The measured pore diameter was about 35 nm on the front side. The oxide disc had a thickness of about 15.5 µm. In general, the observed pore sizes were little smaller compared to the standard oxide discs produced. As discussed earlier, it is likely that the solution temperature of the DisA process played a key role.

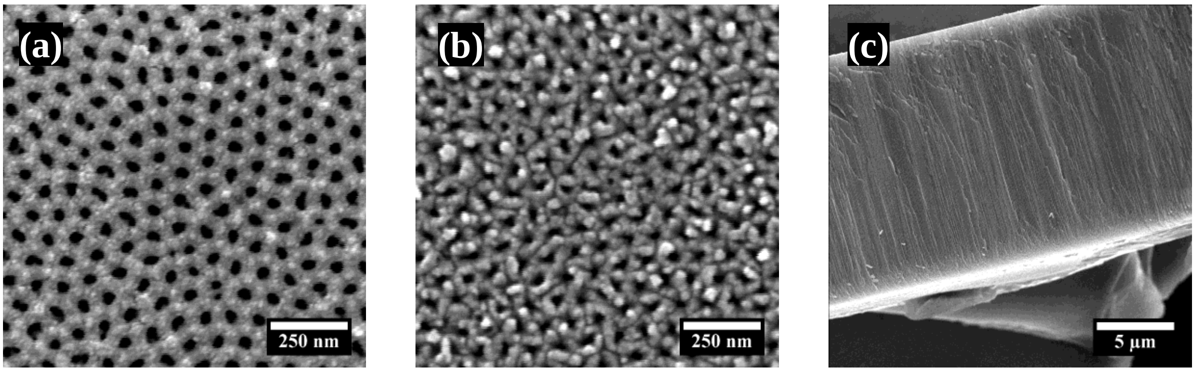

Figure 4.75: SEM images of a 20 mm oxide membrane (35 V, 2 h): (a) front side, (b) back side, and (c) cross-sectional view.

Figure 4.76: Photograph of an AAO membrane of 30 mm diameter (area of 7 cm^2).

SEM analysis revealed even for AAO of 30 mm diameter a homogeneous order and pore size distribution over the whole surface. Figure 4.76 shows a corresponding photograph of a stable oxide disc with an area of about 7 cm^2.

Table 4 lists in analogy to Table 3 parameters as current flow and densities, oxide growth rates and efficiency for the 20 and 30 mm disc size. The increase in diameter from 13 to 16 mm implied already an efficiency loss. A further increase to 20 mm consumed an even higher number of electrons to generate the same amount of anodic oxide by volume (compare with Table 3).

It was observed with raising sample size that even if the experimental conditions were all the same, the current flow varied strongly. In particular, anodizations to yield 30 mm discs required high current (compare Table 4). Thus, an explanation for the variations observed could be local heating. However, pore sizes and also the generated oxide layer thickness were not influenced.

Table 4: Comparison of current flow and density, oxide growth rate, and efficiency of the electrochemical oxidation process for 20 mm and 30 mm disc anodization at 25 °C. Range of values indicate no steady current flow.

		20 mm disc size			30 mm disc size		
Reaction Temperature	Voltage / V	Current flow / mA (current density / mA cm^{-2})	Growth rate / µm h^{-1}	Efficiency / mm^3 oxide mAh^{-1}	Current flow / mA (current density / mA cm^{-2})	Growth rate / µm h^{-1}	Efficiency / mm^3 oxide mAh^{-1}
25 °C	35 V	17 (6)	8	0.15 – 0.18	38-40 (6)	*not determined*	
	50 V	35 (11)	20		70-100 (10-14)		

4.8.4 Filtration of Nanoparticle Dispersions

4.8.4.1 Transport Processes through AAO Membranes

For further filtration experiments, nanoparticle (NP) dispersions were used. A big issue in nanoparticle synthesis is the desired sharp particle size distribution as polydispersity complicates the analysis of strongly size-dependent properties, e.g. self-assembly. Among others, filtration through typically polymeric membranes is a known alternative for the purification and size-fractionation of NPs.[159] Thus, the applicability of AAO membranes as filtration device was tested regarding the separation or fractionation of polydisperse NPs. Sweeney *et al.* demonstrated a continuous cross-flow diafiltration setup with a peristaltic pump to fractionate water-soluble gold nanoparticles. Even though no AAO but a 50 kDa protein membrane was used, the approach is similar to the projected (see Chapter 1.3).[160]

Examples for macromolecular filtration with AAOs are reported.[159] Proteins with effective sizes between about 2 and 15 nm were filtered through modified commercial Anopore™ membranes using an overpressure of about 0.2 bar. Thereby, membrane fouling could be significantly reduced compared to polymeric membranes.[143]

Yamaguchi *et al.* presented an application of nanoporous anodic aluminum oxide in the separation of protein molecules of > 4 nm from molecules with < 2.4 nm diameter. Inside of the large pores of Anopore™ membranes, a silica-surfactant nanocomposite was synthesized to reduce the pore size.[160] Applying same approach, El-Safty and coworkers fractionated noble metal nanoparticles and semiconductor nanocrystals using a common filtration setting connected to a vacuum pump.[161,162][163]

The transport through mesoporous materials follows different physical models. As the diameter of the pores is in the range of the mean free path as gas molecules, the dominant transport process is Knudsen-diffusion for pore sizes between 2 and 50 nm. Further, surface adsorptive diffusion and capillary condensation contribute.

Mardilovich *et al.* found the permeability of N_2-gas to be 1.5 cm/s atm for a 40 µm AAO membrane with pore diameter of 64 nm and a porosity of 14 %.[144] De L. Lira *et al.* observed a gas flow through AAO to be proportional to the pressure difference, thus, only Knudsen-diffusion occurs. Further, the permeability of the membranes was found to be inversely proportional to the square root of the molecular weight of the gas used.[131]

Regarding the pressure induced filtration, the transport of a permeate through an ultrafiltration membrane, with pore diameters between 2 and 100 nm, can be described by the Hagen-Poiseuille equation (eq 4.2). For the volumetric flow rate J_V of the liquid volume V through membrane area A by the time t, it holds

$$J_V = \frac{V}{A \cdot t} = \frac{r^2 \cdot \varepsilon \cdot \Delta p}{8 \cdot \eta \cdot \tau \cdot z} \tag{4.2}$$

with radius of the pores r, porosity ε, pressure difference Δp, dynamic fluid viscosity η, tortuosity τ, and membrane thickness z. The tortuosity factor τ is 1 for cylindrical pores perpendicular to membrane surface, which is typical for AAO membranes. Going from diffusion to a pressure driven flow, the pores' radius becomes a very crucial aspect because of its quadratic dependence for the flow. As a consequence, in industrial ultrafiltration processes overpressure of 3 – 10 bar is necessary to separate particles in the range of 10 – 100 nm.[161]

For nanofiltration processes, the Hagen-Poiseuille model has to be extended by solvent and membrane parameters to consider stronger interactions. The viscosity of the solvent plays an amplified role and the importance of the convective term seems to be greater than that of the diffusive term.[162] A study on the hydraulic permeability of pure water across AAO membranes showed also for this membrane type a different, manifold higher, flow rate as predicted by Hagen-Poiseuille.[163]

In literature, few groups report the filtration of nanoparticle dispersions through AAO membranes. Analogous to results published for ATO membranes, merely diffusion of dye molecules, easy to monitor, is discussed. The typical experiment comprises a feed chamber, containing the detectable substance, which is separated from the permeate chamber by the membrane. In the following, the concentration gradient is traced over hours or days to find increasing analyte concentration in the opposite chamber. An interesting example for medical applications was reported by Gong *et al.*, who anodized an aluminum tube to form an AAO capsule as a model for drug release.[164]

Further, nanoparticles were studied concerning their diffusion behavior through AAO membranes too. Stephens *et al.* reported investigations on $CoFe_2O_4$ particles with diameter below 15 nm, whose transport through commercial membranes of 100 and 200 nm pore diameter was monitored by change in UV absorbance. The flux increases when the AAO membranes had been functionalized with alkylsilanes. As it is expected, the flux decreases with increasing particle size and increases with pore diameter.[165]

4.8.4.2 Filtration Tests with As-Prepared AAO Membranes

The literature examples presented in the previous chapter demonstrate the high potential of AAO membranes in filtration applications. However, experiments were limited to commercially available substrates without possibility of taking influence on membrane parameters. The testing of the as-prepared AAO membranes required the determination of certain experimental parameters to guarantee a high reproducibility. On the one hand, the membranes were mounted always to face the NP dispersion with the front side having the bigger pore entrances. Even though blockage could occur as well, the inflow of the particles into the channels seemed to be a crucial point. Once trapped inside, the pressure differential would lead to a controlled transport through the channels. On the other hand, the pressure difference should be kept as low as possible to antagonize breaking of the fragile membranes. Before using the membranes in tests, its tightness in the filtration holder was monitored by the speed of water flow through the membranes.

As a standard, membranes were produced by anodization at 50 V and 35 °C for 2 h, usually with subsequent pore widening of further 2 h. In analogy to previously discussed results (see Chapter 4.6), this approach at elevated temperature resulted in very stable filtration discs of 65 – 70 µm thickness, penetrated by channels of about 60 nm diameter. However, while the front side openings facing the particles were of about 80 nm, the smallest diameter to pass was the back side opening with about 55 nm (see Figure 4.77).

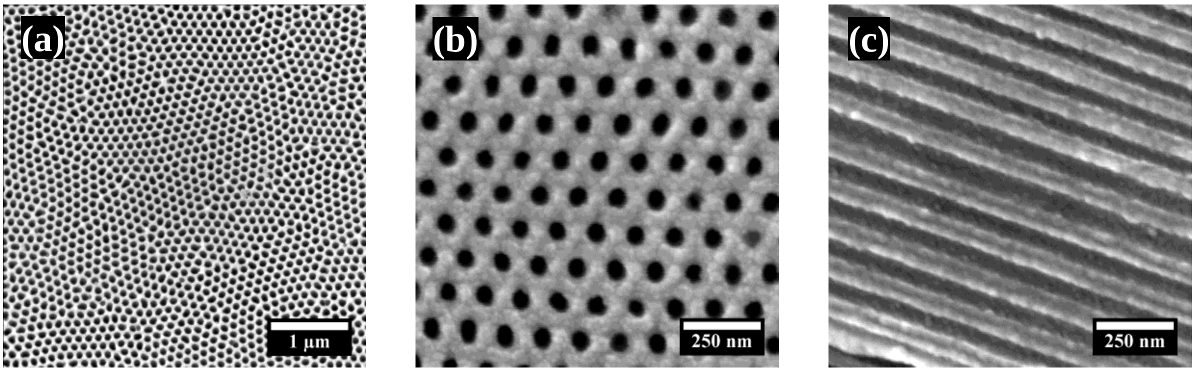

Figure 4.77: SEM images of a typical standard filtration membrane (50 V, 2 h, 35 °C): (a) front side with large pores, (b) back side with lowest diameter of 55 nm, and (c) cross-sectional view onto the channels of about 60 nm.

As already illustrated in Chapter 4.8.2, the AAO membranes were glued together with aluminum grids into the filter holder. Usually, the standard disc size of 16 mm was employed, in fewer cases also 20 mm discs allowed higher flow. The use of adhesives to fix the membranes limited the application to aqueous solvents so that swelling or even dissolution of the glue was prevented.

In our workgroup, various NPs are synthesized for different purposes. Among catalytic active nanoparticles (e.g. from V_2O_5) or semi-conductive nanoparticles (e.g. from TiO_2), especially nanoparticles combining different functionalities are created for the wide field of "theranostics", therapy and diagnostic. Mesoporous or hollow NPs as drug-carriers, with controlled load and release, are in the focus. Moreover, NPs are investigated for synchronous biolabeling, separation, and the detection of multimodal magnetic resonance imaging (MRI) and computer tomography (CT) imaging, e.g. from $Fe_3O_4@SiO_2$,[169] and $MnO@SiO_2$,[166] $Au@MnO@SiO_2$,[167] $FePt@MnO$,[168] and $Co@Fe_2O_4$.[169] The knowledge in NP design was used for custom-made nanoparticles to analyze size and surface chemistry effects on filtrations.[a] As microscopical techniques were not suitable to analyze the filtration of NP

---

[a] [redacted] gave general advice concerning the nanoparticle selection.

dispersions through membranes, the NPs were designed to absorb light at distinct frequencies. The characteristic absorption of light resulted from metallic cores, fluorescence, plasmon resonance, or just by dye coupled to the particles. UV-Vis spectroscopy is a method to survey the concentration of diluted nanoparticle dispersions. The absorbance A becomes linear with the concentration c according to the Lambert-Beer law (eq 4.3)

$$A = \varepsilon \cdot l \cdot c \tag{4.3}$$

with the absorptivity of the attenuator ε and the path length l. If single absorption bands of mixture components do not overlap, even the ratio of the components in the mixture is measurable. However, nanoparticle dispersions show a high degree of light scattering. Therefore, this linear relation can only be applied as indicator for a semi-quantitative analysis. For the tests, small silica nanoparticles, citrate stabilized gold nanoparticles, and different bigger heavy metal nanoparticles were chosen. The water solubility was provided by silica encapsulation. Typically, the NP dispersions were diluted with water so that the absorption maximum was measured to below 1. The obtained dispersions were slightly colored or fluorescent. Thus, passing particles could be observed immediately with the naked eye.

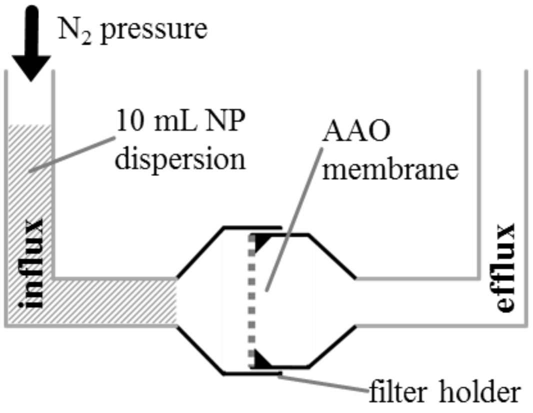

Figure 4.78: Sketch of the filtration setting.

Figure 4.78 provides a sketch of the filtration setting, which made use of the filter holder pictured in Figure 4.71. In general, 10 mL of dispersion were subjected to the filtration. The flexible tube at the efflux contained some water to observe the escaping air from the holder when applying the pressure.

Depending on the filtration velocity, most liquid was recovered after some hours. Slow filtrations were usually stopped after 12 – 24 h, even if only small amounts passed to this point. The pressure was raised to max. 1 bar, if a starting pressure of 200 – 400 mbar showed no significant flow. Slow filtration progress could have several reasons. The membrane’s size and the way, the membranes were glued into the holder, had a big impact on their active surface. Usually, filtration membranes showed a flow in the area of between 3 mL / h at 200 mbar and 4.5 mL / h at 400 mbar. In order to increase the number of filtration tests, most membranes had to be used more than once. Partial blocking or gradual corrosion of the amorphous filters exposed to the solutions could happen. However, general aspects and tendencies were analyzed.

The tightness of filters and the intactness of the membranes was controlled by application of nanoparticles, which were definitively too large to pass. As an example, $(Au@Fe_3O_4)@SiO_2$ nanoparticles, embedded as groups into very large silica shells of about 150 nm (see Figure 4.79), [a] should not be detected in the filtrate. Figure 4.80 (a) shows the violet-brownish dispersion losing its color when pressed through the filter. The filter was not stained afterwards, indicating that no particles entered the pores blocking them. In front of the filter, a retentate of particles could be recovered (see Figure 4.80 (b)). The absorption spectra of the dispersion showed an absorption due to plasmon resonance of the Au at about 550 – 600 nm and an absorption shoulder in the blue region. The filtrate, however, did not show any absorption band (see Figure 4.80 (c)).

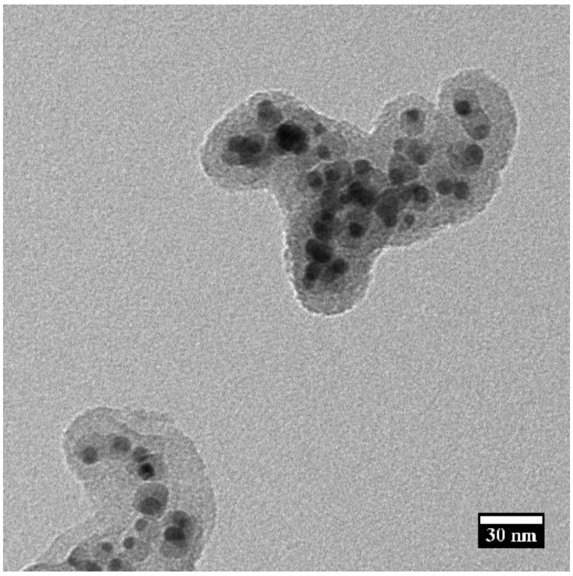

Figure 4.79: TEM image of $Au@Fe_3O_4@SiO_2$ NPs agglomerated by large Si shells. The image was taken by [redacted].

As mentioned before, the used membranes had pore diameters of about 55 nm at its narrowest point. Of course, particles have to be much smaller to pass the channels. The TEM analysis, used to determine the NP size, gives just an idea of the core size of the particles. In order to form long-time stable dispersions, the NPs have to be solvated. This shell of solvent molecules leads to an increased hydrodynamic diameter compared to the core size, which is determined by dynamic light scattering (DLS) in solution.

For a first test, the transport of very small nanoparticles was analyzed. Silica nanoparticles, which show a blue fluorescence, were generated by a microwave-assisted synthesis.[b] The NPs were too small and showed a bad contrast to be resolved with standard TEM methods, but certainly, their size was below 5 nm.

---

[a] Synthesis according to Wu *et al.*[175] by [redacted] under survey of [redacted].

[b] Synthesis adapted from Zhong *et al.*[173] by [redacted] and [redacted].

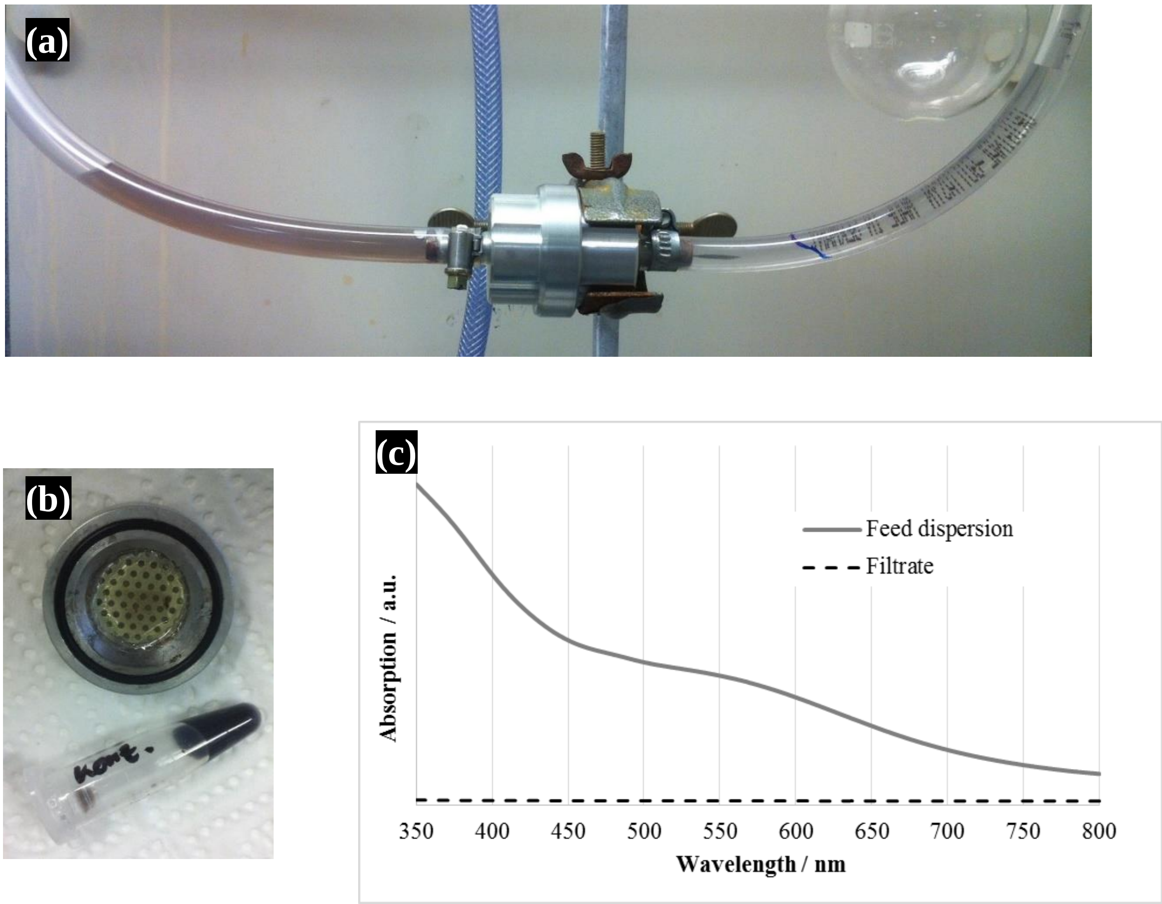

Figure 4.80: Filtration experiment with Au@Fe_3O_4@SiO_2 NP agglomerates: (a) Photograph of the filtration setting with colored feed and colorless eluate, (b) filtration membrane in the holder with NP retentate, and (c) absorption spectrum of NP feed dispersion and its filtrate after the filtration experiment.

The fluorescent liquid was subjected to filtrations with different filter membranes. The fluorescence of the particles was immediately detectable as soon as the first drops of filtrate became visible in the flexible tube at the efflux. The missing delay indicated that the small nanoparticles moved with about the solvent's velocity through the channels of the membrane. Comparison of the absorption spectra of the NP dispersion before the filtering and of the filtrate showed no significant differences in the intensity of the absorption (see Figure 4.81). However, a slight shift of the maximum and a sharper absorption band were observed.

Subsequent to this proof of general permeability for nanoparticles, the size of the particles was enlarged. Test objects were Fe_3O_4@SiO_2-FITC NPs, consisting of a 7 nm iron oxide core with silica shell and a total diameter of 14 nm (by TEM, see Figure 4.82).[a] The dye FITC (see Figure 4.64) incorporated into the shell had the advantage of a distinct and strong absorption band at low concentration. However, the hydrodynamic diameter was determined to be about

---

[a] Synthesis according to Schladt *et al.*[166] and DLS data by [redacted].

22 nm. This nanoparticle system already had to make use of 15 – 20 % of the pore profile taking the hydrodynamic value as a basis.

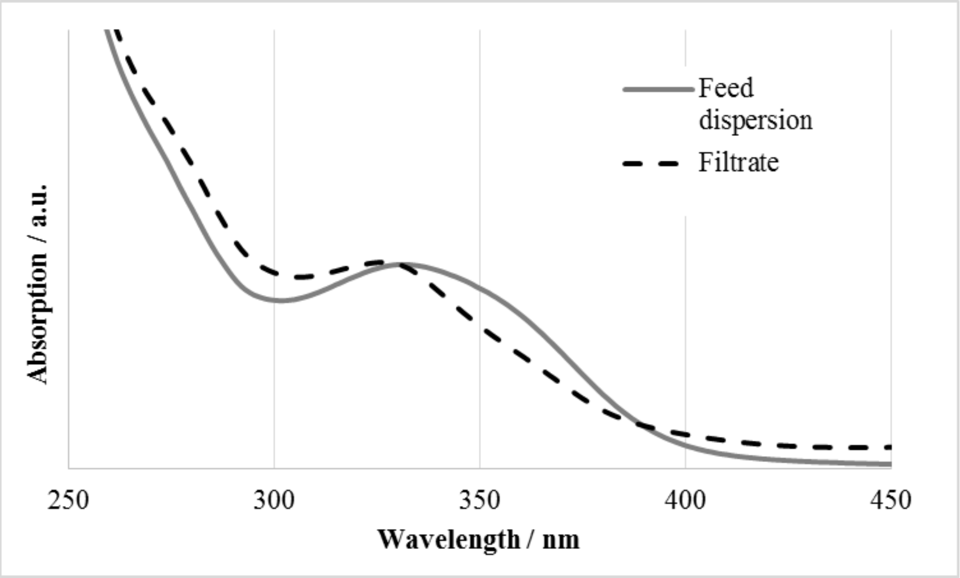

Figure 4.81: Absorption spectra of SiO_2 NP feed dispersion and its filtrate after the filtration experiment.

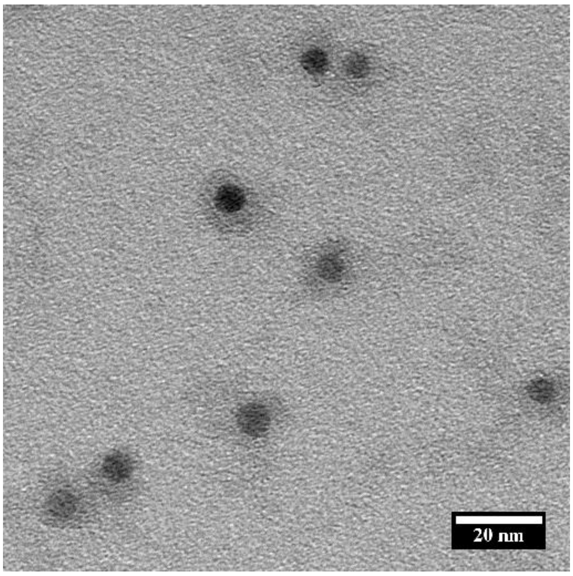

Figure 4.82: TEM image of Fe_3O_4@SiO_2-FITC NPs with total diameter of 14 nm. The image was taken by [redacted].

Three similar filtration experiments were performed, a very slow flow was observed whereby high overpressure and a long filtration period was necessary in all cases to collect the filtrate. The filtrate did not show any of the light brown, fluorescent green color of the stock solution, and only small amounts of FITC were detected by absorption (see Figure 4.83).

Comparing the absorption spectra of feed and filtrate, it can be concluded that a small amount of particles passed. However, the spectral intensity of the NPs was reduced to below 10 % of the former value. Free FITC in the initial NP dispersion could be excluded due to effective washing. In addition, the filtrate showed absorption in the blue region likewise. Observed precipitation in front of the membrane pointed towards an agglomeration of retained particles at the pore openings. In comparison to the small silica NPs used in the previous experiments, not only the size of the particles differed. The NP synthesis procedures made use of two different capping agents, determining the surface chemistry of the particles. The core shell particles exhibited PEG on its surface, the smaller pure silica particles were capped with APTES. It is most likely, that not only the size, but also different interactions with the membrane's surface had impact on the permeability.

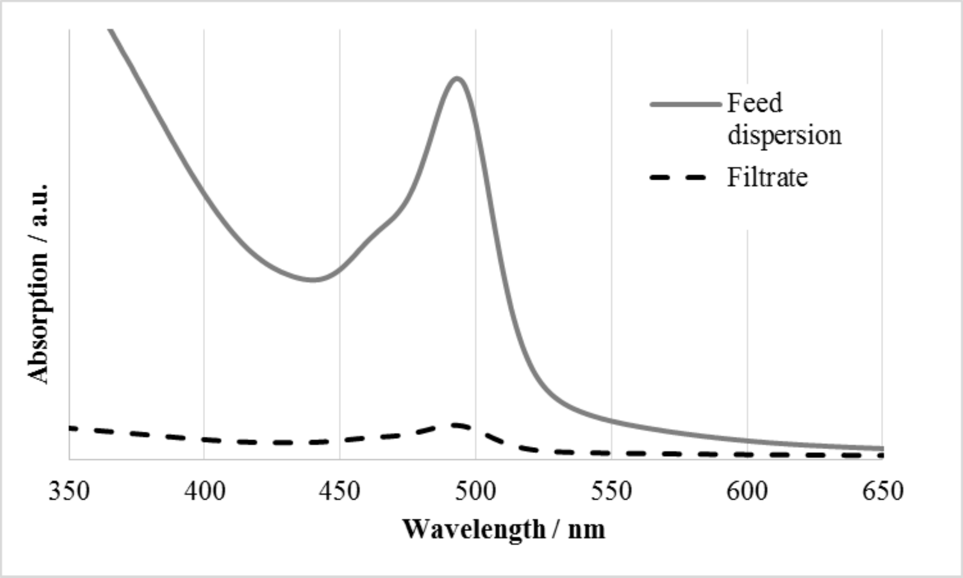

Figure 4.83: Absorption spectra of $Fe_3O_4@SiO_2$-FITC NP (14 nm diameter by TEM, 22 nm hydrodynamic diameter) feed dispersion and its filtrate after the filtration experiment.

It is supposed that the AAO filters work chromatographic as in membrane chromatography, a well-known technique used for protein separation.[170] The nanoparticles would need an extended period to pass the small channels of the membrane. As long as the NP dispersion remains stable, addition of extra solvent could accomplish a total recovering. The same principle is used in size exclusion chromatography (SEC), the most popular chromatographic technique to fractionate nanoparticles. This technique is based on differences in hydrodynamic volumes and interaction of these particles with the stationary phase is negligible. Usually, SEC is performed with columns filled by microparticles containing mesopores. This leads to the counterintuitive result that small particles move slower because they fit into the pores as compared to larger particles, which travel along the microparticles.[159]

Furthermore, a completely different NP system was tested, when choosing citrate stabilized gold nanoparticles.[a] The particles formed an extraordinary stable violet dispersion in water and showed a characteristic absorption due to plasmon resonance. The particle size was determined by TEM to be less than 10 nm, thus, should be small enough to enter the channels (see Figure 4.84).

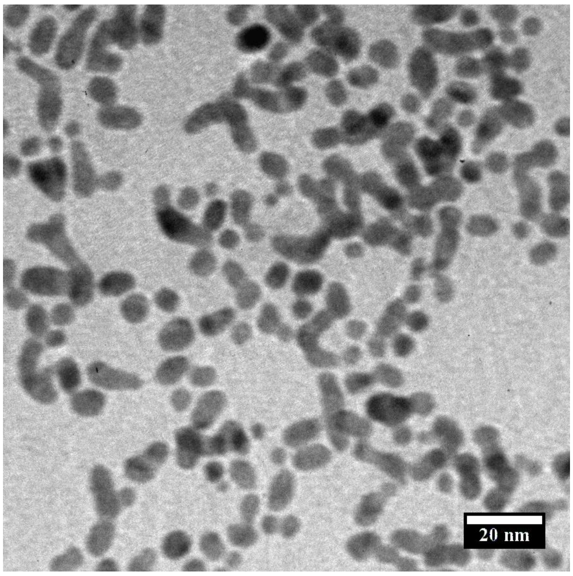

Figure 4.84 TEM image of citrate-capped Au NPs with total diameter of less than 10 nm. The image was taken by [redacted].

First filtration results showed the characteristic violet color of the Au nanoparticles in the filtrate (see Figure 4.85 (a)). However, all further tests showed almost no more absorption of gold in the filtrate (see Figure 4.85 (b)). The filtration membranes were afterwards one-sided stained by the gold. However, the particles in or on the membrane could not be washed out by purging with water using the filtration setup. The violet-blackish color changed after some days to golden (see Figure 4.85 (c)). Due to the smaller size compared to the tested core shell particles before, a considerably higher permeability was expected. As this was not the case, the charged surface of the particles must be the reason for the changed behavior. The surfaces of AAO films are reported to bear positive charges due to oxygen vacancies that attract ions with opposite charge.[153] The negatively charged Au citrate NPs, counter ion was sodium, could behave in a similar way. The intense staining of the membranes born out this assumption.

APTES functionalized AAO membranes have been used as templates to form nanotubes out of citrate stabilized nanoparticles.[176,177] However, the NPs were reported to interact with the amine groups of the silane and no immobilization was observed without membrane silanization. But in contrast to the as-prepared filtration membranes, AAO with very large pore diameter of 220 nm were used in literature. Therefore, literature reports of passing nanoparticles do not disagree with the observations reported herein. In future work, the impact of the surface chemistry and polarity of the particles will have to be further analyzed, e.g. by

---

[a] Synthesis according to Jana *et al.*[171] by [redacted] and [redacted] under survey of [redacted].

zeta potential measurements. In SEC, anionic surfactants have already been used to prevent adsorption of citrate NPs on the polymeric stationary phase.[178] This approach could lead to a permeation control of the Au citrate particles.

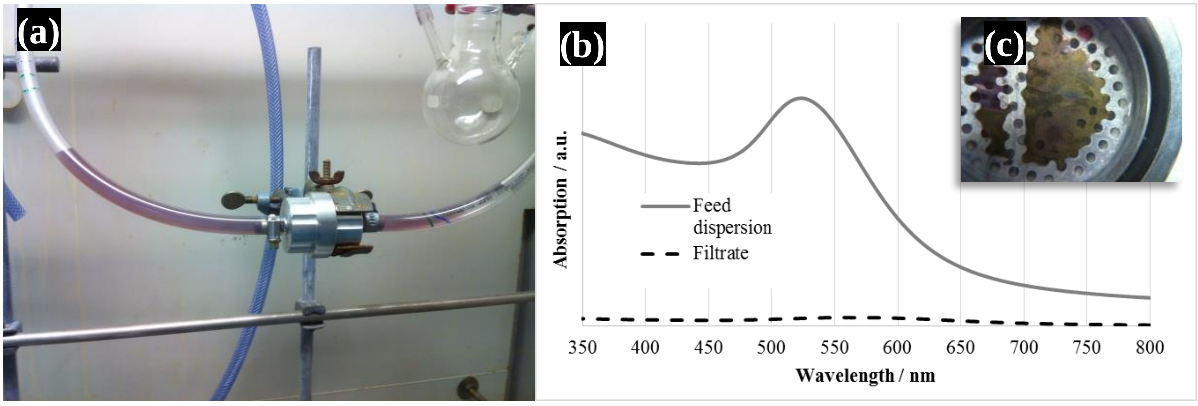

Figure 4.85: Filtration experiments with citrate-capped Au NPs: (a) Photograph of the colored dispersion, (b) absorption spectra of feed dispersion and filtrate showing almost no more NPs, and (c) photograph of the stained, golden filter after two days.

Up to now, only permeabilities of nanoparticle dispersions containing one NP type were analyzed. It was observed that, depending on its size, particles immediately passed the membrane with the solvent, were slowed down with respect to the solvent, or even could not pass at all. Moreover, the surface interactions with the pore walls seemed to play an important role. This strong influence of surface interactions guarantees the selectivity of the as-prepared, AAO for future biofiltering purposes as recommended in Chapter 1.3.

However, the separation capacity of the membranes was not demonstrated yet. In order to explore the limits of the filtration membrane, a most challenging separation problem was designed. NPs of different types were mixed together, thus, the mixture contained a high variety of particle sizes. A first fraction consisted of the citrate-capped Au particles already described (see Figure 4.84). A second fraction contained Au@MnO@SiO_2 Janus particles, too big to pass. But the batch contained a high amount of smaller SiO_2 NPs without core, as well as single Au cores (see Figure 4.86 (a, b)).[a] A third fraction consisted of MnO@SiO_2 NPs with incorporated FITC in the shell and a diameter of about 30 nm (see Figure 4.86 (c)).[b] The particle fractions were mixed in a way that the absorption of the single components was comparable. The dispersion was filtered very quickly through the AAO membrane and its color changed from intense into pale brown (see Figure 4.87 (a, b)). The filter was not stained,

---

[a] Synthesis according to Schick *et al.*[167] by [redacted].

[b] Synthesis according to Schladt *et al.*[166] by [redacted].

but some debris could be washed off. In particular, it was free from adhesives especially at the points, where the liquid streamed through the stabilizing Al grid (see Figure 4.87 (c))

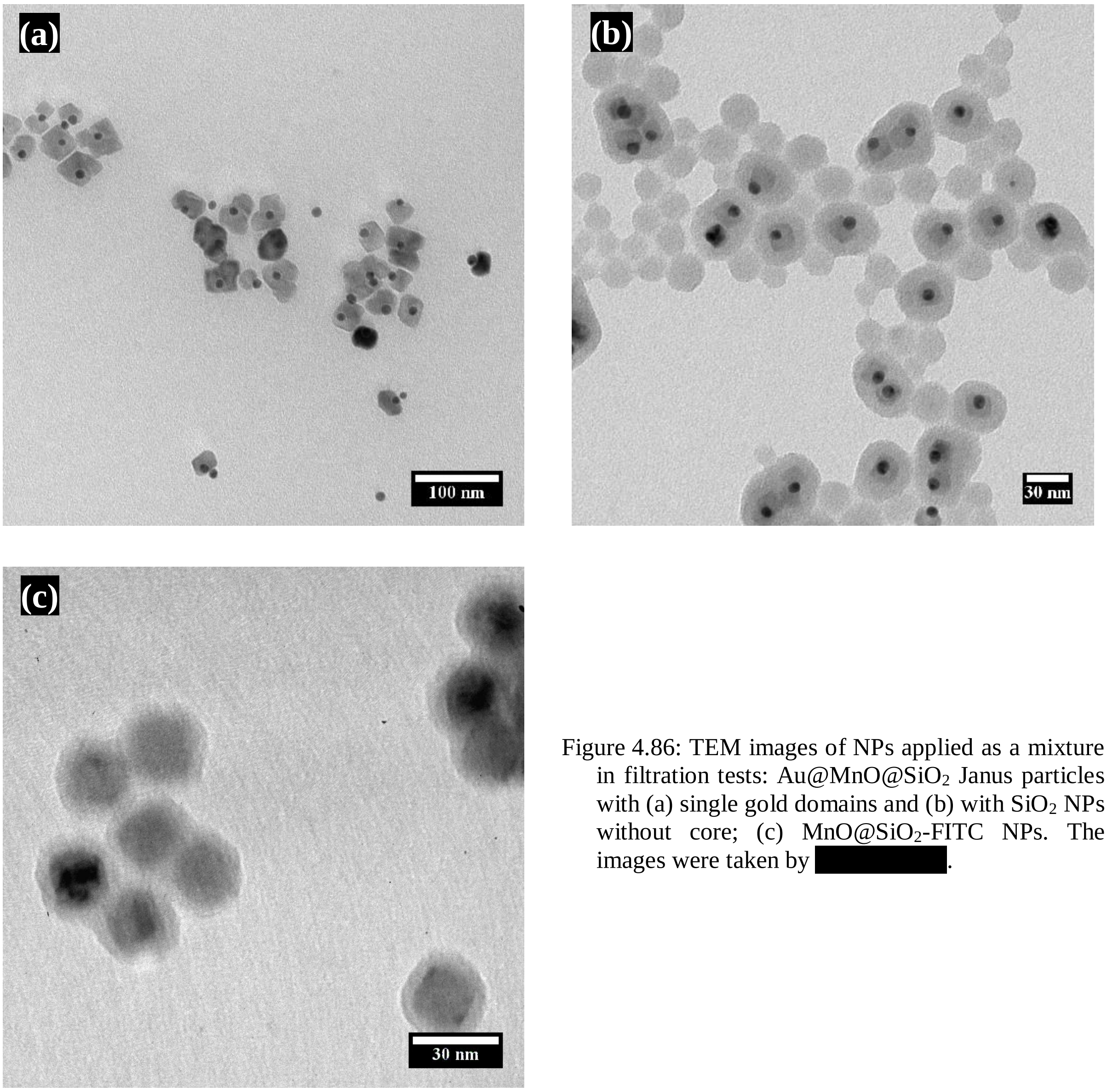

Figure 4.86: TEM images of NPs applied as a mixture in filtration tests: Au@MnO@SiO_2 Janus particles with (a) single gold domains and (b) with SiO_2 NPs without core; (c) MnO@SiO_2-FITC NPs. The images were taken by [redacted].

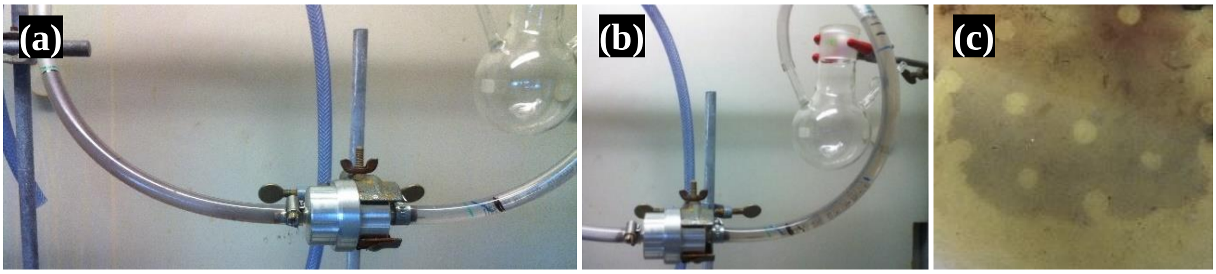

Figure 4.87: Filtration experiment with “most challenging” NP mixture: Photographs of (a) the feed before and (b) the eluate after the filtration, and (c) appearance of the filter membrane after the filtration.

The mixture of NPs was analyzed by TEM. The particle composition in the feed (see Figure 4.88 (a)) did not differ much from that of the filtrate (see Figure 4.88 (b)). A closer look to the images taken of the filtrate revealed that no particles larger than about 25 nm could be found. However, gold particles were observed to pass in high number. Au and Mn were also detected by SEM-EDX on the the back side of the membrane facing the efflux during the filtration (see appendix, Section 7). Once again, the gold NPs behaved inconclusive. A reason for the passing could be found in interactions with other particles.

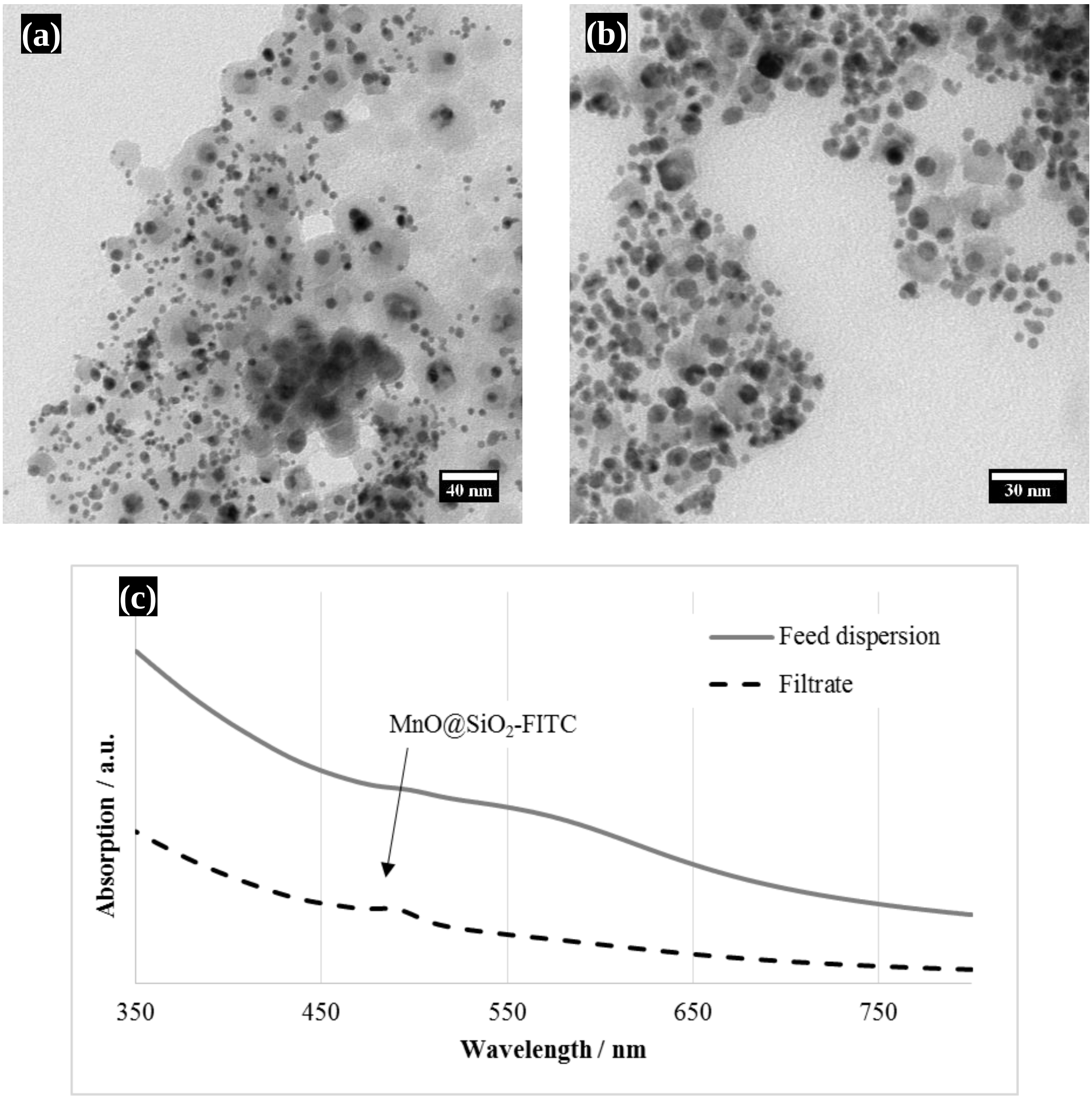

Figure 4.88: Filtration experiment of “worst case” NP mixture: TEM images of NP composition (a) before and (b) after the filtration, and (c) absorption spectra of feed NP dispersion and filtrate. TEM images were taken by [redacted].

The corresponding absorption spectra in turn did not facilitate the interpretation of the filtration test (see Figure 4.88 (c)). In the filtrate, the absorption of gold particles with maximum at about 500 – 550 nm (see Figure 4.85) was strongly reduced as well as the absorption of the Au@MnO@SiO$_2$ NPs with a maximum at 570 – 575 nm. The absorption band of the FITC labeled MnO@SiO$_2$ particles at about 495 nm was in contrast better resolved compared to the mixture.

The aforementioned Fe$_3$O$_4$@SiO$_2$-FITC nanoparticles of 14 nm diameter by TEM showed a low mobility in former filtration experiments (see Figure 4.83). Two more distinctive 2-component mixtures were created containing this particle type. In a first filtration experiment, separation from very large particles of the same type, but labeled with the dye rhodamine-B-isothiocyanate (RITC, see Figure 4.89 (a), Fe$_3$O$_4$@SiO$_2$-RITC was examined.[a]

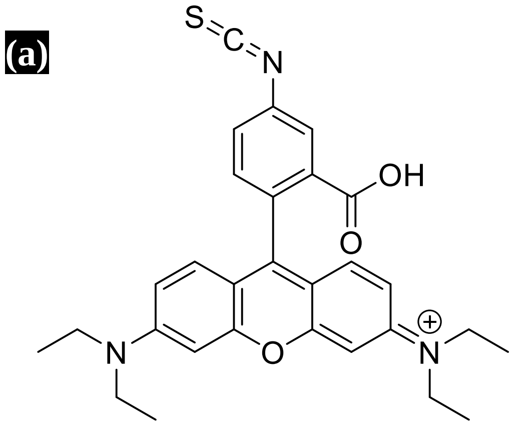

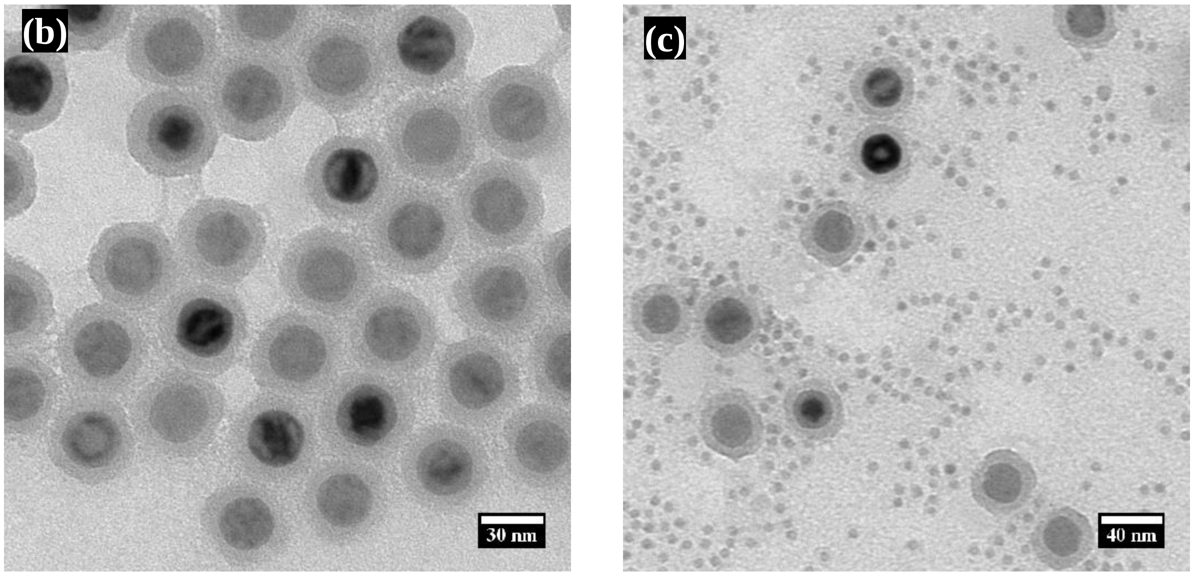

Figure 4.89: (a) Structural formula of RITC, (b) TEM image of Fe$_3$O$_4$@SiO$_2$-RITC NPs of 42 nm diameter (by TEM), and (c) TEM image of Fe$_3$O$_4$@SiO$_2$-RITC NPs in a mixture with much smaller Fe$_3$O$_4$@SiO$_2$-FITC NPs of 14 nm.

---

[a] Synthesis according to Schladt *et al.*[166] and dynamic light scattering data by [redacted].

The particles were measured by TEM to have a diameter of 42 nm (see Figure 4.89 (b, c)). Dynamic light scattering yielded 48 nm as dynamic diameter, which should not allow an effective passing. In a second filtration experiment, a mixture with small silica nanoparticles, proved to pass the channels (see Figure 4.81), was applied.

Filtration of the first mixture of Fe_3O_4@SiO_2-FITC and Fe_3O_4@SiO_2-RITC resulted in a colorless filtrate. The corresponding absorption spectrum showed only a minimum signal of the smaller component. Consequentially, particles were found to be concentrated in front of the filter, but the absent staining did not suggest a blocking of the filter by the larger particles.

However, the filtrate of the second mixture with small silica nanoparticles showed a considerable absorption for both species and a recovering of the FITC-component of about 50 % (see Figure 4.90).

Any quantitative evaluation of the silica particles with absorption maximum at about 330 nm was not possible due to the overlap with absorption of Fe_3O_4. The comparably high share of Fe_3O_4@SiO_2-FITC particles in the filtrate of the second with respect to the first mixture points to considerable interactions between the particles. It was evident that big and slow particles in a mixture will reduce the permeation of smaller particles. The other way around, it might be that small and fast particles carry bigger particles along. However, this suggestion has to be substantiated by further filtration experiments.

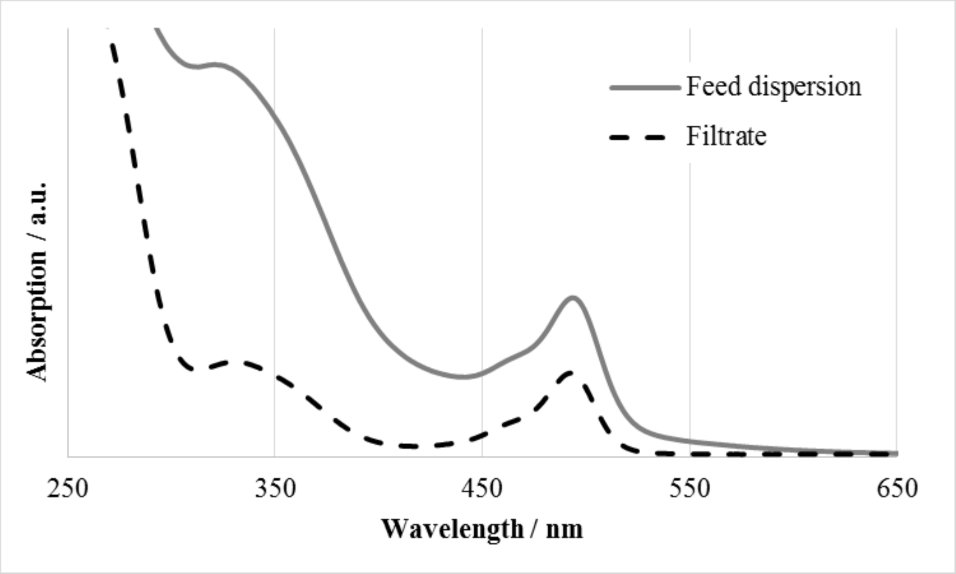

Figure 4.90: Absorption spectra a mixture of Fe_3O_4@SiO_2-FITC NPs with small silica NPs before and after the filtration experiment.

The filtrations presented could not bring evidence to all applied nanoparticle species, yet. Particles being too large in size were reliably prevented from passing the pores. Therefore, proving of the membrane's intactness over the whole area could be demonstrated. Obviously, the surface chemistry of channel walls and nanoparticles played an important role for the permeability. In particular, surface charges of AAO as well as nanoparticles seemed to have a great impact on retention, adsorption, or passing of the NPs. An accurate pH control could influence the permeability too. However, the size of the particles often seemed to be subordinate. Regarding all aspects, more experiments have to be designed in future works to illuminate the main decisive factors.

Two more separation concepts shall be shortly introduced that do not use a pressure gradient as driving force, the filtration of nanoparticles by magnetic forces and the separation of charged nanoparticles by the electroosmotic effect. Stephens *et al.* analyzed the diffusion of $CoFe_2O_4$ nanoparticles through AAO membranes and found that applied magnetic fluxes increased the rate of larger particles with respect to smaller particles.[172] Toh and Coworkers sputtered platinum electrodes directly onto both sides of AAO membranes and used the electroosmotic approach to transport proteins, but also citrate-capped Au nanoparticles. By the help of an additional pumping it was possible to combine electrophoresis and membrane separation technique.[173,174] Figure 4.91 shows settings how both approaches could be realized in future experiments.

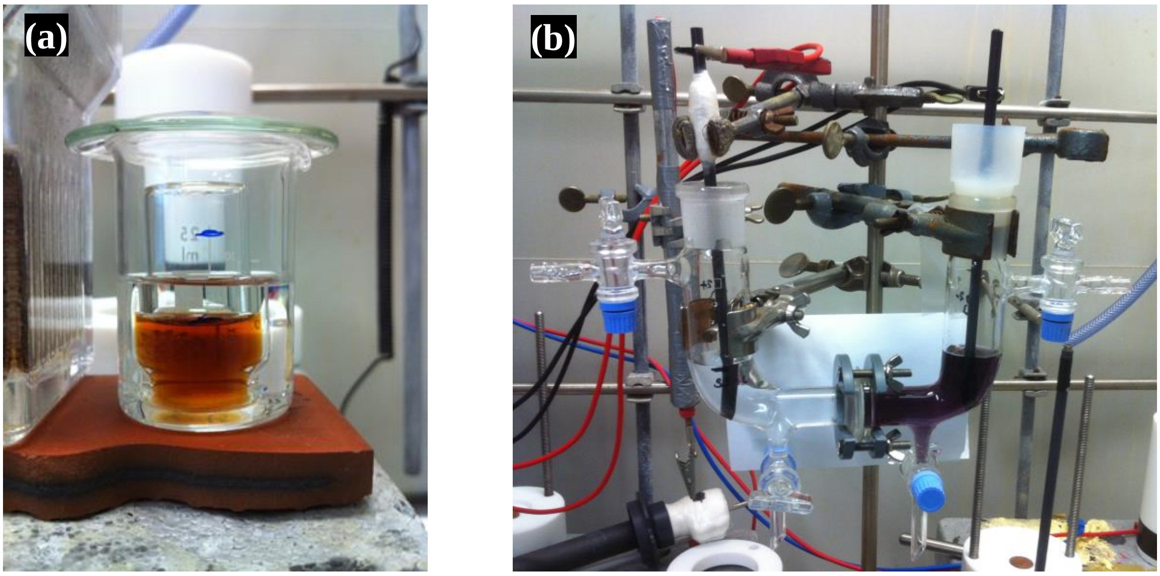

Figure 4.91: Photographs showing approaches for (a) a filtration of nanoparticles by magnetic forces and (b) a filtration of charged nanoparticles by the electroosmotic effect.

On the one hand, the diffusion of magnetic Fe_3O_4 NPs along an applied magnetic field, out of a container that is sealed by the AAO membrane, could be studied. On the other hand, an U-shaped tube with an AAO membrane inserted could be used.

An applied potential by two external electrodes could induce e.g. the previously described Au citrate nanoparticles to pass the membrane.

4.8.5 Concepts for an Intrinsic Stabilization of AAO Filtration Membranes

As demonstrated in the previous chapter, the application as filter could proof the capability of the synthesized AAO discs as separation membranes. However, several drawbacks should not be concealed. To withstand higher pressures, membranes of some ten micrometers thickness were chosen. For efficient and fast bioseparation (see Chapter 1.3), a thickness of below ten micrometers was intendeded to enhance the flow rate. Large area filter membranes would have a need for a stabilization of the brittle AAO material. The aluminum grid used for this purpose was rather intricate, in particular with the sealing, and reduced the active filter surface strongly.

Without this extra device, maybe progress towards more comfortable flat sealings instead of adhesives could be considered. The commercial Anopore™ membranes are also available with supporting plastic ring fixed around the membranes, which eases the handling. It was examined if the aluminum ring could work the same way, since it remained anyway after the anodization. Compared to the multi-step synthesis summed up in Figure 4.67, a change in the DisA step had to be made. Therefore, after the PO step, the anodized foil was removed from the setup, upturned, and remounted in the Cu-block Setup. Its PTFE vessel was now used as a container for the HCl/Cu^{2+}-solution and the sealing protected the aluminum ring from being dissolved.

The result was a round window, the “glass” being from the aluminum oxide and with a frame of aluminum. However, the cohesion of the two components was poor and the AAO very easily broke out of the frame. Possible reasons were either the modified dissolution process or a particular weak connection between the aluminum and the anodic oxide. In order to prevent the latter, PO and DisA were performed in a PTFE vessel with smaller aperture size compared to the one used for the anodization. This allowed a continuous transition from unsupported to supported oxide and the composite was stabilized. However, the active size of the filter was reduced (see Figure 4.92).

Figure 4.92: Photograph of a broken AAO window in its Al frame, produced by a modified DisA procedure.

Alternatively, an intrinsic stabilizing structure could provide an improved strength against pressure. There are different techniques imaginable how areas of the aluminum foil could be protected against the anodization reaction, leaving a metallic stabilization behind. Thormann *et al.* had the idea of mechanically pre-structuring the aluminum foil before the anodization. This resulted in a grid structure in the aluminum that was thicker compared to the parts subjected to anodization.[175] However, the approach had several drawbacks. The requirement of a thermomechanical stamping with 10 kN at 200 °C was a restriction also in terms of foil sizes possible in the used press. Additional lithographic techniques were inevitable to selectively dissolve the aluminum in the anodized area. Finally, to open the pores, a chemical etching step with phosphoric acid was necessary that was known to cause trouble (see Chapter 4.5.1).

For this reason, simplifying changes to the approach were devised. Figure 4.93 illustrates considerations for the different steps necessary to achieve an intrinsic stabilization by metal leavings.

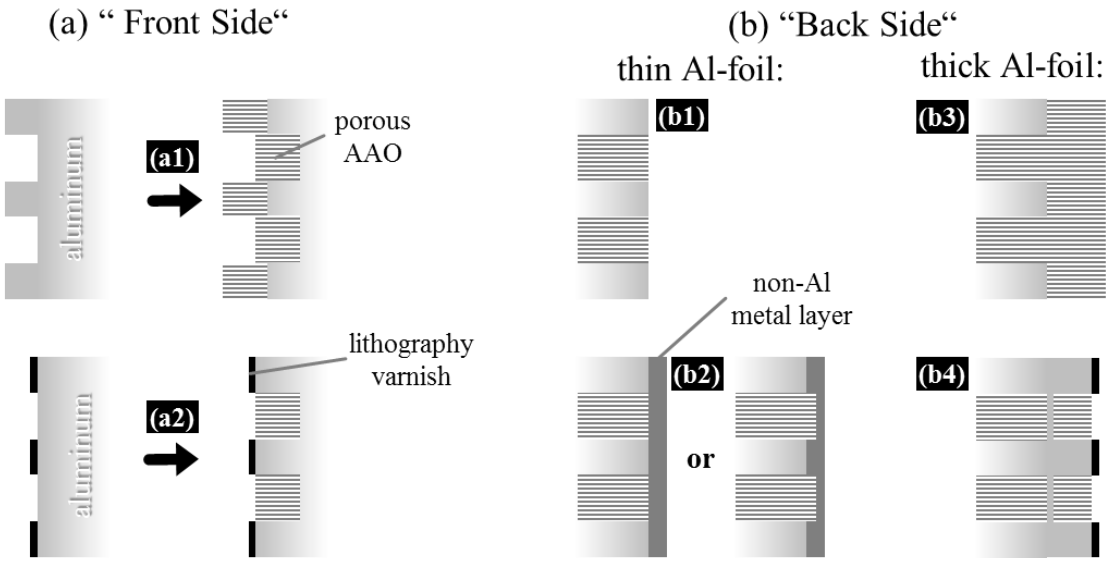

Figure 4.93: Schematic view of considerations to achieve an intrinsic stabilization by metal leavings: (a) Preservation of aluminum in certain areas while anodizing to form a stabilizing grid and (b) variations in the pore opening (PO) and aluminum dissolution step (DisA).

First, the aluminum had to be preserved in certain areas to form a stabilizing grid. Two approaches were considered for that purpose (see Figure 4.93 (a)): A more simple stamping process for the foils had to be developed (a1), or photolithographic or similar techniques to protect selected areas from anodization had to be used (a2). On the one hand, a macroscopic embossing as a one-step-procedure could have the advantage to be applied only once before cutting the metal foil into single discs. The photolithography, on the other hand, is a technique proven to work. However, this extra pretreatment would be laborious with regard to coating the foils with varnish, exposing them to UV light, and partial dissolving the varnish in developer solution.

Second, the difficulty of performing the pore opening and aluminum dissolution process without losing the stabilizing metal was considered (see Figure 4.93 (b)). Using a very thin aluminum foil as starting material, one could prefer a total anodic oxidation of the foil in the thinner or uncovered, respectively, areas (b1). However, miscarried experiments had shown that a total anodization would not support any pore opening approaches. Even though the AAO layers macroscopically did not exhibit any damage, the formed pores did not open on the back side and defect structures were observed (see Figure 4.94). Moreover, a homogeneous anodization was impossible due to a drop in the reaction rate as soon as the first breakthroughs appeared. Nonuniform metal foil thickness, e.g. caused by the electropolishing procedure, or an inhomogeneous electrochemical reaction prevented a simultaneous termination of the reaction in the exposed area.

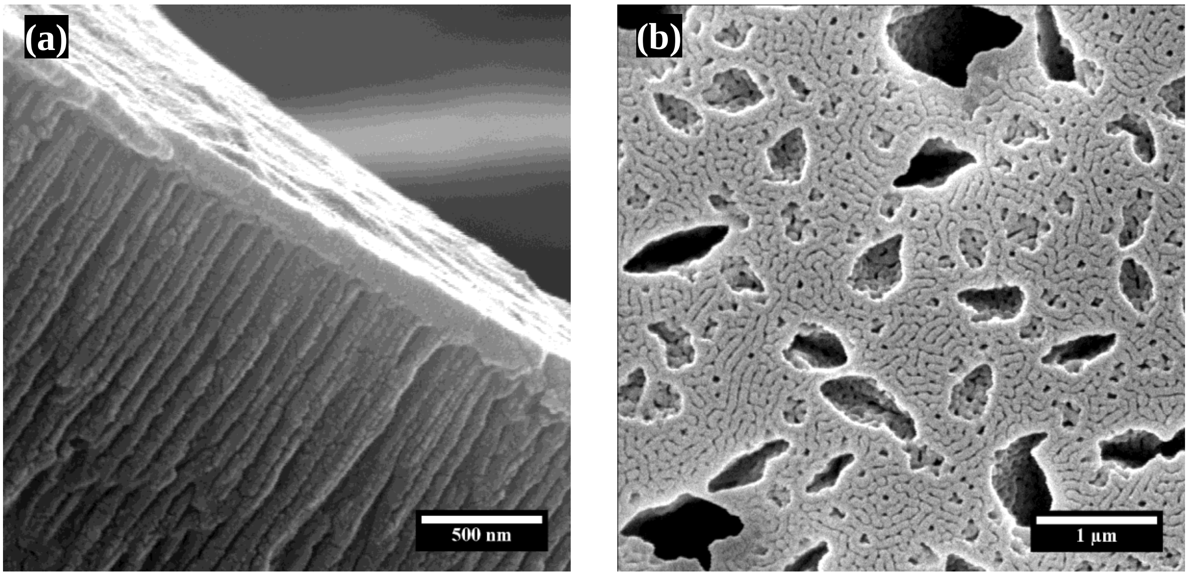

Figure 4.94: SEM images of completely anodized metal foils: (a) cross-sectional view of a massive terminating barrier layer at the back side and (b) frequent defects found thereon.

Further opportunities could be provided by an extra layer of a metal brought to the backside of a thin aluminum foil (b2). This metal could be chosen to be inert against the anodization in oxalic acid electrolyte. It is possible that the barrier layer is preferentially attacked by the strong electrical field where the growing pores touch the inert metal. A total anodization would lead to opened pores if the second metal could be selectively removed after the anodization. Another consideration traces back to Schmuki and Coworkes who found a method to stabilize ATO layers: Bimetals from titanium and aluminum were used, taking advantage of the fact that both metals are able to form pores in fluoride containing electrolyte. After the anodization of the titanium up to the aluminum layer, the aluminum was dissolved, and the ATO membrane remained without an additional pore opening step necessary.[100] The other way around, titanium cannot be used to form stabilized AAO, but tin for example is known to form porous structures in oxalic acid too.[24]

Considerations that do not require bimetals imply lithographical techniques to protect Al foils from anodization. The area selective anodization is stopped after reaching the preferred oxide layer thickness and an electrochemical PO step has to be performed. Dissolution of the aluminum exclusively from the back side, or alternatively, a controlled counter-anodization to consume the Al base, would yield a stabilized membrane (b3). The counter-anodization even could have a destructive influence on the barrier layer of the actual AAO, resulting in a pore opening. The last, most complicated option had to be tested if the methods described would require a spatially resolved control. Counter-anodization or dissolution of the aluminum from the backside only, opposite to the anodized areas, would require even a further lithographic step (b4).

In the following, some intermediate results are documented. First, the feasibility of methods described in Figure 4.93 (a) was examined. In order to keep the approach technically more simple, only a single anodic oxidation was performed. Trials to emboss aluminum without an extra thermal treatment were satisfying. Instead of a designed stamp, a grid from steel was used to test the practice. Deformation caused by a simple hydraulic press led to thicker and thinner parts. However, subsequent electropolishing of stamped foils led to holes and an inhomogeneous surface. A further disadvantage of the stamping was distortion of the metal that led to a corrugated surface not suitable for an anodization of good quality. Figure 4.95 shows survey SEM images of a stamped but non-polished foil, which was completely anodized until its thinnest parts became transparent.

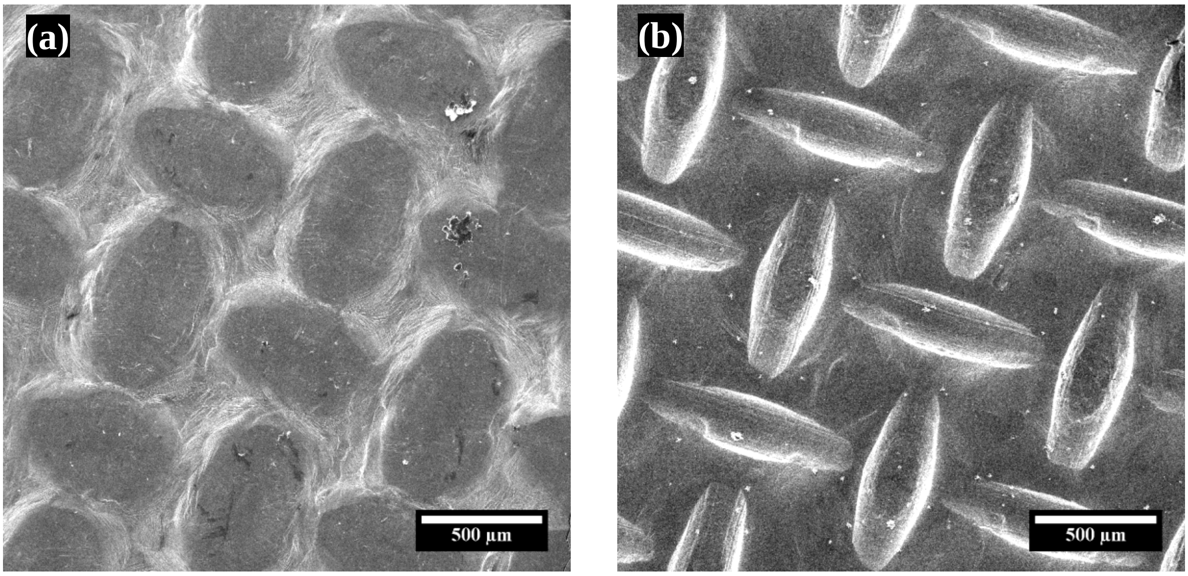

Figure 4.95: Survey SEM images of a stamped but non-polished foil, which was completely anodized until its thinnest parts became transparent: (a) front side and (b) back side.

Figure 4.96: Photograph of a photolithographic pattern on a titanium surface, visualized by different wetting behavior.

Consequently, the photolithographic approach following the method of Schmuki and Coworkers was tested. For a start, polished titanium foils and the positive photoresist system described there were tested. Spincoating of the varnish, UV light exposition, using the hexagonal Al grid pictured in Figure 4.71 (c), curing, and development had to be balanced carefully to give a result as shown in Figure 4.96.[a] The arranged water drops clearly show the unprotected areas.

Unfortunately, the results could not be transferred to the aluminum system yet. The developer for the UV-treated varnish were basic and attacked the aluminum itself. Moreover, even the varnish seemed not to be stable enough for the anodization in acidic electrolyte. Thormann *et al.* used an alternative photolithography system for the work with AAO.[175] Beyond that, a third approach was found to have a certain potential: Perforated adhesive foil to transform windows, e.g. of buses, in semi-transparent advertising space, sticked well to the

---

[a] Photolithography was performed by [redacted].

polished aluminum if hydraulically pressed on. Anodization or electrochemical pore opening did not harm and the foil could be removed easily in organic solvents.

However, more decisive for the successful development of an intrinsic stabilization strategy is the control of the PO and DisA step (see Figure 4.93 (b)). In a first step, extra thin Al foil of 25 µm was used and sputtered with a 50 nm layer of gold. It should be evaluated how the anodic oxide would behave when the electrochemical reaction came to a halt at the noble metal layer. However, when completely anodizing the thin Al foil, the forces were so strong that the whole disc was perforated and broke as soon as the Au layer was reached.

An extra layer of tin, which would take part in the anodization reaction, seemed to be more promising. But sputtering or evaporation of Sn turned out to be ambitious with conventional lab devices. Assemblies of polished aluminum foil and molten Sn did not form because of separative oxide layers.

Hence, it was analyzed how remaining aluminum could be selectively disposed without attacking a grid structure formed in an anodization process (see Figure 4.93 (a)). Using a protection step, and no embossing, a combination with the standard PO process would be possible. After a selective anodization and PO, performed with the described perforated foil, the DisA process was applied from the back side only (analogous to the AAO "windows" presented in Figure 4.92). Even though the reaction with HCl/Cu^{2+}-solution was slow, the result was inhomogeneous and it was not possible to preserve an Al grid structure.

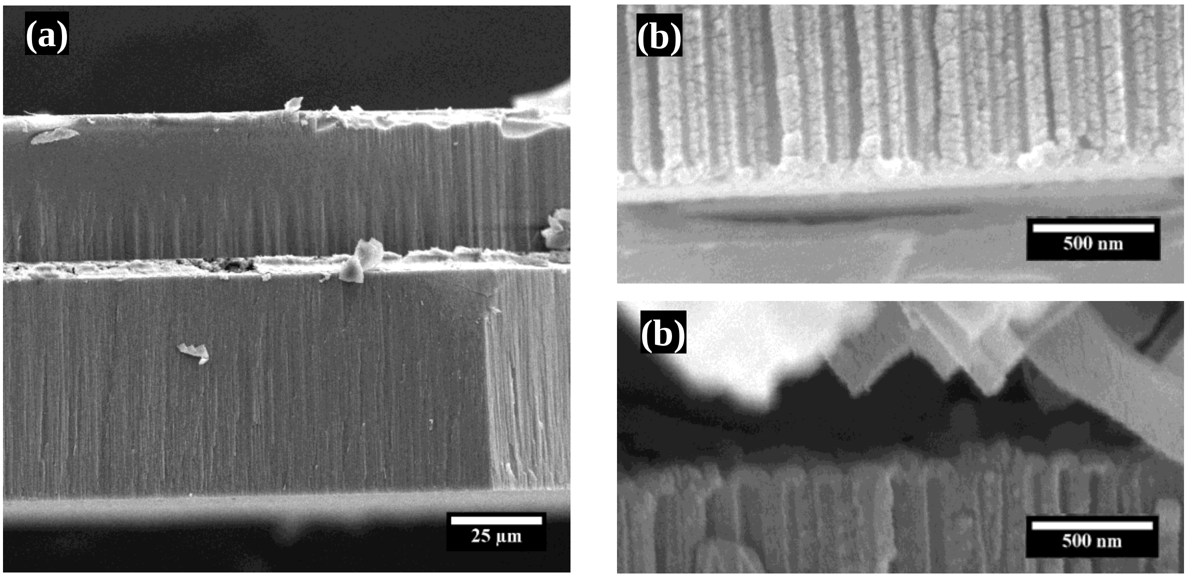

Figure 4.97: SEM cross-sectional images showing an Al foil completely anodized from both sides: (a) layer of aluminum left between the AAO layers and (b) intact barrier layers.

Alternatively, a counter anodization process was tested to replace the dissolution process. A drop in the current flow should indicate the achievement of the zone already anodized. However, large areas with aluminum metal between the two AAO layers remained (see Figure 4.97).

In summary, the tests were not successful yet and investigations concerning a more constant dissolution of the remaining aluminum would be reasonable. However, the use of an Al-Sn-bimetal is considered the most promising approach. Further technical approaches to form large-area bilayers should be explored.

4.8.6 Efficiency and Cost Aspects in the Membrane Production Process

The whole membrane production process shows a high level of productivity. One important factor is the professional electrochemical setup used (detailed description in Chapter 6.1.2). All processes, as there are electropolishing (E), anodizations (A1, A2), and electrochemical pore opening (PO), can be performed therein. The possibility of exchanging the PTFE vessels offers the possibility of variable AAO disc sizes (see Chapter 4.8.3) up to 30 mm in diameter. Even a further upscaling should be possible. The use of stirring cathodes is an elegant solution to guarantee a perfect agitation between the two electrodes.

Cost-efficiency is a further aspect of successful production processes, in particular with regard to the projected application. With the replacement of the commercial high-speed electrode by remodeled laboratory stirrers (see Chapter 6.1.2, the costs of the stirring electrodes are even lower compared to conventional magnetic stirrers. A further idea to increase the number of parallel production stations in “low cost style” was to convert a conventional bench drilling machine into a stirring electrode (see Figure 4.98 (a)), likewise to the laboratory stirrers. The bench drilling machine ran the same speed as the laboratory stirrers and gave comparable results for the performed anodizations (see Figure 4.98 (b)).

The thermostat used for the anodizations controlled the reaction temperature in multiple setups via parallel connection of the cooling coils. Because the reactions were performed at elevated room temperature, the general performance of the thermostat had to be low, even though the used device was very powerful. Fast oxide growth, induced by the comparably high reaction temperature, reduces the reaction period and in the process the power consumption for cooling too.[105] The exact anodization temperature is not a crucial condition for the determination of the free pore diameter of the produced filtration membranes. Therefore, even the abdication of the temperature control could be discussed.

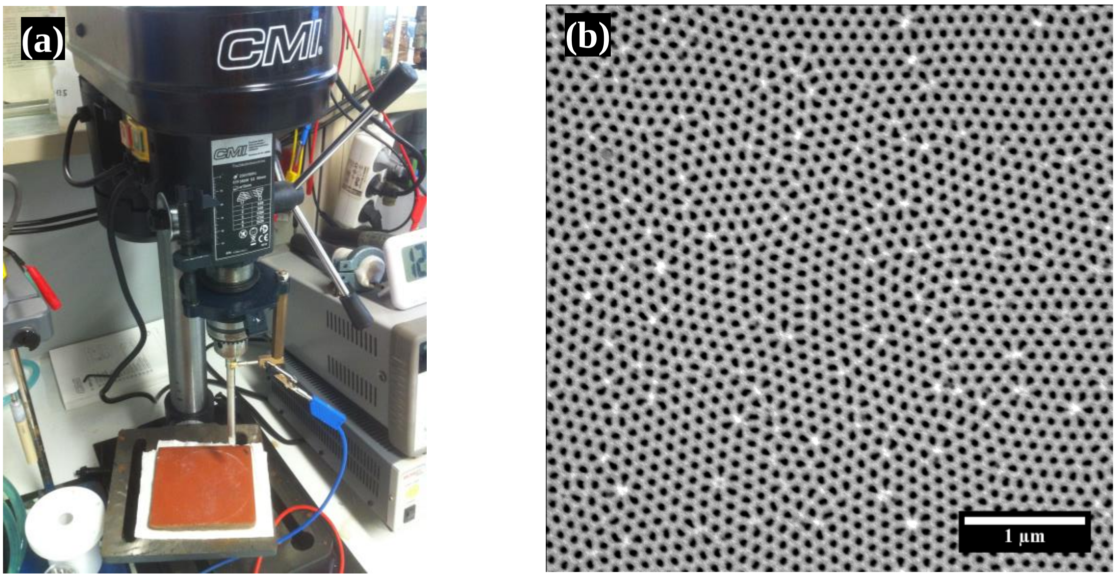

Figure 4.98: Use of a bench drilling machine as stirring electrode: (a) Photograph of the converted bench drilling machine and (b) SEM image of an AAO (50 V, 2 h) self-supporting membrane, with typical pore size of 55 nm, produced with the bench drilling machine.

The relatively high reaction temperature and the selection of the different production steps increased the speed of the described process (see Table 5). Regarding the whole multistep process, only some working hours were necessary to yield the final product.

Table 5: Process time for the single production steps to form AAO filtration membranes.

Production steps	Process time
Cutting and pressing of foils	negligible
Electropolishing (E)	few minutes
1st anodization (A1)	mostly 45 – 75 min (net 30 – 60 min)
Oxide dissolution (DisO)	typically 180 min; reduction to about 60 min possible (compare Chapter 4.5.5)
2nd anodization (A2)	typically 135 min (net 120 min), corresponding to the desired membrane thickness
Pore opening (PO)	few minutes
Dissolution of aluminum (DisA)	few minutes
Pore Widening (PoWi)	60 – 120 min, depending on the desired pore size

As a disadvantage, toxic heavy metals were used in the dissolution processes. However, the used copper chloride is a better choice compared to the alternate mercury chloride. The chromic solution could be reused many times without degradation. Even though the final membrane was not subjected to intense cleaning procedures, cell growth on the material was possible without constrictions (see Chapter 4.8.1.1).

Most important cost driver is the aluminum foil used. For the as-prepared AAO membranes, foil of highest purity, 99.997 %, with a cost of approximately 2 € per standard size, was used. Purities of 99.99 % are common in most research studies. More impure foils are reported to go along with low quality AAO. Pore size and pore size distribution become lower even if the metal foils were annealed prior to the anodization.[112] Using a pulsing technique, acceptable results are reported for foil of 99 % purity as raw material.[176] However, the method is time consuming because of pulse-off periods.

To evaluate the specific influence of the metal foil purity on our AAO result, anodizations with less pure foils of 99.99 % and 99.8 % were performed. Both foils showed comparably good results after electropolishing and behaved similar concerning current flow and oxide growth rate. Figure 4.99 shows the results of an anodization at 50 V for 2 h with the 99.99 % foil as raw material. The pore size was 45 – 50 nm at the front and about 40 nm at the back side. The oxide layer thickness was about 45 µm. The values are in line with the previously reported, even the order of the pores was nearly equal

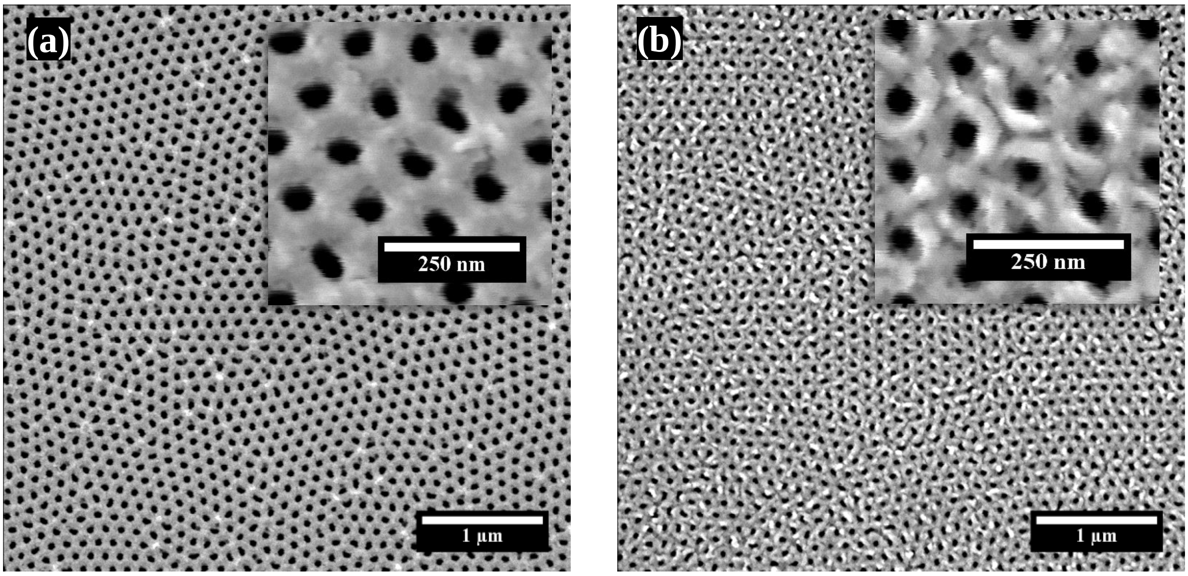

Figure 4.99: SEM images of AAO membrane (50 V, 2 h) by anodization of Al 99.99 % foil: (a) front side and (b) back side. The insets show images of higher magnification.

The examination of the foil of 99.8 % purity as raw material was more intricate because the maximum thickness commercially available was only 50 µm. The anodization period was reduced, but often holes appeared at the edges of the oxidized areas, disturbing the subsequent PO process. Figure 4.100 shows the result of an anodization at 50 V for 1.5 h with pore sizes of 45 nm at the front and about 35 nm at the back side. The PO process was not perfectly conducted, probably due to the mentioned holes.

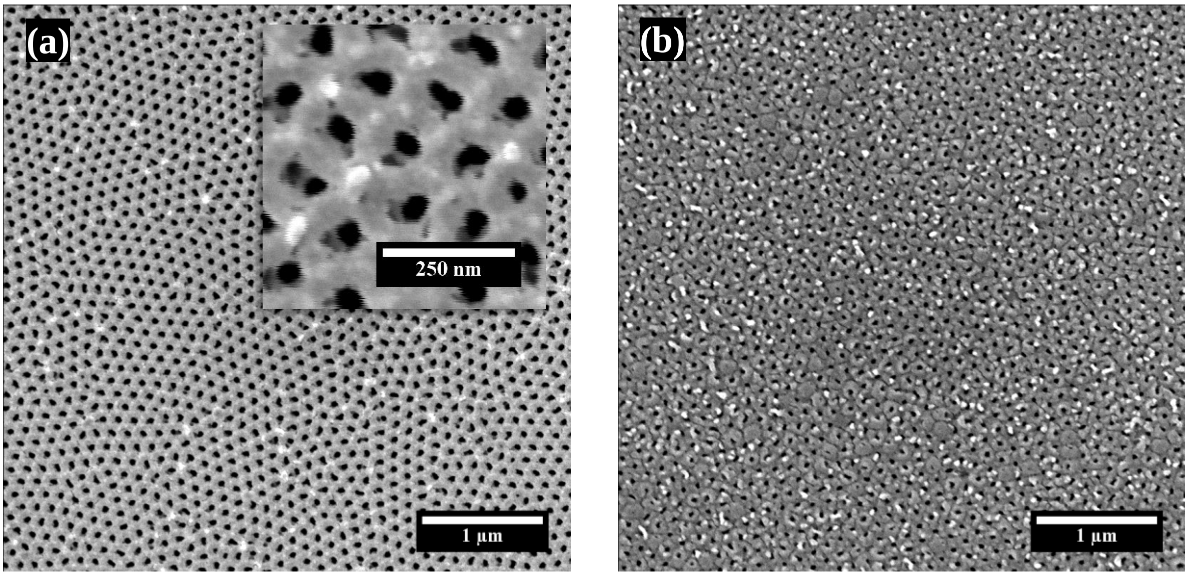

Figure 4.100: SEM images of AAO membrane (50 V, 1.5 h) by anodization of Al 99.8 % foil: (a) front side and (b) back side. The inset shows an image of higher magnification.

The pore diameter at the front side appeared to be smaller as expected and the pore entrances were lacerated (see Figure 4.100 (a)) However, pore order and pore size distribution was acceptable and the membranes were mechanically robust. The results showed that the purity of the aluminum foils could be reduced down to 99.9 %, but in fact, differences in foil price were marginal.

In contrast, a foil with a purity of 99 %, providing a thickness of 0.25 mm, costs only 0.10 € for a standard sample size. However, this further decrease in purity already led to less smooth surfaces after electropolishing. Anodization at 40 V for 2 h resulted in the estimated pore size of 35 – 40 nm before the DisA step, but defects on the surface and twin-pore structures were numerous (see Figure 4.101).

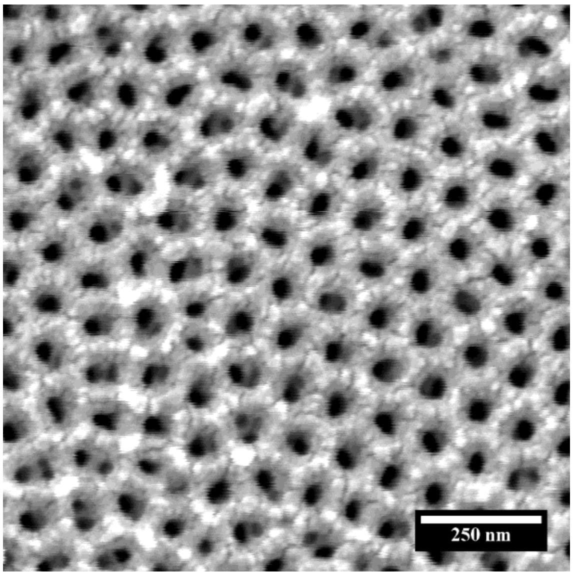

Figure 4.101: SEM image of AAO front side (40 V, 2 h, A2) before PO/DisA by anodization of Al 99 % foil.

Dissolution of the aluminum led to a remarkable widening at the front side. Pore sizes were enlarged to 60 – 65 nm and in some areas, nano grass formation became visible (see Figure 4.102).

The lower purity of the aluminum resulted in a much faster dissolution in the HCl/Cu^{2+}-solution. This generated a high amount of heat and was responsible for the degradation. Therefore, the concentration of the solution was reduced to slow down the dissolution reaction. Nano grass could be avoided, but the defects in the structure remained. Figure 4.103 shows the frequency of these mostly polygonal holes in the structured oxide. The holes were distributed in and over the whole material and were probably a result of metal inhomogeneity in the foil. Not only the defects made the result inappropriate, but also the low pore size distribution and especially the non-parallel, diagonal channels obvious in the cross-sectional studies (see Figure 4.103 (c, d)). Annealing of the impure foils before polishing and anodization did not result in even the slightest improvement of the results. Because attempts with different foils of 99.5 % failed in equal measure, a minimum purity of about 99.9 % can be specified as the lowest purity necessary.

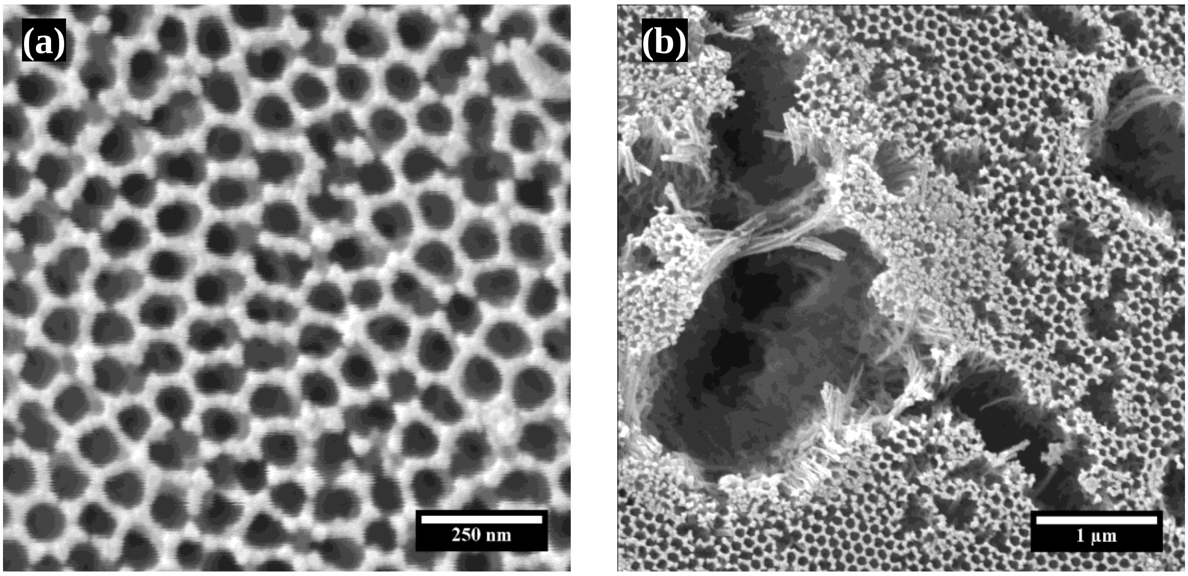

Figure 4.102: SEM images of AAO membrane (40 V, 2 h) by anodization of Al 99 % foil after the DisA process: (a) front side showing widened pores and (b) nano grass formation.

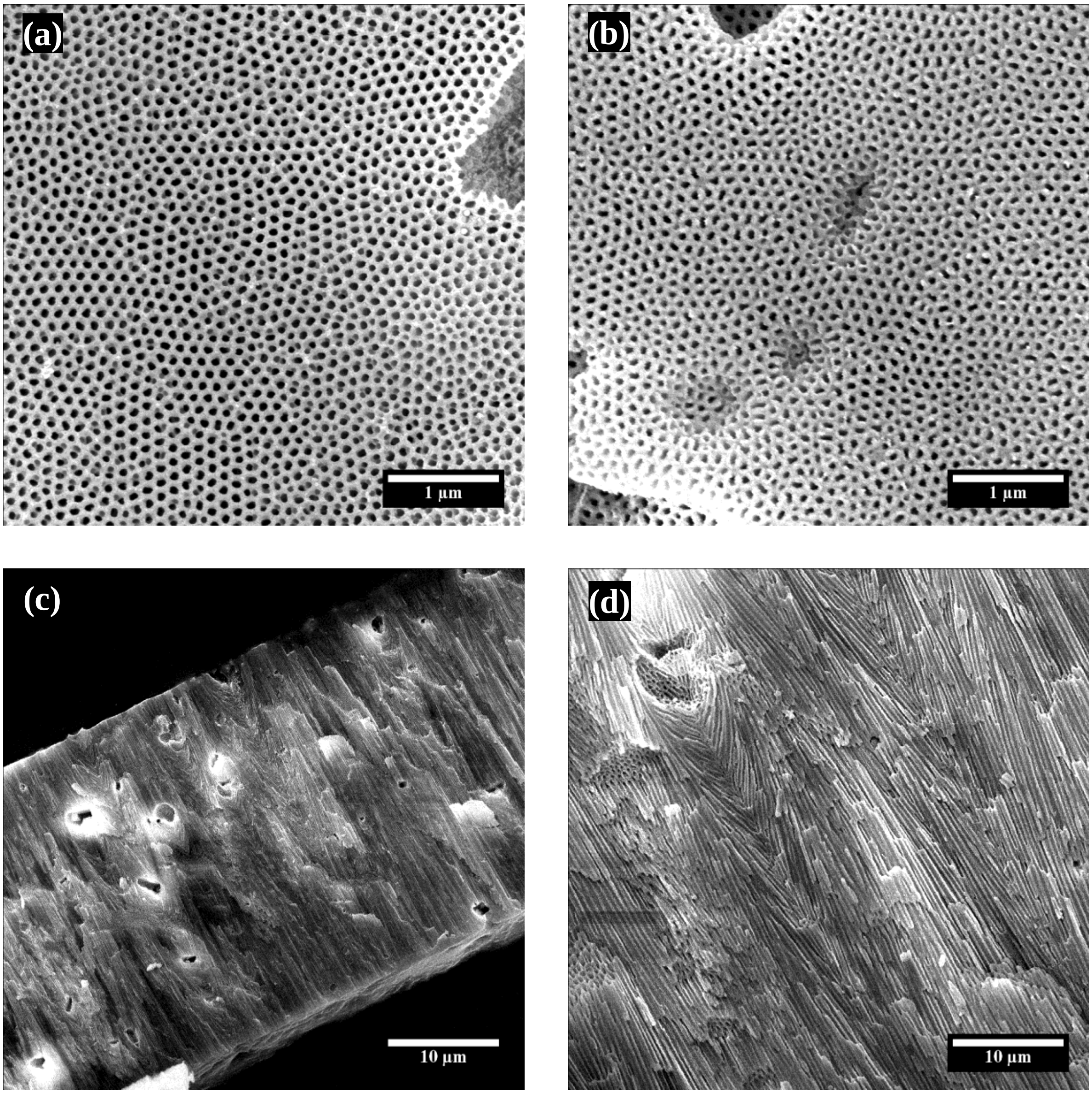

Figure 4.103: SEM images of AAO membrane (50 V, 2 h) by anodization of Al 99 % foil and DisA process in diluted HCl/Cu^{2+}-solution showing defect structures: (a) front side with superstructures and polygonal defects, (b) back side, (c) cross-sectional view showing holes in the material too, and (d) cross-sectional view showing diagonal channels along dislocations.

4.9 Conclusions and Outlook

The scope of this work was to develop a reliable and efficient synthesis protocol for the production of AAO membranes for potential filtration applications. Although AAO membranes were already known, the challenge lay in meeting the target filtration properties: thin, but mechanically stable and self-supporting, uniform across a rather large area, and highly porous with a narrow pore size distribution. Additionally, the known protocols had to be adapted to the specific electrochemical equipment.

This work first describes a holistic optimization of a complete, seven-step AAO synthesis protocol. The individual steps are, namely: the electropolishing, two anodization steps with an oxide dissolution step in between, a back side pore opening, selective dissolution of the Al metal backing, and a pore widening (see Figure 4.67). Numerous approaches for each step have been examined, and the most applicable have been combined for the final protocol. The principles, that were learned with titanium (ATO), were reapplied here. However, the electrochemical setups had to be redesigned. In particular, the need for agitation of the electrolyte was accommodated with an elegant technical solution: a homemade stirring electrode, which is, to our knowledge, unique in the anodic oxidation of aluminum.

In order to provide perfectly flat surfaces and promote the self-ordering of pores in AAO, aluminum foil was electropolished prior to the anodization using an alcoholic perchloric acid solution. Subsequently, a two-step anodization process was conducted to achieve a narrow pore size distribution. The chosen reaction temperatures of 25 or 35 °C exceeded those known in literature and enabled high growth rates of the oxide layer in the range of 10 to 30 µm/h. With excellent reaction control in the design of the setup and under the high growth rate, hexagonal pore ordering was found to be established earlier in the anodization. This increased the efficiency, allowing a reduced process time for the first anodization of one hour or less.

In the course of this work, the impact of an anodization voltage between 25 and 90 V on the pore diameter was analyzed in detail. Within the range of 30 – 50 V, excellent pore ordering was achieved. The surface pore diameters of about 30 to 50 nm were, in the limits of several hours, nearly independent of the reaction period. Below 35 V, the self-ordering forces were strongly decreased. Above 50 V, the AAO tended to develop superstructures, which had serious influence on the pore shape and size distribution.

The pore opening procedure was an intricate step in the synthesis route where large gains were achieved with this work. Commonly used wet chemical etching processes with H_3PO_4 or NaOH turned out to be inappropriate to open the pores without damaging the whole oxide membrane. Efforts to protect the susceptible front side from etching did not improve this process step: The barrier layer was insufficiently dissolved in one region, while collapsing of the pores had already started in another region. A solution to this problem was found by adapting a modified electrochemical pore opening process, which was superior to the conventional methods with regard to uniformity, reproducibility, and efficiency. A complete reaction was achieved after only a few seconds. Combined with subsequent dissolution of the

Al backing, this process delivered an oxide membrane with two very similar surfaces, where the pore sizes at the back side were only slightly smaller as compared to those on the front side.

In total, completely porous membranes of about 7 to 70 µm in thicknesses were produced without any sign of degradation, e.g. nano grass formation. The application of a subsequent pore widening step further increased the pore size and thus the porosity.

The shape of the pores through the oxide layer was an aspect, which was intensively studied for the first time in this work. This required sophisticated sample preparation for SEM analysis to image the cross-sections. Several processes in the synthesis route were identified to cause widening of the pore, across part or its whole length. The funnel-like front side pore opening was explained by the pattern left by the pre-anodization. The anodization temperature promoted chemical etching of the whole pore channel by the oxalic acid during the electrochemical reaction. Etching was more pronounced towards the front side and was amplified with rising temperature. Consequently, two different pore channel structures were produced: a rather cylindrical shape when anodizing at 25 °C and a conical shape, whose channel was slightly larger and narrowed toward the back side, when anodizing at 35 °C. In contrast to the pore opening procedure, which had no impact on the pore diameter, the exothermic dissolution of the aluminum induced a rather constant widening of about 5 nm along the pore channel. Subsequent pore widening by further etching amplified any inhomogeneity of the pore channels and was not found to compensate for inhomogeneous pore diameters resulting from the anodization.

The size of the back side pore was not impacted by variation of the anodization temperature, whereas the front side surface pores showed a significant widening due to chemical etching. However, the width of front side pore openings was secondary for applications as filters, because the back side pore diameter represented the bottle neck. The smallest diameter measured along the pore channel was the crucial parameter to determine the possible flow and capacity of the membrane.

Future projects should further examine ways to create perfectly cylindrical pores. The high impact of the reaction temperature on the asymmetry might be counteracted when a temperature gradient is applied, e.g. by heating the metal foil by means of the Cu block of the setup, and simultaneously cooling the electrolyte.

In preparation for filtration applications, the load capacity of as-prepared AAO membranes was analyzed in hydrostatic tests. Discs of about 50 µm thickness withstood a pressure of

1 bar without breaking when a free area of 1.3 cm^2 was exposed. By redesign of the electrochemical setup, an up-scaling of the circular filtration membranes from typically 2 cm^2 (16 mm diameter) to an area of 7 cm^2 was demonstrated.

Filtration with nanoparticle dispersions was performed with membranes of about 65 µm thickness and a minimum pore size of 55 nm. Small silica nanoparticles of < 5 nm passed through the membranes unhindered, while larger, silica-coated core shell particles showed a reduced concentration in the filtrate. Here, exclusion of particle sizes greater than about 25 nm, measured by TEM, was observed. Smaller particles bearing an anionic charge, however, showed a high retention by the positivistic AAO membrane. Hence, the surface chemistry of channel walls and nanoparticles could be used to achieve a selective permeability.

In future experiments, the main decisive factors for permeability will have to be further elucidated. Tests with hydrophobically-functionalized membranes could give valuable information. Moreover, the potential of the membranes in separation methods without pressure gradient as the driving force, e.g. the filtration of nanoparticles by magnetic forces and the separation of charged nanoparticles by the electroosmotic effect, should be investigated.

Concepts to provide an intrinsic stabilization of the membrane against higher pressure were discussed, and first approaches have been presented in this work. In this context, Al-Sn-bimetals are proposed as a promising substrate for anodizations and are an avenue for membrane synthesis, making pore opening procedures obsolete.

5 Anodization of Vanadium

5.1 Introduction

Vanadium is a further metal numbered among the valve metals, but forms, in contrast to titanium and aluminum, more than one stable oxide. Its variable oxidation states show unique properties, which make them suitable for diverse applications.

For instance, V_2O_3 has a metal-insulator transition at 160 K, whereas the tetravalent VO_2 was observed to have a semiconductor-metal transition at 340 K.[177] Moreover, VO_2 shows metal-insulator transitions if present in a disordered state.[178] V_2O_5 is for various reasons of interest for photovoltaics: It is a good conductor with a band gap of 2.8 eV,[179] exhibits a photovoltaic effect,[180] and it could already be used as hole conducting material in inverted tandem solar cells.[181]

Vanadium oxides are, due to their chemical and mechanical stability, widely used as catalysts for many industrially important reactions: oxidation of sulfur dioxide to SO_3 or methanol to formaldehyde, selective reduction of nitric oxide, or partial oxidation of hydrocarbons, e.g. *o*-xylene to phtalic anhydride, and n-butane to maleic anhydride.[182–186]

As a matter of course, nano-structured vanadium oxides show their best performance as soon as surface reactions are considered. All kinds of nanoarchitectures, especially nanoparticles, wires, and thin films were investigated in applications such as supercapacitors,[187] photocatalysis,[188] electrochromics,[189] light detectors and temperature sensors,[184,190] and chemical sensors.[191,192] Vanadium oxide is suitable as an anode material for lithium ion batteries,[193,194] where the nano-sized surfaces provide higher power densities and shorter lithium diffusion lengths compared to bulk material.[195]

Numerous techniques to yield vanadium oxide in nano dimensions are established, notably hydrothermal-,[196] surfactant-,[197] sol-gel-,[198] or template-assisted synthesis.[199]

A couple of serious drawbacks to the described techniques are that high temperatures are often necessary and multiple step procedures have to be performed. In contrast, an electrochemical approach by anodization would represent not only a simple and low-temperature approach, but would also grant access to ordered arrays of vanadium oxide nanotubes instead of randomly oriented assemblies.

Vanadium meets the requirements of a valve metal in general, but its oxides are unfortunately soluble in most commonly used electrolytes.[200,201] When vanadium is anodized in an aqueous solution, the vanadium oxide film tends to dissolve in the solution as vanadyl ions.[202–204] This might have been the reason that numerous past attempts failed to anodically grow V_2O_5 nanotubes or ordered porous layers.[202,205,206]

Recently, Schmuki and coworkers succeeded first with the anodization of titanium-vanadium alloys, yielding an ordered array of V_2O_5-TiO_2 nanotubes.[207] The key to their success was the modification of experimental parameters used for the electrochemical synthesis of porous titanium oxide.

Shortly after, reliable results in anodizing bare vanadium metal foils were presented by the same work group, proving the general feasibility for the synthesis of ordered vanadium oxide nanostructures by anodization. The selected electrolyte and other experimental parameters used for the electrochemical synthesis derived again from the ones utilized for the anodization of pure titanium metal. The problem of the mentioned instability of vanadium oxide in any water-containing electrolyte was apparently overcome using complex fluoride electrolytes such as $[BF_4]^-$ or $[TiF_6]^{2-}$. Thereby extra HF had to be added to get the desired nanoporous result. In addition, many other typical electrolytes known to form oxide nanotubes when used with other transition metals were tested, but failed.[34]

Subsequently, the as-produced nanoporous anodic vanadium oxide (AVO) layers were demonstrated to possess lithium-ion intercalation properties and to show electrochromism.[208] Furthermore, its use in several oxidation reactions was proved: oxidative deprotection of acetals, oxidation of alcohols to ketones, C-H-oxidation of ethyl benzene, oxidative esterification of aldehydes, oxidative deprotection of dithianes.[209]

In our group, we followed a different pathway to electrochemically anodize vanadium foils using much simpler and non-hazardous agents. The approach was inspired by earlier investigations into how compact oxide layers can be formed on vanadium: It was observed that vanadium oxides did not dissolve in electrolytes composed of acetic acid, small amounts of water and sodium tetraborate.[210] Stefanovich *et al.* grew non-porous vanadium oxide films via anodic oxidation using a similar electrolyte consisting of acetone, sodium tetraborate and benzoic acid.[201]

Based on the mentioned results, electrochemical anodization of vanadium to obtain ordered arrays of vanadium oxide nanotubes was investigated in our workgroup. Multiple different electrolytes were tested. As etching agents, ammonium fluoride and oxalic acid were investigated in aqueous as well as different glycolic solutions. The saturation of the solvent with boric acid played the key role even though its role could not be explained definitively.[74]

5.2 Synthesis of Porous Vanadium Oxide

5.2.1 Electropolishing of Vanadium Foils

The necessity of a prior polishing already was discussed in general in Section 2. Within the previous work by Dominik Koll,[74] different electropolishing methods were tested. A mixture of 20 vol% sulfuric acid and 80 vol% methanol with little water[211] was found to be the most promising approach.

Electropolishing according to this recipe already gave good results using the Cu-block Setup with a carbon cathode (for further details see Chapter 6.1.2) and a potential of 10 V for 4 min for the typical foil size of 20 mm diameter. As a result of strong gas generation leading to interruption of electric current, the distance of the two electrodes was set to 17 mm, higher than the usual value. Figure 5.1 shows optical microscope and 3D laser scanning microscope images of unpolished and polished foils, clearly demonstrating a smoother surface after polishing. A current-time curve for the polishing step can be found in the appendix (Section 7).

Nevertheless, the surface roughness of the purchased vanadium foils varied strongly depending on the delivery batch. For the more deeply scratched and rather irregular foils (see Figure 5.2), the applied electropolishing method was insufficient to provide as smooth a surface. In a series of experiments, a suitable way to polish the substrate for the subsequent anodization was sought. First of all, the established conditions were adopted in a way that the applied electropolishing solution would be more aggressive. Etching deeper into the material was necessary due to the deep scratches, and the polishing had to equalize the surface level to the lowest sites of the foil. In limits set by generation of heat and gas formation during the reaction, polishing was conducted with potentials of no more than 20 V and with cooled (- 25 °C) solution. Above 20 V, gas evaporation was too strong, disturbing the current flow through the solution and leading to uneven and non-reproducible results. Since the solution was not stirred, polishing was stopped after 4 min due to the exponential decay of the current caused by gel-like vanadate forming directly on top of the polished foil. Its yellow-orange color indicated the existence of decavanadate $[V_{10}O_{28}]^{6-}$ (orange) and/or VO_2^+ (yellow).

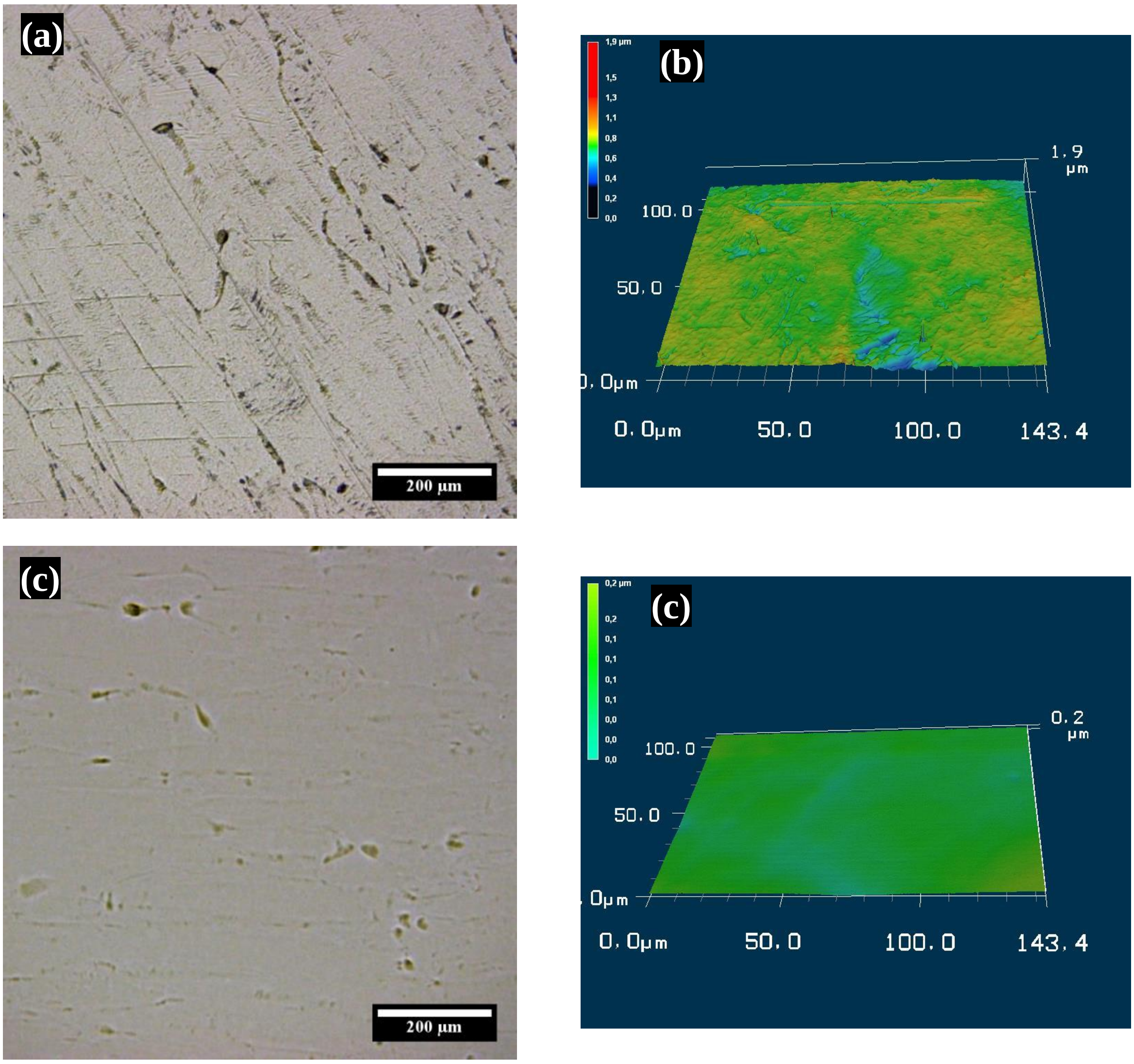

Figure 5.1: (a) Light microscopy and (b) 3D topology laser scanning microscopy images of unpolished foils, (c, d) of polished foils. The 3D laser scanning microscope images were extended 10-fold in thez-axis.

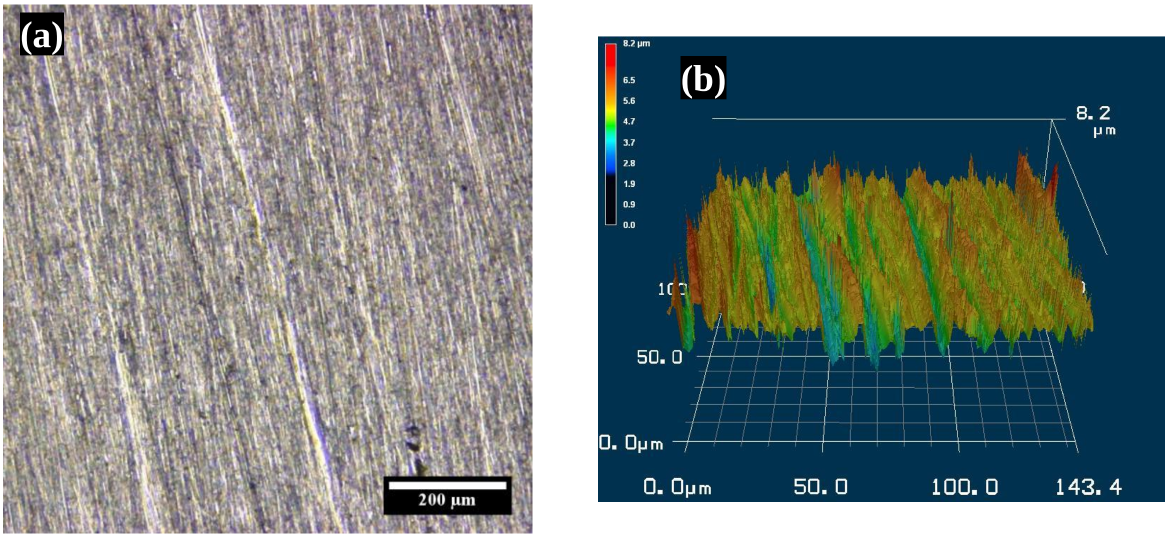

Figure 5.2: (a) Light microscopy and (b) 3D topology laser scanning microscope images of unpolished, deeply scratched foils. The 3D laser scanning microscopy image was extended 10-fold in the z-axis.

No notable improvements in surface quality over that by the original polishing method were observed. At best, the surface became smoother than with the original parameters, 10 V and 4 min, but it did not lose its scratchy appearance (see Figure 5.3).

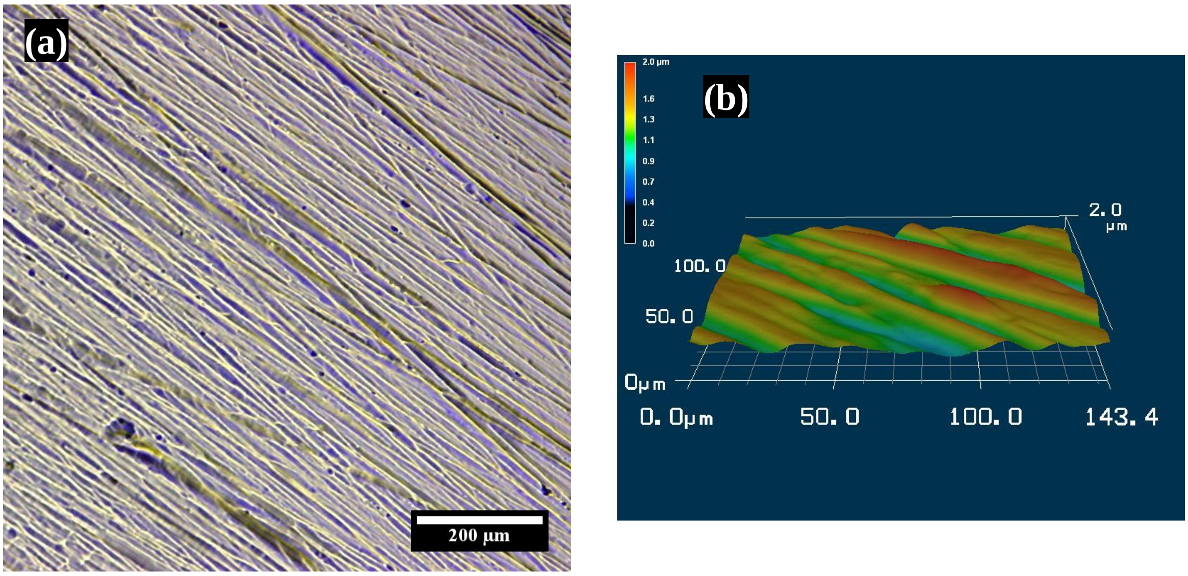

Figure 5.3: (a) Light microscopy and (b) 3D topology laser scanning microscopy images of insufficiently polished foils using the standard polishing conditions. The 3D laser scanning microscopy image was extended 10-fold in the z-axis.

Alternative electropolishing procedures for vanadium were taken from literature as a basis for investigations on other electrolytes: a 2:3 solution of H_2SO_4 in ethanol at a current of approximately $0.5\ \mathrm{A\ cm^{-2}}$ [201] and a 4:1 composition of methanol and H_2SO_4 at constant voltage between 10 and 25 V for 5 min.[212]

Different mixtures with varied ratios of H_2SO_4, MeOH, EtOH, and water were tried, using potentiostatic as well as galvanostatic conditions, without tremendous influence on the result (Table 13 in Chapter 6.5.1 gives an overview of the specific experiments). The performance with most approaches became even worse compared to the original conditions.

Finally, it was succeeded by simply repeating the original method of electropolishing about 4 times, unless the surface had a very good quality (see Figure 5.4). This result was not self-evident insofar as similar efforts to increase the flatness of titanium foil by repeated polishing had failed in the past. Between the short polishing steps, the polishing solution had to be mixed to dilute the vanadate on top of the foil. Otherwise, this layer would lower the electric current and prevent an effective abrasive polishing. Although the resulting electropolishing solution became richer in vanadium species with every mixing, no impact on surface etching or even tiny changes in electric current flow could be detected (see the current-time curve found in the appendix (Section 7)).

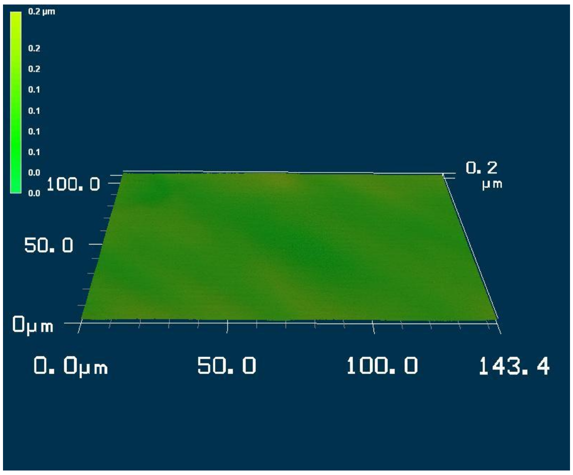

Figure 5.4: 3D topology laser scanning microscopy image of a 4-fold polished foil (10 – 12 V, 4 min). The 3D laser scanning microscopy image was extended 10-fold in the z-axis.

The mass loss of the used metal foils in each polishing step was about only 5 mg (approx. 1 %) and therefore not crucial for the subsequent anodization. The total abrasion was so low that no height difference at the edge polished/nonpolished area could be detected by 3D laser microscopy. Moreover, a linescan over the whole etched diameter of 16 mm gave no obvious depression due to the metal dissolution.

5.2.2 Preliminary Work and Test of Anodization Conditions

Dominik Koll found that an electrolyte composed of diethylene glycol (DEG) saturated with boric acid, 2 % water, and 0.5 % oxalic acid as etching and complexing agent could give well-ordered arrays of vanadium oxide nanopores.[74]

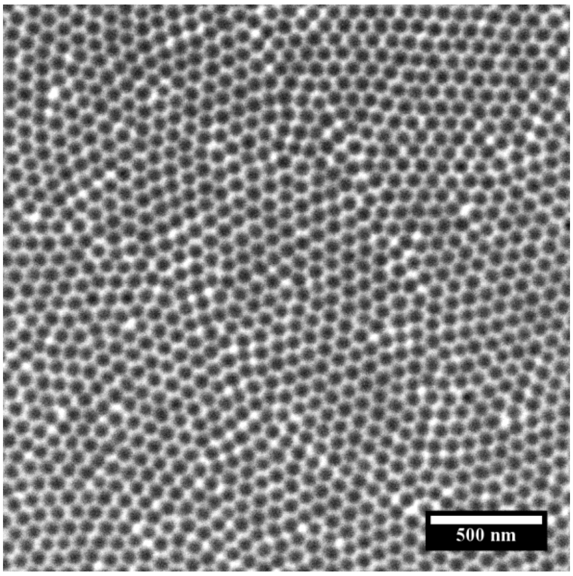

Figure 5.5: SEM image of anodized vanadium foil (40 V) bearing an ordered porous structure.

Mostly uniform surfaces over the whole metal oxide were obtained. Reproduction with a potential of 40 V for 3 h using the Cu-block Setup at 25 °C led to surfaces with well ordered, nearly monodisperse pores of about 50 – 60 nm diameter (see Figure 5.5).

Thereby, the found pore size was slightly lower than the previously reported of roughly 70 nm. However, in several cases obviously inhomogeneous behavior of electrolyte and other reaction conditions led to likewise inhomogeneous pore appearance or even defect structures. The pores could rather appear as a network structure or even as sealed combs (see Figure 5.6). Often areas with different appearances were detected on the same anodized foil.

The shape of the corresponding current-time-curves (see Figure 5.7) can be interpreted in accordance with general anodic oxide formation steps (see Section 2): Usually current flowed right at the beginning with about 8 – 9 mA, followed by a strong decay, indicating the formation of a compact barrier layer. After a short rise in the current, dissolution by the etching agent, oxalic acid, and pore formation should have subsequently led to a steady state. Instead of a plateau, however, a slow but steady decline, 5 to 3 mA over a period of 60 to 90 min, was usually observed. This indicated that either the vanadium oxide formation is dominant over the dissolution, or that vanadium oxide precipitation on top of the nanopores hinders the current flow.[74]

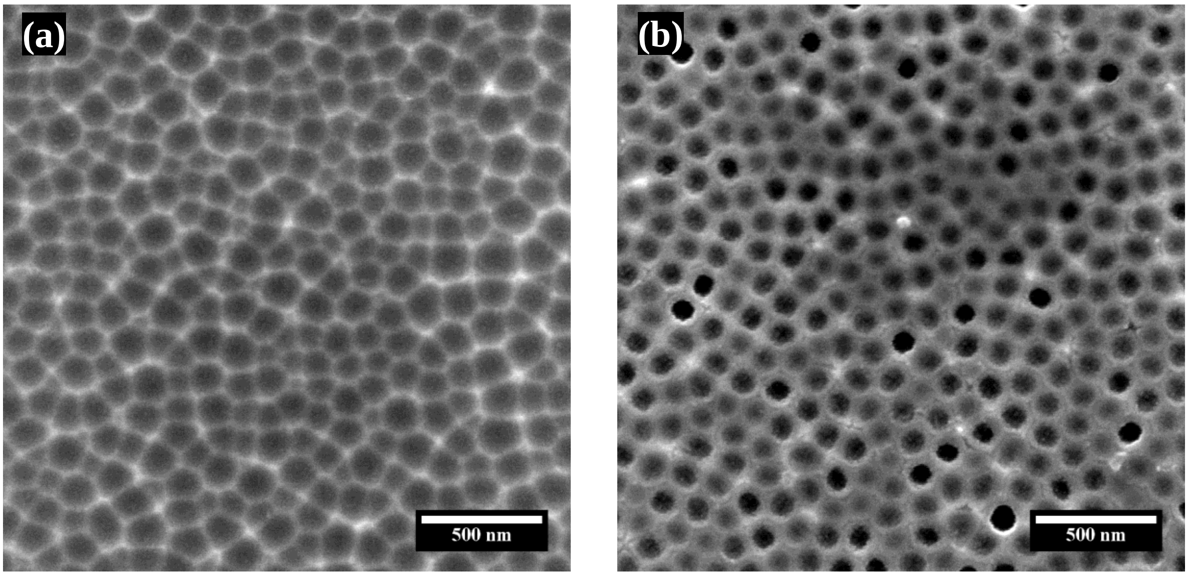

Figure 5.6: SEM images of anodized vanadium foil (40 V) showing two different appearances: (a) network structure and (b) sealed comb structure.

This region of steady decline was followed by a further, rather exponential decay. Even though the current-time curves were of characteristic, similar shape, variations in absolute current values and the duration, as well as intensity of decay, showed numerous exceptions from the average. Those variations were thought to be related to the high viscosity of the electrolyte, which was not easy to handle. In particular, the viscous solution was prone to air or gas bubbles, which disturbed the electric field. Furthermore, recrystallization of boric acid due to possible supersaturation had to be prevented.

After the anodization step itself, the electrolyte had to be washed away to obtain the oxidized (but almost blank) sample. Water was used to clean the samples and free them from orange gel-like precipitation that was thought to be a poorly soluble vanadate species,[74] as it was already observed in the polishing step.

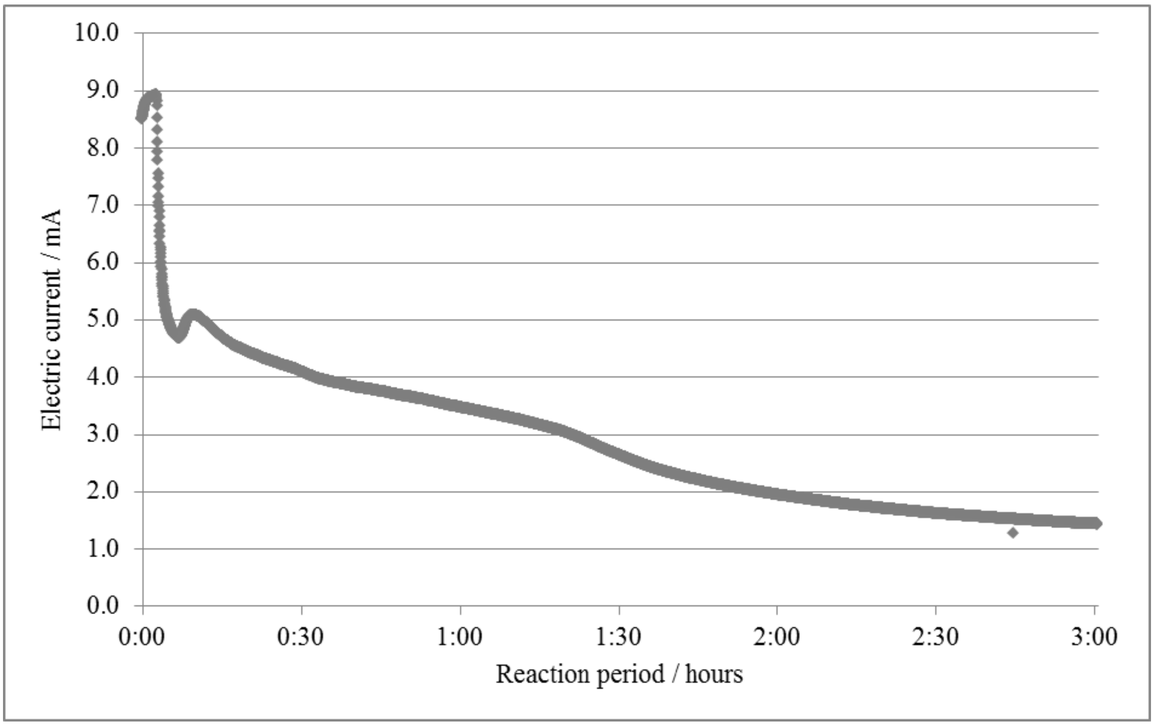

Figure 5.7: Typical current-time curve for an anodization at 40 V for 3 h, showing characteristic regions (strong decay, steady decline, exponential decay).

By means of particularly controlled reaction conditions, attempts were made to prevent defects like etched craters and other surface inhomogeneity (see Figure 5.8).

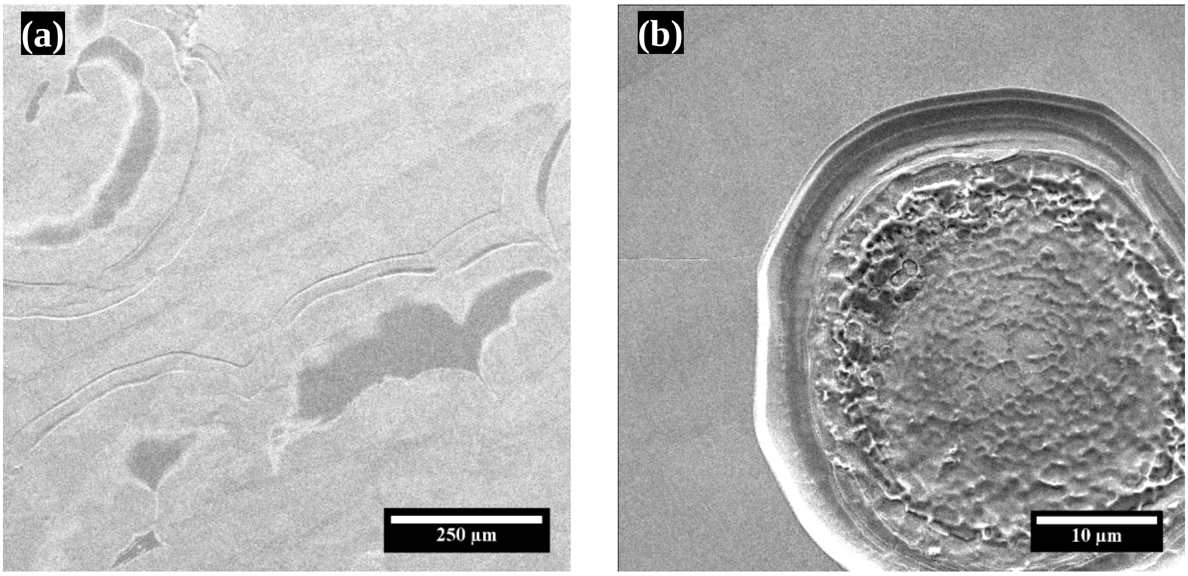

Figure 5.8: SEM images of (exemplary chosen) surface defects: (a) contrast changes indicating inhomogeneity (without change in nanostructure) and corrugations, (b) deeply etched craters.

On the other hand, sometimes local structures were found showing surprisingly better results compared to homogeneous, smooth samples (see Figure 5.9).

Large, hexagonal ordered pores existed right next to absolutely non-porous areas. Pore size and order apparent in defect structures often differed from the normal case concerning the pore diameter. In craters, as it is shown in Figure 5.8 (b), very small pores were frequently found.

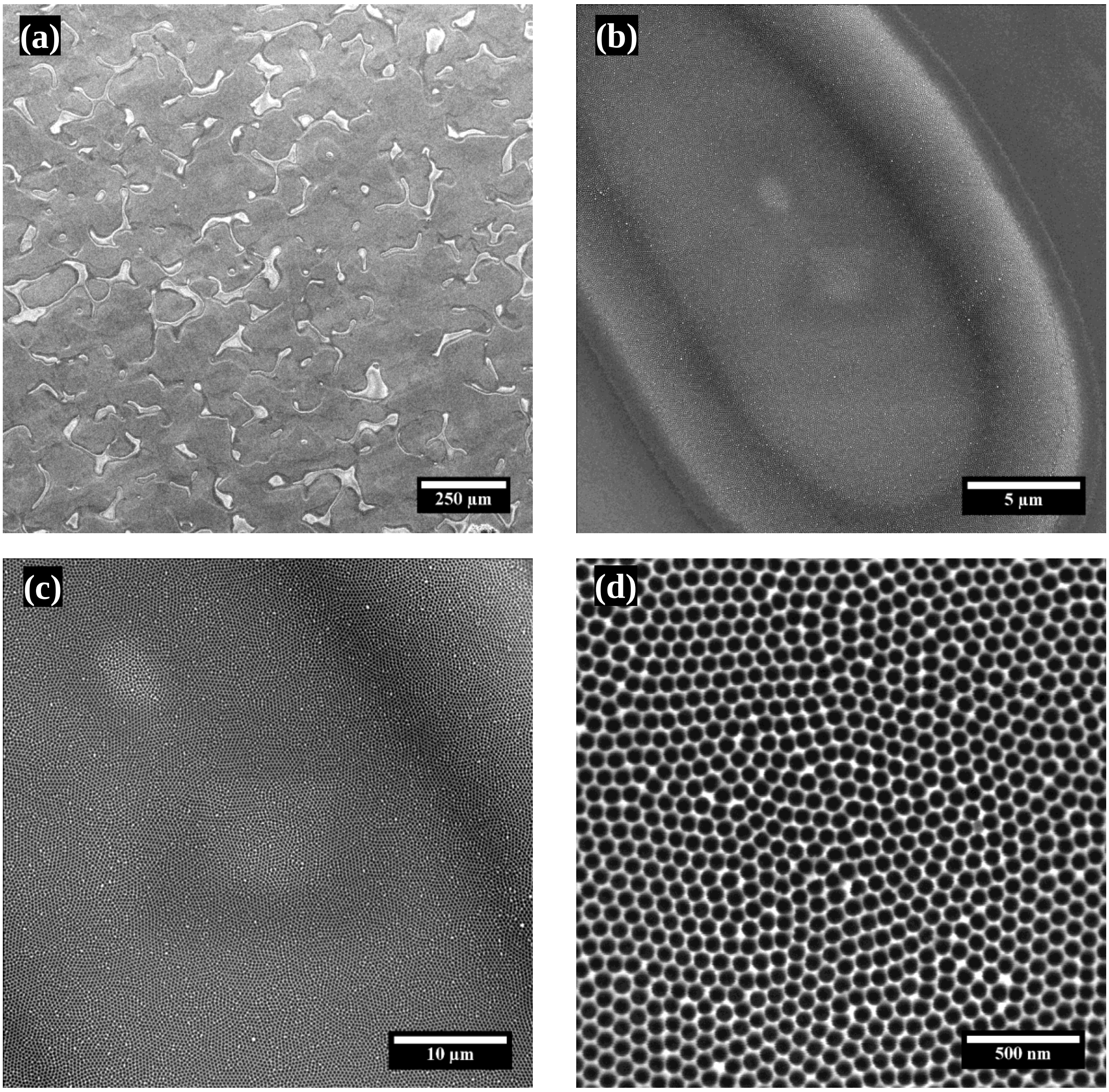

Figure 5.9: SEM images of inhomogeneously anodized surface in rising magnification (a-d). Light grey areas in (a) indicate highly ordered pores, while darker areas were nonporous.

As previously mentioned, the high amount of boric acid in the electrolyte tended to cloud during the anodization. That is why the DEG was saturated at elevated temperatures and left for days in which excess of boric acid could reprecipitate. The boric acid was absolutely necessary to yield a porous result and not just only an etched surface.[74] A reduction of the boric acid concentration prevented the formation of pores. Figure 5.10 shows the result of an anodization with just half the concentration of boric acid in DEG. Due to strong etching effects, no more smooth, porous surfaces could be obtained. A possible explanation could be that the solubility of the formed vanadium oxide in the acidic electrolyte is enhanced if the electrolyte is not already saturated by boric acid.

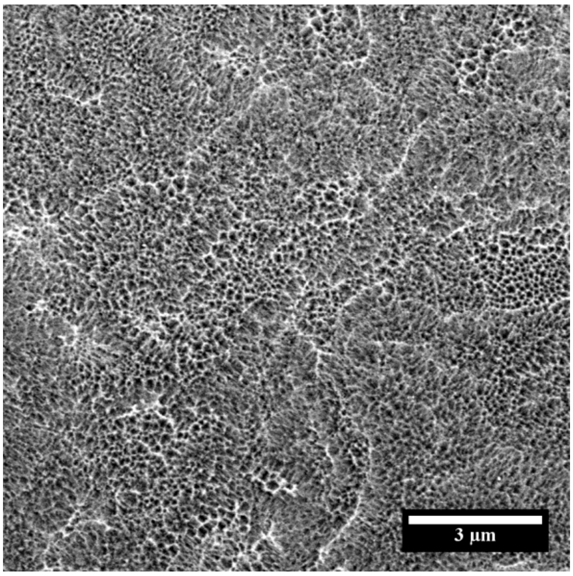

Figure 5.10: SEM image of corroded surface using half-concentrated boric acid in DEG for the anodization electrolyte.

On the other hand, the influence of the etching agent oxalic acid was investigated. If the concentration was lowered, the size of the obtained pores contracted. Figure 5.11 shows the result of anodizations with 0.20 % and 0.15 % oxalic acid. The pore size was thereby reduced to about 50 nm and 40 nm, respectively. Moreover, with less oxalic acid, the pore homogeneity was lowered. The electric current was considerably decreased, a direct consequence of the reduced number of electron transporting ions in the electrolyte.

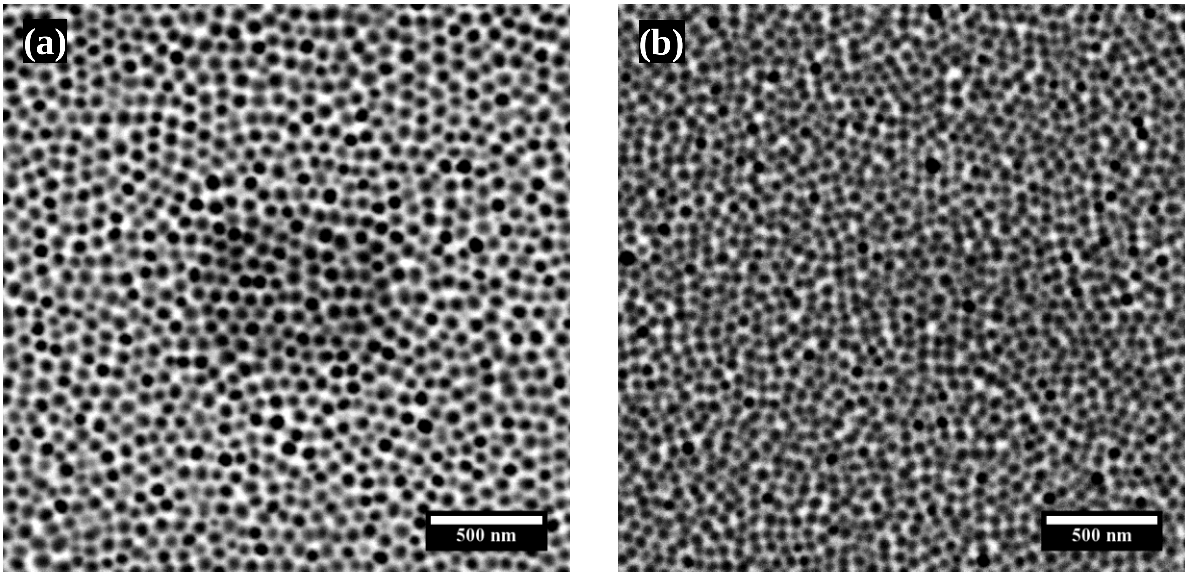

Figure 5.11: SEM images after anodization at 40 V with (a) 0.20 % oxalic acid (about 50 nm pore size) and (b) 0.15 % oxalic acid (about 40 nm pore size).

5.2.3 Identification of the Oxide Layer

It was remarkable that the SEM images of vanadium oxide pores in general did not show high contrast (see e.g. Figure 5.5 and Figure 5.6). Naturally, every material gives a different brightness when partially charged under electron bombardment, but comparison with titanium oxide ATO (see Section 3) shows significant differences. The vanadium oxide surfaces seemed to be of shallow depth. Even though X-ray photoelectron spectroscopy (XPS) studies of the anodized surfaces gave hints at higher oxidation states of vanadium species compared to only polished, untreated samples (for further details see Chapter 5.3), some further observations were perplexing:

First, instead of choosing the typical 3 h, the anodization period was extended to 16 h. The only significant difference observed in the SEM images was the pore size, which was increased by a large extent and can be explained in accordance with observations made with ATO (see Chapter 3.3).[74] Remarkably, with increasing reaction time, no hints of a growing thickness of the produced porous oxide were found. There was no higher contrast or even sample charging detectable by scanning electron microscopy.

Second, the oxidic top porous layer in general was too soft to be broken, bending instead. Therefore, the layer thickness could not be measured by SEM cross-sectional pictures, as it was done for titanium and aluminum samples. Any attempts to harden the oxide by annealing or to separate from the metal by hot/cold temperature shocks did not succeed. Analysis of pores with atomic force microscopy (AFM) did not give the necessary depth resolution in consideration of AFM cantilever dimensions.[74]

Third, no visible oxide could be detected after the anodization by eye, even though vanadium oxides in general show characteristic colors: V_2O_5 is orange, VO_2 is described to be either dark blue/green up to blackish.

Sometimes small areas apart from the rather homogeneous surfaces were found to have evidently deeper pores. Figure 5.12 (a) shows residues of a porous layer, in parts dissolved, in others covered by a precipitate, or even plugged like capped honeycombs as it was shown in Figure 5.6. In Figure 5.12 (b), two porous oxide layers can be clearly distinguished on the flat surface.

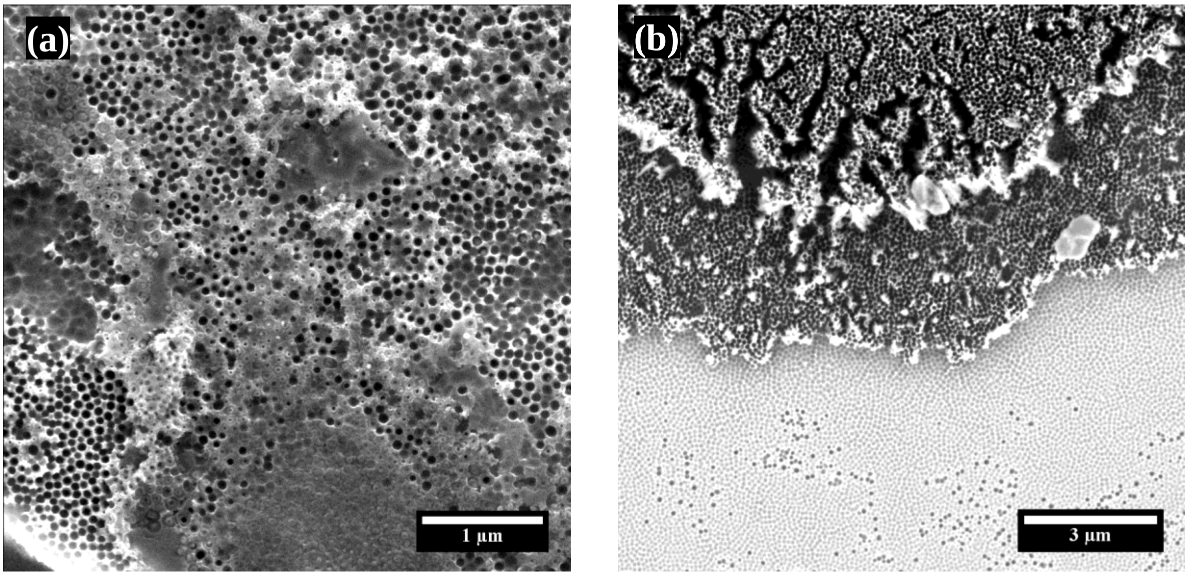

Figure 5.12: SEM images showing residues of porous oxide: (a) dissolved pores next to capped pores and (b) layered porous structures.

Those observations gave a new understanding of the samples investigated so far: Although V_2O_5 is only poorly soluble in aqueous solvents, it is at the same time of amphoteric nature. Oxalic acid, as a moderately strong acid, caused the dissolution of the formed oxide via vanadates, aided mechanically by the final washing procedure with water:

$$\mathrm{VO_4^{3-}} + 4\,\mathrm{H^+} \rightarrow \mathrm{VO^{2+}}(\mathrm{yellow}) + 2\,\mathrm{H_2O} \tag{5.1}$$

The kind of slimy, orange debris on top of the samples (see Figure 5.13 (a)), considered to be a vanadate precipitate[74] formed during anodization by acidic catalyzed condensation reactions, was in fact the wanted product. When formerly analyzed for checking purposes, it never seemed to be porous (see Figure 5.13 (b)), probably due to intense washing or slow drying, and was therefore discarded.

This sometimes loose precipitate turned black within minutes when drying, which can be explained by the reduction from V(V) to V(IV). V(IV) is in fact the more stable oxidation state, compared to V(V), which is a moderate oxidant. V_2O_5 easily loses oxygen, e.g. at elevated temperatures, to become an oxide mixture of the general formula $V_nO_{(2n+1)}$ ($n = 3, 4, 6$). The presence of the reducing agent oxalic acid makes sure that either $V_nO_{(2n+1)}$ or VO_2 is formed, both blackish in color. VO_2 is also amphoteric but almost water insoluble. If the orange oxide was washed away with excess water, a further color change to green was often observed, which is most likely caused by a further reduction process to V(III).

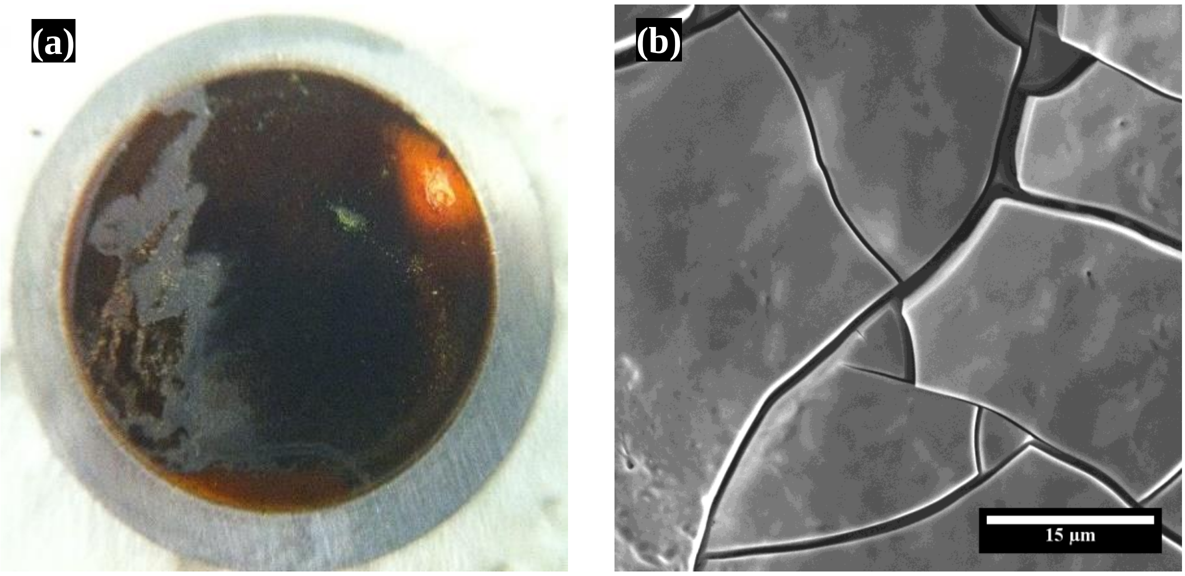

Figure 5.13: (a) Photograph of orange vanadium oxide right after anodization (without washing process) and (b) SEM image of compact oxide showing no porous structures.

The samples investigated so far corresponded mainly to the imprints induced by the real porous oxide, in accordance with two-step anodization processes for ATO and AAO. It was imperative to keep the soft orange oxide and stabilize the layer to preserve the porous result. As observed with the variation of the oxalic acid concentration (see Chapter 5.2.2), the amount of orange oxidic precipitate rose with enhanced acid concentration. Variation of anodization time showed that after 30 min, at the earliest, the desired orange color was visible, but after 15 min porous structures could already be detected with the SEM. The reaction time until visible orange oxide was discovered corresponds very well with the regions identified in the current-time curves (see Figure 5.7). The plateau-like region, which formed after about 30 min, seemed to correspond to the pore growth. The slow decay often observed may be attributed to dissolution and reprecipitation processes restraining the ion transport.

5.2.4 Variation of the Electrolyte Composition

Further examinations of more carefully washed oxide showed all kinds of corroded porous oxide (see Figure 5.14). Usually, the oxide was crossed by deep cracks, sometimes rudiment pores or channels were visible, but nonporous layers were also detected. Between these extreme cases more or less deep pore structures became visible.

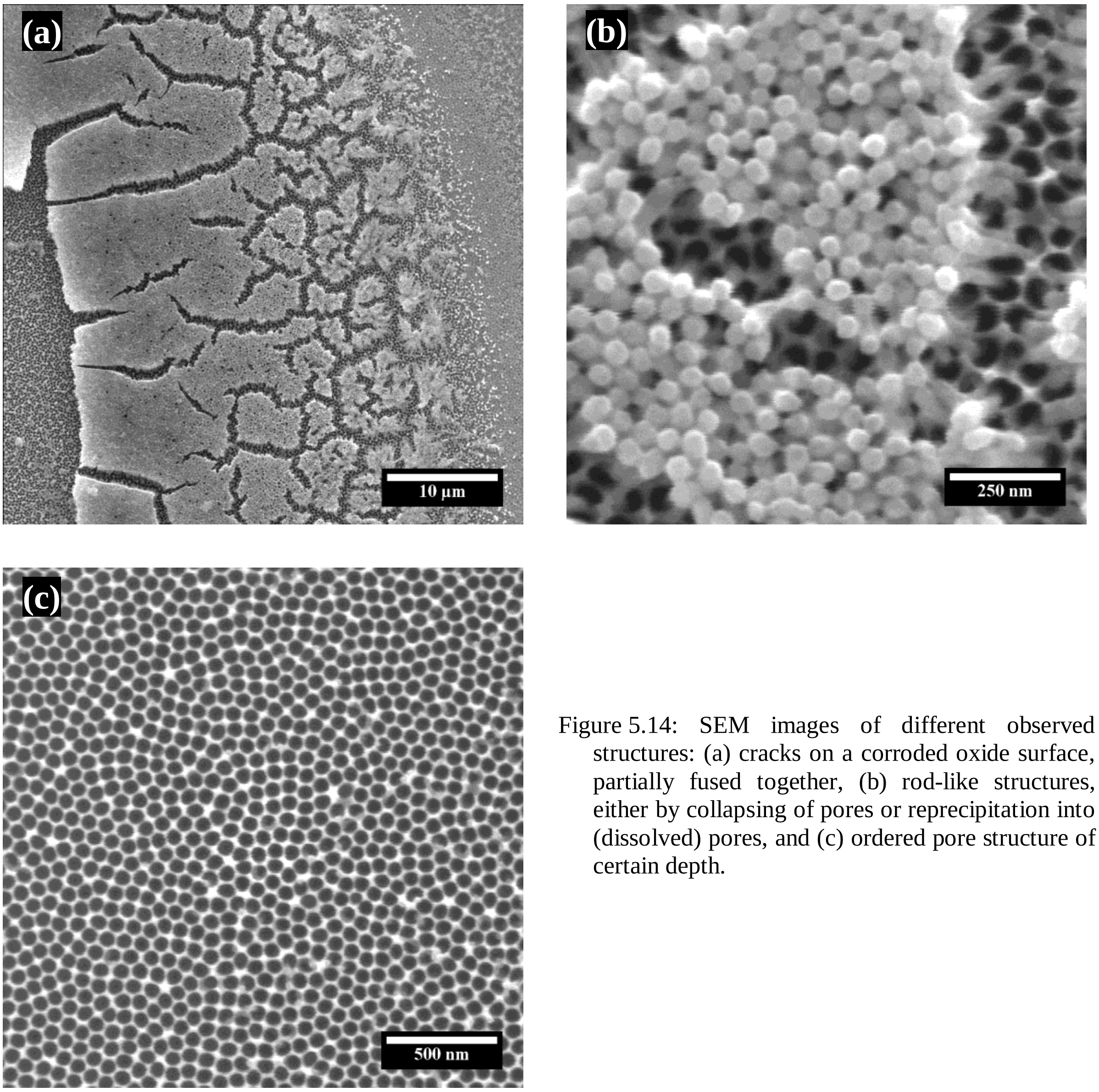

Figure 5.14: SEM images of different observed structures: (a) cracks on a corroded oxide surface, partially fused together, (b) rod-like structures, either by collapsing of pores or reprecipitation into (dissolved) pores, and (c) ordered pore structure of certain depth.

Further experiments performed aimed to stabilize the oxide to enable investigations with SEM. In doing so, it was assumed that the well-ordered imprints analyzed in Chapter 5.2.2 were just a mirror image of the porous AVO above which had been washed off. Therefore, the best reaction conditions identified so far were not seriously changed to obtain good porous results. The following setup parameters were varied instead: First, the inter-electrode distance was changed to influence the ion mobility. Second, the active sample size was reduced from 16 to 10 mm diameter by exchange of the Cu-block Setup’s PTFE vessel to improve the homogeneity of the electric field. Third, the whole setup was replaced by a simple vertical setting, following popular constructions (see Section 2). A glass beaker was filled with electrolyte and equipped with a graphite sheet electrode. The vanadium foil, as anode, was dipped into the solution and held by an alligator clamp. The setup was used with or without magnetic stirring. No parameter change had a positive influence on keeping more oxide with pores. Instead, the use of the vertical setting resulted in gravity-induced thickness inhomogeneity of the soft oxide. Additional stirring was not a crucial factor.

Furthermore, the electrolyte itself was modified to reduce the dissolution of the oxide in the electrolyte: First, the water content was lowered to 0.25 or 0.1 %, but this did not seem to have an enormous influence on the result. A higher water ratio of about 5 %, however, gave no more precipitate at all. This is in line with former observations that the amount of water seemed not to be very critical, and that tetraborate, alternatively the boric acid here, is said to act as the source of the oxygen for the film too.[203] But a certain amount of added water allowed an adequate dissolution of the oxalic acid. Second, the effect of additional vanadium(V) oxide or ammonium oxalate, to buffer the pH, was investigated, but no impact was observed. Third, experiments to anodize in the cold, at 2 – 3 °C, failed due to very low current caused by the highly viscous glycolic electrolyte. Fourth, diethylene glycol (DEG) was replaced by ethylene glycol (EG), which is less viscous and more easily removed with wash water. Using EG, porous layers could be generated, but results were comparable and not significantly better.

Finally, it was ascertained that the exact reaction parameters were obviously secondary and insignificant compared to the work-up procedure after the anodization itself.

5.2.5 Washing and Drying Procedures to Keep the AVO Layer

As already described, washing of the anodized foils with water resulted in fast dissolution of the orange oxide with simultaneous reduction of the vanadium(V) to tetra- or even trivalent vanadium, indicated by color change. In praxis, the oxide-bearing vanadium foils had to be washed free of the electrolyte, composed of viscous DEG and remaining oxalic acid. A balance therefore had to be found such that the surfaces were subsequently adequately dry and free from residues on the one hand and that as much undamaged oxide as possible could be kept on the other hand.

Aside from the described variation of water content in the electrolyte, different water-free washing processes were tested. Yang *et al.* described EtOH as washing and stabilizing agent, even storing the samples after anodization in this solvent.[34]

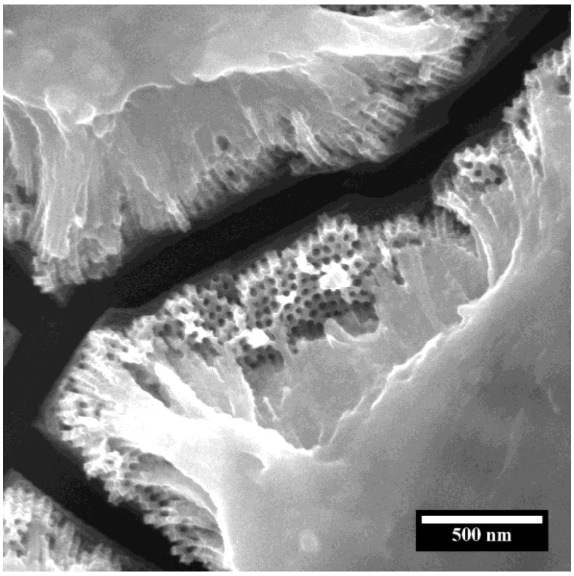

Figure 5.15: SEM image of superficial fused pores after washing with EtOH.

Results with EtOH were already better as Figure 5.15 shows. Pores were often still fused together, but below a compact top layer they became visible. It is most likely that even if the oxide from the top seemed to be compact when analyzed by SEM, pores were hidden underneath. Further experiments using isopropanol or dry acetonitrile also led to comparably good results. Washing after anodization always had to be done with care. It was generally not possible to keep the whole oxide layer intact. If the oxidized metal sheet was washed insufficiently or not washed at all, the electrolyte was not completely removed and the samples dried very slowly, giving the chemicals (acids, water) time to do their destructive work. Thick, but compact, appearing layers were the result. Too much washing or insertion into a washing agent led to nearly complete dissolution of the oxide and showed mainly the formerly described „imprint“ structures, with some residues as consequence.

Figure 5.16 gives several views of different states of typically found porous oxide layer conservation. Non-ideal washing processes resulted in either collapsing of the channel entrances to form a short nano grass layer or irregular porous surface reminiscent of maritime coral. “melting” of the channels could be observed as well as almost completely dissolved layers.

Acetone as a highly volatile and DEG miscible washing agent gave finally the best results. The eroded surfaces (see Figure 5.17 (a) and (b)) with signs of nano grass formation show that perfect stabilization of the oxide could not yet be ensured. Recovered oxide layer thickness was always about 2 to 3 µm, independent of if the reaction time was extended to more than 1 h. This might be an indicator that the oxide layer did not grow further after leaving the observed plateau-like region in the current-time curve (see Figure 5.7). The following region with a stronger decay of current could then be related to conditions where the pore entrances collapse by proceeded chemical dissolution and the ion transport is slowed down.

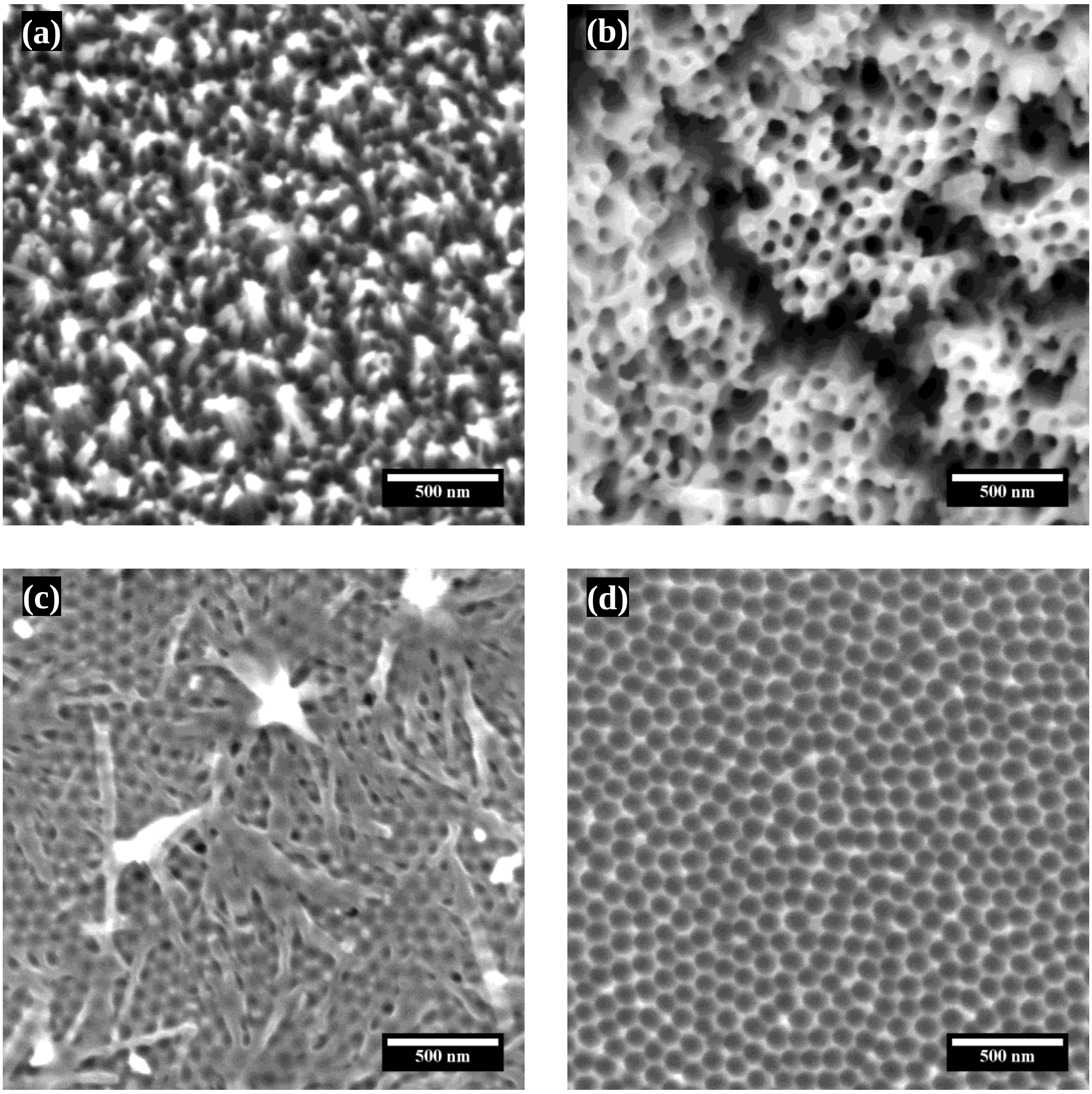

Figure 5.16: SEM images of different non-ideal washing results: (a) short nano grass on top of porous surface, (b) “coral” shaped corroded pores, (c) “molten” channels, and (d) pores of low depth.

Another explanation would be a stronger dissolution of the oxide layer, balancing its formation, and leading to a vanadate-rich phase over the oxide, likewise restricting the transport.

Pores of the oxide layers were less ordered compared to the imprint structures (see Figure 5.5), but rather monodisperse and of the same magnitude, 55 – 60 nm. This result is in line with observations made for the first anodization of titanium or aluminum and corresponding indentation structures (see Chapters 3.2 and 4.3).

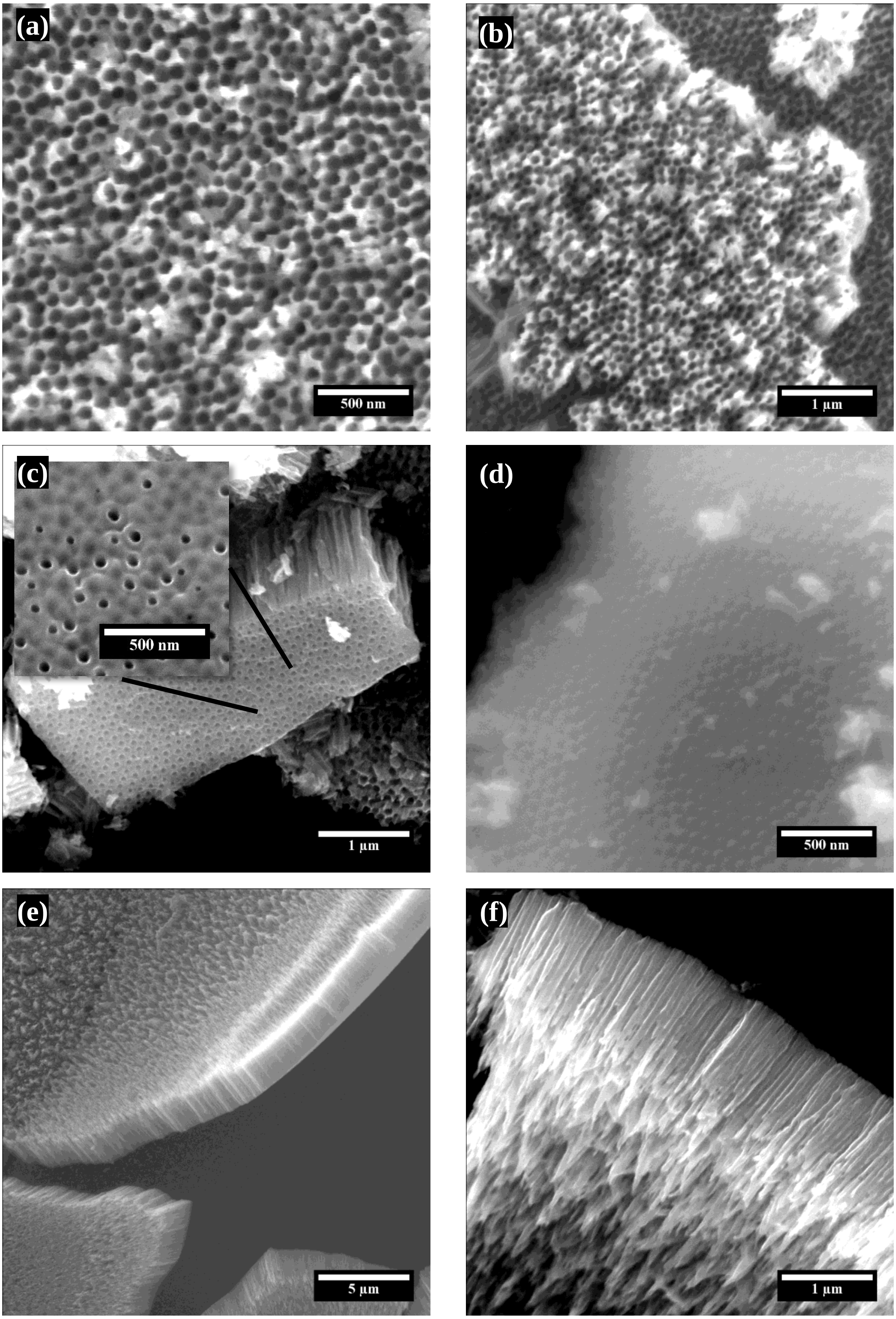

Figure 5.17: SEM images of AVO produced at 40 V and subsequently washed with acetone: (a, b) front side, (c, d) back side with either opened (by etching) or closed pores, (e, f) cross-sectional studies of oxide flakes detaching from the vanadium metal.

After removing the primary oxide by washing, a second anodization, however, was not found to improve the final result. With respect to the steady oxide layer thickness, it is most likely that a certain part of the oxide is dissolved probably upon the anodization step. The high solubility in the acidic electrolyte would then disturb the adjustment of stable pore forming conditions, leading to the observed moderate results.

The cross-sectional SEM images of the oxide show the characteristic anisotropic structure, well known from ATO and AAO. Even though Yang *et al.* obtained mainly tubular AVO with their approach,[31] the structures presented herein can be described rather as porous (see Figure 5.17 (e, f)). The backside of detached oxide flakes usually showed pores closed by the barrier layer, as expected. However, some partially open areas were found, probably caused by dissolution processes (see Figure 5.17 (c, d)). Figure 5.18 gives an impression of the synthesized porous AVO if carefully washed and dried on the vanadium metal. Deep cracks may furrow the surface as a result of material stress, an observation that was also made with ATO (see Chapter 3.4.1). However, the results show a considerable step forward in obtaining a membrane-like porous oxide.

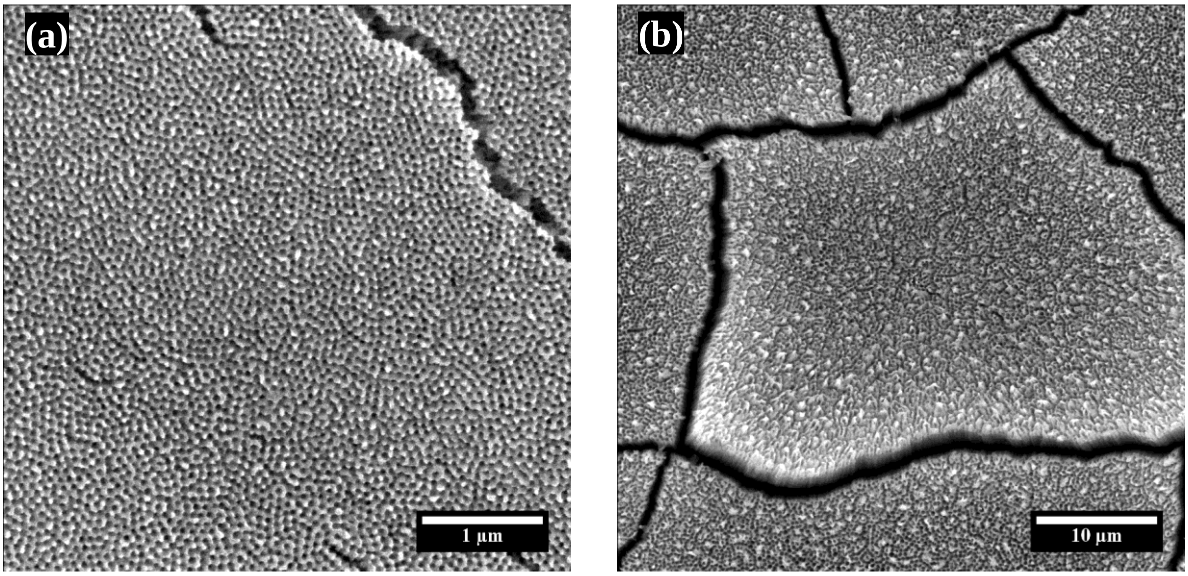

Figure 5.18: SEM images of AVO after careful washing with acetone, showing a continuous and homogeneous porous oxide layer disrupt by cracks.

The process with the necessary highly volatile acetone often led to intense flaking of the oxide (see Figure 5.17 (e, f)). Instead of simple air-drying, drying by heat or vacuum was tested. For the oxides grown in fluoride-containing electrolyte, it was found by Yang *et al.* that the anodized structures decompose for hygroscopic reasons and have to be annealed at 200 °C to be stabilized.[34] Annealing of the as-prepared foils after anodization, in contrast, did not have a positive influence on the structure. On the contrary, the oxide flake’s roll off from the metal was increased. Sometimes the oxide even totally lost its porous appearance, probably due to residual moisture within the pores leading to fast dissolution and reprecipitation in the heat. Drying in vacuum, in contrast, most suitably by the use of a vacuum drying cabinet at moderately warm temperature, was favorable. However, as soon as the oxide layers were dry, the porous structures were stable at normal air conditions. A new analysis of anodized foils after more than one year showed no change in appearance.

The change of color after anodization from bright orange to black or even greenish indicated a change of oxidation state, at least at the observable surface. Changes in the oxidation state can be a serious reason for a collapse of porous structures. Even though the electrochemically produced oxide was amorphous by XRD analysis (see appendix, Section 7) and therefore at least no destructive recrystallization processes were expected, the preservation of the vanadium(V) state would be desirable. Because oxalic acid is known to be a reducing agent able to react with vanadium(V), experiments were carried out to destroy the oxalic acid immediately after anodization or to maintain the conditions directly after anodization. As long as the electric current was on, the electric forces might stabilize the fragile balance, keeping the pores open for ion exchange. The annealing at 200 °C did not have influence on the blackening, so higher temperatures were tested when drying the foil after anodization in the oven (650 °C) or by heat gun. But at the used temperatures apparently crystallization was induced (for SEM image see the appendix, Section 7,), leading to destruction of the anodized structures. Further approaches to slow down the reduction process at low temperature, in the freezer or with liquid nitrogen, while drying the sample, or an oxidative destruction of the oxalic acid when the anodization was complete, were unsuccessful.

The conclusion of the experiments to synthesize a porous vanadium oxide (AVO) was that the anodization had to last at least 1 h with an electrolyte containing 2 % water or less. Washing with a highly volatile solvent was advantageous, because it was intense enough to remove the electrolyte but did not dissolve the product. The samples were subsequently dried in the vacuum.

Because the results published by Schmuki and coworkers[34] indicated a favored product with respect to obtained oxide layer thickness and oxidation state of the product, a reproduction of their results was pursued. The use of a less acidic electrolyte without a reducing agent promised to be advantageous.

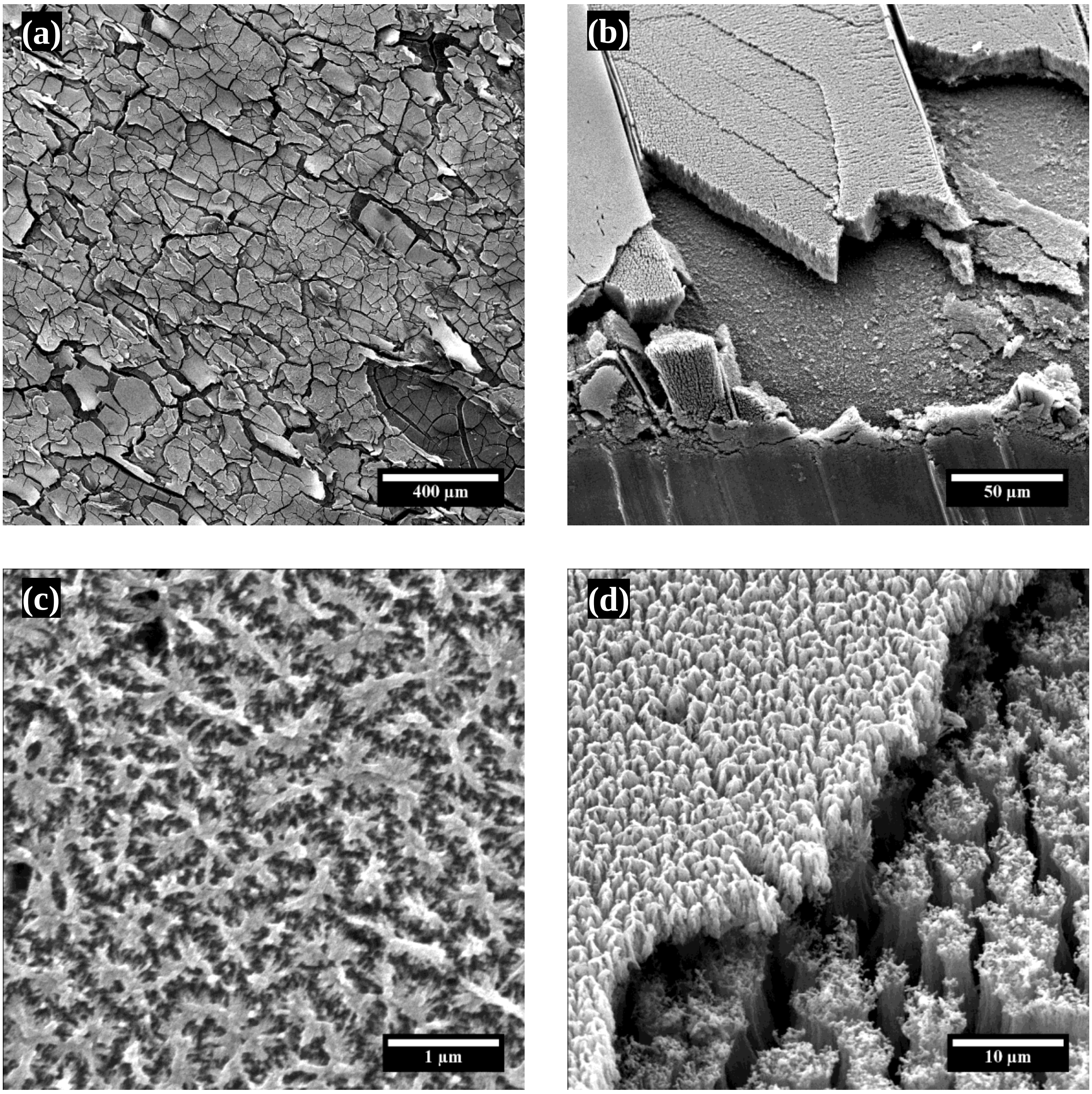

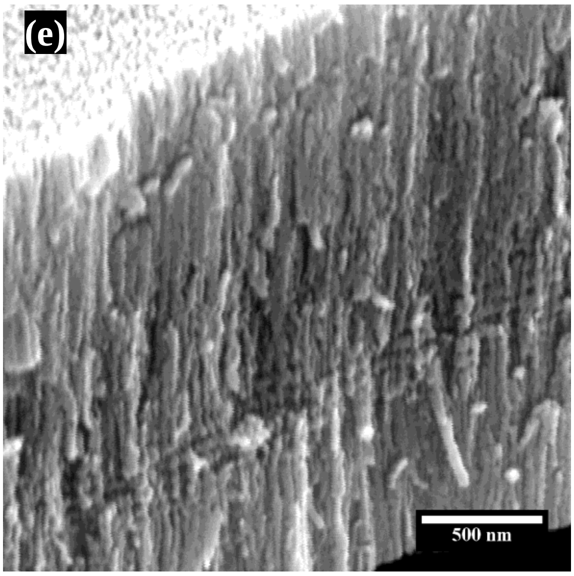

Figure 5.19: SEM images of AVO, based on a method published by Yang *et al.*[34]: (a, c, e) images of a black product obtained, similar in appearance to results described in the present work; (b, d) images of a thick yellow oxide, non-porous but highly corroded.

Even though slight modifications had to be made (for further details, see the experimental details in Chapter 6.5.2), anodization in EG with small amounts of HF and $[TiF_6]^{2-}$, from dissolution of Ti metal in HF, indeed resulted in an orange-yellow oxide layer. Its color was kept by laying in EtOH, overnight as recommended. The subsequent annealing at 200 °C for 3 h gave an orange result in one case, a black in the other case. SEM pictures of the black sample did not show remarkable differences from our approach, with again 2 – 3 µm of oxide layer thickness (see Figure 5.19 (a, c, e)). The yellowish product was found to have an oxide layer of about 11 µm, but no pores were observed, only bundles of nano grass (see Figure 5.19 (b, d)). The results showed that even with the use of another electrolyte, high effort has to be made to gain reproducible, good porous oxide.

5.3 Characterization of AVO by XPS Studies

As was already discussed, there was evidence that a vanadium(V) oxide formed during the anodization (orange color) was reduced by the present oxalic acid to form an oxide of lower oxidation state (blackish). In particular for possible applications in catalysis, the exact oxidation state would be essential information. The ability of the produced layers to change the oxidation state and, at the same time, preserve their structure, is another interesting feature. X-ray diffraction as reported allowed no conclusions about the composition due to the amorphous nature of the as-grown oxide. Consequently, XPS analysis was used for determination of the oxidation states of vanadium in the oxidic film.

General Remarks about XPS Measurements[213]

X-ray Photoelectron Spectroscopy (XPS), also known as Electron Spectroscopy for Chemical Analysis (ESCA), is a prevalent analysis method for studying the chemical composition of material surfaces. In a high vacuum chamber, a solid substance is therefore irradiated with X-rays of specific wavelength, and the emitted electrons are analyzed. The interaction of usually Mg Kα (1253.6 eV) or Al Kα (1486.6 eV) soft X-rays with atoms leads to emitted electrons according to the photoelectric effect, having the kinetic energy

$$\mathrm{KE} = h\,\upsilon - \mathrm{BE} - \phi_s \tag{5.2}$$

with Binding energy BE and spectrometer work function ϕ_s

The plotted spectrum gives the number of detected electrons versus their calculated, original binding energy. The Fermi level corresponds to zero binding energy. The spectrum of an element mixture is just the sum of the peaks of the individual components. Chemical states can often be identified from exact measurement of peak positions, generally calibrated to adventitious carbon, C1s 284.8 eV. Quantitative information arises from the determination of peak heights or peak areas.

p-,d- and f-shell electrons show a split signal upon ionization. The spin-orbit splitting ratio is 1:2, 2:3, 3:4 concerning the peak area and express the probability of the ionization process. Electrons that have lost energy usually increase the background level at binding energies higher than the peak energy, making a complex background subtraction necessary. In addition to photoelectrons, via a two-electron effect Auger electrons may be emitted: An outer electron falls into the inner orbital vacancy (relaxation), and a second electron is simultaneously emitted, carrying off excess energy.

Even though the X-rays penetrate some micrometers deep into the matter, only near-surface electrons from a few nanometers in depth can leave without inelastic energy loss. This fact makes XPS an extreme surface sensitive analytic method, detecting e.g. thin surface functionalization layers, but also contaminations.

To get rid of contaminations, surfaces can be sputtered with argon, but this application of energy may cause changes in chemical states and results have to be handled with care.

Specific Remarks about Measuring Vanadium

Stefanovich *et al.* summarized identified compositions of many different previously, anodically grown compact vanadium oxides as either V_2O_5, VO_2 or a mixture of V_2O_5 and lower oxides.[201] The data evaluation presented herein was based on a XPS study published by Mendialdua *et al.*,[214] which was already considered by Schmuki and coworkers.[34] For their prepared porous vanadium oxide, the chemical composition was found to be V_2O_5, interpreting only measured binding energies of 517.54 eV for $V2p_{3/2}$ and 525.03 eV for $V2p_{1/2}$. In view of the numerous conflicting publications providing XPS-data of vanadium oxides (see Table 6), absolute values for the $V2p_{3/2}$, $V2p_{1/2}$ and O1s are not sufficient to determine the oxidation state of vanadium oxides. Furthermore, without an adequate fitting procedure, not even obvious signal maxima can reliably be consulted for the oxidation state analysis.

Table 6: XPS results for vanadium and different vanadium oxides collected by Mendialdua *et al.*.[214] The indicated energy ranges represent different values found in literature.

	$V2p_{3/2}$ (eV)	Lambda/ FWHM	O1s (eV)	Delta O > $V2p_{3/2}$ (eV)
V	512.4 – 512.7	1.0 – 2.0		
VO	513.5 – 513.7			
V_2O_3	515.2 – 515.9	4.2 – 4.9	529.6 – 530.1	14.2 – 14.8
VO_2	515.7 – 516.2	2.0 – 4.5	529.4 – 530.0	13.7 – 14.4
V_6O_{13}	516.3	2.5	529.6	13.3
V_2O_5	516.6 – 517.7	0.9 – 2.0	529.6 – 530.5	12.8 – 13.1

Mendialdua *et al.* found the O1s peak of the vanadium to be best suited as the energy reference, instead of the usually used C1s signal. The energy difference between O1s and $V2p_{3/2}$, designated as "delta", is taken into account. On the other hand, the full width at half maximum (FWHM) of $V2p_{3/2}$, designated as "lambda", gives information about the phase purity and the oxidation state. Both values, lambda and delta, increase with decreasing oxidations state (see also Table 6).[214]

But the FWHM-value is strongly affected by how the background correction of the XPS spectra is performed. A further problem is that the most likely anodization products VO_2 or V_2O_5 are partially oxidized and reduced, respectively, under ambient conditions.[214] We could confirm this by measuring powder standards of vanadium oxides (not shown here), but being different in structure and surface conductivity, powder samples cannot be reliably compared with nanostructured AVO on top of vanadium foils.

Characterization of the Synthesized AVO

The XPS spectrum, the vanadium and oxygen area, of an anodized vanadium foil bearing the previously described blackish oxide layer and its corresponding structure, SEM image, is shown in Figure 5.20. The broad signals for $V2p_{3/2}$ and $V2p_{1/2}$ indicate that more than one oxide is present. Considering the mentioned difficulties with absolute energy values for the signals, just a comparison of foils with different oxide composition may lead to evidence about the oxidation states.

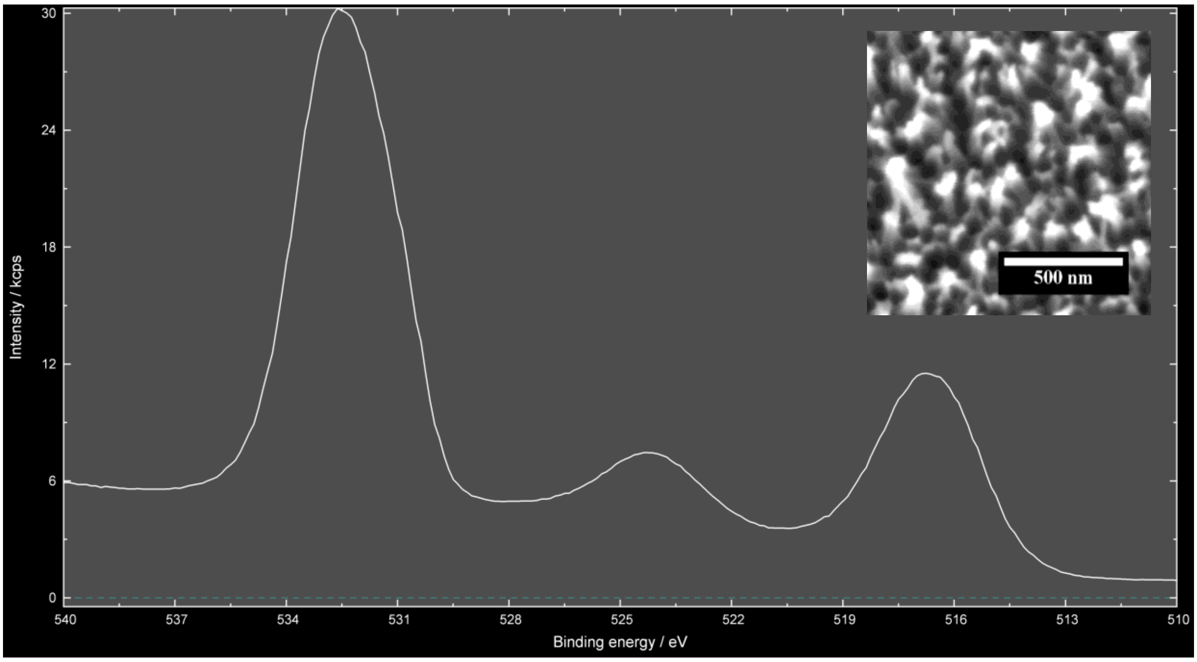

Figure 5.20: XP spectrum of an AVO surface considering the V2p and O1s region. The inset shows a SEM image corresponding to the analyzed surface.

The challenge was approached by taking the spectrum of an electropolished foil (see Figure 5.21), which was shortly sputtered with Ar^+ ions in the high vacuum chamber of the XPS. The sputtering was performed to get rid of the very thin natural oxide, forming after polishing by reoxidation, to yield the pure vanadium metal.

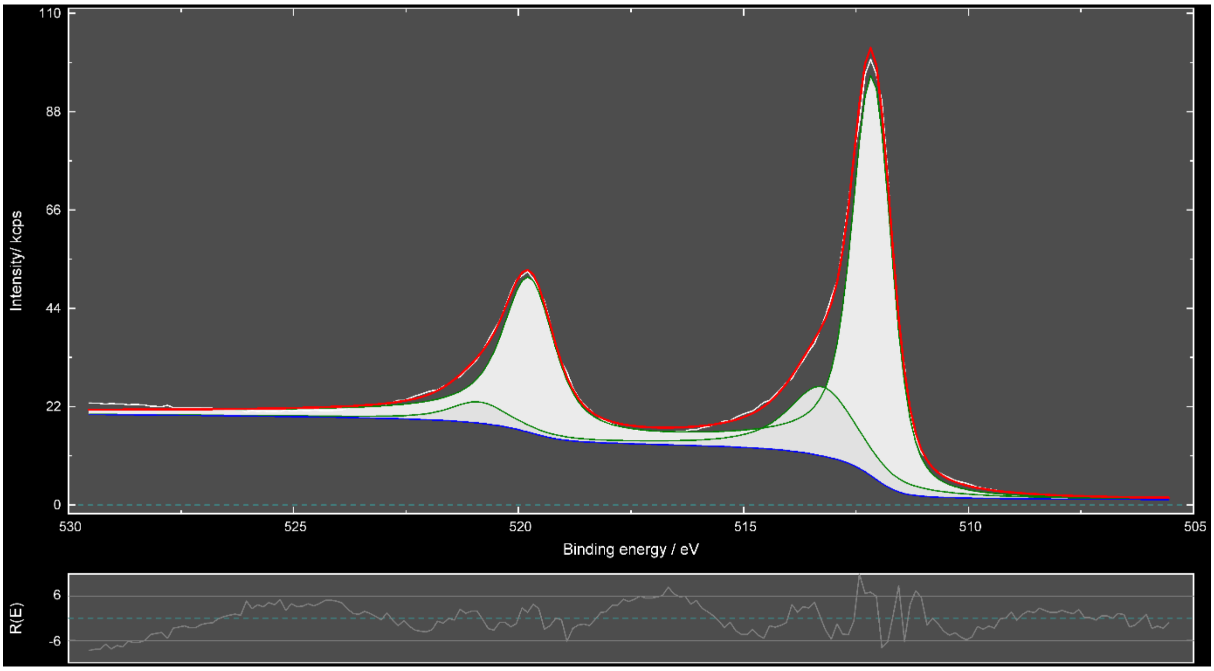

Figure 5.21: XP spectrum and fitting of vanadium foil, electropolished and Ar^+ sputtered.

Table 7: Fitting results of vanadium foil, electropolished and Ar^+ sputtered (Figure 5.21).

Identified species	Position of doublet V $2p_{3/2}$ and V $2p_{1/2}$ (eV)		Area ratio V $2p_{3/2}$: V $2p_{1/2}$	Share (%)
V (metal)	512.12	519.74	1.93 : 1	81.2 %
“VO”	513.26	520.88	4.05 : 1	18.8 %

Fitting of the signals indicated two components. Table 7 gives an overview of the found parameters. Correction of the spectrum by the C1s signal gave the absolute value of 512.12 eV for the metal component and 513.26 eV for a further compound denoted as oxide “VO”. It is most likely that sputtering could not remove any oxide, even though a strong O1s signal was missing. Most of the signal could be determined definitely to be vanadium metal, showing a characteristic asymmetry in peak shape.

For an identification of further vanadium oxides, the spectrum of the (same) polished, but non-sputtered foil, bearing the natural thin oxide, was taken. Figure 5.22 shows, without further analysis, a great many signals, which were fitted by employing the findings for V(0) and the lower oxide “VO”.

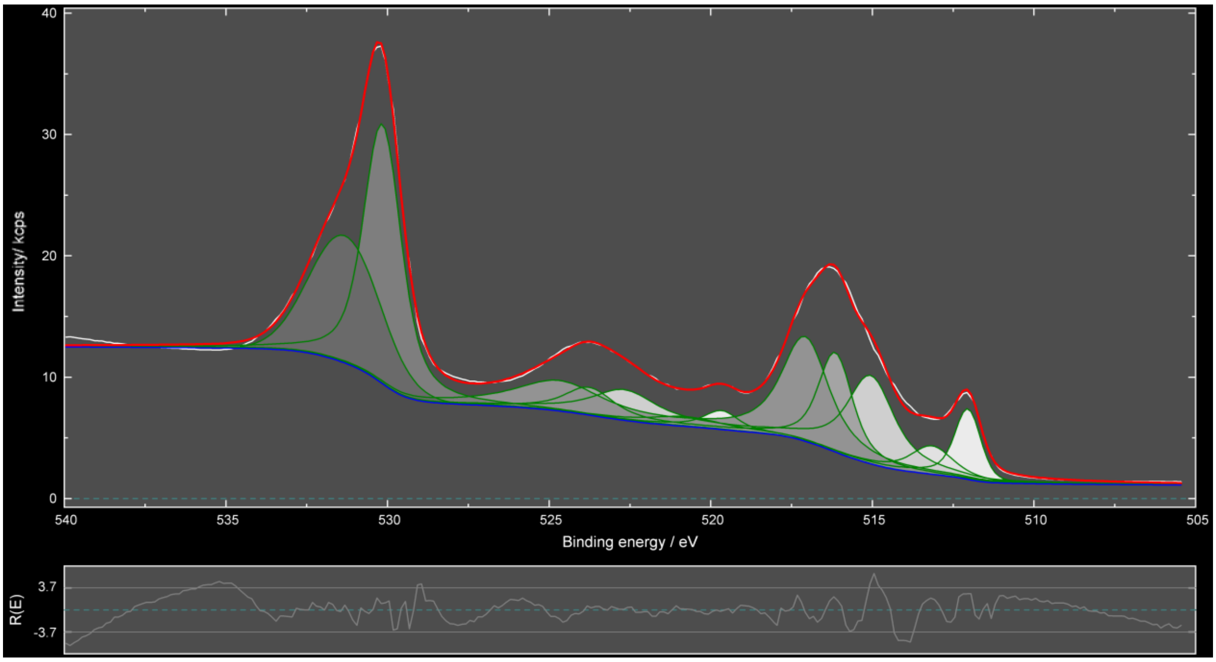

Figure 5.22: XP spectrum and fitting of electropolished vanadium foil.

Table 8: Fitting results of electropolished vanadium foil (Figure 5.22).

Identified species	Position of doublet V $2p_{3/2}$ and V $2p_{1/2}$ (eV)		Area ratio V $2p_{3/2}$: V $2p_{1/2}$	Share (%)
V (metal)	512.12	519.74	1.93 : 1	81.2 %
“VO”	513.26	520.88	4.05 : 1	18.8 %
V_2O_3	515.15	522.77	2.03 : 1	26.1 %
V_6O_{13}	516.25	523.87	2.30 : 1	20.3 %
V_2O_5	517.18	524.80	1.78 : 1	33.6 %
O-1	530.26			
O-2	531.43			

Fitting of the spectrum was, however, hardly possible. To obtain a better result, the convolution method was chosen to adopt the peak shape, having the disadvantage that FWMH-values were mathematically not determinable and, therefore, could not be consulted for the peak analysis. Furthermore, the O1s signals and the background were included in the iterative fitting procedure. The signal for the vanadium metal was taken to correct the spectrum. The mentioned proposed correction to the O1s signal was not applied due to at least two different attributes found to not match perfectly to reported values for vanadium oxides. The reason for the broad signals was probably formed hydroxide or surface adsorbed oxygen. Three further, in sum four, oxides could be identified and allocated to the oxides V_2O_3 (515.15 eV), V_6O_{13} (516.25 eV) and V_2O_5 (517.18 eV), with regard to the absolute values (see Table 8). Even though it can be assumed that VO_2 is also present in the redox equilibrium, fitting without a further component in the area of 516 eV (see Table 6) was favorable. The high number of identified surface oxides was often reported. By use of angle-resolved XPS, it was found for vanadium foils, bearing a thin natural oxide layer, that the outer part of the oxide film is enriched in V(V) and V(IV) oxidation states, while V(III) and V(II) oxidation states are located in the inner region of the thin film.[215]

However, it was not possible to respect the statistical proportion of peak area, about 2:1 for $p_{3/2}$-$p_{1/2}$-systems, in the fitting procedure for all components. Many reasons can be quoted that especially complicate the vanadium oxide system:

The interference of V2p and O1s is “one of the most serious interference with prominent lines in any spectrum”.[215] A combined fitting, as it was performed, is necessary. This would be further complicated if more oxygen species would arise, e.g. from residues of boric or oxalic acid on the pore walls.

Transition metals of first series have low values for photoelectron efficiencies, leading to comparably low counts, in general.

Photoelectron lines of pure metals can show the mentioned asymmetry. Moreover, energy loss phenomena (to conducting electrons as “plasmons”) may produce measured intensity of about 20 – 25 eV above the binding energy of the parent line. For the vanadium(0) signal at about 512.4 eV, this would mean a possible influence on the O1s signal.

More complex photoelectric processes lead to ions left in an excited state a few electronvolts above the ground state, reducing the measured kinetic energy (increasing the calculated binding energy) of the photoelectrons and leading to shake-up lines. The intensity of shake-up satellites may approach that of the main line.[213] The satellites are often observed with paramagnetic compounds, which applies to V(II) – V(IV) oxide. Therefore, they must be considered in XPS V2p fits.[216] Zimmermann *et al.* showed a strong hybridization between V3d and O2p levels as responsible for the satellites of $V2p_{3/2}$, found between the $V2p_{1/2}$ and O1s signals, and on the high binding energy side of O1s peak for $V2p_{1/2}$.[217]

The assumed satellites especially could have an enormous influence on the moderate quality of the fitting, but it was impossible to include ratios for the satellites on top. However, it seemed that the ratios of the identified oxides balanced each other with no particular emphasis for a specific oxidation state. The indicated share of V(V) is probably too high because of possible satellite contribution to $V2p_{1/2}$. In contrast, it is also reported that V_2O_5 degrades slowly under the X-ray beam to V(IV) compounds.[218]

The oxygen signals were not evaluated at all. In general two peaks at 529.8 eV and 530.0 eV are expected for the oxides.[214] The spectra taken always showed energy contributions of more than 530 eV. The spectra of the anodically oxidized foils discussed in the following hypothesize detected residues of the electrolyte components boric or oxalic acid.

Figure 5.23 shows the fitted spectrum for an anodized foil (see also Figure 5.20). In comparison with the foil reoxidized by air (see Figure 5.22), several differences are striking: The signal for metallic vanadium vanished, the peak shapes are much more symmetric, and the intensity shifted to higher binding energies. Fitting confirmed higher oxidation states (binding energies) compared to the previous samples, as expected. The fit for the components V_2O_3, VO_2, and V_6O_{13} was quite good. Even the tendency for the 2:1 splitting ratio could be passably maintained. Again, the approximation for V_2O_5 was less sufficient, but nevertheless a high share of the V(V) oxidation state of more than 50 % was determined (see Table 9).

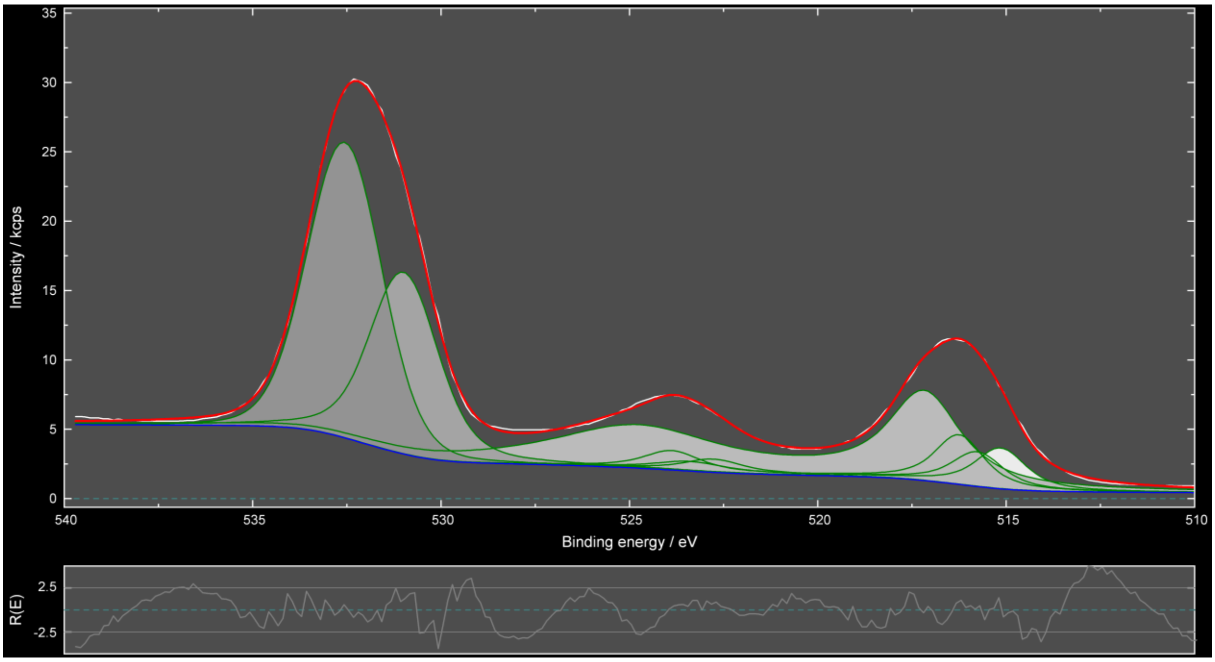

Figure 5.23: XP spectrum and fitting of anodized vanadium foil (AVO).

Table 9: Fitting results of anodized vanadium foil (AVO) (Figure 5.23).

Identified species	Position of doublet V $2p_{3/2}$ and V $2p_{1/2}$ (eV)		Area ratio V $2p_{3/2}$: V $2p_{1/2}$	Share (%)
V_2O_3	515.15	522.77	2.58 : 1	12.8 %
VO_2	515.77	523.79	2.52 : 1	11.2 %
V_6O_{13}	516.25	523.87	2.12 : 1	15.8 %
V_2O_5	517.18	524.80	0.85 : 1	60.1 %
O-1	531.00			
O-2	532.56			

The results show that, even though the anodized foils lost their orange appearance to become blackish, a high amount of V_2O_5 must still be present. The synthesized porous oxides were definitely of higher oxidation state than the natural oxide on vanadium foils. The mixture of different oxides may not even be a disadvantage for applications in catalysis, where switching of the states plays a crucial role.

The short washing procedure after the anodization and the multiple O1s contributions moreover hypothesized possible residues of electrolyte within the pores. This could have an impact on the distribution of the different oxides in the layer. For analysis, the anodized foil was sputtered to measure a depth profile, and again a spectrum was taken (see Figure 5.24). The spectrum showed a very broad signal for the vanadium species, definitely lower oxidized than the surface. Fitting was of low quality by with the values found for the different oxides so far, especially in the region of 514 eV binding energy. Obviously, even contributions of strongly reduced vanadium oxide “VO” had to be considered.

Remarkably, the contribution of V_6O_{15} was missing. In other, even worse fitting models, VO_2 was alternatively missing. However, still a high share of V_2O_5 was detected (see Table 10). An explanation may be provided by the porous structure of the oxide, consisting of “protected” oxide within the pore walls and material being exposed via the channels to redox active components. The backbone of the structure would probably still consist of V_2O_5, formed by the anodization. The contact with oxalic acid at the channel walls, however, would lead to reductive processes.

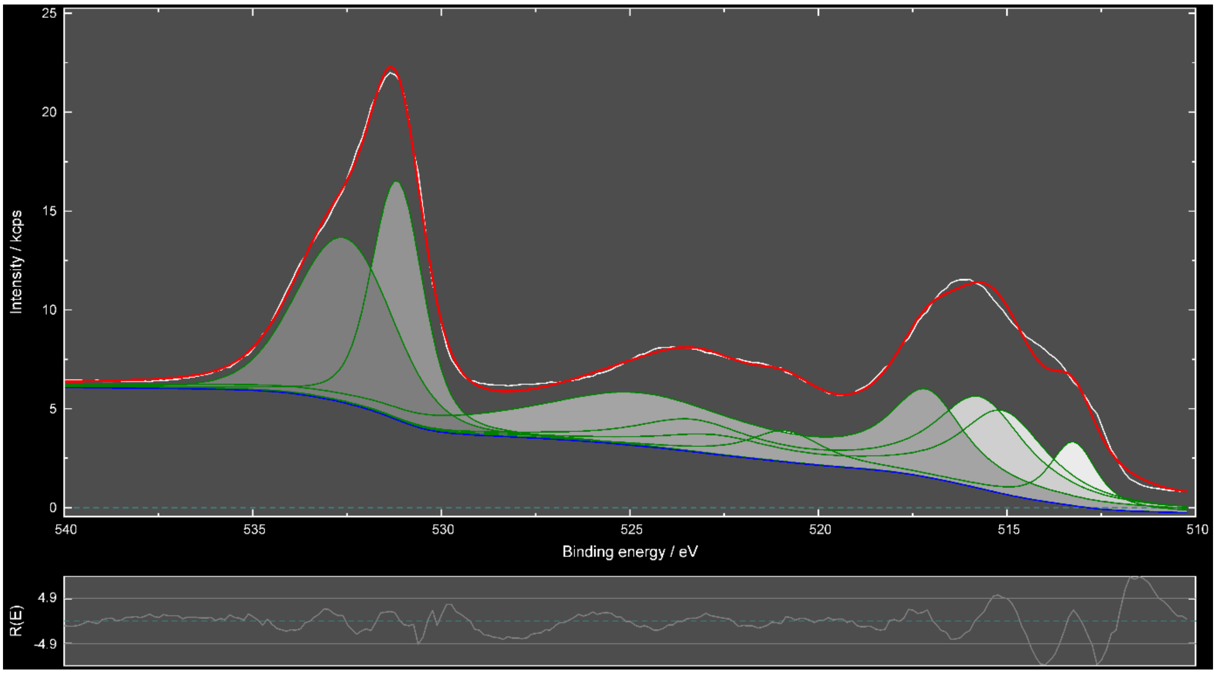

Figure 5.24: XP spectrum and fitting of anodized vanadium foil (AVO) that was Ar^+ sputtered.

Table 10: Fitting results of anodized vanadium foil (AVO), Ar^+ sputtered (Figure 5.24).

Identified species	Position of doublet V $2p_{3/2}$ and V $2p_{1/2}$ (eV)		Area ratio V $2p_{3/2}$: V $2p_{1/2}$	Share (%)
"VO"	513.26	520.88	1.14 : 1	11.9 %
V_2O_3	515.15	522.77	3.47 : 1	21.6 %
VO_2	515.77	523.79	2.31 : 1	27.4 %
V_2O_5	517.18	524.80	0.53 : 1	39.1 %
O-1	531.19			
O-2	532.60			

5.4 Application of Porous AVO in Catalysis

Due to the catalytic properties of V_2O_5, it is no wonder that vanadium is also found in many biological systems. Especially where the metal is easy available, as in several marine organisms (ascidians, algae) or fungi,[219–221] it acts mostly as active center or co-factor in enzymes. Vanadium haloperoxidases use hydrogen peroxide, H_2O_2, to catalyze the oxidation of halides to the corresponding hypohalous acids.[222] In organisms, the produced halogenated compounds seem to play a key role as biocides. Vanadium haloperoxidases were employed beyond halogenations[223] to sulfoxidations[224,225] and behaved similar to the famous horseradish peroxidase with peroxidase substrates.[226]

In laboratory, many compounds were developed mimicking the vanadium haloperoxidase activity. The mainly used organometallic complexes show good results for e.g. halogenation,[227] sulfoxidation,[228] epoxidation,[238] hydroxylation of alkenes,[229] oxidation of alcohols,[230] and oxidative dehydrogenation of alkanes.[231] The active species in these catalysts were found to be oxoperoxovanadium(V) complexes.[232]

Bulk vanadium pentoxide, what it is currently in use as a catalyst, is required in high amounts due to low surface to volume ratio.[233,234] However, vanadium oxide nanoparticles or other nanoarchitectures, such as wires, allow for significantly better performances for haloperoxidase activity.[235–237]

TiO_2/V_2O_5 composites on top of a polymer-supporting layer are capable of filtering water and removing water pollutants to produce clean water without membrane fouling.[238] Mesoporous nanocomposite membranes with vanadium oxide embedded in Al_2O_3 were investigated for styrene oxidation[239] and cyclohexane dehydrogenation.[240]

In principle, an application of the AVO layers as self-supporting membranes, when separated from the underlying metal, would be imaginable. For a start, the vanadium peroxidase-like activity of the AVO was studied to analyze its potential to act as a catalytic membrane in reaction flow processes.[a]

Because self-supporting oxide layers were not accessible yet, the reactions were performed including the supporting metal. The nanoporous oxide layers show a significant reaction using the chromogenic heme peroxidase substrate 2,2-azino-bis(3-ethylbenzothiazoline-6-sulfonic acid) (ABTS). In the presence of H_2O_2, a green (maximum absorbance 405 nm) radical cation ABTS^{*+} is created, even if just one-eigth of the whole 2 cm circular specimen is used as catalyst for the peroxidative reaction (see Figure 5.25). A possible catalytic mechanism was proposed based on the layered V_2O_5 orthorhombic structure by experimental results of nanowires.[235]

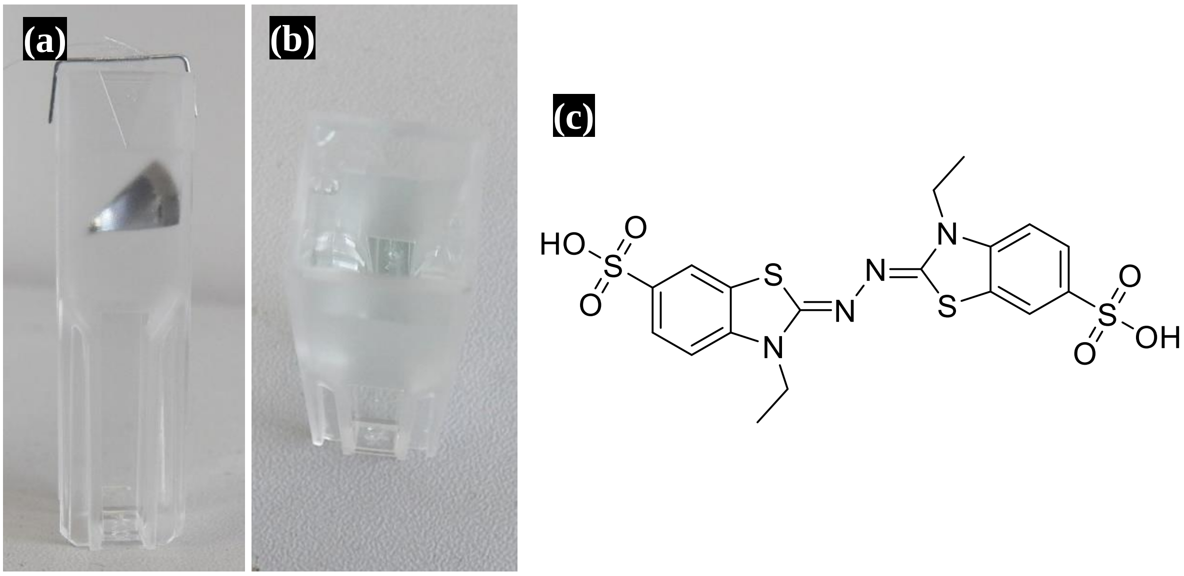

Figure 5.25: Photographs (taken by [redacted]) showing (a) the test arrangement by using the oxidized metal foil directly within a measuring cuvette, fixed by a nylon band; (b) greenish solution after the reaction indicating the formation of ABTS^{*+}; (c) structural formula of ABTS.

The slope of the absorption of light at 405 nm, determined after the detected start of the oxidation reaction, is a measure of the catalytic activity of the analyzed surface. Figure 5.26 reflects the average results of the reaction speed for measured anodized foils.

---

[a] Approach and catalytic tests are in analogy to André *et al.*[235]. The tests were performed by [redacted].

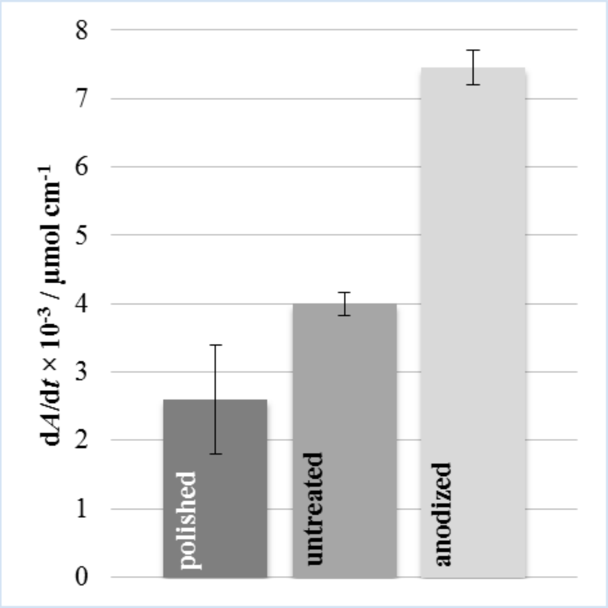

Figure 5.26: Catalytic activity of vanadium surfaces (polished, untreated, anodized) by determination of the slope of the absorption at 405 nm ($ABTS^{*+}$) with reaction time.

To ensure that the measured peroxidase-like activity was a property of the oxide layer formed by anodization, pieces of vanadium foil were analyzed which were either untreated or only electropolished. The untreated foils were used as purchased, bearing oxide formed during the production process. The polished foils were covered just by the very thin oxide layer of a few nanometers due to reoxidation in air.

It is obvious that the oxidation reaction forming the green radical cation was much faster if anodic oxide was present on the vanadium foils. In comparison, the electropolished foil showed the lowest catalytic effect (see Figure 5.26). The catalytic effect of vanadium oxide becomes even more distinct if the active surface of the used small metal pieces is considered. The experimental arrangement did not allow the testing of only the activated, by anodization, or deactivated, by electropolishing, areas. Because the back side of the metal pieces was included, more than 50 % of the surfaces were always identical.

All foils showed a certain peroxidase activity toward the ABTS test, but no significant oxidation reaction was observed if the vanadium was completely omitted from the experimental setup. Additional control experiments using the anodized foils in the absence of either the electron donor (ABTS) or H_2O_2 showed that no oxidative reaction occurs. Both components are required for the reaction, as is also the case for vanadium haloperoxidase.[241,242]

However, the anodized oxide layers tended to dissolve in the test solutions, always exposing a fresh surface until the foils became blank after a while (see Figure 5.27 (a)). A possible reason for the instability of V_2O_5, known to be amphoteric, might be the low pH. On the other hand, even the oxidative conditions could have an influence due to the fact that the XPS analysis showed the coexistence of lower oxidation states. To display the change in the catalytic surface, measurements were performed with virgin foils, repeatedly resubmitted. Figure 5.27 (b) shows the calculated slopes of the absorption curve for three consecutively made measurements. The loss of anodic oxide drastically reduced the activity until only a basic reactivity was left, comparable to what was found for the polished foils. The results clearly show the superiority of the produced anodic oxide. An effect of dissolved vanadium oxide on the catalytic ABTS test can be excluded. In a comparable testing series with V_2O_5 nanowires, it was shown that the catalytic properties are surface-dependent and that free orthovanadate anions VO_4^{3-} show no reaction with the ABTS test.[235]

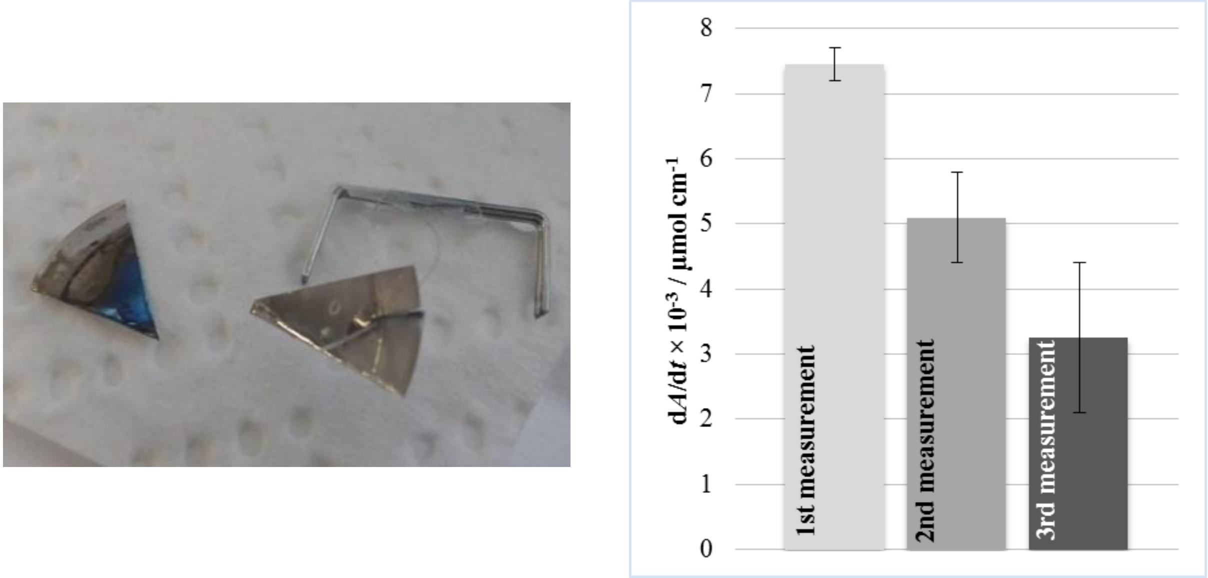

Figure 5.27: (a) Photograph (taken by [redacted]) of oxidized foil before (left) and after reaction (right). (b) Catalytic activity of anodized vanadium surfaces for three consecutively made measurements by determination of the slope of the absorption at 405 nm ($ABTS^{\bullet+}$) with reaction time.

5.5 Conclusions and Outlook

This work reports the second known preparation protocol for ordered AVO and is the first to use a HF-free route. Additionally, the chemical nature of the AVO was studied in detail with XPS, and its catalytic activity was examined.

The generation of AVO membranes is very challenging due to the fact that vanadium oxides are amphoteric and thus require very precise conditions in order to balance the competition between chemical etching on the surface and electrochemical growing of AVO at the oxide/metal interface. This behavior is well-illustrated by the characteristic shape of the current-time curves obtained and discussed in this work.

Building on previous work in our group, the anodization of vanadium foils was established using an electrolyte composed of diethylene glycol, saturated with boric acid, small amounts of water, and oxalic acid as the etching and complexing agent. This resulted in well-ordered arrays of vanadium oxide nanopores. Applying a voltage of typically 40 V yielded pore diameters of 50 – 60 nm.

The post-treatment turned out to be extremely important for AVO and necessary modifications have been implemented. By a careful washing and drying procedure, an oxide layer of up to 3 µm thickness could be stabilized. In contrast to the results published by Yang *et al.*,[31] the use of complex, fluoride-containing electrolytes could be avoided. Additionally, porous rather than tubular structures have been obtained here.

The (partial) reduction of the freshly formed vanadium(V) oxide to vanadium(IV) by residual oxalic acid was already visible by a color change from orange to black. This was confirmed in this work by a detailed XPS analysis. An adequate fitting procedure revealed that a high share, more than 50 % overall, vanadium(V) was still present, even though the oxide appeared blackish. Analysis of oxide from deeper layers within the AVO membrane showed that the less effective washing of the porous layer inside the pores led to a stronger degree of oxide reduction by the residual oxalic acid. Nevertheless, it was shown that the oxidation state of the anodized oxide was still higher compared to the “natural oxide” which had been formed on the metal foil during its fabrication process.

The applicability of AVO as a catalyst was successfully demonstrated. A peroxidase activity test was conducted using the oxidized metal foils. The test showed that the ABTS oxidation reaction monitored in the test was accelerated by the anodic oxide, indicating high catalytic activity.

For future applications, it would be desirable to further reduce the solubility of the formed AVO in the electrolyte to yield an increased oxide layer thickness. Additionally, a stabilization of the highest oxidation state vanadium(V) would be beneficial. Therefore, different etching agents with less reduction potential than oxalic acid should be tested in future experiments. Increasing the electrolyte’s pH could likewise lead to improved oxide layers.

6 Experimentals

6.1 Starting Materials and Electrochemical Equipment

6.1.1 Metal Foils and Chemicals

All starting materials and chemicals were used without further purification. As basic raw materials, commercially available metal foils were purchased from the suppliers ABCR, Sigma Aldrich, Alfa Aesar, and Goodfellow in sheets of minimum 10 × 10 cm up to roll good (see Table 11). If not otherwise noted, the foils were used as delivered.

Table 11: List of metal foils used for the electrochemical anodization reactions. Lines marked in bold represent the standard foil used in most reactions.

Purity (metals base)	Thickness	Supplier	Product information
Titanium[(a)]			
99.7 %	**0.25 mm**	**Sigma Aldrich**	
Aluminum[(b)]			
99.997 %	**0.1 mm**	**Alfa Aesar**	***Puratronic®***
99.99 %	0.1 mm	Alfa Aesar	
99.8 %	0.05 mm	Sigma Aldrich	
99.5 %	0.1 mm	Goodfellow	
99.45 %	0.025 mm	Alfa Aesar	
99 %	0.25 mm	Alfa Aesar	*annealed; Si and Fe (combined) typically 1 %*
Vanadium[(a)]			
99.8 %	**0.127 mm**	**ABCR**	

(a) Foils were machined to 20 mm circular size by cylindrical turning (workshop).

(b) Foils were cut down to a diameter of 20 mm (alternatively 25 mm or 35 mm) using a stamping tool.

Frequently Used Chemicals (in Alphabetical Order)

Acetone (p.a., VWR)
Ammonium fluoride (p.a., Sigma Aldrich)
1-butanol (99 %, Acros)
Boric acid (p.a., Roth)
Chromium(VI) oxide (Sigma Aldrich)
Copper(II) chloride dihydrate (VWR Prolabo)
Diethylene glycol (DEG) (99 %, Sigma Aldrich)
Ethanol (abs., 99.8 %, Sigma Aldrich)
Ethylene glycol (EG) (99 %, Chempur)
Hydrochloric acid (37 %, VWR Prolabo)
Methanol (p.a., Sigma Aldrich)
Oxalic acid dihydrate (p.a., Sigma Aldrich)
Perchloric acid (70 %, Acros)
Phosphoric acid (85 %, p.a., Acros)
Sodium hydroxide (98.5 %, p.a., Acros)
Sulfuric acid (95 – 97%, p.a., Sigma Aldrich)
Water (MilliQ, 18.2 MΩ cm)

6.1.2 Electrochemical Setups and Equipment

For the electrochemical reactions, two different types of setups were used, the so-called PTFE Setup and the Cu-block Setup. Both systems were homemade by the institute's workshop and share a common concept: Circular metal foils as starting material were fixed by sealing horizontally onto a copper contact. The upper side, where the electrochemical reaction takes place, was facing the electrolyte. The electrolyte was stored in a PTFE vessel, in which the counter electrode (cathode) was immersed. All electrochemical reactions were performed with a two-electrode setting. More details for the two standard setups, including modifications, are given in the following pages.

PTFE Setup

The PTFE Setup, together with the graphite rod cathode, was the standard setup for all Ti anodization reactions. It consists of three parts manufactured out of PTFE and completely insulating from the exterior. The bottom part includes the sample holder, a 20 mm copper contact in the center, on which a same-sized, circular metal foil of starting material was placed. The middle section is a long cylindrical reaction vessel, which has a 15 mm wide and 18 mm deep hole in its bottom, connecting the metal foil on the copper contact with the electrolyte. Both parts are connected by O-ring seals and are topped by a third piece, which is used to tightly screw the vessel and bottom together (see Figure 6.1).

Figure 6.1: Photographs of the PTFE Setup showing (a) the bottom part with Cu contact, (b) the vessel mounted, and (c) the whole setting.

Figure 6.2: Photograph of a graphite rod electrode with Centering Device and thermometer.

Electrolyte, usually 50 mL, was filled in and the counter electrode (cathode) was placed from the upper side into the electrolyte to the desired depth. In order to center graphite rod electrodes and keep a set distance between the two electrodes, a “Centering Device” was developed. This extra part fixes the cathode directly on top of the PTFE Setup, while still providing apertures for gas exchange and a thermometer to control the internal temperature (see Figure 6.2). The whole setup is placed by an attachment bar deeply in a temperature bath, which is controlled via a copper coil by a (cryo-) thermostat. Indirect cooling through the PTFE walls of the reaction vessel led to relatively long heating and cooling times of usually 15 – 30 min to the desired temperature). However, the use of PTFE makes the setup inert to every electrolyte, in particular fluoride and HF-containing mixtures used for the anodization of titanium. The slow heat exchange and the high corrosiveness were reasons why a PTFE-covered glass thermometer was used instead of an external sensor to measure and control the temperature by the thermostat.

Cu-Block Setup

In conjunction with diverse cathodes, the Cu-block Setup was used for the polishing of titanium and vanadium foils. Moreover, it was used for the anodization of aluminum and vanadium. The construction of the Cu-block Setup offers an enhanced application spectrum compared to the PTFE Setup. A bottom of solid copper, 10 cm in diameter, with high heat capacity serves as the cylindrical mounting platform and electric contact for the metal foils. The block is topped by a vessel of PTFE, with an aperture of typically 15 mm in diameter and 12 mm in depth on the bottom, and tightened by an O-ring and six screws. The profile of the O-ring seal, however, resulted in a higher active area, usually about 1 mm in extra diameter, leading to a 16 mm total oxidation diameter.

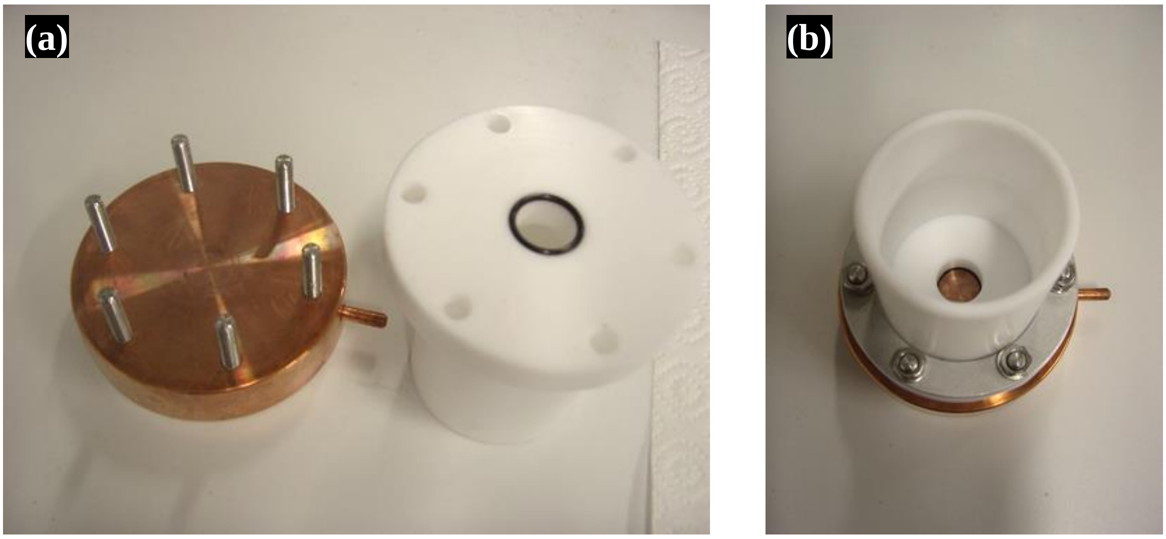

Figure 6.3: Photographs of the Cu-block Setup showing (a) the single parts and (b) the mounted setup.

Low height of the vessel makes an inside cooling by a glass coil possible (see Figure 6.4 (a)). Moreover, external cooling by a temperature bath was not possible due to the lack of insulation around the copper block. The very effective direct control enabled fast and strong cooling/heating possible. Thus, the temperature was reliably adjusted by a connected cryostat. Polishing of the aluminum foils was performed in a modified PTFE vessel. The 12 mm thick bottom part was machined conically down to 5 mm to allow better convection of the polishing electrolyte.

Fluoride-containing electrolytes are not compatible with the cooling glass coil. For these cases, an alternative PTFE coil was hot-cured from a tube, though its heat exchange capacity was slightly lower (see Figure 6.4 (a)).

For the production of aluminum oxide discs with varying diameter, PTFE vessels with aperture sizes other than the standard were established. Therefore, two-part vessels were developed consisting of a common cylindrical container and separate, exchangeable bottom parts of different apertures (see Figure 6.4 (b)).

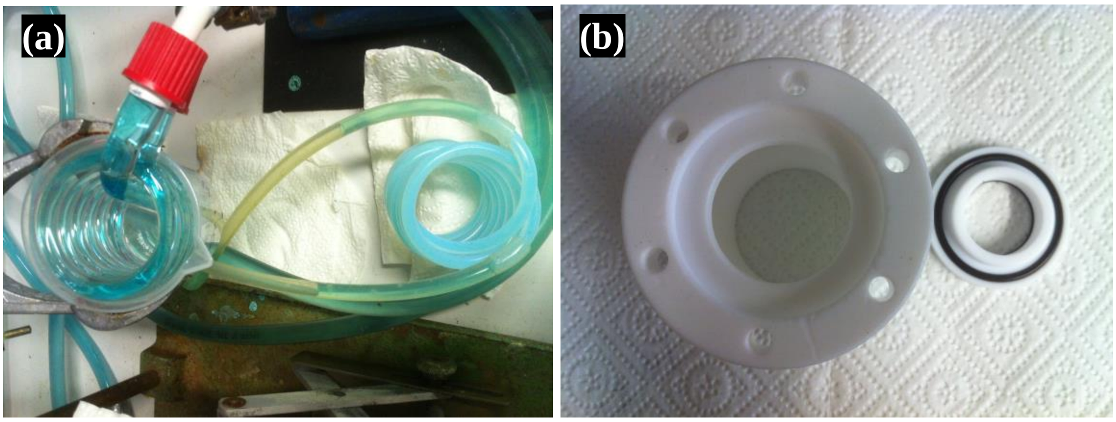

Figure 6.4: Photographs of (a) the used cooling coils from glass and PTFE and (b) the PTFE two-part vessel.

All in all, vessels with aperture sizes of 10 mm, 15 mm (for the common 16 mm oxide disc size and for 13 mm with an alternative flat seal), 20 mm, and 30 mm were provided.

For the production of 20 and 30 mm oxide discs, polishing was naturally performed using the corresponding vessels.

Electrodes (Cathodes)

Different electrodes were used as cathodes for the electrochemical reactions. The set distance to the anode, the metal foil, was typically measured from the bottom of the setup vessels and, in most cases, from an extra 2 mm above the aperture. However, the absolute distance between anode and cathode is indicated for each electrochemical reaction type in the respective Chapters 6.3 to 6.5.

Graphite rod electrodes with a diameter of 25 mm were used for the anodization of titanium (in combination with the PTFE Setup and typically the Centering Device) as well as the electropolishing and anodization of vanadium (in combination with the Cu-block Setup). Titanium sheets from the standard titanium foil were used as cathodes for the electropolishing of titanium. Bent in an “L”-shape, the bottom part of the cathode was oriented parallel to the metal foils to be polished. Likewise, a palladium sheet electrode was applied typically for the reverse-bias method to separate titanium and its anodic oxide in solution as well as for the electrochemical pore opening procedure of aluminum oxide.

Stirring Electrodes

For the electropolishing and anodization of aluminum, stirring electrodes were used due to the need for extra agitation. The placement of the foil on the ground of the reaction vessel makes the application of magnetic stir bars unfavorable, which is the common way stirring is conducted elsewhere.

For first anodization experiments and for the electropolishing, a high-speed rotating disk electrode (Autolab RDE, Eco Chemie/Metrohm) was used. The active part of the cathode is a 3 mm Pt disc. The velocity necessary for effective stirring was 5000 rpm. Maximum current has to be fixed at 500 mA, limiting the current within the first seconds of a typical aluminum electropolishing.

Figure 6.5: Photograph of the homemade rotating electrode showing the motor and the stirring part.

A homemade electrode was used replacing the high speed electrode in the anodization of aluminum. The electrode is composed of a laboratory stirring device (Velp Scientifica Stirrer ES), electrically insulated to the stirring part, which is contacted by a brass sliding contact. An alligator clamp connects the sliding contact with the power supply. As the moving part, a massive titanium, diameter of 12 mm, with machined cavities for a better stirring was used. The motor speed for sufficient convection was the maximum rate of 1300 rpm (see Figure 6.5).

The moving parts had to be checked from time to time due to abrasion of the brush contact. Non-optimal connection then led to current oscillation which, however, usually had no influence on the result, not even on the thickness of the produced oxide layer. On the other hand, very close contact between the brush and stirrer caused heat formation, leading to softening and deformation of the polymeric electric insulation against the motor.

As an advantage, it emerged that both different stirring electrode systems led to passably similar current flow and therefore could replace each other within the limits.

Power Supplies and Electric Equipment

Electric direct current for the electrochemical reactions was provided using one the following regulated power supplies: Voltcraft PSP 1204 (Conrad Electronics) power sources were used up to 80 V. A Voltcraft PSP 1803 (Conrad Electronics) double power source was alternatively used up to 40 V. A Keithley 2430 SourceMeter (Keithley) high precise power source was used up to 105 V.

The reactions were performed in potentiostatic mode, allowing the current to adjust after the resistance. Different accuracy of the power supplies did not seem to have a crucial influence on the anodization results. For the rare application of galvanostatic mode to electropolishing, the Keithley power supply was used.

Electric current flow was directly controlled in electropolishing reactions (high current) by the power supplies, and in anodization reactions (low current) by connected multimeters (Voltcraft VC960 and VC170, Conrad Electronics). Current-time curves were recorded using multimeter VC960 with automated data acquisition (usual recording time every 2 s).

All connections between sources, multimeters, and setups were made with banana plugs and alligator clamps.

6.2 Analytical Methods

Scanning Electron Microscopy (SEM)

The surface topography of the anodic oxides was examined using a Quanta 200 FEG (FEI/ Philips) scanning electron microscope and ETH (Everhard Thornley) detector. The anodized metal foils or anodic oxide flakes were attached to an aluminum stub using adhesive conductive carbon tape. Titanium and vanadium oxide was measured without further treatment. Aluminum oxide was sputtered with a layer of gold in order to avoid surface charging (7.5 nm by a sputter coater BAL-TEC MED 020, equipped with BAL-TEC QSG 070 quartz crystal microbalance).

Energy Dispersive X-ray Spectroscopy (EDX)

Space-resolved elemental analysis was performed using SEM-EDX at a NovaNano FEG-SEM 630 (FEI/ Philips) scanning electron microscope equipped with a built in EDAX Genesis detector.

SEM-EDX on used AAO filtration membranes was done by [redacted].

Transmission Electron Microscopy (TEM)

The size of the nanoparticles was determined using transmission electron microscopy. Predominantly, a Philips EM420 instrument with an acceleration voltage of 120 kV and LaB_6-cathode as electron source was used; images were taken by a slow-scan CCD-camera. In single cases, a Zeiss LEO 906e instrument was alternatively used. Specimens for TEM measurements were prepared by dropping ultrasonicated suspensions of the particles onto a Cu grid coated with an amorphous carbon layer.

The TEM images of the nanoparticles used for the filtration experiments were taken by [redacted]. [redacted] and [redacted] took the image of the broken ATO tubes.

3D-Laser Scanning Microscopy

The surface morphology of electropolished metal foils was investigated with a Keyence VK-8710 laser microscope equipped with a movable x/y-stage. For clarification, the obtained 3D images were extended by factor of 10 on the z-axis, corresponding to the sample's height. Surface roughness is commonly measured as R_a (roughness average) or, as it was determined here with surfaces after polishing, by the value R_q, the root-mean-squared deviation of the average roughness:

$$R_q = \sqrt{\frac{1}{MN} \times \sum_{m=1}^{M} \sum_{n=1}^{N} (z(x_m, y_n) - < z >)^2}$$

with height z in x,y-site and mean value for z < z >.

Confocal laser scanning microscopy (CLSM)

Functionalization of AAO membranes with the aminosilane APTES was analyzed by the emission of coupled FITC dye. The excitation was performed by a 488 nm blue Ar laser. The images were taken with a Leica TCS Sp2 X1 microscope and an objective lens HC PL FLUOTAR 50.0 x 0.80 by [redacted].

X-ray Photoelectron Spectroscopy (XPS)

Oxidation states of the anodic vanadium oxide were determined by an X-ray photoelectron spectrometer PHI 5600 ci (Physical Electronics). The instrument was equipped with a standard Mg K_α X-ray tube and an Al K_α monochromator X-ray source (14 kV, 300 W). All scans were performed using monochromated X-rays. The pass energy of survey scans was set to 187.85 eV, while the analyzed and fitted determinations of vanadium oxidation states were carried out with a pass energy of 58.7 eV.

Metal foil samples were degassed for several hours (powder samples overnight) in pre-vacuum before entering the analysis chamber. Measurements were performed for 1 – 6 h, during which the pressure in the analysis chamber was maintained between 10^{-9} and 10^{-10} Pa.

To clean surfaces from adhesives or analyze even deeper layers within the materials, some specimens were sputtered directly in the analysis chamber. The Ar^+ bombardment was performed with an ion current of about 10 mA, rastered over an area of 2 mm × 2 mm.

Fitting and plotting of the spectra was performed using Unifit 2011 software (Unifit Scientific Software GmbH). Background correction (via Shirley function) was involved in the fitting of the signals with mixed Lorentzian-Gaussian curves using the convolution method. The spectra were generally calibrated to adventitious carbon (C 1s 284.8 eV), unless otherwise specified.

Determination of the oxidation states of anodic vanadium oxide on vanadium foil was performed in the following order: A polished (and sputtered) vanadium foil was analyzed to determine the V(0) signal. The gap between $V2p_{3/2}$ and $V2p_{1/2}$ was determined to be 7.62 eV and the Gauss parameter of the signals was 0.763 eV. Both values were retained for the further fittings of the O1s and V2p area. The theoretical 2:1 spin-orbit splitting ratio for the V2p signal area was considered the best possible.

Absolute values for different vanadium oxides were identified by measuring a vanadium foil bearing just a thin natural oxide layer. Calibration was performed here to the value for V(0) and identification of oxidation states was in accordance with literature data. The oxygen signal was usually fitted with two different components but not interpreted. Analysis of anodic vanadium oxide was done by comparison with known determined absolute values for different vanadium oxides. For the analysis of non-surface oxide, vanadium foils bearing anodic vanadium oxide were sputtered for 5 min. Exact fitting parameters can be found in the appendix (see Section 7).

X-ray Diffraction (XRD)

Crystallinity of anodic oxide layers was surveyed by X-ray diffraction patterns recorded with a Bruker AXS D8 Discover diffractometer equipped with a HiStar detector using graphite monochromatized Cu Kα radiation. Individual frames were typically recorded at $2\Theta = 24°$, 34°, 44°, 54°, 64°, 74°, 84° (detector distance 150 mm, detector range $\Delta(2\Theta) = 35°$). X-ray diffraction patterns were integrated from individual frames using the Bruker AXS GADDS software package and merged using Bruker AXS EVA (assisted by [redacted]).

UV-Vis Spectroscopy

The relative concentration of nanoparticle dispersions was determined by UV-Vis absorption measurements using a Varian Cary 5000 UV/VIS-NIR spectrophotometer. In this context, Hellma quartz glass Suprasil® cuvettes with layer thickness of 10 mm (volume 1 mL) were used.

Catalytic tests with anodic vanadium oxide were performed with 2.5 mL plastic cuvettes containing a small piece of metal foil.

BET Surface Area Determination

The surface area of anodic aluminum oxide was determined by a Quantachrome Autosorb AS-6B instrument applying multipoint BET (Brunauer, Emmett, Teller) measurements.

The pore size distribution was calculated from the adsorption branch according to the BJH method (Barrett, Joyner, Halenda), taking the capillary condensation effect as a basis.

For the measurements, four unopened AAO membranes (35 V, 2 h) were crushed and weighed to a total of 22.9 mg.

BET measurements and analysis was performed by [redacted].

6.3 Synthesis of Anodic Titanium Oxide (ATO)

6.3.1 Electropolishing (E) of Titanium

Circular cut titanium foils, 20 mm in diameter, were cleaned by ultrasonication in acetone and water for about 5 min, followed by rinsing with acetone. The foils were inserted into the Cu-block Setup (15 mm aperture) and subjected to electropolishing using 50 mL of an electrolyte. The refrigerated electrolyte was composed of perchloric acid (60 %), butanol, and methanol in a 1:6:9 volumetric ratio.[75] Polishing was carried out with a titanium sheet cathode, set to a distance of about 25 mm from the foil, at a potential of 30 V for 15 min. With time, whitish debris formed on top of the titanium foil, but was washed off after the polishing. After electropolishing, the samples were again sonicated, rinsed, and dried.

6.3.2 Anodization (A1, A2) of Titanium

As for the electropolishing, a two-electrode assembly was used, but with the PTFE Setup instead. Clean, polished foils were brought into the setup, equipped with a graphite rod cathode set to a distance of 20 mm. To keep the cathode centered and at the right height, a special Centering Device was typically mounted on the PTFE vessel of the setup. The electrolyte was freshly prepared: 50 mL of ethylene glycol containing 0.38 % NH_4F and 1.79 % water were used.[75] Anodization reactions were carried out typically between 30 V and 60 V at a reaction temperature of 20 to 25 °C. The temperature was controlled by an external cooling bath. The reaction was started as soon as the setup, including the electrolyte, was in its thermal equilibrium, typically after about 15 – 20 min. The reaction period was adjusted from some minutes to several hours, depending on the intended oxide layer thickness. Depending on the reaction period, a transparent, colorless or opaque golden to olive-green oxide layer was produced.

The subsequent step was chosen according to the anodization purpose: If the performed anodization was the first step (A1) in the typical two-step procedure, the oxidized foil was washed first with water, then acetone, and the oxide layer was subsequently detached by an air blast. The anew blank foil was cleaned by sonication and, again, subjected to a second anodization (A2). Alternatively, if the oxide layer should be kept, typically after A2, the procedure continued as described in the following.

6.3.3 Oxide Layer Separation and Wet Chemical Pore Opening Process

Subsequent to the anodization, various post-treatments applied to ATO layers of 20 – 30 µm thickness, produced at 40 – 60 V. If the surface topography and pore sizes of the samples were checked by SEM, the ATO was treated analogous to the oxide layers after A1 by washing with water and acetone, followed by drying. Depending on the oxide layer thickness, the foil was either analyzed directly or curling of the layer led to detachment of the oxide. Alternatively, the oxidized foil was not removed from the PTFE Setup for washing in order to proceed with a chemical etching of the ATO back side and avoid curling,. The used electrolyte was discarded and, after washing the vessel with water, was replaced by 50 mL of 1 M H_2SO_4. Separation of the oxide from the metal was caused by applying a reverse-bias voltage of - 2.25 V (pole change) for 5 min[92] using a Pd sheet electrode instead of the graphite rod electrode. The detached oxide layer was carefully transported into a water bath for washing and kept wet.

Chemical etching with different kinds of HF-containing etching media was explored. The following diluted solutions of HF were prepared to etch the as-prepared ATO:

First, 1 M H_2SO_4 solution containing 5 % NH_4F according to Fang *et al.*[88] led to dissolution of ATO layers within 2 min. Second, according to Banerjee *et al.*,[93]5 % HF solution likewise led to dissolution of ATO layers. Further tests were made with diluted 2 % HF solution and very short treatment of several seconds. The ATO layers were floated backwards onto the solution to reduce front side etching. Third, the front side was protected with an adhesive polymer from a UV curing glue (Acrifix®192) to prevent etching. Instead of using the reverse-bias method to separate metal and oxide right after the anodization, the oxidized metal foil was washed with EtOH, acetone, and toluene to reduce the water content at the surface while keeping the surface wet. The surface was coated with the glue and cured. The stabilized ATO did not show curling and could be separated from the metal by using a punching tool. Thus, etching of solely the back side was performed with diluted 1 % HF solution for reaction periods of up to ten minutes. The layers were washed with water and the polymeric glue was dissolved in toluene overnight to recover the bare oxide. Alternatively, HF vapor was used as an etching medium. In this approach, dried ATO layers were mounted back side down over PTFE beakers containing 48 % HF solution on polymeric gauze. A short reaction period of 5 min led to inhomogeneous etching, while longer reaction periods led to considerable dissolution of the oxide. None of the described methods with HF led to homogeneous back side etching.

6.3.4 Electrochemical Pore Opening Process and Flattening of the Membranes

Anodizations at 40 or 50 V were terminated by switching the anodization voltage to 80 V, adapted from Wang *et al.*,[97] for a reaction period of 10 min. In the following, the described reverse-bias method was used to detach the ATO from the underlying metal.

Stabilization of the produced membranes in dry state was achieved by wetting with ethylene glycol and drying between flat tiles on a heating plate (200 °C). The membranes kept their flat morphology until a less pronounced curling was observed after some days.

6.4 Synthesis of Anodic Aluminum Oxide (AAO)

This experimental section is arranged according to the consecutive steps in the production of AAO filtration discs. At first, the standard (best working) processes are described for each production step, followed by variations thereof, likewise discussed in Section 4. After giving the experimental details for the filtrations, the section is completed by post-treatments irrespective of the filtration membrane's synthesis procedure.

6.4.1 Electropolishing (E) of Aluminum

Aluminum foil was cut typically to discs of 20 mm in diameter using a stamping tool. Subsequently, these were flattened by a hydraulic press (2-3 tons) to equalize the curved surface after the stamping. The round foils were cleaned in acetone without use of sonication to prevent damaging the soft metal. The foils were inserted into the 15 mm Cu-block Setup, equipped with the conically machined PTFE vessel. Then, electropolishing was performed using 30 mL of a refrigerated electrolyte composed of EtOH or MeOH and $HClO_4$ (70 %) in a 4:1 volumetric ratio.[103] Polishing was carried out with the high-speed stirring electrode set to a distance of 6 mm from the foil, at a potential of 40 V for 2 min. After electropolishing, the samples were rinsed with water and acetone. To reduce the thinning of the metal foil by the polishing, e.g. if extra thick AAO should be produced, the reaction period could be shortened to 1 min without inordinate quality loss.

The standard procedure provided an actual polished area with a diameter of 16 mm. For the electropolishing of areas with 20 or 30 mm diameters, the respective PTFE vessels of the Cu-block Setup were used with circular Al foils cut to typically 5 mm larger in size. Here, the homemade stirring electrodes with the titanium bar were used and also adjusted to 6 mm distance from the foils.

6.4.2 Anodization (A1, A2) of Aluminum

As described for the electropolishing with the two-electrode assembly, clean, polished foils were again brought into the Cu-block Setup with the standard PTFE vessel. The homemade stirring electrode was used as cathode, and adjusted to 14 mm from the foil. 50 mL of a 0.3 M oxalic acid solution was used as electrolyte and kept at 25 °C in analogy to Sulka *et al.*[103] by a cooling coil inside the vessel. Alternatively, 35 °C were used as reaction temperature for an increased growth rate. Anodization reactions were typically carried out between 35 and 50 V, with reaction periods varying between 0.5 to 3 h, depending on the intended oxide layer thickness. As a result, highly transparent, colorless to yellowish oxide covered the active surface of the metal foil and was subsequently washed away with water and acetone.

In general, two-step anodizations were performed with the same reaction parameters, except for the reaction period. If the anodization was the first step (A1), the primary oxide layer was dissolved (DisO) according to Chapter 6.4.3 before re-anodizing (A2) the pre-patterned surface. Otherwise, the procedure continued directly with the pore opening process (PO, compare Chapter 6.4.4) and dissolution of the Al metal (DisA, compare Chapter 6.4.5).

To produce AAO discs of different diameter, the respective PTFE vessels of the Cu-block Setup were used. All other parameters were kept the same.

6.4.3 Dissolution of the Preliminary Oxide Layer (DisO)

The oxide obtained by the pre-anodization A1 was dissolved in a solution composed of 5.88 g H_3PO_4 (85 %) and 1.27 g CrO_3 in 76.18 g H_2O. The oxidized aluminum discs were immersed in about 15 mL of the described etching solution and either treated at RT overnight or at 60 – 70 °C for 3 h (according to Haberkorn *et al.*[101]). Subsequent to the treatment, the foils were washed with water and acetone. The stock of solution was reused several times until its bright orange color became weak and brownish.

For A1 oxide layers of up to about 45 µm thickness, corresponding to e.g. 50 V anodization for 2 h, the reaction period could be reduced to 1 h at elevated temperature conditions.

6.4.4 Back Side Pore Opening Process (PO)

The standard method for the back side pore opening was an electrochemical approach, here described first. The oxidized Al foils were, typically after A2, not removed from the Cu-block Setup, but only washed with water and acetone to dry the surface. Using a Pd sheet cathode set to a distance of about 20 mm, the PO reaction was performed with a voltage 5 V higher than the original anodization voltage in about 30 mL of an electrolyte of $HClO_4$/EtOH 1:1. The reaction period was set to only 3 s. An extension to 5 s turned out to be advantageous, if either the anodization voltage was ≥ 50 V, the reaction temperature was 35 °C, or the oxide disc diameter was larger than the standard 16 mm. When washing the metal foil thereafter with water and acetone, a bubble trapped between the oxide and metal indicated the reaction's success. To avoid high energy input, the maximum current allowed was set to 1 A at the power supply. The reaction was usually started within 30 s after filling in the electrolyte, and the subsequent dissolution of the aluminum followed immediately. Both actions reduced the contact time with the aggressive etching solution.

Chemical etching to open the pores on the oxide's back side was tried after dissolving the aluminum (see Chapter 6.4.5) to obtain the bare oxide discs. All approaches were performed with A2 oxide discs of 16 mm diameter and turned out to give inhomogeneous etching results: First, the oxide layers were immersed in either 5 % H_3PO_4 or 0.2 % NaOH solution for periods of up to 2 h or 4 h, respectively. Second, the oxide discs floated backwards onto an etching solution with increased viscosity. For this purpose, PEG 20000 was dissolved 1:1 by weight in 0.4 % NaOH solution. The reaction period was up to 3 h, whereby a cover sheet prevented surface drying of the gel. To free the oxide from the gel, intense washing with water was necessary. In further experiments, the concentration of base in the solution was enhanced to 1 and 2 %. Third, the protection of the front side was achieved by application of conventional nail polish or UV curing glue (Acrifix®192). The oxide was covered before dissolving the metal and subsequently brought onto the acidic or basic etching solution (see above). After the etching, it was immersed in toluene overnight to dissolve the protective layer. Fourth, the oxide was annealed at 650 °C for 6 h between tiles prior to the etching to improve the chemical resistivity and maintain the flat morphology.

6.4.5 Dissolution of Aluminum Base (DisA) and Pore Widening Procedure (PoWi)

Typically, the aluminum was dissolved to yield the bare oxide disc after the pore opening process. The oxide-metal composite was treated with about 10 mL of a solution of 8.5 g $CuCl_2 \times 2\,H_2O$ in 500 mL half-concentrated HCl.[107] The aluminum started immediately dissolving in an exothermic reaction under H_2 evolution. After a few minutes, the oxide disc was free of metal, and Cu metal had formed as a precipitate. The oxide was removed from the solution and washed with water an acetone. Careful attention was paid not to mix up the front and the back side of the membrane.

The dissolution was much faster if the PO process was performed before, resulting in a fast detachment of the oxide from the metal. Therefore, oxide layers with a diameter larger than 16 mm had were treated in a slightly different way. Permeation of the etching solution through the opened pores led to a pressure increase by gas evolution between the oxide and metal, thus breaking the disc. Consequently, the aluminum was first etched from only one side until a gas outlet was generated between the layers. Afterwards, the whole oxide-metal composite was immersed in the solution.

The pore widening procedure was analogously performed with the described Cu^{2+}/ HCl solution. The bare oxide discs were immersed in about 5 mL fresh solution for typically a further 1 to 2 h. To control the etching at the back side surface, floating experiments on gelled etching solution were again conducted, similar to the process described in Chapter 6.4.4. PEG 20000 was added in a concentration of 1.5 or 2.5 g to 5 mL etching solution. Alternatively, a doubly concentrated solution of Cu^{2+} in HCl was mixed with the PEG. Because this procedure showed no distinct improvements, it was not applied in the standard membrane production process.

6.4.6 Filtration Experiments with Nanoparticle Dispersions

The AAO membranes were prepared by standard conditions: Second anodization at 50 V and 35 °C for 2 h, usually followed by are pore widening step of further 2 h. Because tightening with rubber sealings was not successful, the oxide membranes were glued in a homemade filter holder from aluminum (see Chapter 4.8.2 and Figure 4.71 (a) for the filter holder). Exchangeable insets allowed the use of either 16 or 20 mm oxide discs. The oxide was glued in and sealed with an acrylate glue (Acrifix®192) or a silicone glue (Momentive™ Silicone Rubber Adhesive Sealant), together with an Al grid (see Figure 4.71 (b)) to stabilize the brittle oxide against the pressure.

The filter holder was connected to flexible tubes for taking up the feed dispersion and filtrate. Stable nanoparticle dispersions in water were used for the filtration experiments. Nanoparticle types and their synthesis routes are listed in Table 12. Filtration experiments were usually performed with N_2 overpressure of 200 or 400 mbar for some hours. With slow filtrations, the pressure was raised to max. 1 bar and stopped at the latest after 12 – 24 h. Further, individual filtration details are discussed in Chapter 4.8.4.2. Some filtration membranes were used more than once. For a detailed analysis of the membranes after use, the adhesive was dissolved in ethyl acetate.

Table 12: Nanoparticles (NP) used for the filtration, their synthetic routes, and experimenters.

NP type	Synthesis route	Experimenters
$Au@Fe_3O_4@SiO_2$	Synthesis according to Wu *et al.*[243]	[redacted]
SiO_2	Synthesis(a) adapted from Zhong *et al.*[244]	[redacted]
$Fe_3O_4@SiO_2$-FITC	Synthesis according to Schladt *et al.*[166]	[redacted]
Au-citrate	Synthesis according to Jana *et al.* [171]	[redacted]
$Au@MnO@SiO_2$	Synthesis according to Schick *et al.*[167]	[redacted]
$MnO@SiO_2$-FITC	Synthesis according to Schladt *et al.*[166]	[redacted]
$Fe_3O_4@SiO_2$-RITC	Synthesis according to Schladt *et al.*[166]	[redacted]

(a) Synthesis with adapted parameters: 3.73 g Na_3-citrate, 10 mL APTES, 80 mL H_2O, stirring of 7 h; use of microwave oven MARS 5 (CEM) at 20 bar for 15 min; neutralization of the dispersion with HCl.

6.4.7 Post-Treatments

Functionalization With Silanes (compare Chapter 4.7)

According to an internal procedure used for nanoparticle functionalization in our workgroup, the surfaces of the membranes were functionalized by immersing the oxide discs in a solution of 2 – 3 drops silane (APTES or 18-TMS) in 10 mL of acetone over night. For testing the addressability of the amino functions provided by the APTES, a condensation reaction with FITC was performed. Dried membranes were immersed in a solution of 5 mg FITC in 5 mL anhydrous DMF for 2 h. The membranes were afterwards rinsed several times with water to remove excess dye.

Pre-Tests for Intrinsic Filter Membrane Stabilization (compare Chapter 4.8.5)

Tests with extra thin aluminum foil (25 µm, compare Chapter 6.1.1) were performed. The electropolishing was reduced to 30 s to prevent pitting. Beyond this, anodizations was possible in general.

As a test for a protection of certain areas on the aluminum foil against the anodic oxidation, the coating of photoresist on polished titanium foils was examined. Microposit® S 1813 G2 Positive Photoresist (DOW) was applied using a spin coater (WS-400, Laurell) and the following parameters: 7000 rpm, 0.2 mL photoresist, 10 s spinning time. The dye was cured for 2 min at 150 °C. When exposing the coating to UV light, an aluminum grid was used as mask. A coated pattern was yielded after dipping the metal foil into either Microposit® 351 Developer or Microposit® Developer Concentrate (DOW). The coating tests were performed by [redacted].

6.5 Synthesis of Anodic Vanadium Oxide

6.5.1 Electropolishing of Vanadium Foils

Circular cut vanadium foils of 20 mm diameter were cleaned by ultrasonication in acetone and water for about 5 minutes, followed by rinsing with acetone. The foils were inserted into the 15 mm Cu-block Setup and subjected to electropolishing. 50 mL of an electrolyte composed of 20 vol% sulfuric acid and 80 vol% methanol was used. Polishing was carried out with a graphite rod cathode, set 17 mm from the foil, at a potential of 10 – 12 V for 4 – 5 minutes. The solution became slightly yellow right above the vanadium foil. Foils of batches with intensely scratched surfaces were usually polished 4 times until the morphology was sufficient. Therefore, the electrolyte was reused after mixing between the steps to disperse the yellow, gel-like, isolating layer. After electropolishing, the samples were again sonicated, rinsed, and dried.

In order to improve the polishing of foils with rougher surfaces, different experimental conditions were tested (see Table 13), but not found to be advantageous.

Table 13: Polishing conditions for rough vanadium surfaces, which did not lead to flat surfaces.

Electrolyte	Voltage/ Current	Reaction period
MeOH : H_2SO_4 (4:1)	10 or 20 V	4 min
MeOH : H_2SO_4 (4:1), cooled electrolyte (-25 °C)	20 or 30 V	4 min
MeOH : H_2SO_4 (4:1)	100 mA (galvanostatic)	4 min
MeOH : H_2SO_4 (2:1)	10 or 20 V	4 min
MeOH : H_2O : H_2SO_4 (7:2:1)	10 or 20 V	4 min
MeOH : H_2O : H_2SO_4 (2:2:1)	10 V	4 min
MeOH : H_2SO_4 (8:1)	10 or 30 V	4 min
EtOH : H_2SO_4 (3:2)	100 mA (galvanostatic)	4 min

6.5.2 Anodization of Vanadium Foils

As described for the electropolishing with the two-electrode assembly, clean, polished foils were again brought into the Cu-block Setup. In deviation from the polishing step, the distance to the counter electrode was set to only 13 mm.

For the electrolyte used for standard anodizations, diethylene glycol, saturated with boric acid (about 25 g/100 mL), was mixed with water and oxalic acid dihydrate to yield a final composition of 2 % water and 0.5 % $H_2C_2O_4 \times 2\ H_2O$. For each reaction, 60 g (about 50 mL) of electrolyte were freshly prepared. The dissolution of the oxalic acid was accelerated by sonication. The highly viscous mixture was carefully poured into the setup to avoid bubbles. The typical potential was 40 V and the reaction temperature was 25 °C, controlled by a glass cooling coil. The reaction period was varied between 1 and 3 h. Anodization resulted in a bright orange color of the oxidized surface with tendencies to leach into the electrolyte. Subsequent washing of the oxidized foils was optimally done briefly with acetone. Alternatively, ethanol, isopropanol, and acetonitrile also could be used. Washing instead with water led to dissolution of the formed oxide layer. After washing the oxide bearing foil, it was dried in vacuum or in a vacuum oven at low temperature.

Deviations from the standard electrolyte were tested with respect to the oxalic acid and water content. The oxalic acid content was varied in limits of 0.15 to 0.5 % and the water content in limits of 0 to 5 % with corresponding adaption of the glycolic part.

Further test series were performed, having either no significant or even a negative influence on the outcome of the anodization reaction:

The electrolyte was modified in that

- an extra amount of vanadium (V) oxide was added (spatula tip).
- an extra amount of ammonium oxalate was added (474 mg).
- the standard electrolyte was reused for a further anodization.
- DEG was replaced by ethylene glycol (saturated with boric acid).

The reaction conditions and the setup were modified such that

- the controlled temperature was lowered to 2-3 °C.
- the active sample size was reduced from 16 to 10 mm in diameter by use of a PTFE vessel with a smaller aperture.
- the inter-electrode distance was increased to 17 mm.
- the whole setup was replaced by a simple vertical setting: A glass beaker (250 mL, tall form) was filled with about 100 mL electrolyte, with or without magnetic stirring, and was equipped with a graphite sheet electrode. The vanadium foil as anode was held dipped into the solution by an alligator clamp.

In dependence on anodization conditions published by Yang *et al.*,[34] a comparative test series was launched. The Cu-block Setup was used in combination with a Pd sheet cathode and 50 mL of electrolyte. For the electrolyte, 33 mg of titanium powder was dissolved in 1 g HF solution (40 %) and diluted with ethylene glycol up to 100 mL. Anodization was performed at 105 V for 3 h. The oxidized vanadium foils were stored in ethanol overnight and subsequently annealed for 3 hat 200 °C.

6.5.3 Catalytical Activity of the Anodic Oxide

Measurements of 2,2'-azino-bis(3-ethylbenzothiazoline-6-sulphonic acid) (ABTS) oxidation activity were carried out in 2.5 mL plastic cuvettes containing 2305 µL sodium acetate buffer (100 mM, pH 4.0), 170 µL ABTS (1 mM), and 25 µL H_2O_2 (10 mM), in which one-eighth of a freshly anodized metal disc was dipped.

The activity was determined spectrophotometrically by measuring the formation of the radical cation $ABTS^{*+}$ from ABTS at 405 nm. The slope of the absorption was determined over a period of 3 min as soon as the oxidation started. Total measuring time was 10 – 15 min, until the reaction was complete. As a control, either untreated or only polished pieces were used in place of the anodized vanadium foils, and autooxidation was measured without vanadium species at all.

The peroxidase like activity tests adapted from on André *et al.*[235] and were performed by [redacted].

7 Appendix

7.1 Acronyms, Abbreviations

3 D	3-dimensional
18-TMS	Octadecyltrimethoxy silane
AAO	anodic aluminum oxide
ABTS	2,2-azino-bis(3-ethylbenzothiazoline-6-sulfonic acid)
AFM	atomic force microscopy
APTES	(3-aminopropyl)triethoxysilane
ATO	anodic titanium oxide
AVO	anodic vanadium oxide
AVO	anodic vanadium oxide
BE	binding energy
BET	Brunauer, Emmett, and Teller method
BJH	Barrett, Joyner, and Halenda method
d	pore diameter
DEG	diethylene glycol
d_I	inter-pore distance / cell size
DLS	dynamic light scattering
EG	ethylene glycol
ESCA	electron spectroscopy for chemical analysis
EtOH	ethanol
FITC	fluorescein isothiocynate
h	Planck constant
KE	kinetic energy
MeOH	methanol
min	minute
P	porosity
p.a.	pro analysis
p/p_0	relative pressure
PEG	polyethylene glycol
PTFE	polytetrafluoroethylene
R_a	average roughness
RITC	rhodamine-B-isothiocyanate
R_q	root-mean-squared deviation of the average roughness
RT	room temperature
SAM	self-assembled monolayer
UV-Vis	UV-/ visible light
vol%	volume percentage
XPS	X-ray photoelectron spectroscopy
ν	frequency of electromagnetic wave
ϕ_S	XP spectrometer work function

7.2 List of Figures

Figure 1.1: Illustration of dimensions down to the nanoscale.[2] 5

Figure 1.2: SEM images of long-range ordered AAO with (a, c) hexagonal and (b, d) square arrangement of nanopores, generated by imprint stamp pre-structuring.[18] 7

Figure 1.3: SEM images of a Whatman® Anopore™ AAO membrane with pore size of 20 nm (manufacturer specification): (a) Macroporous side as backbone, (b) side with functional layer of mesopores, (c) defects in the functional layer, and (d) cross-sectional view on the thin functional layer. 10

Figure 2.1: SEM images of (a) AAO and (b, c) ATO, showing the differences between both structural types. 13

Figure 2.2: Current-time curve and model of the pore formation stages for AAO and ATO, in analogy to literature.[52] 16

Figure 2.3: Model of porous anodic oxide showing characteristic parameters as pore diameter/size *d*, interpore distance d_I (cell diameter), wall thickness (d_I - d), and pore length, respectively oxide layer thickness *h*, in analogy to literature.[35] 17

Figure 3.1: Light microscopy (a, c) and 3D topology laser scanning microscopy images (b, d) of a raw (unpolished) standard titanium foil (a, b) and a polished foil (c, d). The 3D images were extended 10-fold in z-axis. 22

Figure 3.2: SEM images of (a) a polished titanium surface showing grains (different shading) and (b) the imprint pattern with sticking A1 oxide, produced at 50 V (A1). 23

Figure 3.3: SEM images comparing the results of A1 and A2 anodizations at 50 V: (a) A1 oxide for 3 h and (b) A2 for 5 min reaction period. The insets show images with higher magnification. 24

Figure 3.4: (a) Photograph of a thin ATO layer (A2, 50 V, 5 min) and (b) SEM image showing superstructures on its surface.. 25

Figure 3.5: SEM image of ATO produced at 50 V for 5 min with initial potential ramp of 1 V/s, resulting in a hexagonal network superstructure. 26

Figure 3.6: SEM images of ATO front side (insets show back side) produced with 2 h reaction period and an anodization voltage of (a) 20 V, (b) 30 V, (c) 40 V, and (d) 50 V; (e) plot of frontal pore diameter against the applied voltage showing a linear trend.............................. 27

Figure 3.7: Photograph showing the curling of thick ATO layers from the underlying metal. 28

Figure 3.8: SEM images of ATO front side, produced at 40 V (a – c) and 50 V (d – f), the reaction period was 0.25 h for (a, d), 2 h for (b, e), and 4 h for (c, f); (g) plot of diameter against reaction period showing an approximation to a maximum value with time. 29

Figure 3.9: SEM images of ATO produced at 50 V in order (a – c) of an increasing reaction period, showing different stages of chemical etching: (a) hexagonal shaped pores, (b) crimping surface with starting degradation, and (c) nano grass forming at the front side as result of intense chemical etching. 30

Figure 3.10: SEM images of the chemically robust porous top layer: (a) Layer covering the formed ATO tubes (see arrow) and (b) detached layer, as a result of nano grass formation, found on the ATO back side; the inset shows the network on top of back side tubes. 30

Figure 3.11: SEM images of ATO tubes produced at 45 V for 4.5 h, illustrating the dependency of the inner diameter on the layer thickness: (a) Cross section of tubes close to the back side with diameter of 30 nm and (b) cross section of tubes close to the front side with larger diameter of 40 nm.. 31

Figure 3.12: Plot of the ATO layer thickness as a function of the reaction period for 30, 40, and 50 V, showing a reduced growth rate with time. The insets show cross-sectional SEM images of variable reaction conditions; for 6 h reaction period, starting attack on the porous front side is shown too.. 32

Figure 3.13: Current-time curve for a typical anodization at 45 V, the inset shows the progress of within the first 5 min when the pores start to form. 33

Figure 3.14: SEM image of a diagonal broken ATO layer (50 V, 2 h) showing explicit the tubular structure. 33

Figure 3.15: (a) Photograph of strongly curling oxide layer when separating from the metal in dry state and (b) SEM image of ATO surface exhibiting stress induced cracks. 34

Figure 3.16: SEM images of the ATO back side (50 V, 2 h): (a) Pore bottoms as cross-sectional view with round-shaped caps and (b) bottom view of capped tubes and broken tubes showing the pores. 35

Figure 3.17: SEM images of an ATO membrane (60 V, 2 h) after floating back side down on 2 % HF solution: (a) Backside after 15 s etching showing diverging tubes, (b) backside after 30 s with tendencies of nano grass formation, (c) corroded front side, and (d) side view on reduced layer thickness after 30 s of etching. The insets show images with higher magnification. 37

Figure 3.18: TEM image of ATO (60 V) tube bottoms showing enhanced barrier layer thickness (75 nm) compared to the tube walls (45 nm). The image was taken by [redacted] [redacted] and [redacted] 38

Figure 3.19: SEM images of ATO (50 or 60 V) membrane back sides after selective etching of the bottom with 1 % HF solution for a) 1 min, b) 2 min, c) 5 min, and d) 10 min. 39

Figure 3.20: SEM images taken at different positions of the same ATO back side (50 V, 4 h) after 5 min exposition to HF vapor, showing different intensity of etching: (a) Separation of tubes, (b) partially opened tubes and first nano grass tendencies, and (c) collapsing tubes. ... 40

Figure 3.21: SEM images of the back side of completely porous ATO membranes (50 V, 2 h) after applying 80 V for additional 10 min to open the pores and a reverse bias (- 2,25 V, 5 min) to separate oxide and metal: (a, b) opened back side and (c) cross-sectional view. 41

Figure 4.1: (a) Light microscopy image and (b) 3D topology laser scanning microscopy image of raw (unpolished) standard aluminum foil. The 3D image was extended 10-fold in z-axis. 47

Figure 4.2: 3D topology laser microscopy images of aluminum surfaces polished with 4:1 alcohol/$HClO_4$ electrolyte using the homemade laboratory stirring electrode for (a) 1 min, (b) 2 min, and (c) 4 min. The 3D image was extended 10-fold in z-axis. 48

Figure 4.3: Light microscopy image of a polished aluminum surface showing grain boundaries. 48

Figure 4.4: 3D topology laser microscopy images of aluminum surfaces polished with the high-speed stirring electrode (a) using the standard PTFE vessel for 5 min reaction period and (b) using the conically modified vessel and only 2 min reaction period. The 3D image was extended 10-fold in z-axis. 49

Figure 4.5: SEM images of porous aluminum oxide after the first anodization (A1) with 40 V for 3 h, showing irregular pores arranged in (a) lines and (b) along wave-like superstructures. The inset shows an image with higher magnification. 50

Figure 4.6: SEM image of the back side of porous aluminum oxide (A1, 40 V, 3 h) after dissolving the Al metal. 51

Figure 4.7: SEM image of the pattern left in the aluminum after dissolving the A1 pre-oxide. 52

Figure 4.8: SEM images of porous aluminum oxide after the second anodization (A2) with 40 V for 2 h, showing monodisperse pores of about 35 nm. 53

Figure 4.9: Current-time curves for A1 and A2 anodizations at a potential of 40 V. The inset shows the progress of within the first minutes when the pores start to form. 53

Figure 4.10: Photograph of an A2 16 mm oxide disc after the dissolution of supporting metal. 54
Figure 4.11: SEM images of porous aluminum oxide (40 V, 2 h) after the DisA process, showing widened pores of about 45 nm at the front side. 55
Figure 4.12: SEM cross-sectional images showing the channel diameter at (a) the pore bottom, (b) the middle section, and (c) the pore openings. 56
Figure 4.13: SEM images of AAO formed at 35 V (a, b) and 30 V (c, d), after A2 (a, c) and after dissolution of the metal base (DisA) leading to widened pores (b, d). 57
Figure 4.14: SEM images of AAO formed at (a) 25 V and (b) its partially degeneration to nano grass due to extended reaction time. 58
Figure 4.15: SEM images of AAO formed at 50 V after anodization A2 (a, c) and after DisA (b). 59
Figure 4.16: SEM images of AAO after DisA, formed at (a) 60 V, (b) 70 V, and (c) 90 V. The insets show images with higher magnification. 60
Figure 4.17: Plot of pore diameters (measured at the front side by SEM) and inter-pore distances after metal dissolution (DisA) as a function of the anodization voltage. The inter-pore distance for 60 V, 70 V, and 90 V is replaced by the cell size (measured on the back side). The arrows indicate the huge distribution of measured values. 61
Figure 4.18: SEM images of AAO back sides with closed pores (combs) formed at (a) 30 V, (b) 35 V, (c) 50 V, and (d) 60 V. 62
Figure 4.19: Plot of steady current values measured for standard anodizations (16 mm sample diameter) against the anodization voltage. The arrows at higher voltages indicate the non-uniform current obtained. 63
Figure 4.20: Photograph of two AAO after DisA, anodized at the same voltage for (a) a short and (b) a prolonged reaction period. 64
Figure 4.21: SEM cross-sectional studies of AAO produced at 40 V for 1 to 4 h (a-d). 65
Figure 4.22: SEM cross-sectional studies of AAO produced within 2 h at (a) 35 V, (b) 40 V, and (c) 50 V. 66
Figure 4.23: Plot of the oxide layer thickness against the reaction period for different anodization voltages. 67
Figure 4.24: SEM cross-sectional study of AAO channels (A1, 40 V, 2 h) along the whole oxide layer thickness: (a) front side, (b) middle section, and (c) bottom side.........................68
Figure 4.25: SEM images of the same AAO surface (50 V, back side with opened pores), taken with (a) 15 kV and (b) 30 kV acceleration voltage. 69

Figure 4.26: SEM images of the same AAO surface (50 V, 10 min) (a) without gold layer and (b) with conductive gold layer of 7.5 nm. 70

Figure 4.27: SEM cross-sectional studies showing (a) the funnel shaped pore apertures at the front side of AAO surfaces and (b) the resulting nano-structuring. 71

Figure 4.28: SEM image of the barrier layer formed by anodization at 40 V. 72

Figure 4.29: SEM images, not representative, of AAO (35 V, 2 h, DisA) after treatment with 5 % H_3PO_4 for 1 h: (a) front side with widened pores and (b) back side with opened pores. 73

Figure 4.30: SEM image of a corroded part of an AAO layer (35 V, 2 h, DisA) after H_3PO_4 treatment 74

Figure 4.31: SEM images of different stages of degradation due to H_3PO_4 treatment: (a, b) Collapsing pore walls and (c, d) nano grass formation from top and cross-sectional view 75

Figure 4.32: SEM images of AAO (35 V, 2 h) after treatment with 0.2 % NaOH solution for 1 h: (a) Corroded front side, (b) back side with partially opened pores, and (c) cross section showing initial nano grass formation. 76

Figure 4.33: SEM images of (a) front and (b) back side of AAO (30 V, 3 h) after back side floating on NaOH-PEG for 90 min. 77

Figure 4.34: SEM images of AAO (35 V, 2 h) have been protected with nail polish and subsequently treated with 5% H_3PO_4 for 90 min: (a) front side after dissolution of the nail polish, (b) back side, (c) cross-sectional study, and (d) channel structure. 79

Figure 4.35: SEM images of AAO annealed at 650 °C: (a) front side of annealed but untreated membrane (40 V, 4 h), (b, c) back side after floating on 0.2 % NaOH for 1 h ((b) 40 V, 3 h; (c) 35 V, 2 h). 80

Figure 4.36: Photograph of AAO separated from the underlying Al metal by a voltage pulse, exhibiting a bubble formed between oxide and metal. 82

Figure 4.37: SEM images of AAO (35 V, 2 h) after separation from the Al metal with the voltage pulse method: (a) front side, (b) opened back side bearing debris, and (c) cross-sectional view onto the continuous channel structure. 83

Figure 4.38: SEM images of an AAO membrane (35 V, 2 h) after separation from the Al metal with the voltage pulse method (PO) and subsequent dissolution of Al (DisA): (a, b) front side and (c, d) opened back side. 84

Figure 4.39: SEM images of an AAO filtration membrane with highlighted distinctive features for (a) front and (b) back side. 85

Figure 4.40: SEM image of an AAO (produced at 50 V for 2 h) back side, incompletely opened with a short 55 V-3 s-voltage pulse. 86

Figure 4.41: SEM images of AAO (50 V, 2 h) after applying a + 10 V-pulse for (a) 3 s and (b) 5 s instead of the usual + 5 V-pulse to open electrochemically the back side pores. 87

Figure 4.42: SEM images of AAO (35 V, 2 h, A3), produced on reused Al after the voltage pulse detachment (PO) of the A2 oxide and mechanical separation of oxide and metal; (a) front side and (b) back side...87

Figure 4.43: SEM images of AAO (40 V, 3 h) left in HCl/Cu^{2+}-solution (DisA) for more than 1 h after the pore opening procedure; (a) front side and (b) cross-sectional channel view. 88

Figure 4.44: Equilateral triangle and formula to calculate the porosity of AAO. 89

Figure 4.45: SEM image of AAO (50 V, 2 h) front side after a pore widening procedure for 3 h with HCl/Cu^{2+}-solution...89

Figure 4.46: SEM images of AAO membrane (50 V, 2 h) without (a, c, e) and after pore widening step for 2 h (b, d, f) of the front side (a, b), the back side (c, d) and cross-sectional channel view (e, f). 91

Figure 4.47: SEM images of AAO pre-anodized at 50 V (A1) and afterwards anodized at 40 V (A2) showing (a) characteristics of a 50 V-anodization at the front side and (b) of 40 V-anodization on the back side..92

Figure 4.48: SEM images of an AAO (35 V, 2 h) membrane: (a) front side after A2 (on the metal), (b) front side after DisA, and (c – e) cross-sectional studies along the channels after DisA ((d) shows scanning artifact)...94

Figure 4.49: Photograph of a piece of Al foil bearing a residue of A1 oxide (white spot) after 0.5 h treatment with phosphochromic acid..95

Figure 4.50: SEM images of A1 oxide (50 V, 1 h) without treatment (a) and after etching in phosphochromic for 2 h, 4 h, and 6 h at RT (b – d). The insets show images with higher magnification. 96

Figure 4.51: SEM images of a pre-pattern (50 V) left after etching the AAO with phosphochromic acid for (a) 0.5 h, (b) 1 h, and (c) 2 h at a temperature of about 65 °C.........97

Figure 4.52: Scheme of an AAO pore exhibiting four distinctive diameters $d1$-$d2$ across the oxide layer thickness in deviation of a perfect cylindrical shape. 97

Figure 4.53: SEM images of AAO membranes (40 V, 3 h) showing (a – c) the front side, (d – f) the back side, and (g – i) a cross-sectional channel view, (a, d, g) without pore widening step (PoWi), (b, e, h) after 30 min PoWi, and (c, f, i) after 60 min PoWi...............................99

Figure 4.54: SEM images of AAO (50 V, 2 h) after floating on HCl/Cu^{2+}-gel for 2 h, (a) front side and (b) back side. 100

Figure 4.55: SEM images of AAO (50 V, 2 h) after floating on a concentrated HCl/Cu^{2+}-gel for 2 h, (a) front side and (b) back side. 100

Figure 4.56: SEM images of AAO (50 V, 2 h) front side, showing several „twin pore“ defects; (a) without and (b) with 2 h pore widening. 101

Figure 4.57: SEM images of an AAO (60 V, 2 h) membrane (a, b) before and (c – f) after a pore widening procedure for 2 h; (a, c) show the front side, (b, d) the back side, and (e, f) show cross-sectional studies. 102

Figure 4.58: SEM images of AAO (70 V, 1.5 h) front side (a) before and (b) after 2 h PoWi. 103

Figure 4.59: SEM images of an AAO (90 V, 0.5 h) membrane showing the back side (a) before and (b) after the pore widening procedure applied for 2 h. 104

Figure 4.60: SEM images of AAO membranes (after PO) anodized at 5 °C: (a, b) front and back side of AAO anodized at 50 V for 3 h and (c, d) front and back side of AAO anodized at 80 V for 1 h. The insets show images with higher magnification. 106

Figure 4.61: SEM images of AAO anodized at 35 °C (after PO): (a, b) front and back side of AAO anodized at 35 V for 2 h and (c, d) front and back side of AAO anodized at 50 V for 2 h. 107

Figure 4.62: SEM images of AAO anodized at 35 °C: (a – c) front side, cross section and back side of AAO anodized at 35 V for 2 h and 1 h pore widening; (d – f) front side, cross section and back side of AAO anodized at 50 V for 2 h and subsequent 2 h pore widening. 109

Figure 4.63: SEM images of an AAO membrane produced at 50 °C (50 V, 1.5 h) showing (a) partially front side corrosion, (b) front side pores, and (c) back side pores. 109

Figure 4.64: Structural formula of fluorescein isothiocyanate (FITC). 111

Figure 4.65: SEM images of AAO front and back side (50 V, 2 h) after functionalization with APTES and FITC. 112

Figure 4.66: (a – c) CLSM images of FITC-functionalized AAO (50 V, 2 h) in cross-sectional view, (a) green emission of the dye (excitation 488 nm, detection bandpass 500 – 535 nm), (b) red reflection of the laser excitation (633 nm), and (c) overlay of emission and reflection (all three images taken by [redacted]); (d) photograph of a functionalized membrane. 113

Figure 4.67: Scheme of the complete AAO synthesis route to prepare suitable filtration membranes. 114

Figure 4.68: Photographs of the homemade hydrostatic pressure setup: (a) An AAO disc of 16 mm diameter used, (b) the disc inside the filter holder from water-tap connecting parts, exposing a free diameter of 13 mm, (c) the mounted holder, loaded with a red-colored liquid column, and (d) 5 m of hydrostatic pressure acting on a disc of about 50 µm thickness (40 V, 4 h). 116

Figure 4.69: SEM image showing the surface of an AAO membrane after impact by a solution of pH 11 for 1 h. 117

Figure 4.70: Photographs of tested filter holders: (a) Commercial 25 mm plastic filter holder (Whatman), (b) reproduction from aluminum for 16 mm discs, and (c) manufactured holder with device against twisting. 119

Figure 4.71: Photographs of (a) the used filter holder with replaceable insets to glue in membrane discs of different sizes, (b) an AAO membrane fixed in an inset, and (c) the stabilizing Al grid with 1 mm apertures. 119

Figure 4.72: Photographs of the filtration setup showing (a) the feed liquid column containing red dye, (b) the filter holder including the AAO filtration membrane, and (c) the efflux. 120

Figure 4.73: (a) Photograph of the stained AAO membrane in the filter inset and (b) SEM image of the AAO backside showing residues of the dye. 121

Figure 4.74: SEM images of a 13 mm oxide membrane (50 V, 3 h) after 2 h pore widening: (a) front side, (b) back side, (c) cross-sectional view, and (d) close view to the channels. 122

Figure 4.75: SEM images of a 20 mm oxide membrane (35 V, 2 h): (a) front side, (b) back side, and (c) cross-sectional view. 124

Figure 4.76: Photograph of an AAO membrane of 30 mm diameter (area of 7 cm^2). 124

Figure 4.77: SEM images of a typical standard filtration membrane (50 V, 2 h, 35 °C): (a) front side with large pores, (b) back side with lowest diameter of 55 nm, and (c) cross-sectional view onto the channels of about 60 nm. 128

Figure 4.78: Sketch of the filtration setting. 129

Figure 4.79: TEM image of Au@Fe_3O_4@SiO_2 NPs agglomerated by large Si shells. The image was taken by [redacted]. 130

Figure 4.80: Filtration experiment with Au@Fe_3O_4@SiO_2 NP agglomerates: (a) Photograph of the filtration setting with colored feed and colorless eluate, (b) filtration membrane in the holder with NP retentate, and (c) absorption spectrum of NP feed dispersion and its filtrate after the filtration experiment. 131

Figure 4.81: Absorption spectra of SiO_2 NP feed dispersion and its filtrate after the filtration experiment. 132

Figure 4.82: TEM image of Fe_3O_4@SiO_2-FITC NPs with total diameter of 14 nm. The image was taken by [redacted]. 132

Figure 4.83: Absorption spectra of Fe_3O_4@SiO_2-FITC NP (14 nm diameter by TEM, 22 nm hydrodynamic diameter) feed dispersion and its filtrate after the filtration experiment. 133

Figure 4.84 TEM image of citrate-capped Au NPs with total diameter of less than 10 nm. The image was taken by [redacted]........ 134

Figure 4.85: Filtration experiments with citrate-capped Au NPs: (a) Photograph of the colored dispersion, (b) absorption spectra of feed dispersion and filtrate showing almost no more NPs, and (c) photograph of the stained, golden filter after two days........ 135

Figure 4.86: TEM images of NPs applied as a mixture in filtration tests: Au@MnO@SiO_2 Janus particles with (a) single gold domains and (b) with SiO_2 NPs without core; (c) MnO@SiO_2-FITC NPs. The images were taken by [redacted]........ 136

Figure 4.87: Filtration experiment with “most challenging” NP mixture: Photographs of (a) the feed before and (b) the eluate after the filtration, and (c) appearance of the filter membrane after the filtration. 136

Figure 4.88: Filtration experiment of “worst case” NP mixture: TEM images of NP composition (a) before and (b) after the filtration, and (c) absorption spectra of feed NP dispersion and filtrate. TEM images were taken by [redacted]. 137

Figure 4.89: (a) Structural formula of RITC, (b) TEM image of Fe_3O_4@SiO_2-RITC NPs of 42 nm diameter (by TEM), and (c) TEM image of Fe_3O_4@SiO_2-RITC NPs in a mixture with much smaller Fe_3O_4@SiO_2-FITC NPs of 14 nm........ 138

Figure 4.90: Absorption spectra a mixture of Fe_3O_4@SiO_2-FITC NPs with small silica NPs before and after the filtration experiment. 139

Figure 4.91: Photographs showing approaches for (a) a filtration of nanoparticles by magnetic forces and (b) a filtration of charged nanoparticles by the electroosmotic effect........ 140

Figure 4.92: Photograph of a broken AAO window in its Al frame, produced by a modified DisA procedure. 142

Figure 4.93: Schematic view of considerations to achieve an intrinsic stabilization by metal leavings: (a) Preservation of aluminum in certain areas while anodizing to form a stabilizing grid and (b) variations in the pore opening (PO) and aluminum dissolution step (DisA). 142

Figure 4.94: SEM images of completely anodized metal foils: (a) cross-sectional view of a massive terminating barrier layer at the back side and (b) frequent defects found thereon. . 143

Figure 4.95: Survey SEM images of a stamped but non-polished foil, which was completely anodized until its thinnest parts became transparent: (a) front side and (b) back side. 145

Figure 4.96: Photograph of a photolithographic pattern on a titanium surface, visualized by different wetting behavior. 145

Figure 4.97: SEM cross-sectional images showing an Al foil completely anodized from both sides: (a) layer of aluminum left between the AAO layers and (b) intact barrier layers. 146

Figure 4.98: Use of a bench drilling machine as stirring electrode: (a) Photograph of the converted bench drilling machine and (b) SEM image of an AAO (50 V, 2 h) self-supporting membrane, with typical pore size of 55 nm, produced with the bench drilling machine. 148

Figure 4.99: SEM images of AAO membrane (50 V, 2 h) by anodization of Al 99.99 % foil: (a) front side and (b) back side. The insets show images of higher magnification. 149

Figure 4.100: SEM images of AAO membrane (50 V, 1.5 h) by anodization of Al 99.8 % foil: (a) front side and (b) back side. The inset shows an image of higher magnification. 150

Figure 4.101: SEM image of AAO front side (40 V, 2 h, A2) before PO/DisA by anodization of Al 99 % foil. 151

Figure 4.102: SEM images of AAO membrane (40 V, 2 h) by anodization of Al 99 % foil after the DisA process: (a) front side showing widened pores and (b) nano grass formation. 151

Figure 4.103: SEM images of AAO membrane (50 V, 2 h) by anodization of Al 99 % foil and DisA process in diluted HCl/Cu^{2+}-solution showing defect structures: (a) front side with superstructures and polygonal defects, (b) back side, (c) cross-sectional view showing holes in the material too, and (d) cross-sectional view showing diagonal channels along dislocations. 152

Figure 5.1: (a) Light microscopy and (b) 3D topology laser scanning microscopy images of unpolished foils, (c, d) of polished foils. The 3D laser scanning microscope images were extended 10-fold in thez-axis. 160

Figure 5.2: (a) Light microscopy and (b) 3D topology laser scanning microscope images of unpolished, deeply scratched foils. The 3D laser scanning microscopy image was extended 10-fold in the z-axis. 160

Figure 5.3: (a) Light microscopy and (b) 3D topology laser scanning microscopy images of insufficiently polished foils using the standard polishing conditions. The 3D laser scanning microscopy image was extended 10-fold in the z-axis. 161

Figure 5.4: 3D topology laser scanning microscopy image of a 4-fold polished foil (10 – 12 V, 4 min). The 3D laser scanning microscopy image was extended 10-fold in the z-axis. 162

Figure 5.5: SEM image of anodized vanadium foil (40 V) bearing an ordered porous structure. 162
Figure 5.6: SEM images of anodized vanadium foil (40 V) showing two different appearances: (a) network structure and (b) sealed comb structure. 163
Figure 5.7: Typical current-time curve for an anodization at 40 V for 3 h, showing characteristic regions (strong decay, steady decline, exponential decay). 164
Figure 5.8: SEM images of (exemplary chosen) surface defects: (a) contrast changes indicating inhomogeneity (without change in nanostructure) and corrugations, (b) deeply etched craters... 164
Figure 5.9: SEM images of inhomogeneously anodized surface in rising magnification (a-d). Light grey areas in (a) indicate highly ordered pores, while darker areas were nonporous. . 165
Figure 5.10: SEM image of corroded surface using half-concentrated boric acid in DEG for the anodization electrolyte. 166
Figure 5.11: SEM images after anodization at 40 V with (a) 0.20 % oxalic acid (about 50 nm pore size) and (b) 0.15 % oxalic acid (about 40 nm pore size)... 166
Figure 5.12: SEM images showing residues of porous oxide: (a) dissolved pores next to capped pores and (b) layered porous structures. 168
Figure 5.13: (a) Photograph of orange vanadium oxide right after anodization (without washing process) and (b) SEM image of compact oxide showing no porous structures. 169
Figure 5.14: SEM images of different observed structures: (a) cracks on a corroded oxide surface, partially fused together, (b) rod-like structures, either by collapsing of pores or reprecipitation into (dissolved) pores, and (c) ordered pore structure of certain depth. 170
Figure 5.15: SEM image of superficial fused pores after washing with EtOH. 172
Figure 5.16: SEM images of different non-ideal washing results: (a) short nano grass on top of porous surface, (b) “coral” shaped corroded pores, (c) “molten” channels, and (d) pores of low depth.. 173
Figure 5.17: SEM images of AVO produced at 40 V and subsequently washed with acetone: (a, b) front side, (c, d) back side with either opened (by etching) or closed pores, (e, f) cross-sectional studies of oxide flakes detaching from the vanadium metal. 174
Figure 5.18: SEM images of AVO after careful washing with acetone, showing a continuous and homogeneous porous oxide layer disrupt by cracks... 175

Figure 5.19: SEM images of AVO, based on a method published by Yang *et al.*[34]: (a, c, e) images of a black product obtained, similar in appearance to results described in the present work; (b, d) images of a thick yellow oxide, non-porous but highly corroded. 177

Figure 5.20: XP spectrum of an AVO surface considering the V2p and O1s region. The inset shows a SEM image corresponding to the analyzed surface. 181

Figure 5.21: XP spectrum and fitting of vanadium foil, electropolished and Ar^+ sputtered. . 181

Figure 5.22: XP spectrum and fitting of electropolished vanadium foil. 182

Figure 5.23: XP spectrum and fitting of anodized vanadium foil (AVO). 185

Figure 5.24: XP spectrum and fitting of anodized vanadium foil (AVO) that was Ar^+ sputtered... 186

Figure 5.25: Photographs (taken by [redacted]) showing (a) the test arrangement by using the oxidized metal foil directly within a measuring cuvette, fixed by a nylon band; (b) greenish solution after the reaction indicating the formation of $ABTS^{*+}$; (c) structural formula of ABTS. 188

Figure 5.26: Catalytic activity of vanadium surfaces (polished, untreated, anodized) by determination of the slope of the absorption at 405 nm ($ABTS^{*+}$) with reaction time.......... 189

Figure 5.27: (a) Photograph (taken by [redacted]) of oxidized foil before (left) and after reaction (right). (b) Catalytic activity of anodized vanadium surfaces for three consecutively made measurements by determination of the slope of the absorption at 405 nm ($ABTS^{*+}$) with reaction time. 190

Figure 6.1: Photographs of the PTFE Setup showing (a) the bottom part with Cu contact, (b) the vessel mounted, and (c) the whole setting. 195

Figure 6.2: Photograph of a graphite rod electrode with Centering Device and thermometer. 195

Figure 6.3: Photographs of the Cu-block Setup showing (a) the single parts and (b) the mounted setup... 196

Figure 6.4: Photographs of (a) the used cooling coils from glass and PTFE and (b) the PTFE two-part vessel. 197

Figure 6.5: Photograph of the homemade rotating electrode showing the motor and the stirring part. 198

Figure 7.1: Results of a WST8-essay with Caki-1 cells. Compared with the control, two different AAO discs showed only a marginal reduction of the cell viability, equivalent to no cytotoxicity. 228

Figure 7.2: Calculation of AAO (35 V, 2 h) surface area from the isotherme at a gauge pressure p/p_0 of 0.05 – 0.3 according to the BET-method. 229

Figure 7.3: Calculation of AAO (35 V, 2 h) pore size distribution from the isotherme's adsorption branch at a gauge pressure p/p_0 of > 0.35 according to the BJH-method be based on capillary condensation. 229

Figure 7.4: SEM-EDX of AAO filter discs back sides after the filtration showing residues of NPs (compare with SEM images). The elements Au, Si and Mn could be identified, belonging to NPs. In contrast to other SEM images shown in this work, the samples were sputtered for reasons of conductivity with silver instead of gold. 230

Figure 7.5: Typical current-time curve for an electropolishing at 10 V for 4 min. 231

Figure 7.6: Typical current-time curve for an electropolishing of a deeper scratched vanadium foil at 12 V for 4 × 4 min. 231

Figure 7.7: Diffraction pattern of anodic vanadium oxide showing one to two distinctive reflexes, which can be assigned to vanadium metal. There was no contribution of any vanadium oxide except for the amorphous background. 232

Figure 7.8: SEM image of anodized vanadium oxide after annealing at 650 °C and formation of crystalline structures. 232

7.3 Aluminum

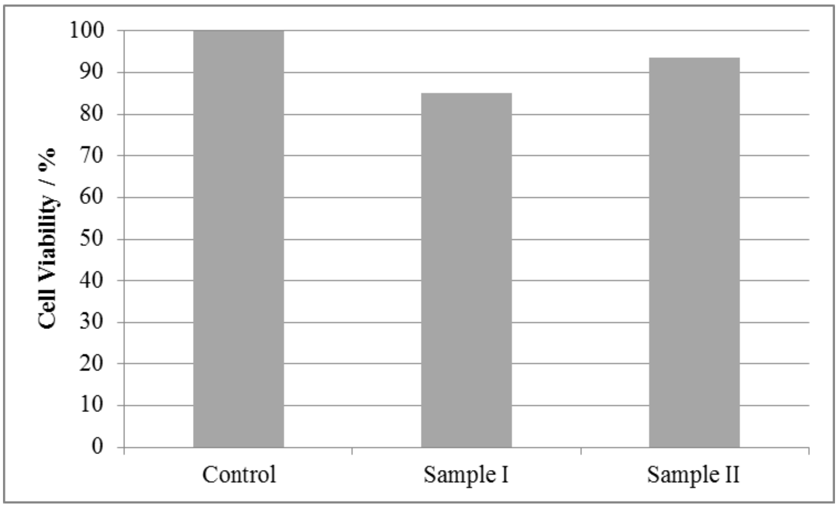

Figure 7.1: Results of a WST8-essay with Caki-1 cells. Compared with the control, two different AAO discs showed only a marginal reduction of the cell viability, equivalent to no cytotoxicity.

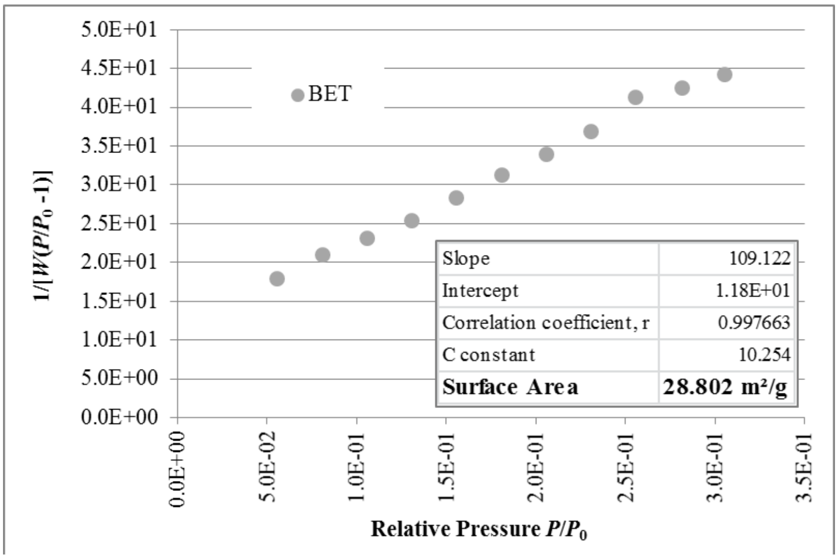

Figure 7.2: Calculation of AAO (35 V, 2 h) surface area from the isotherme at a gauge pressure p/p_0 of 0.05 – 0.3 according to the BET-method.

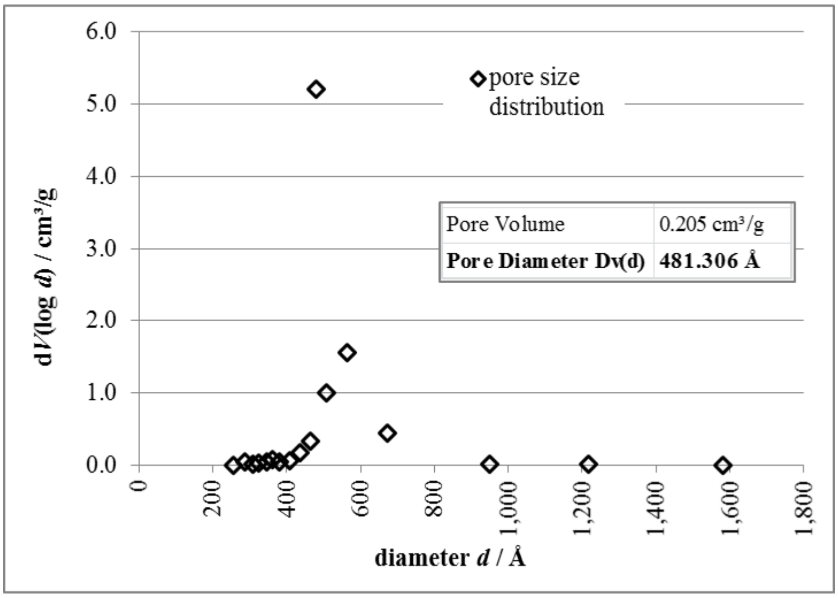

Figure 7.3: Calculation of AAO (35 V, 2 h) pore size distribution from the isotherme's adsorption branch at a gauge pressure p/p_0 of > 0.35 according to the BJH-method be based on capillary condensation.

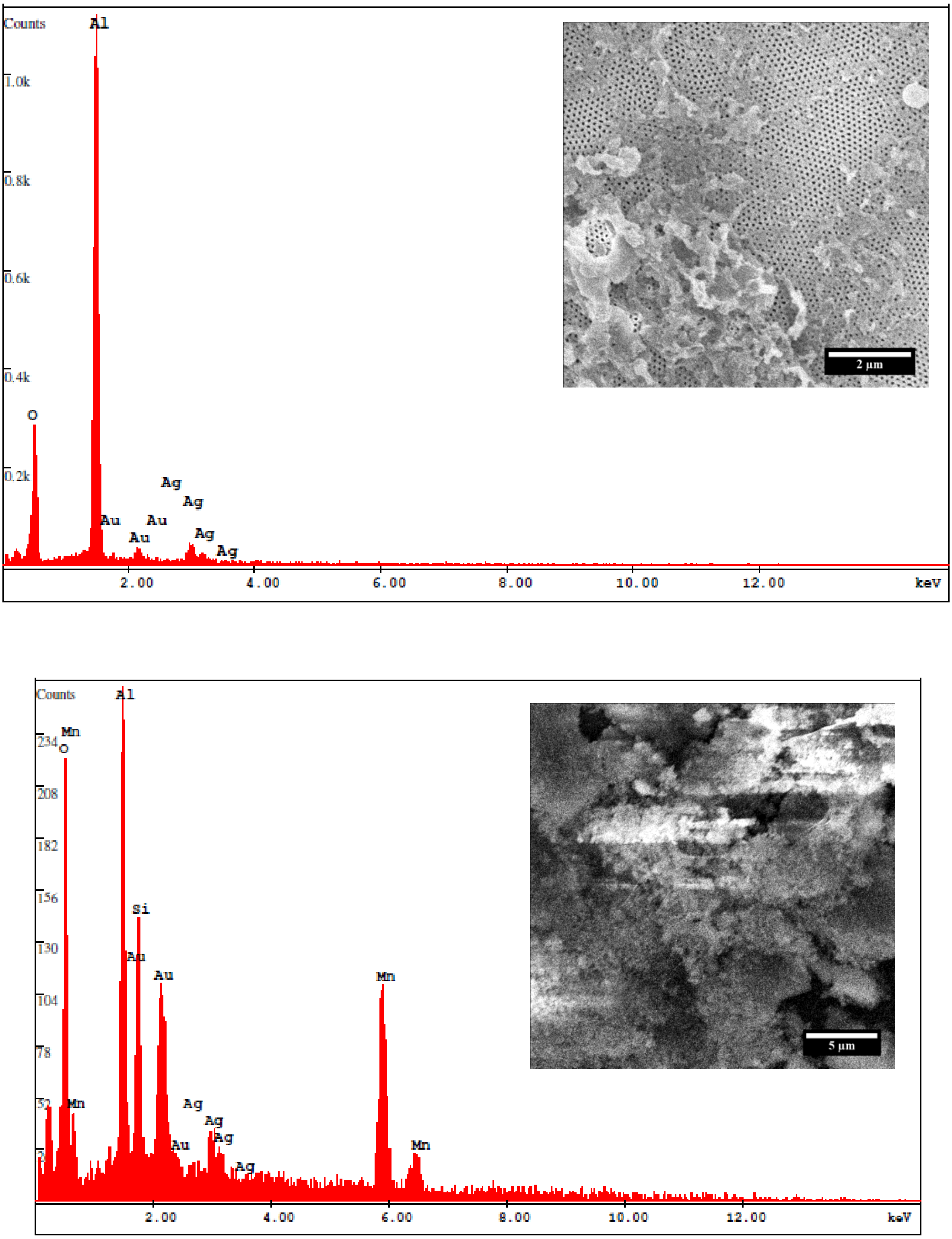

Figure 7.4: SEM-EDX of AAO filter discs back sides after the filtration showing residues of NPs (compare with SEM images). The elements Au, Si and Mn could be identified, belonging to NPs. In contrast to other SEM images shown in this work, the samples were sputtered for reasons of conductivity with silver instead of gold.

7.4 Vanadium

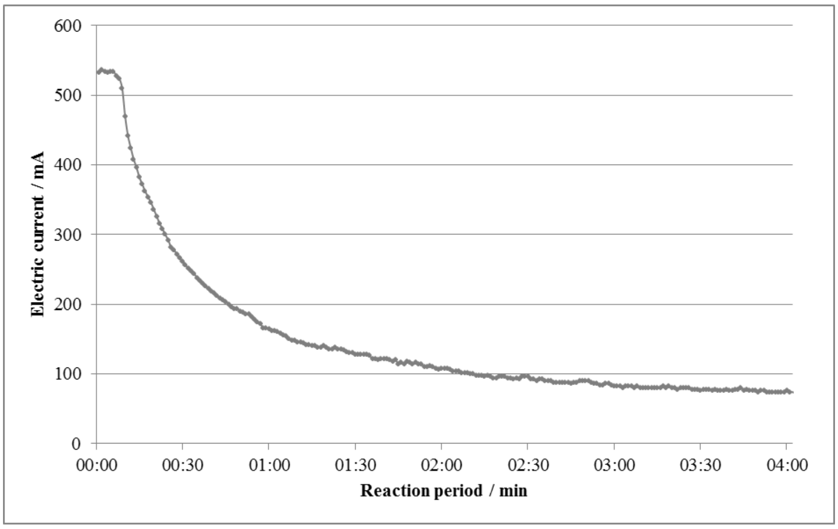

Figure 7.5: Typical current-time curve for an electropolishing at 10 V for 4 min.

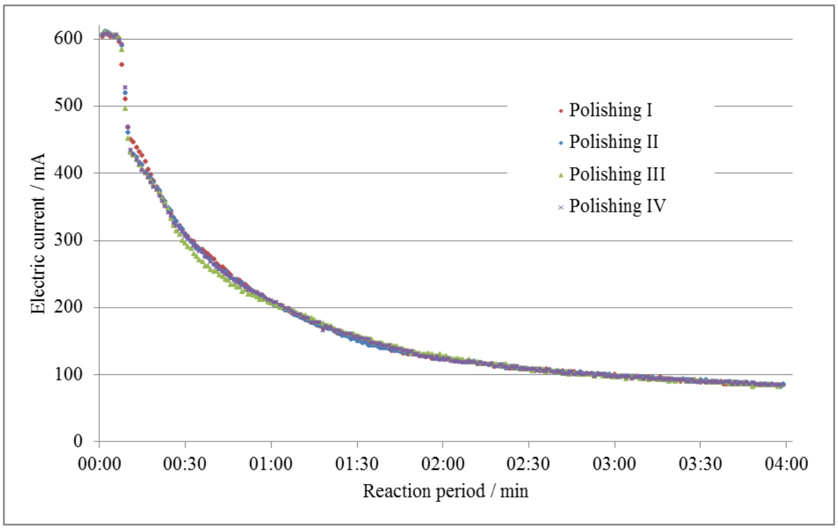

Figure 7.6: Typical current-time curve for an electropolishing of a deeper scratched vanadium foil at 12 V for 4 × 4 min.

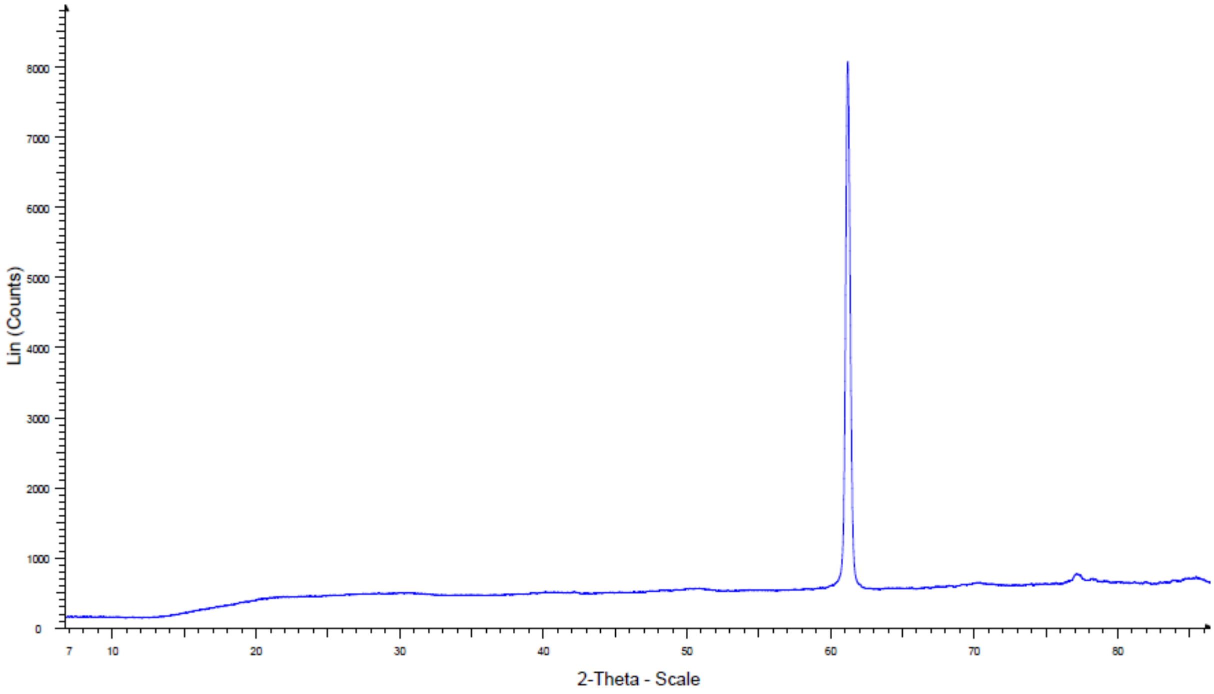

Figure 7.7: Diffraction pattern of anodic vanadium oxide showing one to two distinctive reflexes, which can be assigned to vanadium metal. There was no contribution of any vanadium oxide except for the amorphous background.

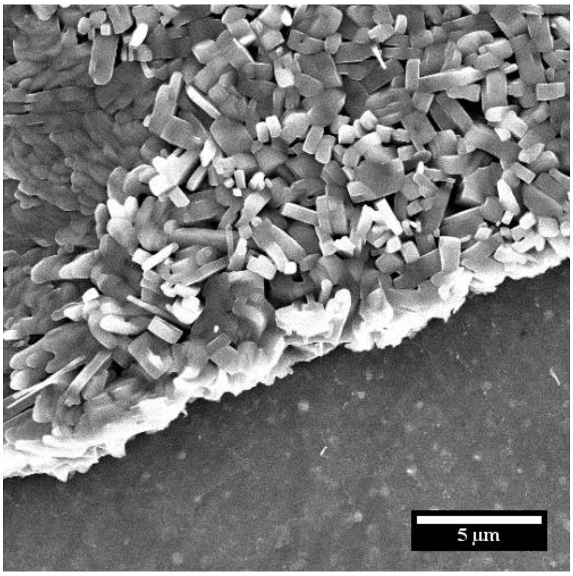

Figure 7.8: SEM image of anodized vanadium oxide after annealing at 650 °C and formation of crystalline structures.

Table 14: Raw data from the fitting of the XPS curves obtained by Unifit 2011 software (relative values).

a) polished and sputtered vanadium foil, corresponding to Figure 5.21.

Doublet	Peak height/ cps	GP-width/ eV	Position/ eV	LP-width/ eV	Asymmetry	Abs. area/ cps eV	Rel. area/ %
V (metal)	89396.7	0.76288	512.1154	0.39607	0.06	138975	53.51
	0.37527	1	7.6212	2.13166	1	71931	27.69
“VO”	0.17287	1	1.1409	3.66687	0	39169	15.08
	0.29596	1	7.6212	0.76259	0	9662	3.72

b) polished vanadium foil, corresponding to Figure 5.22.

Doublet	Peak height/ cps	GP-width/ eV	Position/ eV	LP-width/ eV	Asymmetry	Abs. area/ cps eV	Rel. area/ %
V (metal)	5804.2	0.763	512.12	0.27739	0.06	8206	4.93
	0.25803	1	7.6212	2.53968	1	2968	1.78
“VO”	0.39951	1	1.14	4.21908	0	5050	3.03
	0.34046	1	7.6212	2.18768	0	3203	1.92
V_2O_3	1.24584	1	3.0336	5	0	17818	10.7
	0.33978	1	7.6212	1.58814	0	8783	5.27
VO_2	0	1	3.6732	0	0	0	0
	0	1	7.6212	0	0	0	0
V_6O_{15}	1.40005	1	4.1261	2.80962	0	13824	8.30
	0.27749	1	7.6212	1.95012	0	6007	3.61
V_2O_5	1.46979	1	5.061	5	0	21080	12.65
	0.28456	1	7.6212	2.28697	0	11837	7.11
O1	3.67619	1.20876	18.1391	2.73657	0	38844	23.32
	0	1	0	0	0	0	0
O2	1.80699	3.38916	19.3068	0.1	0	28961	17.93
	0	1	0	0	0	0	0

c) anodized vanadium foil (AVO), corresponding to Figure 5.23.

Doublet	Peak height/ cps	GP-width/ eV	Position/ eV	LP-width/ eV	Asymmetry	Abs. area/ cps eV	Rel. area/ %
V_2O_3	2930.1	0.763	515.15	1.24467	0	6590	4.09
	0.31881	1	7.6212	1.27613	0	2559	1.59
VO_2	0.84859	1	0.617	1.02562	0	5717	3.55
	0.27194	1	7.6212	1.60486	0	2266	1.41
V_6O_{15}	1.21297	1	1.1	0.93484	0	7678	4.77
	0.38692	1	7.6212	1.30023	0	3629	2.25
V_2O_5	2.10537	1	2.03	1.58320	0	19709	12.24
	0.49029	1	7.6212	2.75807	0	23206	14.41
O1	4.4680	2.22427	15.8491	0.63095	0	34155	21.21
	0	0	0	0	0	0	0
O2	7.27175	2.84157	17.4091	0.25098	0	55517	34.48
	0	0	0	0	0	0	0

d) anodized and sputtered (depth profile) vanadium foil (AVO), corresponding to Figure 5.24.

Doublet	Peak height/ cps	GP-width/ eV	Position/ eV	LP-width/ eV	Asymmetry	Abs. area/ cps eV	Rel. area/ %
“VO”	3212.4	0.763	513.26	1.01522	0	6147	4.11
	0.48792	1	7.6212	2.09320	0	5378	3.59
V_2O_3	1.29816	1	1.87	2.55705	0	16199	10.83
	0.20909	1	7.6212	1.37852	0	4662	3.12
VO_2	1.42248	1	2.49	2.66086	0	18501	12.36
	0.32757	1	7.6212	1.32268	0	8001	5.35
V_6O_{15}	0	1	2.97	1	0	0	0
	1	1	7.6212	1	0	0	0

V_2O_5	1.24674	1	3.9	2.02178	0	13176	8.80
	0.65357	1	7.6212	3.38776	0	24668	16.48
O1	3.75815	1.62868	17.9325	0.62212	0	24002	16.04
	0	0	0	0	0	0	0
O2	2.59992	3.50983	19.3435	0.63094	0	28898	19.31
	0	0	0	0	0	0	0

8 Bibliography

[1] K. J. Klabunde (Ed.), *Nanoscale materials in chemistry*, Wiley-Interscience, New York **2001**.

[2] NanoDimension Inc., *Nanoscale* **2007**, http://www.nanodimension.com.

[3] G. A. Ozin, A. C. Arsenault, *Nanochemistry: A chemical approach to nanomaterials,* Royal Society of Chemistry, Cambridge, UK **2005**.

[4] A. Ghicov, P. Schmuki, *Chem. Commun.* **2009**.

[5] H. Cölfen, S. Mann, *Angew. Chem. Int. Ed.* **2003**, *42*, 2350.

[6] G. Whitesides, J. Mathias, C. Seto, *Science* **1991**, *254*, 1312.

[7] S. Tibbits, *Self-Assembly* **06/11/14**, http://www.selfassemblylab.net.

[8] J. J. Gooding, F. Mearns, W. Yang, J. Liu, *Electroanalysis* **2003**, *15*, 81.

[9] E. Gomar-Nadal, J. Puigmartí-Luis, D. B. Amabilino, *Chem. Soc. Rev.* **2008**, *37*, 490.

[10] J. W. Schultze, M. M. Lohrengel, *Electrochimica Acta* **2000**, *45*, 2499.

[11] Poinern, Gerrard Eddy Jai, N. Ali, D. Fawcett, *Materials* **2011**, *4*, 487.

[12] F. Keller, M. S. Hunter, D. L. Robinson, *J. Electrochem. Soc.* **1953**, *100*, 411.

[13] J. P. O'Sullivan, G. C. Wood, *Proceedings of the Royal Society of London. Series A, Mathematical and Physical Sciences (Proc. R. Soc. London, Ser. A)* **1970**, *317*, 511.

[14] G. E. Thompson, G. C. Wood, *Nature* **1981**, *290*, 230.

[15] K. Uosaki, K. Okazaki, H. Kita, H. Takahashi, *Anal. Chem.* **1990**, *62*, 652.

[16] C. R. Martin, *Science* **1994**, *266*, 1961.

[17] H. Masuda, K. Fukuda, *Science* **1995**, *268*, 1466.

[18] W. Lee, R. Ji, C. A. Ross, U. Gösele, K. Nielsch, *Small* **2006**, *2*, 978.

[19] W. Lee, R. Ji, U. Gösele, K. Nielsch, *Nat Mater* **2006**, *5*, 741.

[20] W. Lee, K. Schwirn, M. Steinhart, E. Pippel, R. Scholz, U. Gösele, *Nature Nanotech* **2008**, *3*, 234.

[21] J. J. Kelly, *Electrochimica Acta* **1979**, *24*, 1273.

[22] V. Zwilling, E. Darque-Ceretti, A. Boutry-Forveille, D. David, M. Y. Perrin, M. Aucouturier, *Surf. Interface Anal. (Surface and Interface Analysis)* **1999**, *27*, 629.

[23] V. Zwilling, M. Aucouturier, E. Darque-Ceretti, *Electrochimica Acta* **1999**, *45*, 921.

[24] H.-C. Shin, J. Dong, M. Liu, *Adv. Mater.* **2004**, *16*, 237.

[25] I. Sieber, H. Hildebrand, A. Friedrich, P. Schmuki, *Electrochemistry Communications* **2005**, *7*, 97.

[26] J. Choi, J. H. Lim, S. C. Lee, J. H. Chang, K. J. Kim, M. A. Cho, *Electrochimica Acta* **2006**, *51*, 5502.

[27] S. Berger, H. Tsuchiya, A. Ghicov, P. Schmuki, *Appl. Phys. Lett.* **2006**, *88*, 203119.

[28] H. Zheng, A. Z. Sadek, K. Latham, K. Kalantar-Zadeh, *Electrochemistry Communications* **2009**, *11*, 768.

[29] Y. Shin, S. Lee, *Nanotechnology* **2009**, *20*, 105301.

[30] S. Banerjee, S. K. Mohapatra, M. Misra, *Chem. Commun.* **2009**.

[31] T. J. LaTempa, X. Feng, M. Paulose, C. A. Grimes, *J. Phys. Chem. C* **2009**, *113*, 16293.

[32] N. K. Shrestha, M. Yang, P. Schmuki, *Electrochem. Solid-State Lett.* **2010**, *13*, C21.

[33] X. Qiu, J. Y. Howe, H. M. Meyer, E. Tuncer, M. P. Paranthaman, *Applied Surface Science* **2011**, *257*, 4075.

[34] Y. Yang, S. P. Albu, D. Kim, P. Schmuki, *Angew. Chem. Int. Ed.* **2011**, *50*, 9071.

[35] Md Jani, Abdul Mutalib, D. Losic, N. H. Voelcker, *Progress in Materials Science* **2013**, *58*, 636.

[36] H. Masuda, M. Satoh, *Jpn. J. Appl. Phys.* **1996**, *35*, L126.

[37] Guo, L.-J. Wan, C.-F. Zhu, D.-L. Yang, D.-M. Chen, C.-L. Bai, *Chem. Mater.* **2003**, *15*, 664.

[38] C. J. Brumlik, C. R. Martin, *J. Am. Chem. Soc.* **1991**, *113*, 3174.

[39] J. Bao, C. Tie, Z. Xu, Q. Zhou, D. Shen, Q. Ma, *Adv. Mater.* **2001**, *13*, 1631.

[40] P. Roy, D. Kim, K. Lee, E. Spiecker, P. Schmuki, *Nanoscale* **2010**, *2*, 45.

[41] N. K. Allam, C. A. Grimes, *Langmuir* **2009**, *25*, 7234.

[42] A. G. Kontos, A. Katsanaki, T. Maggos, V. Likodimos, A. Ghicov, D. Kim, J. Kunze, C. Vasilakos, P. Schmuki, P. Falaras, *Chemical Physics Letters* **2010**, *490*, 58.

[43] O. K. Varghese, D. Gong, M. Paulose, K. G. Ong, E. C. Dickey, C. A. Grimes, *Adv. Mater.* **2003**, *15*, 624.

[44] N. K. Shrestha, J. M. Macak, F. Schmidt-Stein, R. Hahn, C. T. Mierke, B. Fabry, P. Schmuki, *Angew. Chem. Int. Ed.* **2009**, *48*, 969.

[45] K. C. Popat, M. Eltgroth, T. J. LaTempa, C. A. Grimes, T. A. Desai, *Biomaterials* **2007**, *28*, 4880.

[46] P. Roy, S. Berger, P. Schmuki, *Angew. Chem. Int. Ed.* **2011**, *50*, 2904.

[47] M. E. Warkiani, Bhagat, Ali Asgar S., B. L. Khoo, J. Han, C. T. Lim, H. Q. Gong, A. G. Fane, *ACS Nano* **2013**, *7*, 1882.

[48] P. Stroeve, N. Ileri, *Trends in Biotechnology* **2011**, *29*, 259.

[49] H. Asoh, S. Ono, in *Electrocrystallization in Nanotechnology* (Ed.: G. Staikov), Wiley-VCH Verlag GmbH & Co. KGaA. Weinheim, Germany **2007**, p. 138.

[50] C. A. Grimes, G. K. Mor, *TiO_2 nanotube arrays: Synthesis, properties, and applications*, Springer, Dordrecht, New York **2009**.

[51] H. Tsuchiya, S. Berger, J. M. Macak, A. Ghicov, P. Schmuki, *Electrochemistry Communications* **2007**, *9*, 2397.

[52] S. Berger, H. Tsuchiya, P. Schmuki, *Chem. Mater.* **2008**, *20*, 3245.

[53] Delstar Metal Finishing, Inc., *Electropolishing: A users guide to applications, quality standards and specifications* **2003**.

[54] S. Ono, N. Masuko, *Surface and Coatings Technology* **2003**, *169-170*, 139.

[55] V. P. Parkhutik, V. I. Shershulsky, *J. Phys. D: Appl. Phys.* **1992**, *25*, 1258.

[56] V. P. Parkhutik, V. T. Belov, M. A. Chernyckh, *Electrochimica Acta* **1990**, *35*, 961.

[57] I. Brown, M. E. Bowden, T. Kemmitt, K. MacKenzie, *Current Applied Physics* **2006**, *6*, 557.

[58] S. Bauer, S. Kleber, P. Schmuki, *Electrochemistry Communications* **2006**, *8*, 1321.

[59] J. M. Macák, H. Tsuchiya, P. Schmuki, *Angew. Chem. Int. Ed.* **2005**, *44*, 2100.

[60] J. M. Macák, H. Tsuchiya, L. Taveira, S. Aldabergerova, P. Schmuki, *Angew. Chem. Int. Ed.* **2005**, *44*, 7463.

[61] K. Yasuda, J. M. Macak, S. Berger, A. Ghicov, P. Schmuki, *J. Electrochem. Soc.* **2007**, *154*, C472.

[62] S. Ono, M. Saito, M. Ishiguro, H. Asoh, *J. Electrochem. Soc.* **2004**, *151*, B473.

[63] Z. Su, W. Zhou, *Adv. Mater.* **2008**, *20*, 3663.

[64] O. Jessensky, F. Müller, U. Gösele, *Appl. Phys. Lett.* **1998**, *72*, 1173.

[65] J.-F. Vanhumbeeck, J. Proost, *Electrochimica Acta* **2008**, *53*, 6165.

[66] P. Skeldon, G. E. Thompson, S. J. Garcia-Vergara, L. Iglesias-Rubianes, C. E. Blanco-Pinzon, *Electrochem. Solid-State Lett.* **2006**, *9*, B47.

[67] S. J. Garcia-Vergara, P. Skeldon, G. E. Thompson, H. Habazaki, *Electrochimica Acta* **2006**, *52*, 681.

[68] G. Singh, A. Golovin, I. Aranson, *Phys. Rev. B* **2006**, *73*.

[69] L. Stanton, A. Golovin, *Phys. Rev. B* **2009**, *79*.

[70] K. R. Hebert, J. E. Houser, *J. Electrochem. Soc.* **2009**, *156*, C275.

[71] J. E. Houser, K. R. Hebert, *Nat Mater* **2009**, *8*, 415.

[72] G. C. Wood, *J. Electrochem. Soc.* **1996**, *143*, 74.

[73] S. P. Albu, A. Ghicov, S. Aldabergenova, P. Drechsel, D. LeClere, G. E. Thompson, J. M. Macak, P. Schmuki, *Adv. Mater.* **2008**.

[74] D. Koll, *Three Approaches Towards one Aim: Nanostructured Photovoltaic Devices*, Mainz **2011**.

[75] Y. Shin, S. Lee, *Nano Lett.* **2008**, *8*, 3171.

[76] G. K. Mor, O. K. Varghese, M. Paulose, C. A. Grimes, *Sen Lett* **2003**, *1*, 42.

[77] A. Kuhn, *Metal finishing* **2004**, *102*, 80.

[78] G. Ali, S. H. Yoo, J. M. Kum, Y. N. Kim, S. O. Cho, *Nanotechnology* **2011**, *22*, 245602.

[79] J. Macák, *Growth of Anodic Self-Organized Titanium Dioxide Nanotube Layers*, Erlangen **2008**.

[80] R. Rokicki, *Metal finishing* **1990**, *88*, 65.

[81] Z.-Z. Gu, A. Fujishima, O. Sato, *Appl. Phys. Lett.* **2004**, *85*, 5067.

[82] K. Kant, S. P. Low, A. Marshal, J. G. Shapter, D. Losic, *ACS Appl. Mater. Interfaces* **2010**, *2*, 3447.

[83] N. K. Allam, C. A. Grimes, *Solar Energy Materials and Solar Cells* **2008**, *92*, 1468.

[84] H. E. Prakasam, K. Shankar, M. Paulose, O. K. Varghese, C. A. Grimes, *J. Phys. Chem. C* **2007**, *111*, 7235.

[85] J. Wang, Z. Lin, *Chem. Mater.* **2008**, *20*, 1257.

[86] M. Paulose, H. E. Prakasam, O. K. Varghese, L. Peng, K. C. Popat, G. K. Mor, T. A. Desai, C. A. Grimes, *J. Phys. Chem. C* **2007**, *111*, 14992.

[87] J. C. Nelson, R. A. Oriani, *Corrosion Science* **1993**, *34*, 307.

[88] D. Fang, K. Huang, S. Liu, D. Qin, *Electrochemistry Communications* **2009**, *11*, 901.

[89] S. P. Albu, A. Ghicov, J. M. Macak, R. Hahn, P. Schmuki, *Nano Lett.* **2007**, *7*, 1286.

[90] J. H. Park, T.-W. Lee, M. G. Kang, *Chem. Commun.* **2008**.

[91] C.-J. Lin, W.-Y. Yu, Y.-T. Lu, S.-H. Chien, *Chem. Commun.* **2008**.

[92] J. Liao, S. Lin, X. Li, S. Li, X. Cao, Y. Cao, *Cryst. Res. Technol.* **2012**, *47*, 731.

[93] S. Banerjee, M. Misra, S. K. Mohapatra, C. Howard, S. K. Mohapatra, S. K. Kamilla, *Nanotechnology* **2010**, *21*, 145201.

[94] D. I. Petukhov, A. A. Eliseev, I. V. Kolesnik, K. S. Napolskii, A. V. Lukashin, A. V. Garshev, Y. D. Tretyakov, D. Chernyshov, W. Bras, S.-F. Chen, C.-P. Liu, *J Porous Mater* **2012**, *19*, 71.

[95] K. Kant, D. Losic, *phys. stat. sol. (RRL)* **2009**, *3*, 139.

[96] S. LI, G. ZHANG, *J. Ceram. Soc. Japan* **2010**, *118*, 291.

[97] D. Wang, L. Liu, *Chem. Mater.* **2010**, *22*, 6656.

[98] Y. Jo, I. Jung, I. Lee, J. Choi, Y. Tak, *Electrochemistry Communications* **2010**, *12*, 616.

[99] G. Liu, N. Hoivik, K. Wang, H. Jakobsen, *J Mater Sci* **2011**, *46*, 7931.

[100] S. P. Albu, A. Ghicov, S. Berger, H. Jha, P. Schmuki, *Electrochemistry Communications* **2010**, *12*, 1352.

[101] N. Haberkorn, Weber, Stefan A. L., R. Berger, P. Theato, *ACS Appl. Mater. Interfaces* **2010**, *2*, 1573.

[102] R. Zhang, K. Jiang, Y. Zhu, H. Qi, G. Ding, *Applied Surface Science* **2011**, *258*, 586.

[103] G. D. Sulka, W. J. Stępniowski, *Electrochimica Acta* **2009**, *54*, 3683.

[104] C. Y. Han, G. A. Willing, Z. Xiao, H. H. Wang, *Langmuir* **2007**, *23*, 1564.

[105] L. Zaraska, G. D. Sulka, M. Jaskuła, *J Solid State Electrochem* **2011**, *15*, 2427.

[106] M. Shimura, *J. Chem. Soc., Faraday Trans. 1* **1976**, *72*, 2248.

[107] T. T. Xu, R. D. Piner, R. S. Ruoff, *Langmuir* **2003**, *19*, 1443.

[108] J. H. Yuan, F. Y. He, D. C. Sun, X. H. Xia, *Chem. Mater.* **2004**, *16*, 1841.

[109] G. Q. Ding, M. J. Zheng, W. L. Xu, W. Z. Shen, *Nanotechnology* **2005**, *16*, 1285.

[110] F. Zhang, X. Liu, C. Pan, J. Zhu, *Nanotechnology* **2007**, *18*, 345302.

[111] Z. Su, W. Zhou, *J. Mater. Chem.* **2010**, *21*, 357.

[112] D. Lo, R. A. Budiman, *J. Electrochem. Soc.* **2007**, *154*, C60.

[113] Y. Y. Zhu, G. Q. Ding, J. N. Ding, N. Y. Yuan, *Nanoscale Res Lett* **2010**, *5*, 725.

[114] K. Itaya, S. Sugawara, K. Arai, S. Saito, *J. Chem. Eng. Jpn.* **1984**, *17*, 514.

[115] M. Lillo, D. Losic, *Journal of Membrane Science* **2009**, *327*, 11.

[116] J. Choi, G. Sauer, K. Nielsch, R. B. Wehrspohn, U. Gösele, *Chem. Mater.* **2003**, *15*, 776.

[117] W. L. Xu, H. Chen, M. J. Zheng, G. Q. Ding, W. Z. Shen, *Optical Materials* **2006**, *28*, 1160.

[118] Jani, Abdul Mutalib Md, I. M. Kempson, D. Losic, N. H. Voelcker, *Angewandte Chemie International Edition* **2010**, *49*, 7933.

[119] J. J. Schneider, J. Engstler, K. P. Budna, C. Teichert, S. Franzka, *Eur. J. Inorg. Chem.* **2005**, *2005*, 2352.

[120] K. Nielsch, J. Choi, K. Schwirn, R. B. Wehrspohn, U. Gösele, *Nano Lett.* **2002**, *2*, 677.

[121] J. Gong, W. H. Butler, G. Zangari, *Nanoscale* **2010**, *2*, 778.

[122] C.-C. Chen, Y. Bisrat, Z. P. Luo, R. E. Schaak, C.-G. Chao, D. C. Lagoudas, *Nanotechnology* **2006**, *17*, 367.

[123] Y. Zhao, M. Chen, Y. Zhang, T. Xu, W. Liu, *Materials Letters* **2005**, *59*, 40.

[124] L. Ba, W. S. Li, *J. Phys. D: Appl. Phys.* **2000**, *33*, 2527.

[125] T. Xu, G. Zangari, R. M. Metzger, *Nano Lett.* **2002**, *2*, 37.

[126] M.-N. Lin, M.-T. Lin, C. Y. Liu, M. Y. Lai, N. W. Liu, C. Y. Peng, H. H. Wang, Y. L. Wang, *Appl. Phys. Lett.* **2005**, *87*, 173116.

[127] N. Liu, C. Liu, H. Wang, C. Hsu, M. Lai, T. Chuang, Y. Wang, *Adv. Mater.* **2008**, *20*, 2547.

[128] J. Liang, H. Chik, A. Yin, J. Xu, *J. Appl. Phys.* **2002**, *91*, 2544.

[129] B. Yan, Pham, Hoa T. M., Y. Ma, Y. Zhuang, P. M. Sarro, *Appl. Phys. Lett.* **2007**, *91*, 53117.

[130] X. Jiang, N. Mishra, J. N. Turner, M. G. Spencer, *IEEE Trans. Nanotechnology* **2007**, *6*, 328.

[131] Lira, Hélio de L., R. Paterson, *Journal of Membrane Science* **2002**, *206*, 375.

[132] J. H. Yuan, W. Chen, R. J. Hui, Y. L. Hu, X. H. Xia, *Electrochimica Acta* **2006**, *51*, 4589.

[133] S. Zhao, K. Chan, A. Yelon, T. Veres, *Nanotechnology* **2007**, *18*, 245304.

[134] L. Gao, P. Wang, X. Wu, S. Yang, X. Song, *J Electroceram* **2008**, *21*, 791.

[135] A. K. Kasi, J. K. Kasi, N. Afzulpurkar, E. Bohez, A. Tuantranont, *Nanosci Nanotechnol Lett* **2012**, *4*, 530.

[136] H. Masuda, H. Asoh, M. Watanabe, K. Nishio, M. Nakao, T. Tamamura, *Adv. Mater.* **2001**, *13*, 189.

[137] R. Krishnan, C. V. Thompson, *Adv. Mater.* **2007**, *19*, 988.

[138] B. Chen, K. Lu, Z. Tian, *Langmuir* **2011**, *27*, 800.

[139] Z. Sun, H. K. Kim, *Appl. Phys. Lett.* **2002**, *81*, 3458.

[140] V. Stasi, G. Cattaneo, S. Franz, M. Bestetti, M. C. Ubaldi, D. Piccinin, S. M. Pietralunga, *Photonics and Nanostructures - Fundamentals and Applications* **2007**, *5*, 136.

[141] Maria Chong, A. S., L. K. Tan, J. Deng, H. Gao, *Adv. Funct. Mater.* **2007**, *17*, 1629.

[142] A. P. Li, F. Müller, A. Birner, K. Nielsch, U. Gösele, *J. Appl. Phys.* **1998**, *84*, 6023.

[143] R.-L. Chiu, P.-H. Chang, C.-H. Tung, *Thin Solid Films* **1995**, *260*, 47.

[144] P. P. Mardilovich, A. N. Govyadinov, N. I. Mukhurov, A. M. Rzhevskii, R. Paterson, *Journal of Membrane Science* **1995**, *98*, 131.

[145] S. Yeu, J. D. Lunn, H. M. Rangel, D. F. Shantz, *Journal of Membrane Science* **2009**, *327*, 108.

[146] A. Y. Ku, J. A. Ruud, T. A. Early, R. R. Corderman, *Langmuir* **2006**, *22*, 8277.

[147] E. D. Steinle, D. T. Mitchell, M. Wirtz, S. B. Lee, V. Y. Young, C. R. Martin, *Anal. Chem.* **2002**, *74*, 2416.

[148] Y.-H. Zhao, D. F. Shantz, *Journal of Membrane Science* **2011**, *377*, 99.

[149] L. Velleman, G. Triani, P. J. Evans, J. G. Shapter, D. Losic, *Microporous and Mesoporous Materials* **2009**, *126*, 87.

[150] V. Szczepanski, I. Vlassiouk, S. Smirnov, *Journal of Membrane Science* **2006**, *281*, 587.

[151] J. Randon, P. Blanc, R. Paterson, *Journal of Membrane Science* **1995**, *98*, 119.

[152] S.-H. Cho, N. D. Walther, S. T. Nguyen, J. T. Hupp, *Chem. Commun.* **2005**.

[153] J. ter Maat, R. Regeling, C. J. Ingham, Weijers, Carel A. G. M., M. Giesbers, de Vos, Willem M., H. Zuilhof, *Langmuir* **2011**, *27*, 13606.

[154] C. J. Ingham, J. ter Maat, de Vos, Willem M., *Biotechnology Advances* **2012**, *30*, 1089.

[155] J.-Y. Miao, Z.-L. Xu, X.-Y. Zhang, N. Wang, Z.-Y. Yang, P. Sheng, *Adv. Mater.* **2007**, *19*, 4234.

[156] D. Wang, Y. Ruan, L. Zhang, W. Zhu, P. Wang, *Crystal Research and Technology* **2013**, *48*, 348.

[157] S. G. Yang, T. Li, L. S. Huang, T. Tang, J. R. Zhang, B. X. Gu, Y. W. Du, S. Z. Shi, Y. N. Lu, *Physics Letters A* **2003**, *318*, 440.

[158] Y.-Y. Song, H. Hildebrand, P. Schmuki, *Surface Science* **2010**, *604*, 346.

[159] B. Kowalczyk, I. Lagzi, B. A. Grzybowski, *Current Opinion in Colloid & Interface Science* **2011**, *16*, 135.

[160] S. F. Sweeney, G. H. Woehrle, J. E. Hutchison, *J. Am. Chem. Soc.* **2006**, *128*, 3190.

[161] M. Baerns, *Technische Chemie*, Wiley-VCH-Verl, Weinheim **2006**.

[162] P. Marchetti, A. Butté, A. G. Livingston, *Journal of Membrane Science* **2012**, *415-416*, 444.

[163] K. P. Lee, H. Leese, D. Mattia, *Nanoscale* **2012**, *4*, 2621.

[164] D. Gong, V. Yadavalli, M. Paulose, M. Pishko, C. A. Grimes, *Biomedical Microdevices* **2003**, *5*, 75.

[165] J. R. Stephens, J. S. Beveridge, M. E. Williams, *Analyst* **2011**, *136*, 3797.

[166] T. D. Schladt, K. Koll, S. Prüfer, H. Bauer, F. Natalio, O. Dumele, R. Raidoo, S. Weber, U. Wolfrum, L. M. Schreiber, M. P. Radsak, H. Schild, W. Tremel, *J. Mater. Chem.* **2012**, *22*, 9253.

[167] I. Schick, S. Lorenz, D. Gehrig, A.-M. Schilmann, H. Bauer, M. Panthöfer, K. Fischer, D. Strand, F. Laquai, W. Tremel, *J. Am. Chem. Soc.* **2014**, *136*, 2473.

[168] T. D. Schladt, T. Graf, O. Köhler, H. Bauer, M. Dietzsch, J. Mertins, R. Branscheid, U. Kolb, W. Tremel, *Chem. Mater.* **2012**, *24*, 525.

[169] B. Nakhjavan, M. N. Tahir, M. Panthöfer, H. Gao, T. Gasi, V. Ksenofontov, R. Branscheid, S. Weber, U. Kolb, L. M. Schreiber, W. Tremel, *Chem. Commun. (Camb.)* **2011**, *47*, 8898.

[170] A. Saxena, B. P. Tripathi, M. Kumar, V. K. Shahi, *Advances in Colloid and Interface Science* **2009**, *145*, 1.

[171] N. R. Jana, L. Gearheart, C. J. Murphy, *Langmuir* **2001**, *17*, 6782.

[172] J. R. Stephens, J. S. Beveridge, A. H. Latham, M. E. Williams, *Anal. Chem.* **2010**, *82*, 3155.

[173] P.-S. Cheow, Ting, Eugene Zhi Chao, M. Q. Tan, C.-S. Toh, *Electrochimica Acta* **2008**, *53*, 4669.

[174] H. YUAN, P. CHEOW, J. ONG, C. TOH, *Sensors and Actuators B: Chemical* **2008**, *134*, 127.

[175] A. Thormann, N. Teuscher, M. Pfannmöller, U. Rothe, A. Heilmann, *Small* **2007**, *3*, 1032.

[176] C. K. Chung, R. X. Zhou, T. Y. Liu, W. T. Chang, *Nanotechnology* **2009**, *20*, 55301.

[177] S. Surnev, M. Ramsey, F. Netzer, *Progress in Surface Science* **2003**, *73*, 117.

[178] F. A. Chudnovskii, G. B. Stefanovich, *Journal of Solid State Chemistry* **1992**, *98*, 137.

[179] M. R. Parida, C. Vijayan, C. S. Rout, Sandeep, C. S. Suchand, R. Philip, P. C. Deshmukh, *J. Phys. Chem. C* **2011**, *115*, 112.

[180] O. Dvorak, J. Diers, De Armond, M. Keith, *Chem. Mater.* **1992**, *4*, 1074.

[181] T. T. Larsen-Olsen, E. Bundgaard, K. O. Sylvester-Hvid, F. C. Krebs, *Organic Electronics* **2011**, *12*, 364.

[182] B. M. Weckhuysen, D. E. Keller, *Catalysis Today* **2003**, *78*, 25.

[183] J. Döbler, M. Pritzsche, J. Sauer, *J. Am. Chem. Soc.* **2005**, *127*, 10861.

[184] V. E. Henrich, P. A. Cox, *The surface science of metal oxides*, Cambridge University Press, Cambridge, New York **1994**.

[185] R. Grabowski, B. Grzybowska, J. Haber, J. Słoczynski, *React Kinet Catal Lett* **1975**, *2*, 81.

[186] T. Blasco, J. Nieto, *Applied Catalysis A: General* **1997**, *157*, 117.

[187] M. Jayalakshmi, M. M. Rao, N. Venugopal, K.-B. Kim, *Journal of Power Sources* **2007**, *166*, 578.

[188] B. Li, Y. Xu, G. Rong, M. Jing, Y. Xie, *Nanotechnology* **2006**, *17*, 2560.

[189] C. Xiong, A. E. Aliev, B. Gnade, K. J. Balkus, *ACS Nano* **2008**, *2*, 293.

[190] M. Ghanashyam Krishna, Y. Debauge, A. K. Bhattacharya, *Thin Solid Films* **1998**, *312*, 116.

[191] Y. Wang, G. Cao, *Chem. Mater.* **2006**, *18*, 2787.

[192] J. Liu, X. Wang, Q. Peng, Y. Li, *Adv. Mater.* **2005**, *17*, 764.

[193] N. A. Chernova, M. Roppolo, A. C. Dillon, M. S. Whittingham, *J. Mater. Chem.* **2009**, *19*, 2526.

[194] P. Liu, L. Se-Hee, C. E. Tracy, Y. Yan, J. A. Turner, *Adv. Mater.* **2002**, *14*, 27.

[195] A. S. Aricò, P. Bruce, B. Scrosati, J.-M. Tarascon, W. van Schalkwijk, *Nat Mater* **2005**, *4*, 366.

[196] M. E. Spahr, P. Bitterli, R. Nesper, M. Müller, F. Krumeich, H. U. Nissen, *Angew. Chem. Int. Ed.* **1998**, *37*, 1263.

[197] V. Luca, J. M. Hook, *Chem. Mater.* **1997**, *9*, 2731.

[198] A. Manthiram, J. Kim, *Chem. Mater.* **1998**, *10*, 2895.

[199] K. Takahashi, S. J. Limmer, Y. Wang, G. Cao, *J. Phys. Chem. B* **2004**, *108*, 9795.

[200] J.-M. Jehng, G. Deo, B. M. Weckhuysen, I. E. Wachs, *Journal of Molecular Catalysis A: Chemical* **1996**, *110*, 41.

[201] G. B. Stefanovich, A. L. Pergament, A. A. Velichko, L. A. Stefanovich, *J. Phys.: Condens. Matter* **2004**, *16*, 4013.

[202] S. Hornkjøl, I. M. Hornkjøl, *Electrochimica Acta* **1991**, *36*, 577.

[203] M. B. Lewis, *J. Electrochem. Soc.* **1979**, *126*, 544.

[204] Ameer, Magda A. M., *J. Electrochem. Soc.* **1995**, *142*, 4082.

[205] R. G. Keil, R. E. Salomon, *J. Electrochem. Soc.* **1968**, *115*, 628.

[206] W. Fan, D. Kirkwood, J. Lu, S. A. Wolf, *Appl. Phys. Lett.* **2009**, *95*, 232110.

[207] Y. Yang, D. Kim, M. Yang, P. Schmuki, *Chem. Commun.* **2011**, *47*, 7746.

[208] Y. Yang, D. Kim, P. Schmuki, *Electrochemistry Communications* **2011**, *13*, 1198.

[209] E. T. Drew, Y. Yang, J. A. Russo, M. L. Campbell, S. A. Rackley, J. Hudson, P. Schmuki, D. C. Whitehead, *Catal. Sci. Technol.* **2013**, *3*, 2610.

[210] B. H. Ellis, M. A. Hopper, De Smet, D. J., *J. Electrochem. Soc.* **1971**, *118*, 860.

[211] O. Piotrowski, C. Madore, D. Landolt, *Plating and Surface Finishing* **1998**.

[212] E. M. Savitskii, *Superconducting materials*, Plenum Press, New York **1973**.

[213] J. F. Moulder, W. F. Stickle, P. E. Sobol, K. D. Bomben, *Handbook of X-Ray Photoelectron Spectroscopy*, Perkin-Elmer, Eden Prarie, MN **1992**.

[214] J. Mendialdua, R. Casanova, Y. Barbaux, *Journal of Electron Spectroscopy and Related Phenomena* **1995**, *71*, 249.

[215] N. Alov, D. Kutsko, I. Spirovová, Z. Bastl, *Surface Science* **2006**, *600*, 1628.

[216] G. Silversmit, D. Depla, H. Poelman, G. B. Marin, R. de Gryse, *Journal of Electron Spectroscopy and Related Phenomena* **2004**, *135*, 167.

[217] R. Zimmermann, R. Claessen, F. Reinert, P. Steiner, S. Hüfner, *J. Phys.: Condens. Matter* **1998**, *10*, 5697.

[218] M. C. Biesinger, L. W. Lau, A. R. Gerson, R. S. Smart, *Applied Surface Science* **2010**, *257*, 887.

[219] E. M. Oltz, R. C. Bruening, M. J. Smith, K. Kustin, K. Nakanishi, *J. Am. Chem. Soc.* **1988**, *110*, 6162.

[220] H. Vilter, *Phytochemistry* **1984**, *23*, 1387.

[221] van Schijndel, Johannes W.P.M., E. G. Vollenbroek, R. Wever, *Biochimica et Biophysica Acta (BBA) - Protein Structure and Molecular Enzymology* **1993**, *1161*, 249.

[222] E. de Boer, Y. van Kooyk, M. Tromp, H. Plat, R. Wever, *Biochimica et Biophysica Acta (BBA) - Protein Structure and Molecular Enzymology* **1986**, *869*, 48.

[223] J. S. Martinez, G. L. Carroll, R. A. Tschirret-Guth, G. Altenhoff, R. D. Little, A. Butler, *J. Am. Chem. Soc.* **2001**, *123*, 3289.

[224] ten Brink, Hilda B., A. Tuynman, H. L. Dekker, W. Hemrika, Y. Izumi, T. Oshiro, H. E. Schoemaker, R. Wever, *Inorg. Chem.* **1998**, *37*, 6780.

[225] A. Butler, M. Sandy, *Nature* **2009**, *460*, 848.

[226] ten Brink, Hilda B, H. L. Dekker, H. E. Schoemaker, R. Wever, *Journal of Inorganic Biochemistry* **2000**, *80*, 91.

[227] M. J. Clague, N. L. Keder, A. Butler, *Inorg. Chem.* **1993**, *32*, 4754.

[228] T. S. Smith, V. L. Pecoraro, *Inorg. Chem.* **2002**, *41*, 6754.

[229] H. Mimoun, L. Saussine, E. Daire, M. Postel, J. Fischer, R. Weiss, *J. Am. Chem. Soc.* **1983**, *105*, 3101.

[230] S. Velusamy, T. Punniyamurthy, *Org. Lett.* **2004**, *6*, 217.

[231] F. Cavani, N. Ballarini, A. Cericola, *Catalysis Today* **2007**, *127*, 113.

[232] A. Butler, M. J. Clague, G. E. Meister, *Chem. Rev.* **1994**, *94*, 625.

[233] U. Bora, G. Bose, M. K. Chaudhuri, S. S. Dhar, R. Gopinath, A. T. Khan, B. K. Patel, *Org. Lett.* **2000**, *2*, 247.

[234] U. Bora, M. K. Chaudhuri, D. Dey, S. S. Dhar, *Pure and Applied Chemistry* **2001**, *73*.

[235] R. André, F. Natálio, M. Humanes, J. Leppin, K. Heinze, R. Wever, H.-C. Schröder, Müller, Werner E. G., W. Tremel, *Adv. Funct. Mater.* **2011**, *21*, 501.

[236] F. Natalio, R. André, A. F. Hartog, B. Stoll, K. P. Jochum, R. Wever, W. Tremel, *Nature Nanotech* **2012**, *7*, 530.

[237] F. Natalio, R. André, S. A. Pihan, M. Humanes, R. Wever, W. Tremel, *J. Mater. Chem.* **2011**, *21*, 11923.

[238] P. Gao, M. H. Tai, D. D. Sun, *ChemPlusChem* **2013**, *78*, 1475.

[239] A. L. Ahmad, B. Koohestani, S. Bhatia, B. S. Ooi, *J Sol-Gel Sci Technol* **2013**, *67*, 221.

[240] P. C. Stair, C. Marshall, G. Xiong, H. Feng, M. J. Pellin, J. W. Elam, L. Curtiss, L. Iton, H. Kung, M. Kung, H.-H. Wang, *Top Catal* **2006**, *39*, 181.

[241] A. Butler, *Coordination Chemistry Reviews* **1999**, *187*, 17.

[242] D. C. Crans, J. J. Smee, E. Gaidamauskas, L. Yang, *Chem. Rev.* **2004**, *104*, 849.

[243] B. Wu, S. Tang, M. Chen, N. Zheng, *Chem. Commun.* **2013**, *50*, 174.

[244] Y. Zhong, F. Peng, F. Bao, S. Wang, X. Ji, L. Yang, Y. Su, S.-T. Lee, Y. He, *J. Am. Chem. Soc.* **2013**, *135*, 8350.